

---

## **Declaration**

---

This thesis describes work carried out by the author between October 2005 and March 2009 in the University Chemical Laboratory, University of Cambridge, under the supervision of Dr Melinda Duer. Except where otherwise stated, the contents are the original work of the author and nothing is contained which is the outcome of work done in collaboration. This dissertation has not previously been submitted in whole or in part for any degree or diploma at this or any other university. The number of words does not exceed sixty thousand.

Matthew Ironside  
April 2009

---

# Acknowledgements

---

First of all, a massive thanks goes to Melinda Duer for giving me the opportunity to study in her research group, and for her support, encouragement and advice.

I am also grateful to the other occupants of Room 251: Robin Stein and Robin Orr for their patience in teaching me the basics of experimental NMR; Dave Reid for his contribution to the biological aspects of the bis-phosphonate project, and his ceaseless enthusiasm and motivation; Andy Pell for assistance with L<sup>A</sup>T<sub>E</sub>X typesetting and general banter; and Erica Wise for the never-ending supply of nutritious cakey goodness and natural bone NMR spectra.

Jonathan Green (Novartis) and Steve Byard (Sanofi-Aventis) are thanked for their donation of the bis-phosphonates, zoledronate and tiludronate respectively, as is Tomislav Friščic for help with PXRD. I would like to thank the Engineering and Physical Sciences Research Council (EPSRC), Robinson College and the Experimental NMR Conference (ENC) for financial support.

And finally I must not forget my friends and family: thank you to all of you!

---

# Abstract

---

Solid-state nuclear magnetic resonance (NMR) is one of a number of techniques that comprise a chemist's toolkit for structural determination of crystalline and amorphous solids. Chapters 1–3 introduce the background theory solid-state NMR and some of the other techniques that comprise this toolkit, and then move on to describe some examples of how the toolkit, and in particular solid-state NMR, has been used previously in structural studies.

This thesis focuses mainly on one aspect within solid-state NMR, namely the chemical shift anisotropy (CSA). The CSA of a nuclear spin depends upon the local environment of that spin, and so measurement of the CSA provides a route to determine an unknown structure. Three methods have been developed for the purpose of measuring CSA more accurately. The first two methods (Chapters 4 and 5) involve improvements to the data analysis routine of two current experiments, CSA-amplified PASS and MAS-CSA. Also investigated is how to set up these experiments to get the most accurate measurement of CSA possible for a range of systems, including where two components share the same isotropic chemical shift and so have overlapping signals. The third method, detailed in Chapter 6, is an improvement of an experiment, developed by de Swiet, making the experiment less sensitive to pulse errors and reducing signal loss through relaxation, so that the CSA can be measured more accurately from the resulting spectrum. Each of the three methods are tested extensively by computer simulation, and in at least two experimental trials using  $^{31}\text{P}$ -NMR and  $^{13}\text{C}$ -NMR at natural abundance.

The final two chapters then set about using measured CSA values, alongside measurements of other NMR parameters, in structural investigations of complex systems. The first investigation, in Chapter 7, is into the conformation and dynamics of bis-phosphonate drug molecules bound to the surface of bone mineral. The second investigation, in Chapter 8, is an attempt to determine the crystal structure of an uncharacterised polymorph of a bis-phosphonate drug, neridronate. Although neither structure is completely solved in this thesis, significant progress has been made; with further work (particularly computer simulations) it is believed that the solid-state NMR data, including the CSA measurements, will prove to make a useful contribution towards a complete structural solution.

---

# Contents

---

<b>1 Solid materials</b>	<b>1</b>
1.1 Crystal structure . . . . .	2
1.2 Amorphous materials . . . . .	4
1.3 Techniques for solid materials . . . . .	5
1.4 Computational methods . . . . .	7
<b>2 Theory and principles of solid-state NMR spectroscopy</b>	<b>10</b>
2.1 Quantum mechanics of nuclear spin . . . . .	11
2.2 Free precession in a static magnetic field . . . . .	18
2.3 The Fourier transform and signal processing . . . . .	23
2.4 Nuclear spin interactions . . . . .	27
2.5 Chemical shift anisotropy . . . . .	30
2.6 Further aspects of experimental SS-NMR . . . . .	38
<b>3 Methods and applications of solid-state NMR</b>	<b>48</b>
3.1 CSA recoupling experiments . . . . .	48
3.2 Recoupling dipolar interactions . . . . .	61
3.3 SS-NMR in structural investigations . . . . .	64
<b>4 Sideband–sideband correlation</b>	<b>70</b>
4.1 Peak intensities in CSA-amplified experiments . . . . .	71
4.2 Investigation by computer simulations . . . . .	78
4.3 Experimental examples . . . . .	87
4.4 Experimental procedure . . . . .	95
4.5 Conclusions . . . . .	96
<b>5 Sideband–powder correlation</b>	<b>99</b>
5.1 MAS-CSA correlation patterns . . . . .	100
5.2 Simulations . . . . .	102
5.3 Experimental examples . . . . .	105
5.4 Experimental procedure . . . . .	110
5.5 Conclusions . . . . .	113

<b>6 The de Swiet experiment</b>	<b>115</b>
6.1 Basic theory . . . . .	116
6.2 Improved implementations . . . . .	126
6.3 Simulated examples . . . . .	140
6.4 Experimental examples . . . . .	142
6.5 Experimental procedure . . . . .	146
6.6 Conclusions . . . . .	148
<b>7 Application to bis-phosphonates bound to bone-mineral</b>	<b>150</b>
7.1 Bis-phosphonates . . . . .	151
7.2 Digested bone mineral . . . . .	156
7.3 $^{31}\text{P}$ CST measurements . . . . .	158
7.4 $^{13}\text{C}-\{^{31}\text{P}\}$ REDOR . . . . .	164
7.5 Experimental procedure . . . . .	173
7.6 Conclusions . . . . .	177
<b>8 Application to crystalline neridronate</b>	<b>179</b>
8.1 PXRD . . . . .	180
8.2 Bond angle measurements by REDOR correlation with $J$ -coupling . .	181
8.3 $^{31}\text{P}$ - $^{31}\text{P}$ DQ-SQ correlation . . . . .	187
8.4 $^{31}\text{P}$ - $^{13}\text{C}$ DCP . . . . .	189
8.5 $^1\text{H}$ - $^{31}\text{P}$ HETCOR . . . . .	191
8.6 $^1\text{H}$ - $^{13}\text{C}$ HETCOR . . . . .	192
8.7 $^{15}\text{N}$ CP-MAS and $^1\text{H}$ - $^{15}\text{N}$ HETCOR . . . . .	194
8.8 Experimental procedure . . . . .	195
8.9 Conclusions . . . . .	196
8.10 Closing remarks . . . . .	198
<b>A Euler angles</b>	<b>200</b>
<b>Bibliography</b>	<b>202</b>

## **Chapter 1**

---

# **Solid materials**

---

The study of solid-state materials poses a different set of challenges to the study of liquids or gases. In a gas, each molecule is isolated and the only interactions are within the same molecule, with the exception of occasional collisions between two molecules. Even in a liquid, where interactions between neighbouring molecules are important, in many circumstances the molecular motions are sufficiently rapid that many interactions are averaged out and the problem of calculating them is greatly simplified.

In a solid, on the other hand, the atoms and molecules remain in largely fixed positions with limited degrees of freedom available to them. The interactions and energies, and therefore the physical properties, of a solid depend on the positions of the atoms within the solid, and in particular, their distances to their neighbouring atoms, which may be in the same molecule, or in different molecules. The total energy (or any other physical property) of a solid system is therefore a function of the positions of all the atoms. If we take a tiny crystal, with a mass of only 1 ng, it could contain hundreds of billions of atoms, and the problem of understanding the structure or any physical properties is already looking quite complex. Factor in the ability of the molecules to move about a bit (around their fixed mean position) and one could be forgiven for quitting at this point and moving into an easier field, such as rocket science.

There are, however, certain shortcuts available that make the study of solids feasible. For instance, there may be patterns in the positions of atoms which, when

repeated over and over again, build up the overall macrostructure; if this is the case (i.e. a crystalline solid) then one need only identify this sub-pattern to understand the properties of the whole crystal (see Section 1.1). Even for an amorphous solid (one which does not possess a convenient repeating pattern), it is not the case that atoms are placed entirely randomly within the solid. The molecules are most likely to be in a range of similar environments where some average internuclear distances could be determined (see Section 1.2).

In either case, crystalline or amorphous, it is the structure on the atomic scale that determines the physical properties of the bulk material. It is of great interest, therefore, to find out as much as possible about the atomic structure of the solids, and a large number of experimental techniques are available to do this. One technique, solid-state nuclear magnetic resonance (NMR) spectroscopy, will comprise the main thrust of this thesis, and is reserved for the following chapters.

However, it is rarely wise to limit oneself to a single technique, since every technique, solid-state NMR included, has its own strengths and weaknesses. Sections 1.3 and 1.4, therefore, will look very briefly at a selection of alternative techniques to solid-state NMR. A number of these techniques are used (or could be used but for the limitations of time and expertise) in conjunction with solid-state NMR in Chapters 7 and 8, where some of the NMR developments that will be described in Chapters 4–6 are put into practice in the structural investigation of some simple drug molecules.

## 1.1 Crystal structure

A crystalline material is one where the structure has long-range translational symmetry. It is built up of an infinite repetition of a small block, called the unit cell. A translation by any integer multiple of the unit cell dimensions brings one to an exactly identical position in the crystal. This is demonstrated in two dimensions in Figure 1.1.

Therefore, in order to know the details of the full structure of a three-dimensional crystal, one only needs to know:

- The crystal system: this is essentially the shape of the unit cell. The options for this are triclinic, monoclinic, orthorhombic, tetragonal, rhombohedral, hexagonal and cubic.
- The unit cell dimensions, giving the translational symmetry of the crystal. This

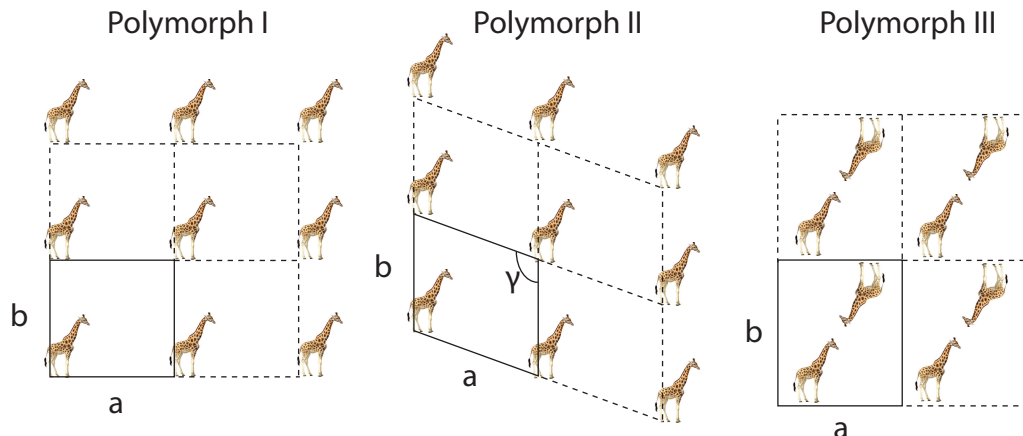


**Figure 1.1** If a giraffe is a molecule, these could be three different two-dimensional crystal structures (polymorphs) for giraffe crystals. In each case the unit cell is contained in a solid box, and the unit cell is repeated in all directions. The unit cell dimensions are the lengths of the sides of the unit cell,  $a$  and  $b$ . For polymorph I, the unit cell is square (this is its crystal system), so  $a = b$ . In polymorph II, the unit cell is oblique; that is  $a \neq b$  and the axes are not perpendicular but the angle between them is  $\gamma$ . In polymorphs I and II, all the giraffes are related by translation, and there is one giraffe per unit cell. In polymorph III, which has a rectangular crystal system, there are two giraffes per unit cell. The two giraffes in the unit cell are equivalent; the second is related to the first by rotational symmetry rather than translational symmetry. This additional symmetry is given by the identity of the space group (P2). There is one giraffe in the asymmetric unit, which is repeated twice in the unit cell, which is repeated to build up the infinite crystal structure. It is possible (not shown) that there are two or more giraffes in a unit cell that are not related by any symmetry, in which case it is said that there are multiple giraffes in the asymmetric unit. In three dimensions, the additional unit cell dimension is  $c$ , and the angles are  $\alpha$  and  $\beta$ .

can require up to three lengths and three angles to be specified (in the case of a triclinic crystal system).

- Any additional symmetry elements of the unit cell. This includes rotation axes, mirror planes, inversion centres and any translational symmetry not covered by the unit cell translations. All these are described by something known as the space group.
- The contents of the asymmetric unit, which is the smallest unit that is duplicated by the symmetry operations of the space group to give the positions of every atom within the unit cell.

For a crystalline system of unknown structure, it is these details that are sought after, by means of solid-state NMR investigation or otherwise.

### 1.1.1 Polymorphs

The same substance may have a number of different crystal structures accessible to it. The different crystal structures of the same material have different physical properties. The crystal structure that is lowest in energy is the most stable and tends to be the one that is found in nature, although the lowest energy crystal structure depends upon temperature and pressure. There may be alternative crystal structures that are similar in energy (under the same conditions) to the lowest energy structure. These may also be found in nature, either because the activation energy for their transition to the lowest energy crystal structure is very high, or because there is some external factor that encourages growth of that particular crystal structure (i.e. a template). The different crystal structures that are available to the same substance are known as polymorphs.

Polymorphs are extremely important in drug patent law. Each polymorph of a particular drug molecule needs to be identified, characterised and patented separately from the other polymorphs of the same drug molecule [1]. If a pharmaceutical company fails to find and patent all the available polymorphs of its drug molecule, then a rival company is able to exploit the gap in the patents, resulting in the loss of revenue for the drug's discoverers.

Sometimes polymorphs can be particularly hard to identify and characterise. Solid-state NMR turns out to be a very useful technique for checking for the presence of hitherto unidentified polymorphs, and characterising known polymorphs [2], for reasons such as the dependence of the chemical shift (see Section 2.4) on hydrogen bonding arrangement, which often differs between polymorphs. It is also particularly good at identifying the number of molecules in the asymmetric unit [3].

## 1.2 Amorphous materials

Amorphous materials do not have the long-range translational symmetry possessed by crystalline ones. They may however have some short-range order. For example, in silica glass, there is local order in the form of  $\text{SiO}_4$  tetrahedra which repeat throughout the structure, but the tetrahedra are essentially arranged randomly with respect to each other.

All real materials have some degree of amorphicity due to crystal defects, and there is no clear dividing line between crystalline and amorphous materials. The surfaces of otherwise crystalline materials can be partially amorphous due to surface

reconstruction\*. This surface effect is particularly important where the crystal size is very small; bone mineral is good example of this [4], that will be visited in Chapter 7.

Amorphous materials can be hard to study using diffraction techniques that depend on long-range order. Solid-state NMR relies on short-range interactions and so is especially suitable for studying amorphous systems.

### 1.3 Techniques for solid materials

A number of techniques exist for the study of solid materials, which probe different aspects of structural data. For instance, diffraction techniques probe long-range order and interatomic distances, whilst vibrational spectroscopy techniques look at particular bond strengths. Together they form a powerful toolkit for gaining a better understanding of the structure of crystalline and amorphous solids. The role of solid-state NMR in this toolkit will be explored in Section 3.3. A brief introduction will be given here to a few of the other most popular techniques, because they have been used to supplement solid-state NMR data either in this thesis, or in the works referenced by it.

#### 1.3.1 X-ray diffraction

X-ray diffraction (XRD) utilises the long-range order of a crystal to measure the size and shape of the unit cell, and the positions of all atoms within the unit cell. The X-rays are diffracted through angles that are related to the spacing between identical planes in the crystal structure. These diffraction angles can be easily (using computer software) related back to the unit cell parameters. Additionally, the intensity of a particular diffraction is determined by the positions of the atoms within the unit cell. So without very much human input, XRD can uncover the position of every atom in a crystal except hydrogens, which are missed because they diffract X-rays weakly. However, XRD requires a sizable crystal for interpretable results. Much effort has been put into growing crystals of large enough size for XRD, but this is not always possible. Problems such as twinning, and crystals that decompose or fracture in the X-ray beam add to the difficulties encountered.

---

\*This is because the atoms in the surface layer have different equilibrium positions than the atoms in the bulk, as the next layer of atoms, that would be present in an infinitely repeating crystal, is absent. The surface disorder can continue several layers of atoms back into the bulk material.

If a substance is crystalline, but the crystals are too small, one may resort to powder X-ray diffraction (PXRD). As the name suggests, this is very similar to XRD, except that the diffraction angles are measured for a powder sample and so lack the orientational information of a single crystal XRD [5]. This makes it much more difficult to determine which plane spacing gives rise to a particular diffraction angle (a process known as indexing).

A considerable amount of research has been invested in methods for determining the unit cell from PXRD data [6]. Essentially this amounts to guessing the unit cell dimensions and seeing if they fit the pattern of diffraction angles, and then refining the solution. A number of computer programs exist for this, notably ITO [7], DICVOL [8] and TREOR [9], each of which has strengths and weaknesses so it is worthwhile trying a selection of these. It is also possible to determine the positions of atoms within the unit cell, by a process known as Rietveld refinement [10], although this is decidedly non-trivial. It is helpful for PXRD to be supplemented with other techniques, such as solid-state NMR, which can provide constraints (such as a distance between two particular atoms) to narrow the search space for a solution to the powder diffraction pattern in Rietveld refinement or otherwise. However, PXRD finds particular use for identification of compounds whose structures are already known, since calculation of a powder diffraction pattern from a known unit cell is very easy, whereas the reverse is fraught with difficulty.

An alternative to X-rays is neutron diffraction; this can locate hydrogens, but usually requires  $^2\text{H}$  substitution and very large crystals [5]. Both X-ray and neutron diffraction techniques are unsuitable for the study of amorphous materials.

### 1.3.2 Raman and infra-red spectroscopy

Infra-red (IR) and Raman spectroscopies (collectively vibrational spectroscopy) are still in regular use for study of solid materials, particularly polymorph characterisation, since the equipment required is inexpensive compared to a solid-state NMR spectrometer [11]. These techniques can probe the vibrational frequency of particular bonds (or groups of bonds) in the molecule/crystal, which can depend upon the conformation of a particular functional group. Raman spectroscopy finds particular use in probing lattice vibrations, which have frequencies typically in the range of  $400\text{--}10\text{ cm}^{-1}$ .

## 1.4 Computational methods

With the ever-increasing power of modern computers, it has become common to use energy calculation to determine the lowest energy crystal structures of a particular molecule. Recently it has been found that, in favourable circumstances, accurate crystal structure prediction can be made without any experimental data [12]. However, computer simulation is even more powerful when used in conjunction with experimental techniques, since the low energy structures that are found from the calculations can have their physical properties (such as NMR or bond frequencies) calculated, and then compared to the experimental data; some examples of this using solid-state NMR will be discussed later in Section 3.3.

There are three broad categories of methods for calculating the energy of the crystal structure, into which the numerous calculation packages fall. These categories are:

- Empirical methods, using pre-determined energy functions (force fields).
- *Ab initio* (first principles) methods, using a full molecular quantum mechanical approach, such as Hartree-Fock (HF).
- Hybrid methods, such as density functional theory (DFT), having both *ab initio* and empirical components.

The basic principles of method in each of these categories, and some of the computer packages that implement them, are introduced at the end of this section.

Some of the problems or difficulties that are general to all the categories of computational methods are:

- The number of interactions (which determine the total interaction energy) grows exponentially with the number of atoms.
- The parameter space (for geometry optimisation) is very large, with three degrees of freedom for every atom.
- It is often found that there are a vast number of low energy crystal structure solutions that are very similar in energy.

- The calculated energies are approximate; the errors in energy are often bigger than the difference in the energy calculated for different structures, often leading to a false identification of the minimum energy structure.
- The different approaches to the calculation can give different minimum energy structures, or different calculated physical properties.

Even with these difficulties, computer simulations are becoming a vital part of structural studies, and the various methods are continually being developed to improve their speed and reliability. However, it is unlikely that computer simulation will ever surplant experimental observation, but they form an excellent complement to each other.

#### 1.4.1 Force field calculation

A force field calculation uses an empirically-derived energy function (force field) to calculate the interactions between atoms. It is the most simplistic of the methods and therefore is computationally undemanding; as it does not need to calculate the electron wavefunctions, it is suitable for high-throughput calculations such as global geometry optimisation. However, inaccuracies in the force field chosen can lead to substantial differences between calculated and actual energies. A number of different force fields exist that are designed for optimum accuracy in different circumstances, such as AMBER [13] for proteins.

Force field calculations can be used to assist XRD structure refinement of proteins [14], using a simulated annealing approach. They can also be used in conjunction with NMR data, and some examples of this will be described in Section 3.3.

#### 1.4.2 Hartree–Fock calculation

The HF methods [15,16] calculate the electron wavefunctions and their energies using a molecular quantum mechanical approach by linear combinations of a chosen set of basis functions. The electronic ground state is found iteratively using the variational principle, minimising the energy. The HF solution is not an exact solution to the non-relativistic Schrödinger equation, as it neglects an electron correlation term, which means that HF systematically overestimates the exact energy. This can be (partially) corrected for by use of Møller-Plesset perturbation theory [17], but this adds an additional layer of computational expense.

An HF calculation is expensive, with computational time rising rapidly with system size. Often only a small number of atoms can be included in the calculation, so it is common to only simulate a small cluster of atoms rather than whole molecules or crystals. Some popular computational programs that deal with HF calculations include GAUSSIAN [18] and GAMESS [19]. Both of these programs are also capable of DFT calculation.

#### 1.4.3 Density functional theory calculation

In DFT methods [20, 21], rather than calculating all the electron wavefunctions and their associated energies, the approximation is made that the energy of a system depends only upon the overall electron density. This misses out two very important terms from the overall energy, namely the exchange and correlation energies that result from interactions between electrons, which are obviously ignored by the approximation. These energies are reintroduced by inclusion of an exchange–correlation functional, an empirically-derived function, which has been developed to compensate for the omission of the exchange and correlation energies. There are a number of such functionals available, the choice of which is extremely important for obtaining accurate energies. The advantage of DFT over HF methods is that the computation time is greatly reduced for large systems, since the exchange–correlation energy calculation is simplified.

An additional shortcut is available for calculating energies for crystalline materials. It is known that the electron density is the same at positions that are related by translational symmetry. This can be taken advantage of by using a plane-wave basis set with periodic boundary conditions, as is done in the CASTEP code [22].

It is also possible to calculate NMR parameters using CASTEP [23]. First-principles calculation can then also be used in conjunction with solid-state NMR in structural studies, by comparing NMR parameters for low energy calculated structures with NMR experimental values. Some of the possibilities, and also the pitfalls, of this combination of CASTEP and solid-state NMR are discussed in a review article [24].

## **Chapter 2**

---

# **Theory and principles of solid-state NMR spectroscopy**

---

NMR spectroscopy utilises the nuclear magnetic moment associated with a quantum mechanical nuclear property known as spin. The behaviour of the nuclear spin magnetic moment when placed in a magnetic field crucially depends upon the local environment of the nucleus in question, and so gives a handle for discovering the nature of this local environment.

In order to understand this behaviour, it is vital to look into the fundamental quantum mechanics of nuclear spin, which is the primary purpose of Section 2.1. This is then developed to describe a very basic conceptual NMR experiment in Section 2.2, and some basic signal processing in Section 2.3, and later some more advanced experimental aspects in Section 2.6. The content of these sections is derived extensively from the references [25–27], although it is by no means specific to these sources.

The influence of local environment on the behaviour of the spins in a magnetic field is described in terms of a number of nuclear spin interactions, which are introduced in Section 2.4. One particular nuclear spin interaction, the chemical shift anisotropy (CSA), detailed in Section 2.5, will form the main focus of later chapters of this thesis, including how to measure it and how to derive structural inferences from it.

## 2.1 Quantum mechanics of nuclear spin

The state of a system, or a particular aspect of its state (here the nuclear spin), can be represented quantum mechanically by a wavefunction,  $\psi$ . The wavefunction is a mathematical function of the spatial and spin co-ordinates of the system (although, for the purposes of NMR, only the spin components are relevant), where the only restrictions on  $\psi$  are that it must be single-valued and normalised. A physical observable, such as energy or magnetic moment, can be represented by an operator,  $\hat{A}$ . The expectation value of the observable for a system in state,  $\psi$ , is given by:

$$\langle \hat{A} \rangle = \int \psi^* \hat{A} \psi \, d\tau, \quad (2.1)$$

where the integral is over all co-ordinate space.

If the wavefunction is an eigenfunction of the operator, that is:

$$\hat{A}\psi = a\psi, \quad (2.2)$$

where  $a$  is a constant, then it can be easily shown that the expectation value of the physical observable for a system in the corresponding eigenstate is  $a$ , which is called an eigenvalue of  $\hat{A}$ . The wavefunction,  $\psi$  does not have to be a solution to an eigenvalue Equation (2.2), but any  $\psi$  can be constructed as a linear combination of all the eigenfunction solutions, which form a complete orthogonal basis set. A wavefunction formed as such a mixture of eigenstates is known as a ‘superposition’ state.

One particular physical observable in NMR is the intrinsic nuclear spin angular momentum squared, which, is represented by the operator,  $\hat{I}^2$ . There are a number of solutions of the eigenvalue equation,

$$\hat{I}^2\psi_I = I(I + 1)\hbar\psi_I, \quad (2.3)$$

which are labeled with the nuclear spin quantum number,  $I$ , which can take integer or half-integer values, and the corresponding nuclear spin angular momentum squared is  $I(I + 1)\hbar$ . For a given nucleus, one particular value of  $I$  is found to have eigenstates with very much lower energy than any others, so, under any normal conditions the nucleus will be in a state with this value of  $I$ . For instance,  $^1\text{H}$ ,  $^{13}\text{C}$  and  $^{31}\text{P}$ , the main nuclei involved in this thesis, have spin  $I = 1/2$  in their ground states.

Another physical observable is the projection of the angular momentum onto the  $z$ -axis of the laboratory frame. This observable is represented by the operator,  $\hat{I}_z$ . Solutions to the eigenvalue equation for  $\hat{I}^2$  are also solutions to the eigenvalue equation for  $\hat{I}_z$ ,

$$\hat{I}_z \psi_{Im} = m\hbar\psi_{Im}. \quad (2.4)$$

Two operators which share the same eigenfunctions are said to ‘commute’. The eigenstate wavefunctions are given an additional label, a quantum number,  $m$ , which (loosely) represents the alignment of the angular momentum with the  $z$ -axis, and which can take on values between  $I$  and  $-I$  in integer steps. So for  $I = 1/2$ , there are two eigenstates that are solutions of both Equations (2.3) and (2.4), with  $m = +1/2$  and  $m = -1/2$ . The corresponding eigenvalues of Equation (2.4) are  $\pm\hbar/2$ .

### 2.1.1 A note on notation

In order to simplify the symbols used to represent wavefunctions (so that the important parts of the  $\psi_{Im}$  symbol are not hidden in the subscripts), it is useful to introduce Dirac’s ‘bra’ and ‘ket’ notation. A wavefunction is written as a ket,  $| \rangle$ , with labels such as quantum number contained inside the ket, so,  $\psi_{Im}$  becomes  $|I, m\rangle$ . The complex conjugate of a wavefunction is written similarly as a bra,  $\langle |$ , so  $\psi_{Im}^*$  becomes  $\langle I, m|$ . Additionally, if a bra and a ket are written together, with the bra to the left of the ket, it implies integration over all co-ordinate space. In this notation, Equation (2.1), for example, can be written as:

$$\langle \hat{A} \rangle = \langle I, m | \hat{A} | I, m \rangle. \quad (2.5)$$

For a spin-1/2 nucleus there are two accessible eigenstates,  $|1/2, 1/2\rangle$  and  $|1/2, -1/2\rangle$ , in Dirac’s notation. Henceforth these shall instead be shown as  $|\alpha\rangle$  and  $|\beta\rangle$  respectively. Also, from now on, the factor of  $\hbar$  in equations shall be dropped.

One final simplification to the notation will be to use matrix notation for the operators. If the basis set consists of  $n$  basis functions, then an operator can be represented as an  $n \times n$  matrix, with elements given by:

$$A_{ij} = \langle i | \hat{A} | j \rangle. \quad (2.6)$$

In the basis set of the  $|\alpha\rangle$  and  $|\beta\rangle$  states of a spin-1/2 nucleus, the angular momentum

projection operators are given by:

$$\hat{I}_x = \begin{pmatrix} 0 & 1/2 \\ 1/2 & 0 \end{pmatrix}, \quad \hat{I}_y = \begin{pmatrix} 0 & -i/2 \\ i/2 & 0 \end{pmatrix}, \quad \hat{I}_z = \begin{pmatrix} 1/2 & 0 \\ 0 & -1/2 \end{pmatrix}, \quad (2.7)$$

where  $\hat{I}_x$  and  $\hat{I}_y$  are the hitherto unmentioned projections of the spin angular momentum onto the  $x$ - and  $y$ -axes, which do not commute with each other or with  $\hat{I}_z$ . It is also useful at this point to define the raising and lowering operators,  $\hat{I}_+$  and  $\hat{I}_-$ :

$$\hat{I}_+ = \hat{I}_x + i\hat{I}_y = \begin{pmatrix} 0 & 1 \\ 0 & 0 \end{pmatrix}, \quad \hat{I}_- = \hat{I}_x - i\hat{I}_y = \begin{pmatrix} 0 & 0 \\ 1 & 0 \end{pmatrix}. \quad (2.8)$$

The importance of these operators will become apparent in Section 2.1.5.

### 2.1.2 Isolated nuclei in a static magnetic field

An NMR spectrometer consists of a large superconducting magnet, in the middle of which is a highly homogenous field in which the subject sample is positioned. A typical field strength is between 5 – 20 T. In the presence of such a field, the operator that represents the energy of the nucleus, called the Hamiltonian, is:

$$\hat{\mathcal{H}} = -\gamma B_0 \hat{I}_z, \quad (2.9)$$

where  $\gamma$  is the gyromagnetic ratio, a constant for a particular nucleus, and  $B_0$  is the magnetic field strength. The  $z$ -axis is defined as being co-incident with the magnetic field direction. The wavefunctions,  $|I, m\rangle$ , are also solutions for the eigenvalue equation  $\hat{\mathcal{H}}$ , for which the eigenvalues (which are the energies of the two states) are  $-\gamma m B_0$ . There is an energy separation,  $\gamma B_0$ , between the two eigenstates of a spin-1/2 nucleus, which gets larger with increasing field strength.

The magnetic moment along the  $z$ -axis,  $\hat{\mu}_z$ , is also proportional to  $\hat{I}_z$  and to  $\gamma$ . It is given by:

$$\hat{\mu}_z = \gamma \hat{I}_z, \quad (2.10)$$

for which the wavefunctions,  $|I, m\rangle$ , are still solutions, with eigenvalues (which are now the magnetic moments of the two states),  $m\gamma$ . Similar equations link the other components of the magnetic moment,  $\hat{\mu}_x$  and  $\hat{\mu}_y$ , to  $\hat{I}_x$  and  $\hat{I}_y$ , though since these do not commute with  $\hat{I}_z$ , they have different eigenstates.

A superposition wavefunction is written as a linear combination of the two eigenstates:

$$|\Psi\rangle = c_\alpha|\alpha\rangle + c_\beta|\beta\rangle, \quad (2.11)$$

where  $c_\alpha$  and  $c_\beta$  are the (normalised) population co-efficients of the two states. The expectation value of  $\hat{I}_z$  for this superposition state, which is proportional to the energy of the system, is given by:

$$\langle\hat{I}_z\rangle = \langle\Psi|\hat{I}_z|\Psi\rangle = \frac{1}{2}(c_\alpha^*c_\alpha - c_\beta^*c_\beta). \quad (2.12)$$

### 2.1.3 Ensembles of isolated spins

It is impossible to perform an NMR experiment on a single nucleus. In a sample there will be a large number of nuclear spins,  $N$ , known as an ensemble. Any measurement of an observable made on the system will be of the sum of the contributions from all  $N$  nuclei in the ensemble. The average value of an observable,  $\hat{A}$ , known as the ensemble average, is given by the symbol,  $\overline{\langle A \rangle}$ .

For instance, the total magnetisation along the  $z$ -axis,  $M_z$ , is the sum of the  $N$  individual magnetic moments:

$$M_z = \sum_{i=1}^N \langle\Psi^{(i)}|\hat{\mu}_z|\Psi^{(i)}\rangle = \sum_{i=1}^N \langle\Psi^{(i)}|\gamma\hat{I}_z|\Psi^{(i)}\rangle, \quad (2.13)$$

where  $\Psi^{(i)}$  is the state of the  $i^{\text{th}}$  nucleus. In terms of the ensemble average, the net  $z$ -magnetisation is:

$$M_z = N\overline{\langle\mu_z\rangle} = N\gamma\overline{\langle I_z\rangle}. \quad (2.14)$$

Now, the expectation value of  $\hat{I}_z$ , for a single spin-1/2 nucleus,  $\langle\hat{I}_z\rangle$ , was given in Equation (2.12). Taking the ensemble average of this and substituting into Equation (2.14) gives:

$$M_z = \frac{1}{2}N\gamma(\overline{c_\alpha^*c_\alpha} - \overline{c_\beta^*c_\beta}). \quad (2.15)$$

However,  $\overline{c_\alpha^*c_\alpha}$  and  $\overline{c_\beta^*c_\beta}$  can be interpreted as the probability of finding an individual spin in states  $|\alpha\rangle$  and  $|\beta\rangle$  respectively. So, summing these probabilities over the whole ensemble gives the populations of the states,  $n_\alpha$  and  $n_\beta$ , as:

$$\begin{aligned} n_\alpha &= N\overline{c_\alpha^*c_\alpha} \\ n_\beta &= N\overline{c_\beta^*c_\beta}, \end{aligned} \quad (2.16)$$

and so:

$$M_z = \frac{1}{2}\gamma(n_\alpha - n_\beta). \quad (2.17)$$

The net  $z$ -magnetisation is thus proportional to the difference in populations of the  $|\alpha\rangle$  and  $|\beta\rangle$  states. The equilibrium populations of  $|\alpha\rangle$  and  $|\beta\rangle$  can be predicted by the Boltzmann distribution from the difference in energy between the states (given by Equation (2.9)) and the temperature. In an ensemble of spins in a static magnetic field, after waiting for the system to equilibrate, there is, therefore, a net longitudinal magnetisation along the direction of the magnetic field. The expectation value of the transverse magnetisation, perpendicular to the magnetic field, is zero.

#### 2.1.4 The density operator

We define a new operator, the density operator, to be:

$$\hat{\rho} = \overline{|\Psi\rangle\langle\Psi|}, \quad (2.18)$$

where  $\Psi$  is a general superposition state. The elements of the matrix representation of this operator are then given by:

$$\rho_{ij} = \overline{\langle i|\hat{\rho}|j\rangle} \quad (2.19)$$

$$= \overline{\langle i|\Psi\rangle\langle\Psi|j\rangle}. \quad (2.20)$$

Now since all eigenfunctions (such as  $|i\rangle$  and  $|j\rangle$ ) are orthogonal, then  $\langle i|\Psi\rangle$  only picks out the  $i^{\text{th}}$ -component of  $\Psi$ , and  $\langle\Psi|j\rangle$  only picks out the  $j^{\text{th}}$ -component of  $\Psi^*$ . Thus:

$$\rho_{ij} = \overline{c_i c_j^*}. \quad (2.21)$$

The density matrix for the spin-1/2 system is:

$$\hat{\rho} = \begin{pmatrix} \overline{c_\alpha c_\alpha^*} & \overline{c_\alpha c_\beta^*} \\ \overline{c_\beta c_\alpha^*} & \overline{c_\beta c_\beta^*} \end{pmatrix}. \quad (2.22)$$

This is useful because the diagonal elements represent the populations of the  $|\alpha\rangle$  and  $|\beta\rangle$  states (the off-diagonal elements will be considered later in Section 2.1.5). The bulk  $z$ -magnetisation from Equation (2.15) can be written in terms of the elements of the density matrix:

$$M_z = \frac{1}{2}\gamma N(\rho_{\alpha\alpha} - \rho_{\beta\beta}). \quad (2.23)$$

In fact, the expectation value of any observable can be written in terms of the density matrix:

$$\langle \hat{A} \rangle = \text{Tr}(\hat{A}\hat{\rho}), \quad (2.24)$$

where the matrix of operator,  $\hat{A}$ , is in the same basis as the density matrix.

It is possible to write the density operator as a linear combination of the operators,  $\hat{I}_x$ ,  $\hat{I}_y$  and  $\hat{I}_z$ , which are given in Equation (2.7), and the identity operator,  $\hat{E}$ :

$$\hat{\rho} = c_E \hat{E} + c_x \hat{I}_x + c_y \hat{I}_y + c_z \hat{I}_z, \quad (2.25)$$

where  $c_E$ ,  $c_x$ ,  $c_y$  and  $c_z$  are the expansion co-efficients. This gives us the components of the density matrix as:

$$\hat{\rho} = \frac{1}{2} \begin{pmatrix} 2c_E + c_z & c_x - \text{i}c_y \\ c_x + \text{i}c_y & 2c_E - c_z \end{pmatrix}, \quad (2.26)$$

and the components can be equated with the previous version of the density matrix in Equation (2.22). The bulk  $z$ -magnetisation is now seen to be:

$$M_z = \frac{1}{2} \gamma N c_z, \quad (2.27)$$

and similarly for the transverse magnetisations. The identity,  $\hat{E}$ , never contributes to any observable magnetisation and so is ignored. At equilibrium,  $M_x$  and  $M_y$  (and thus  $c_x$  and  $c_y$ ) are zero, as there is no transverse magnetisation. This shows us that, for equilibrium magnetisation, aligned with the  $z$ -axis:

$$\hat{\rho}_{\text{eq}} \propto \hat{I}_z, \quad (2.28)$$

which will later prove to be a very useful result indeed. It can also be shown that a density matrix proportional to  $\hat{I}_x$  indicates a net magnetisation along the  $x$ -axis and a density matrix proportional to  $\hat{I}_y$  indicates a net magnetisation along the  $y$ -axis.

### 2.1.5 Coherence

The diagonal elements of the density matrix can be equated to the populations of the appropriate states. The off-diagonal element,  $\rho_{ij}$ , represents what is known as a coherence between the two states,  $|i\rangle$  and  $|j\rangle$ . At equilibrium, the off-diagonal elements are zero, because the spins are incoherent (random distribution of phases).

If the off-diagonal elements were somehow to be non-zero (how this can be achieved will be discussed later), this would imply that there is a coherence and a net  $x$ - or  $y$ -magnetisation, perpendicular to the direction of the magnetic field.

It is usual to talk about coherences in terms of ‘coherence order’. If there is a non-zero off-diagonal element,  $\rho_{ij}$ , then this is described as being a coherence of order,  $p$ :

$$p = \hat{I}_z|i\rangle - \hat{I}_z|j\rangle. \quad (2.29)$$

In other words, the coherence order is the difference in the quantum number,  $m$ , between the two states,  $|i\rangle$  and  $|j\rangle$ .

For the states,  $|\alpha\rangle$  and  $|\beta\rangle$ , the possible coherences are  $(+1)$ - and  $(-1)$ -quantum coherences. The  $(+1)$ -quantum coherence is the complex conjugate of the  $(-1)$ -quantum coherence; the two coherences are not independent. If, for example, the density matrix is proportional to  $\hat{I}_x$ , given in Equation (2.7), then  $\rho_{\alpha\beta} = 1/2$  and  $\rho_{\beta\alpha} = 1/2$ , and so there are equal mixtures of  $(+1)$ - and  $(-1)$ -quantum coherences. The raising and lowering operators, given in Equation (2.8), correspond to pure  $(+1)$ - and  $(-1)$ -quantum coherences respectively (though they are not physically obtainable in isolation from each other).

### 2.1.6 Time evolution of the density operator

The time-dependent Schrödinger equation, which describes how a wavefunction evolves over time is:

$$\frac{d|\Psi(t)\rangle}{dt} = -i\hat{\mathcal{H}}|\Psi(t)\rangle, \quad (2.30)$$

or equivalently in terms of the density operator:

$$\frac{d\hat{\rho}(t)}{dt} = -i(\hat{\mathcal{H}}\hat{\rho}(t) - \hat{\rho}(t)\hat{\mathcal{H}}), \quad (2.31)$$

which is the Liouville-von Neumann equation. The solution to Equation (2.31) is well-known, and is:

$$\hat{\rho}(t) = \exp(-i\hat{\mathcal{H}}t)\hat{\rho}(0)\exp(i\hat{\mathcal{H}}t). \quad (2.32)$$

If the Hamiltonian is time-dependent, each Hamiltonian that occurs in time must be applied in turn, taking care to apply them in the correct time order if the different Hamiltonians do not commute. In Equation (2.32), this means that the earliest Hamiltonians must appear in the middle, and later ones towards the outside.

## 2.2 Free precession in a static magnetic field

The Hamiltonian for a nuclear spin in static magnetic field along the  $z$ -axis is given in Equation (2.9). The solution to the time-dependent Schrödinger equation, (2.31), with this Hamiltonian, given by Equation (2.32), is:

$$\hat{\rho}(t) = \exp(i\gamma B_0 \hat{I}_z t) \hat{\rho}(0) \exp(-i\gamma B_0 \hat{I}_z t). \quad (2.33)$$

The exponential operators in Equation (2.33) can be expanded using a series expansion of  $e^x$ :

$$\exp(i\phi \hat{I}_z) = 1 + i\phi \hat{I}_z + \frac{(i\phi \hat{I}_z)^2}{2!} + \dots \quad (2.34)$$

where  $\phi = -\gamma B_0 t$ . Writing Equation (2.33) out fully using this series expansion gives:

$$\begin{aligned} \hat{\rho}(t) &= \left(1 - i\phi \hat{I}_z - \frac{\phi^2}{2} \hat{I}_z^2 + \dots\right) \hat{\rho}(0) \left(1 + i\phi \hat{I}_z - \frac{\phi^2}{2} \hat{I}_z^2 - \dots\right) \\ &= \hat{\rho}(0) - i\phi [\hat{I}_z, \hat{\rho}(0)] - \frac{\phi^2}{2} [\hat{I}_z, [\hat{I}_z, \hat{\rho}(0)]] + \dots \end{aligned} \quad (2.35)$$

where  $[\hat{A}, \hat{B}]$  indicates the commutator relationship,  $\hat{A}\hat{B} - \hat{B}\hat{A}$ .

At equilibrium, it was shown in Section 2.1.4 that  $\hat{\rho} \propto \hat{I}_z$ . Working this through Equation (2.35), using the fact that  $\hat{I}_z$  commutes with itself, gives:

$$\hat{\rho}(t) = \hat{\rho}(0) = \hat{I}_z \quad (2.36)$$

for all  $t$ . This makes sense, as if the system starts at equilibrium, and the magnetic field is maintained along the  $z$ -axis, then the system remains in at equilibrium, with the magnetisation aligned along  $z$  for all  $t$ .

### 2.2.1 Precession of transverse magnetisation

Suppose that the initial magnetisation at  $t = 0$  is aligned along the  $x$ -axis. This is equivalent to saying that  $\hat{\rho}(0) = \hat{I}_x$ , a mixture of (+1)- and (-1)-quantum coherences. This is different from the previous situation because  $\hat{I}_x$  does not commute with  $\hat{I}_z$ , but the following commutation relations are known:

$$[\hat{I}_x, \hat{I}_y] = i\hat{I}_z, \quad [\hat{I}_y, \hat{I}_z] = i\hat{I}_x, \quad [\hat{I}_z, \hat{I}_x] = i\hat{I}_y. \quad (2.37)$$

Taking these relations and working through Equation (2.35), with  $\hat{\rho}(0) = \hat{I}_x$ , gives:

$$\begin{aligned} \hat{\rho}(t) &= \hat{I}_x + \phi \hat{I}_y - \frac{\phi^2}{2} \hat{I}_x - \dots \\ &= \hat{I}_x \cos \phi + \hat{I}_y \sin \phi \end{aligned} \quad (2.38)$$

where the series expansions of  $\sin x$  and  $\cos x$  have been used to perform the final step.

A density operator proportional to  $\hat{I}_x$  indicates a net magnetisation along the  $x$ -axis, whilst a density operator proportional to  $\hat{I}_y$  indicates a net magnetisation along the  $y$ -axis. The operator,  $\hat{I}_z$ , thus acts as a rotation operator, causing a rotation of the magnetisation through angle  $\phi$  about the  $z$ -axis. Since  $\phi = -\gamma B_0 t$ , this means that if the initial magnetisation is along  $x$ , it will rotate about the  $z$ -axis, in the  $xy$ -plane, with a constant angular velocity,  $-\gamma B_0$ . This effect is known as free precession (or Larmor precession), and the angular velocity is called the Larmor frequency,  $\omega_0 = -\gamma B_0$  (taking careful note of the minus sign). It is this frequency that one wishes to measure in an NMR experiment.

The relationship in Equation (2.38) can be generalised for any initial magnetisation,  $\hat{\rho}(0)$ , and any rotation operator,  $\hat{I}_x$ ,  $\hat{I}_y$  or  $\hat{I}_z$ :

$$\hat{\rho}(t) = \hat{\rho}(0) \cos \phi - i [\hat{I}, \hat{\rho}(0)] \sin \phi, \quad (2.39)$$

using the commutation relations in Equation (2.37).

### 2.2.2 Radiofrequency pulses

This raises the question of how to prepare the magnetisation so that the initial magnetisation lies in the transverse plane. Starting off with magnetisation along the  $z$ -axis, the rotation into the  $xy$ -plane could be achieved if the magnetic field were momentarily switched to the  $y$ -axis. Assuming that this is possible, then the new Hamiltonian is:

$$\hat{\mathcal{H}} = -\gamma B_y \hat{I}_y, \quad (2.40)$$

where  $B_y$  is the magnetic field strength along the  $y$ -axis. Using Equation (2.39), with initial condition,  $\hat{\rho} = \hat{I}_z$ , the evolution of the density operator is found to follow:

$$\hat{\rho}(t) = \hat{I}_z \cos(\omega t) + \hat{I}_x \sin(\omega t), \quad (2.41)$$

where  $\omega = -\gamma B_y$ . If the time,  $t$ , that the magnetic field is along the  $y$ -axis obeys  $\omega t = \pi/2$ , then the magnetisation has been successfully transferred into the transverse plane. Once the field is returned to  $z$ , then the free precession of the transverse magnetisation described in Section 2.2.1 will occur.

So, how does one go about flipping the magnetic field to the  $y$ -axis? The answer is to use a small coil inside the superconducting magnet to produce radiofrequency (rf)

pulses. The rf wave has an oscillating magnetic field, with field strength  $2B_1$ , that is aligned with the  $y$ -axis. However, it is impossible to make this field nearly as strong as the static field,  $B_0$ , so under most circumstances it has little effect on the spins. In order to be effective the radiofrequency pulse needs to be on-resonance. To explain the effect of an rf pulse on nuclear spins, the whole problem needs to be transformed to the rotating frame.

Consider the reference frame that is rotating about the  $z$ -axis at the Larmor frequency,  $\omega_0$ . In this reference frame, the Larmor precession of an individual spin appears static, as the spins precess at the same rate as the rotation of the reference frame. Recalling that  $\omega_0 = -\gamma B_0$ , since the precession frequency in this frame of reference is zero, the apparent static  $B_0$  field is also zero.

The rf field strength along the  $y$ -axis of the laboratory frame,  $B_y$ , varies with time according to:

$$B_y(t) = 2B_1 \cos(\omega_{\text{rf}} t), \quad (2.42)$$

where  $\omega_{\text{rf}}$  is the frequency of the rf field. This can be expressed in terms of two counter-rotating components in the  $xy$ -plane:

$$B_y(t) = B_1 \exp(i\omega_{\text{rf}} t) + B_1 \exp(-i\omega_{\text{rf}} t). \quad (2.43)$$

If  $\omega_{\text{rf}}$  is set to match the Larmor frequency (i.e. the frequency of the rotating frame), one component of the rf field rotates in the opposite direction to the rotating frame. This component is off-resonance and has little effect on the magnetisation, so can be ignored. The other component of the rf field, however, is rotating in the same sense as the Larmor precession, and so appears to be static along the  $y$ -axis of the rotating frame. Since this is now the only field acting in the rotating frame, the situation has been set up where the magnetic field is, for the duration of the rf pulse, aligned with the  $y$ -axis and has field strength,  $B_1$ .

The rate of precession about the rf field, sometimes known as the pulse amplitude,  $\omega_1$ , is given by:

$$\omega_1 = -\gamma B_1. \quad (2.44)$$

The rf power is turned on for a set length of time, the pulse length,  $t_p$ , which is chosen so that  $\omega_1 t_p = \pi/2$ . The result of this is that, at the end of the rf pulse, the net magnetisation lies along the  $x$ -axis, and, once the rf field is turned off, the

magnetisation can precess about the  $z$ -axis at the Larmor frequency (or in the rotating frame, remains static).

### 2.2.3 Signal detection

All the ingredients are almost in place for a mathematical description of a very basic NMR experiment to measure the Larmor frequency. After establishing equilibrium magnetisation along the  $z$ -axis, and applying a rf pulse of given length to transfer magnetisation to the  $x$ -axis, the magnetisation is left to precess under the static magnetic field. The NMR spectrometer measures the signal in the receiver, which is a combination of the instantaneous  $x$ - and  $y$ -magnetisation in the rotating frame. In the situation described in the previous section, where the rf pulse is exactly on-resonance, the receiver would record a constant  $x$ -magnetisation and zero  $y$ -magnetisation.

It is possible that the rf and receiver frequencies (which are usually set to be the same) are not exactly on-resonance with the Larmor frequency, but differ from it by a small amount, the offset,  $\Omega$ , given by:

$$\Omega = \omega_{\text{rf}} - \omega_0. \quad (2.45)$$

In the rotating frame at the rf/receiver frequency, the transverse magnetisation appears to precess, at a rate, which is the offset,  $\Omega$ . This means that the apparent  $B_0$  is not entirely removed, but has a small value given by:

$$B_{0,\text{eff}} = -\Omega/\gamma. \quad (2.46)$$

The resultant field upon application of an rf pulse is the vector sum of this remnant of the  $B_0$  field,  $B_{0,\text{eff}}$ , and the  $B_1$  field, which, provided that  $B_{0,\text{eff}}$  is small, still lies close to the rotating frame  $y$ -axis and rotates most of the initial  $z$ -magnetisation to the  $xy$ -plane.

Once the rf pulse is over, the magnetisation will precess about  $B_{0,\text{eff}}$  in the rotating frame, with an angular velocity that is the offset,  $\Omega$ . The  $x$ - and  $y$ -components of the magnetisation evolve over time according to:

$$M_x(t) = M_0 \cos(\Omega t), \quad M_y(t) = M_0 \sin(\Omega t). \quad (2.47)$$

The complex signal,  $S(t)$ , is constructed out of these using:

$$S(t) \propto M_x(t) + iM_y(t). \quad (2.48)$$

Notice that, given in this form, the operator for the observable signal is proportional to  $\hat{I}_+$ . The expectation value for this observable is given by Equation (2.24):

$$\begin{aligned}\langle \hat{S}(t) \rangle &= \text{Tr}(\hat{I}_+ \hat{\rho}(t)) \\ &= \sum_{mn} \langle m | \hat{I}_+ | n \rangle \langle n | \hat{\rho}(t) | m \rangle \\ &= \langle \alpha | \hat{I}_+ | \beta \rangle \langle \beta | \hat{\rho}(t) | \alpha \rangle \\ &= \rho_{\beta\alpha}(t) \propto \hat{I}_-, \end{aligned}\quad (2.49)$$

which has used the fact that  $\langle m | \hat{I}_+ | n \rangle = 0$  unless  $\langle m | = \langle \alpha |$  and  $|n\rangle = |\beta\rangle$ , and all constants have been dropped. So with the signal arranged as in Equation (2.48), it is actually the  $(-1)$ -quantum coherence that is recorded. It would be simple to record the  $(+1)$ -quantum coherence, by setting up the signal as  $M_x - iM_y$ , but this would be unconventional and would not provide any additional information.

The evolution of  $(-1)$ -quantum coherence, under the rotation operator,  $\hat{I}_z$ , can be calculated using Equation (2.39):

$$\begin{aligned}\hat{\rho}(t) &= \hat{I}_- \cos \phi - i [\hat{I}_z, \hat{I}_-] \sin \phi \\ &= \hat{I}_-(\cos \phi + i \sin \phi) \\ &= \hat{I}_- \exp(i\phi), \end{aligned}\quad (2.50)$$

and so,

$$S(t) = S(0) \exp(i\phi), \quad (2.51)$$

which, since  $\phi = \Omega t$ , is equivalent to Equation (2.48).

#### 2.2.4 Relaxation

In reality, coherences do not last indefinitely. The process of relaxation leads to the returning of the system back to the equilibrium state, with the bulk nuclear spin magnetisation along the  $z$ -axis and any coherences decayed to zero. Relaxation is both a blessing and a curse.

It is helpful because it is essential to start a new experiment that the magnetisation starts off aligned with the  $z$ -axis so that the rf pulse can generate a useful coherence. The process of restoring the equilibrium  $z$ -magnetisation is called longitudinal relaxation and is characterised by the relaxation time constant,  $T_1$ , which limits the minimum delay time between successive experiments.

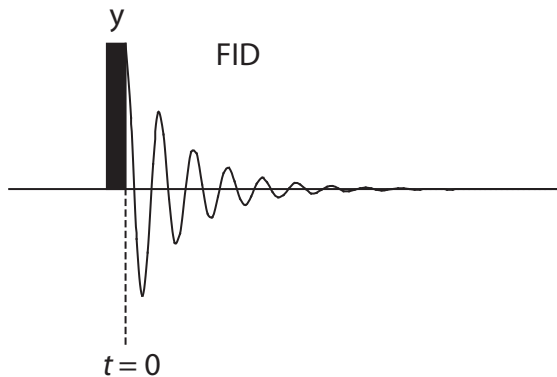


**Figure 2.1** Pulse sequence diagram for the pulse-acquire experiment. Starting at equilibrium, the solid block (with label,  $y$ ) represents an rf pulse that causes a  $90^\circ$  rotation of the magnetisation about the  $y$ -axis, which is followed by the FID, during which time the signal is measured as a function of time and is of the form given in Equation (2.52).

The hindering part of relaxation is the transverse relaxation, which is characterised by the relaxation time constant,  $T_2$ , and concerns the decay of coherences. Small, time-dependent, differences in frequencies over the volume of the sample, caused by, for example, field inhomogeneities, mean that coherences evolve at different rates, and over time become out-of-phase, or incoherent. The amount of time that a coherence survives (and the that NMR signal can be measured for) is determined by  $T_2$ .

The signal recorded, known as the free induction decay (FID), is a product of Equation (2.48) and a decay function, given by:

$$S(t) = S(0) \exp(i\Omega t) \exp\left(\frac{-t}{T_2}\right). \quad (2.52)$$

The simple experiment described so far, of an rf-pulse followed by an FID (the pulse-acquire experiment), is represented pictorially by a pulse sequence diagram, Figure 2.1. This type of diagram will be used later to display more complicated experiments.

### 2.3 The Fourier transform and signal processing

So the FID given in Equation (2.52) has been measured, but it still does not look like a familiar NMR spectrum. The FID is gives the signal as a function of time, but it is more useful to see the spectrum as a function of frequency. The transform needed to

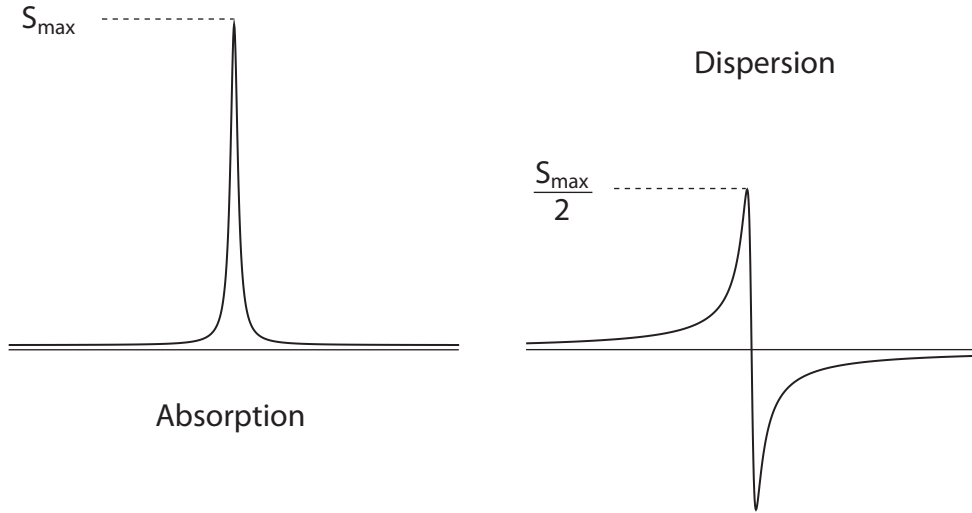


**Figure 2.2** Absorption and dispersion mode Lorentzian lineshapes. The maximum value of the absorption mode lineshape,  $S_{\max}$ , is proportional to  $T_2$ , and is double the maximum value of the dispersion mode lineshape. Also, the peak width (defined as the width of the peak at half the maximum intensity) is much smaller for the absorption mode lineshape.

perform this change is the Fourier transform, given by:

$$\begin{aligned} S(\omega) &= \int_0^\infty S(t) \exp(-i\omega t) dt \\ &= \int_0^\infty \exp(i\Omega t) \exp\left(\frac{-t}{T_2}\right) \exp(-i\omega t) dt. \end{aligned} \quad (2.53)$$

The result of this is well-known:

$$S(\omega) = S_0(\mathcal{A}(\omega) + i\mathcal{D}(\omega)), \quad (2.54)$$

where  $\mathcal{A}$  and  $\mathcal{D}$  are absorption and dispersion mode Lorentzian lineshapes given by:

$$\begin{aligned} \mathcal{A}(\omega) &= \frac{T_2}{1 + (\omega - \Omega)^2 T_2^2} \\ \mathcal{D}(\omega) &= \frac{-(\omega - \Omega) T_2^2}{1 + (\omega - \Omega)^2 T_2^2}, \end{aligned} \quad (2.55)$$

which are shown in Figure 2.2. If there are many components in a spectrum, then the resultant spectrum is the sum of the individual Lorentzian lineshapes for each component, each centered at the offset of that component.

It is highly desirable to display the absorption mode lineshape in the real (displayed) part of the spectrum. This is because the dispersion mode lineshape is much broader and the peak height is lower, which make the peaks difficult to see next to (a) other peaks, or, (b) noise.

### 2.3.1 Discrete sampling

The Fourier transform described in Equation (2.53) is really only valid for continuous data, whereas in reality the spectrometer records the signal at discrete intervals, separated by a short dwell time,  $\tau_d$ . With only a limited number of sampling points, not all frequencies can be distinguished. Any components with frequencies that are separated by integer multiples of  $2\pi/\tau_d$  (rad s<sup>-1</sup>) have the same signal at each sampling point, and so can not be distinguished by the Fourier transform. This problem is known as folding or aliasing. The maximum range of frequencies that avoid the problem of aliasing is called the spectral width, and is  $2\pi/\tau_d$  (rad s<sup>-1</sup>).

### 2.3.2 Signal averaging

The signal-to-noise ratio is the ratio of the intensity of the highest peak in the spectrum to the root mean square value of the noise in the spectrum. It is unusual that one occurrence of the pulse-acquire experiment gives a strong enough signal to be useful, as it is often shrouded in noise. An experiment must be repeated a number of times,  $N$ , and the FIDs are summed. The signal intensity increases linearly with  $N$ , but the random noise only increases with  $\sqrt{N}$ , so the signal-to-noise ratio increases by  $\sqrt{N}$ .

### 2.3.3 Phasing

It is often the case that, at  $t = 0$ , the magnetisation does not begin co-incident with the  $x$ -axis, as was assumed in Equation (2.48), but is somewhere else in the transverse plane. This can be accounted for by including a phase factor,  $\phi$ , in Equation (2.52):

$$S(t) = S_0 \exp(i(\Omega t + \phi)) \exp\left(\frac{-t}{T_2}\right). \quad (2.56)$$

This phase factor carries through the Fourier transform into Equation (2.54), which becomes:

$$S(\omega) = S_0 \exp(i\phi)(\mathcal{A}(\omega) + i\mathcal{D}(\omega)). \quad (2.57)$$

The undesirable effect of this is that there is now a portion of the unwanted dispersive Lorentzian lineshape in the real (displayed) part of the spectrum.

In order to counteract this, a phase correction is applied to the spectrum. The spectrum is multiplied by a phase correction factor,  $\exp(-i\phi)$ , in order to cancel out the phase error in the recorded spectrum, giving pure absorption lineshapes in the displayed real spectrum. However, the value of  $\phi$  is unknown in advance, so many values of  $\phi$  must be tried manually until one is found that subjectively gives the spectrum the appropriate appearance. The corrective phase factor may be linearly frequency dependent.

#### 2.3.4 Artificial linebroadening

NMR spectra have a natural linewidth due to the transverse relaxation, with a linewidth  $1/T_2$ , which comes from the formula for the absorption mode Lorentzian lineshape, Equation (2.55). It is often desirable to multiply the FID by an artificial exponential decay,  $\exp(-t/T_{lb})$ , which increases the apparent linewidth of the spectrum. The reason for doing this, is that at long times most of the desired time domain signal has decayed and most of the recorded signal is random noise. By multiplying the FID by the exponential decay (a windowing function), the weighting of the noise is reduced without significantly affecting the signal, so the overall signal-to-noise ratio is increased at the expense of resolution. Also, if the FID has not fully decayed by the end of the acquisition time, then artefacts known as sinc wiggles will appear in the spectrum; applying artificial linebroadening can make it appear as if the signal has fully decayed, thus removing these artefacts. The best choice for  $T_{lb}$  is a match for  $T_2$ , as this strikes a good balance between improving the signal-to-noise and not sacrificing too much resolution.

The windowing function does not have to be an exponential decay. The other options for windowing functions include Gaussians and shifted sine bells.

#### 2.3.5 Zero filling

The resolution of the spectrum, the ability to distinguish between two components that are close in frequency, depends on the longest time point recorded, since it is only at long time that the two components acquire a measurably different phase. Acquiring the signal for a long time is not a good idea, since if the desired signal has already completely decayed, one will just be acquiring noise. Since it is known that the signal had decayed, additional points can be added to extend the FID, which are zero-valued. This process is known as zero filling. This is done to improve the apparent resolution

of the spectrum.

## 2.4 Nuclear spin interactions

If the frequency,  $\omega_0$ , that can be measured using the basic pulse-acquire experiment described in Section 2.2, depends only upon  $\gamma$ , a constant for a given species of nucleus, and  $B_0$ , a constant for a particular spectrometer, then NMR would not have found the widespread applications in structure identification that it has done. Thankfully, there are a number of small effects depending on the local environment of a nucleus that alter the resonant frequency slightly. The changes in frequency caused by the local effects can therefore be used to draw inferences about the structure.

The spins in a sample do not only interact with the static magnetic field, but also with a small, local, magnetic field,  $\mathbf{B}_{\text{loc}}$ , that is generated within the sample by a number of sources. The only components of the internal field that have a significant effect on the spins are those parallel to  $\mathbf{B}_0$  (which either add to or subtract from  $B_0$ , altering the precession frequency), and those perpendicular to  $\mathbf{B}_0$  that are precessing at the Larmor frequency (and so behave like an rf wave).

The Hamiltonian for this local field is given by:

$$\begin{aligned}\hat{\mathcal{H}}_{\text{loc}} &= -\gamma \hat{\mathbf{I}} \cdot \mathbf{B}_{\text{loc}} \\ \mathbf{B}_{\text{loc}} &= \mathbf{A} \cdot \mathbf{S},\end{aligned}\quad (2.58)$$

where  $\hat{\mathbf{I}}$  is the vector composed of the projection operators,  $\mathbf{A}$  is a  $3 \times 3$  Cartesian tensor that represents the (orientation dependent) strength of the spin interaction, the interaction tensor, and  $\mathbf{S}$  is a vector that represents the original source of the interaction.

The interaction tensor can be written in its principal axis frame (PAF), the frame where the off-diagonal elements of the tensor are zero. The tensor in the PAF,  $\mathbf{A}^{\text{PAF}}$ , is related to the tensor in the laboratory frame,  $\mathbf{A}^{\text{lab}}$ , by a rotation. The values of the diagonal elements of the interaction tensor in its PAF are called the principal values,  $A_{xx}^{\text{PAF}}$ ,  $A_{yy}^{\text{PAF}}$  and  $A_{zz}^{\text{PAF}}$ , with the axes chosen such that:

$$|A_{yy}^{\text{PAF}} - A_{xx}^{\text{PAF}}| \leq |A_{zz}^{\text{PAF}} - A_{yy}^{\text{PAF}}| \leq |A_{zz}^{\text{PAF}} - A_{xx}^{\text{PAF}}|. \quad (2.59)$$

These principle values can instead be expressed in terms of the isotropic value,  $A_{\text{iso}}$ ,

the anisotropy,  $\Delta_A$ , and the asymmetry,  $\eta_A$ , defined by:

$$\begin{aligned} A_{\text{iso}} &= \frac{1}{3} \text{Tr}(\mathbf{A}^{\text{PAF}}) \\ \Delta_A &= A_{zz}^{\text{PAF}} - A_{\text{iso}} \\ \eta_A &= \frac{A_{yy}^{\text{PAF}} - A_{xx}^{\text{PAF}}}{\Delta_A}. \end{aligned} \quad (2.60)$$

#### 2.4.1 Dipolar, quadrupolar and $J$ -coupling

The dipolar coupling arises from the through-space interaction with the magnetic dipole of a neighbouring spin-active nucleus. The interaction tensor is given the symbol,  $\mathbf{D}$ , and the origin of the coupling is the spin on the neighbouring nucleus,  $\hat{\mathbf{I}}_2$ . The Hamiltonian for dipolar coupling is:

$$\hat{\mathcal{H}}_d = -2 \hat{\mathbf{I}}_1 \cdot \mathbf{D} \cdot \hat{\mathbf{I}}_2, \quad (2.61)$$

which acts upon the spin states of both nuclei.

The  $J$ -coupling is also caused by the interaction with the magnetic dipole of a neighbouring nucleus, except, unlike dipolar coupling, it is mediated through-bonds rather than through-space. The Hamiltonian for  $J$ -coupling is:

$$\hat{\mathcal{H}}_J = -2 \hat{\mathbf{I}}_1 \cdot \mathbf{J} \cdot \hat{\mathbf{I}}_2. \quad (2.62)$$

The key difference from the dipolar coupling is that  $\mathbf{J}$  has an isotropic component, whereas  $\mathbf{D}$  does not, as it is traceless.

The quadrupolar coupling is zero for spin-1/2 nuclei, and so it does not feature greatly in this thesis, except in the cases with an  $^{14}\text{N}$  atom directly bonded to  $^{13}\text{C}$ .

#### 2.4.2 Chemical shielding

The interaction called the chemical shielding results from the electrons near to a nuclear spin moving in response to the magnetic field and thereby creating a magnetic field of their own that counteracts the magnetic field that causes the motion, so the magnetic field experienced by the nuclear spin is reduced\*. Its interaction tensor, the chemical shielding tensor (CST), is given the symbol,  $\sigma$ . The original source of this interaction is the static field, so,  $\mathbf{S} = \mathbf{B}_0$ .

---

\*This is actually only part of the chemical shielding, the diamagnetic component. There is also a paramagnetic contribution, which augments the magnetic field.

Since much of this work will be dealing with rotations of the CST, it is useful to express the tensor in its irreducible spherical tensor form, for which the symbol  $\mathbf{A}$  shall be re-used. In this form, the Hamiltonian (previously given by Equation (2.58)) is [28]:

$$\hat{\mathcal{H}}_{\text{loc}} = -\gamma \sum_{k=0}^2 \sum_{q=-k}^k (-1)^q A_{kq}^{\text{lab}} T_{k-q}^{\text{lab}}, \quad (2.63)$$

where  $\mathbf{T}$  is an irreducible spherical tensor comprising components of the spin operator,  $\hat{I}_z$ , and the magnetic field,  $B_0$ , specifically:

$$\begin{aligned} T_{00}^{\text{lab}} &= -\frac{1}{\sqrt{3}} B_0 \hat{I}_z \\ T_{10}^{\text{lab}} &= 0 \\ T_{20}^{\text{lab}} &= \sqrt{\frac{2}{3}} B_0 \hat{I}_z. \end{aligned} \quad (2.64)$$

Components of  $\mathbf{T}$  with  $q \neq 0$  have been ignored, as, provided that  $|B_0| \gg |B_{\text{loc}}|$ , they do not affect spin evolution to the first order, which is the secular approximation [29]. The irreducible spherical tensor representation of the shielding tensor in the PAF can be written in terms of the components of the Cartesian tensor in the PAF,  $\sigma$ :

$$\begin{aligned} A_{00}^{\text{PAF}} &= \sqrt{3} \sigma_{\text{iso}} = A_{00}^{\text{lab}} \\ A_{20}^{\text{PAF}} &= -\sqrt{\frac{3}{2}} \Delta_\sigma \\ A_{21}^{\text{PAF}} &= 0 \\ A_{22}^{\text{PAF}} &= A_{2-2}^{\text{PAF}} = -\frac{1}{\sqrt{6}} \eta_\sigma A_{20}^{\text{PAF}}. \end{aligned} \quad (2.65)$$

Equation (2.63) can be expanded using Equations (2.64) and (2.65):

$$\begin{aligned} \hat{\mathcal{H}}_{\text{loc}} &= -\gamma \left( A_{00}^{\text{lab}} T_{00}^{\text{lab}} + A_{20}^{\text{lab}} T_{20}^{\text{lab}} \right) \\ &= \left( \sigma_{\text{iso}} - \sqrt{\frac{2}{3}} A_{20}^{\text{lab}} \right) \gamma B_0 \hat{I}_z. \end{aligned} \quad (2.66)$$

Adding this to the Hamiltonian for the interaction with the static magnetic field, Equation (2.9), gives the full Hamiltonian for the shielded nucleus:

$$\hat{\mathcal{H}} = \omega_0 \left( 1 - \sigma_{\text{iso}} + \sqrt{\frac{2}{3}} A_{20}^{\text{lab}} \right) \hat{I}_z. \quad (2.67)$$

The first terms in Equation (2.63) gives isotropic frequency,  $\omega_{\text{iso}}$ , which is a small correction to  $\omega_0$  caused by the isotropic shielding:

$$\omega_{\text{iso}} = \omega_0(1 - \sigma_{\text{iso}}). \quad (2.68)$$

It will also be useful to define the frequency caused by the anisotropic component as:

$$\omega_{\Delta} = \omega_0 \sqrt{\frac{2}{3}} A_{20}^{\text{lab}}. \quad (2.69)$$

In liquid-state NMR, rapid molecular tumbling leads to the  $A_{20}^{\text{lab}}$  term in Equation (2.67) averaging to zero, so the frequency that is measured is just  $\omega_{\text{iso}}$ . This frequency can be related back to the shielding and then the chemical environment surrounding the object nucleus.

Since  $\nu_{\text{iso}} = \omega_{\text{iso}}/2\pi$  is typically of the order of 100 MHz, but the full range of plausible  $\nu_{\text{iso}}$  for a given nuclear species is of the order of 20 kHz, it is usual to convert frequency into chemical shift,  $\delta_{\text{iso}}$ , relative to a reference frequency,  $\nu_{\text{ref}}$ , whereby:

$$\delta_{\text{iso}} = \frac{\nu_{\text{iso}} - \nu_{\text{ref}}}{\nu_{\text{ref}}} \times 10^6. \quad (2.70)$$

The units of  $\delta_{\text{iso}}$  are ppm.

## 2.5 Chemical shift anisotropy

In solid-state NMR, the  $A_{20}^{\text{lab}}$  term is important, as it gives rise to the property of CSA. This section will derive its effects on the NMR spectrum for a powdered solid.

A powdered solid sample contains molecules evenly distributed over every possible orientation. The orientation of the PAF with respect to the laboratory frame is described by the Euler angles,  $\Omega_{\text{PL}} = (\alpha_{\text{PL}}, \beta_{\text{PL}}, \gamma_{\text{PL}})$ , where the meaning of the angles is explained in Appendix A. The transformation of the shielding tensor (in its irreducible spherical tensor form) into the laboratory frame is given by:

$$A_{mn}^{\text{lab}} = \sum_k A_{mk}^{\text{PAF}} D_{kn}^{(2)}(\Omega_{\text{PL}}), \quad (2.71)$$

where  $\mathbf{D}^{(2)}(\Omega_{\text{PL}})$  is the Wigner rotation matrix, also described in Appendix A. According to Equation (2.67), the important component of the irreducible spherical tensor is

$A_{20}^{\text{lab}}$ . This is given by:

$$\begin{aligned} A_{20}^{\text{lab}} &= \sum_{k=-2}^2 A_{2k}^{\text{PAF}} D_{k0}^{(2)}(\Omega_{\text{PL}}) \\ &= \sum_{k=-2}^2 A_{2k}^{\text{PAF}} \exp(-ik\alpha_{\text{PL}}) d_{k0}^{(2)}(\beta_{\text{PL}}), \end{aligned} \quad (2.72)$$

where  $\mathbf{d}^{(2)}(\beta_{\text{PL}})$  is the reduced Wigner rotation matrix, also given in Appendix A, and the angle,  $\gamma_{\text{PL}}$ , is omitted as it corresponds to an inconsequential rotation about the laboratory  $z$ -axis.

Working through Equation (2.72) with definitions of the reduced Wigner rotation matrices and of the irreducible spherical tensor components (Equation (2.65)) gives:

$$A_{20}^{\text{lab}} = -\sqrt{\frac{3}{8}}\Delta_\sigma(3\cos^2\beta_{\text{PL}} - 1) + \sqrt{\frac{3}{8}}\Delta_\sigma\eta_\sigma \cos 2\alpha_{\text{PL}} \sin^2\beta_{\text{PL}}. \quad (2.73)$$

This gives the term in Equation (2.67) caused by the anisotropy for a particular crystallite with orientation,  $\Omega_{\text{PL}}$ .

The extreme limits of the value of  $A_{20}^{\text{lab}}$  are found when  $\beta_{\text{PL}} = 0$ , in which case  $A_{20}^{\text{lab}} = -\sqrt{3/2}\Delta_\sigma$ , and when  $\beta_{\text{PL}} = \pi/2$  with  $\alpha_{\text{PL}} = 0$ , in which case  $A_{20}^{\text{lab}} = \sqrt{3/8}\Delta_\sigma(\eta_\sigma + 1)$ . These situations correspond to, firstly, the  $z$ -axis of the PAF being aligned with the magnetic field, and secondly the  $x$ -axis of the PAF being aligned with the magnetic field. The precession frequencies when one of the three principal axes of the shielding tensor are aligned with the magnetic field,  $\omega_x$ ,  $\omega_y$  and  $\omega_z$ , using Equation (2.67), are:

$$\begin{aligned} \omega_z &= \omega_{\text{iso}} + \Delta_\omega \\ \omega_x &= \omega_{\text{iso}} - \frac{1}{2}\Delta_\omega(1 + \eta_\sigma) \\ \omega_y &= \omega_{\text{iso}} - \frac{1}{2}\Delta_\omega(1 - \eta_\sigma), \end{aligned} \quad (2.74)$$

where  $\Delta_\omega$  is the anisotropy of the CST in frequency units, given by  $\Delta_\omega = -\omega_0\Delta_\sigma$  (not to be confused with  $\omega_\Delta$ , which is the anisotropic frequency of a particular crystallite). In between  $\omega_x$  and  $\omega_z$ , there is a continuum of possible frequencies in a powder sample. The resulting spectrum does not show sharp peaks, but a broad peak, centered at  $\omega_{\text{iso}}$ , called a powder pattern, that is the sum of the contribution from every possible crystallite orientation.

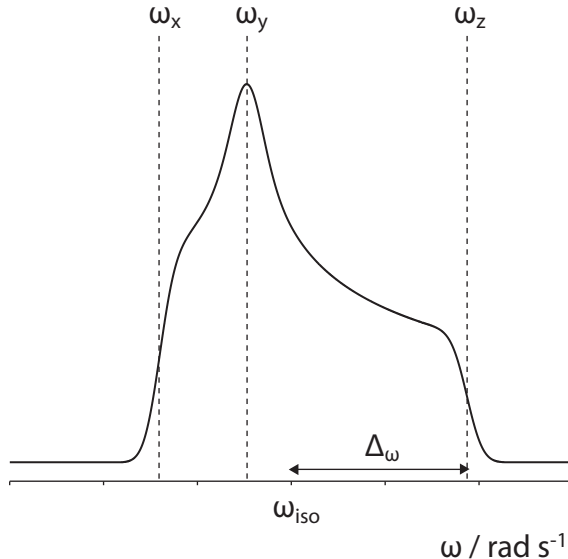


**Figure 2.3** Simulated spectrum showing an example of the form of a powder pattern arising from the CSA. Marked on the spectrum are the principal values, in frequency units, given by Equation (2.74), and the anisotropy, also in frequency units, where  $\Delta_\omega = -\omega_0 \Delta_\sigma$ . The isotropic frequency,  $\omega_{\text{iso}}$ , is in the middle of the spectrum. The asymmetry, which is dimensionless, is  $\eta = 0.5$ .

Powder patterns have a distinctive intensity profile, whose mathematical form is well-known [30]. The typical shape of a powder pattern is shown in Figure 2.3. Whenever powder patterns are calculated in this thesis, however, they will be calculated numerically by summing contributions from a large number of pre-selected orientations, known as a crystallite set. The orientation angles are chosen using the ZCW [31–33] or REPULSION [34] algorithms, which are designed to spread the orientations out as evenly as possible over the surface of a sphere (or part of a sphere).

Powder patterns can be useful because the principal values of the CST can be easily identified with the discontinuities in the powder pattern; they can be read from the spectrum by eye. More commonly, though, the full powder pattern lineshape is fitted to the CST parameters using a least-squares procedure, although it has been suggested that a better procedure is fitting the first derivative powder pattern and only in the three regions around the principal values would be superior [35]. This avoids influence of any errors in the intermediate region, where the spectrum is relatively insensitive to the CST.

A major problem with powder patterns, though, is that if there is more than one

different chemical site in the sample, then the powder patterns from the different chemical sites will overlap, and the features become lost.

### 2.5.1 Magic-angle spinning

Magic-angle spinning [36, 37] (MAS) has become ubiquitous in solid-state NMR as a solution to the problem of the lack of resolution of broad powder pattern signals. In this technique, the sample is loaded into a zirconia rotor, and spun inside the magnet at a very high rate (typically 2–15 kHz), tilted at a predefined angle to the magnetic field.

To deal with this situation, a new reference frame, the rotor frame, is introduced. The rotor frame is the frame which is tilted at the rotor angle,  $\theta_R$ , to the magnetic field, and rotating at the spinning frequency,  $\omega_R$ , about the rotor frame  $z$ -axis. In a powder, the orientation of the PAF of an individual crystallite to the rotor frame is  $\Omega_{PR}$ , and the orientation of the rotor frame with respect to the laboratory frame is  $\Omega_{RL}$ , which is time-dependent and given by:

$$\Omega_{RL}(t) = (\alpha_{RL}(0) - \omega_R t, \beta_{RL}, 0), \quad (2.75)$$

where  $\alpha_{RL}(0)$  gives the arbitrary orientation of the rotor at  $t = 0$ , and  $\beta_{RL}$  is fixed and equal to the rotor angle,  $\theta_R$ .

In order to calculate the components of the shielding tensor of a particular crystallite in the laboratory frame, the tensor in the PAF must first be transformed to the rotor frame and then to the laboratory frame, for which the transformation is given by:

$$\begin{aligned} A_{20}^{\text{lab}}(t) &= \sum_{m=-2}^2 \sum_{n=-2}^2 A_{2m}^{\text{PAF}} D_{mn}^{(2)}(\Omega_{PR}) D_{n0}^{(2)}(\Omega_{RL}(t)) \\ &= \sum_{m=-2}^2 \sum_{n=-2}^2 A_{2m}^{\text{PAF}} D_{mn}^{(2)}(\Omega_{PR}) \exp(-in(\alpha_{RL}(0) - \omega_R t)) d_{n0}^{(2)}(\beta_{RL}). \end{aligned} \quad (2.76)$$

Now if the rotor angle is set to the magic angle, which is  $54.7^\circ$ , then  $d_{00}^{(2)} = \cos^2 \beta - 1 = 0$ , and so all terms in Equation (2.76) with  $n = 0$  drop out. The remaining terms all oscillate with  $\exp(in\omega_R t)$  dependency. If  $\omega_R$  is large compared with  $\Delta_\omega$  then these terms oscillate rapidly, preventing any influence of  $A_{2m}^{\text{PAF}}$  on the magnetisation evolution. This leaves only the influence of the isotropic shift, and leads to a spectrum with one sharp peak per chemical site.

### 2.5.2 Spinning sideband spectra

If  $\omega_R$  is not very large compared with  $\Delta_\omega$ , then anisotropy can influence the final spectrum. For the general case of a sample rotating at the magic-angle, the signal at time,  $t$ , after preparation of transverse magnetisation along the rotating frame  $x$ -axis, is (omitting relaxation):

$$S(t; \Omega_{PR}) = \exp(i\Phi(t, 0; \Omega_{PR})), \quad (2.77)$$

where,  $\Phi(t_b, t_a; \Omega_{PR})$  is the integrated phase function given by:

$$\Phi(t_b, t_a; \Omega_{PR}) = \int_{t_a}^{t_b} \omega(t; \Omega_{PR}) dt, \quad (2.78)$$

where  $\omega(t; \Omega_{PR})$  is the resonance frequency of a particular crystallite with orientation,  $\Omega_{PR}$ , at time,  $t$ .

The anisotropic frequency under MAS, combining Equation (2.69) and Equation (2.76), can be split into the sum of components with different time-dependencies:

$$\omega_\Delta(t; \Omega_{PR}) = \sum_{n=-2}^2 \omega_\Delta^{(n)}(\Omega_{PR}) \exp(in\omega_R t), \quad (2.79)$$

with  $n \neq 0$ , and where the time-independent anisotropic frequencies are given by:

$$\omega_\Delta^{(n)}(\Omega_{PR}) = \omega_0 \sqrt{\frac{2}{3}} \sum_{m=-2}^2 A_{2m}^{\text{PAF}} D_{mn}^{(2)}(\Omega_{PR}) d_{n0}^{(2)}(\beta_{RL}) \exp(-in\alpha_{RL}(0)). \quad (2.80)$$

The value of  $\alpha_{RL}(0)$  is arbitrary and is omitted, as it can be combined with the  $\gamma$  orientation Euler angle within  $\Omega_{PR}$ . Combining Equation (2.80) with the isotropic frequency component of the precession frequency to generate the resonance frequency for crystallite orientation  $\Omega_{PR}$ , i.e.  $\omega(t; \Omega_{PR})$  in Equation (2.78), and integrating over time gives:

$$\Phi(t_b, t_a; \Omega_{PR}) = \omega_{\text{iso}}(t_b - t_a) + \xi(t_b; \Omega_{PR}) - \xi(t_a; \Omega_{PR}), \quad (2.81)$$

where,

$$\xi(t; \Omega_{PR}) = \sum_{n \neq 0} \frac{\omega_\Delta^{(n)}(\Omega_{PR}) \exp(in\omega_R t)}{in\omega_R}. \quad (2.82)$$

The anisotropic  $\xi$  terms in Equation (2.81) are periodic with the rotor cycle. The signal,

$$S(t; \Omega_{PR}) = \exp \{ i[\omega_{\text{iso}}t + \xi(t; \Omega_{PR}) - \xi(0; \Omega_{PR})] \}, \quad (2.83)$$

therefore, has this property:

$$S(t + m\tau_R; \Omega_{PR}) = S(t; \Omega_{PR}) \exp(i m \omega_{iso} \tau_R), \quad (2.84)$$

where  $\tau_R$  is the rotor period,  $2\pi/\omega_R$ , and  $m$  is an integer. The signal can then be written as a Fourier series:

$$S(t; \Omega_{PR}) = \sum_k F^{(k)}(\Omega_{PR}) \exp\{i(\omega_{iso} + k\omega_R)t\}. \quad (2.85)$$

The Fourier transform of this signal gives a series of lines (sidebands) at frequencies,  $\omega_{iso} + k\omega_R$ , where  $k$  is an integer. The intensity of the  $k^{\text{th}}$  sideband is given by a complex factor,  $F^{(k)}(\Omega_{PR})$ . An example of such a spectrum is given in Figure 2.4.

The anisotropic frequency terms in Equation (2.81) vanish in the limit of high  $\omega_R$ , again demonstrating that with sufficiently high MAS rates, the spectrum reduces to a single line at  $\omega_{iso}$ . At lower spinning rates, the sideband intensities are found using:

$$\begin{aligned} F^{(k)}(\Omega_{PR}) &= \frac{1}{\tau_R} \int_{t=0}^{\tau_R} S(t; \Omega_{PR}) \exp(-i(\omega_{iso} + k\omega_R t)) dt \\ &= \frac{1}{\tau_R} \int_{t=0}^{\tau_R} \exp(i\xi(t; \Omega_{PR})) \exp(-ik\omega_R t) dt, \end{aligned} \quad (2.86)$$

and integrating over all possible orientation angles (or, practically, summing over a crystallite set).

For symmetry reasons, all sidebands are in absorption mode [38]. The sample rotation interconverts a subset of orientations, called a carousel, by taking them around the same sequence of orientations with respect to the static field in one rotor cycle. A particular carousel contains crystallites with the same  $\alpha_{PR}$  and  $\beta_{PR}$  angles, but with different  $\gamma_{PR}$  angles ranging from 0 to  $2\pi$ . All members of a carousel experience the same set of resonance frequencies but not at the same time. The resonance frequency of a crystallite, in a carousel denoted by the subscript,  $c$ , with Euler angle  $\gamma_{PR}$  at time  $t$  is related to the resonance frequency of the crystallite in the same carousel but with Euler angle  $\gamma_{PR} = 0$  by:

$$\omega_c(t; \gamma_{PR}) = \omega_c \left( t + \frac{\gamma_{PR}}{\omega_R}; 0 \right), \quad (2.87)$$

and so:

$$\xi_c(t; \gamma_{PR}) = \xi_c \left( t + \frac{\gamma_{PR}}{\omega_R}; 0 \right). \quad (2.88)$$

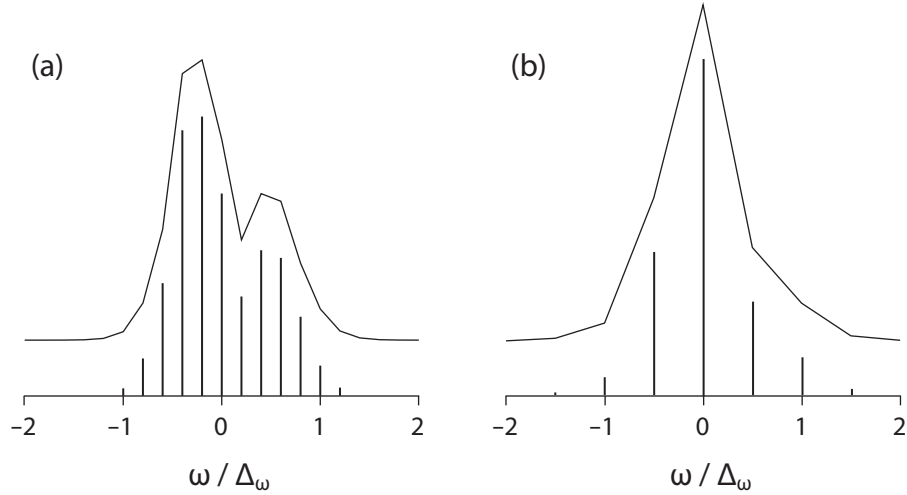


**Figure 2.4** Example spinning sideband spectra: (a)  $\omega_R = 0.2\Delta_\omega$ , and, (b)  $\omega_R = 0.5\Delta_\omega$ . The frequency axis is scaled by the anisotropy. In each case the isotropic frequency is zero, and the asymmetry,  $\eta = 0.5$  (i.e. the same as used in the powder pattern in Figure 2.3). The spectra are series of lines separated by the spinning frequency, the intensity of which depend on the CST and  $\omega_R$ . The envelopes at the top show the sideband intensity against sideband order. This is how sideband patterns will be represented from now onwards in this thesis.

Therefore the signal for this crystallite, using Equation (2.78) is:

$$S_c(t; \gamma_{PR}) = S_c\left(t + \frac{\gamma_{PR}}{\omega_R}; 0\right) S_c\left(\frac{\gamma_{PR}}{\omega_R}; 0\right)^*. \quad (2.89)$$

Using Equation (2.86), the intensity factor for the crystallite with  $\gamma_{PR}$  is thus:

$$F_c^{(k)}(\gamma_{PR}) = \sum_{k'} F_c^{(k)}(0) F_c^{(k')}(0)^* \exp(i(k - k')\gamma_{PR}), \quad (2.90)$$

and taking the average over a whole carousel (i.e. all  $\gamma_{PR}$ ) leaves only terms with  $k = k'$ , and so:

$$\overline{F_c^{(k)}} = |F_c^{(k)}(0)|^2, \quad (2.91)$$

which is real and positive. The total spectrum (for example, Figure 2.4), is the sum of that of all carousels (i.e. all  $\alpha_{PR}$  and  $\beta_{PR}$  angles), so is also real and positive.

The intensities of the sidebands at a moderate spinning rate can be used to determine the CST. A least squares fitting procedure is employed, simulating Equation (2.91) and summing over a crystallite set, for various combinations of  $\Delta_\omega$  and  $\eta$ , to find the combination where  $\chi^2$ , the total sum of the squared differences between sideband

intensities in experimental and simulated sideband patterns, is minimised. It has been shown that the most accurate measurement of the chemical shift anisotropy (CSA),  $\zeta$ , which is related to the anisotropy in the CST,  $\Delta_\omega$ , by:

$$\zeta = -\frac{\Delta_\omega}{\omega_{\text{ref}}} \times 10^6, \quad (2.92)$$

can be made when there are five sidebands [39, 40] (that is sidebands with  $|k| \leq 2$  being visible above the noise level), which is roughly when the MAS rate is:

$$\omega_R = 0.4\Delta_\omega. \quad (2.93)$$

If the sample is spun faster, then the anisotropic component is sufficiently well averaged that only the isotropic shift can be determined; if it is spun more slowly, then there will be many sidebands, but each will be less intense and so noise becomes a problem. Note that, if  $\omega_R = 0$  (i.e. a static powder pattern), then the same intensity is smeared over a continuous range of frequencies, rather than concentrated into a few sidebands, so the signal-to-noise ratio is lower than in sideband spectra, and so the CST is, on the whole, less reliably determined from a powder pattern [39, 40].

### 2.5.3 An alternative derivation

For some later work in Chapters 5 and 6, it will be easier to visualise the complex exponentials in Equation (2.76) if they are expanded as sines and cosines, in which case:

$$\begin{aligned} A_{20}^{\text{lab}}(t) &= c_1 \cos(\omega_R t + \gamma_{\text{PR}}) + c_2 \cos(2(\omega_R t + \gamma_{\text{PR}})) \\ &\quad + s_1 \sin(\omega_R t + \gamma_{\text{PR}}) + s_2 \cos((2\omega_R t + \gamma_{\text{PR}})), \end{aligned} \quad (2.94)$$

where,

$$\begin{aligned} c_1 &= -\sin(2\theta_R) \sin(2\beta_{\text{PR}}) \left[ \frac{3}{4} A_{20}^{\text{PAF}} - \sqrt{\frac{3}{8}} A_{22}^{\text{PAF}} \cos(2\alpha_{\text{PR}}) \right] \\ c_2 &= \sin^2(\theta_R) \left[ \frac{3}{4} A_{20}^{\text{PAF}} \sin^2 \beta_{\text{PR}} + \sqrt{\frac{3}{8}} A_{22}^{\text{PAF}} \cos(2\alpha_{\text{PR}})(\cos^2 \beta_{\text{PR}} + 1) \right] \\ s_1 &= -\sqrt{\frac{3}{2}} \sin(2\theta_R) A_{22}^{\text{PAF}} \sin(2\alpha_{\text{PR}}) \sin \beta_{\text{PR}} \\ s_2 &= -\sqrt{\frac{3}{2}} \sin^2(\theta_R) A_{22}^{\text{PAF}} \sin(2\alpha_{\text{PR}}) \cos \beta_{\text{PR}}. \end{aligned} \quad (2.95)$$

Separating out the time dependence from the  $\gamma$ -angle terms gives:

$$A_{20}^{\text{lab}}(t) = C_1 \cos(\omega_R t) + C_2 \cos(2\omega_R t) + S_1 \sin(\omega_R t) + S_2 \cos(2\omega_R t), \quad (2.96)$$

where,

$$\begin{aligned} C_1 &= c_1 \cos \gamma_{\text{PR}} + s_1 \sin \gamma_{\text{PR}} \\ C_2 &= c_2 \cos(2\gamma_{\text{PR}}) + s_2 \sin(2\gamma_{\text{PR}}) \\ S_1 &= s_1 \cos \gamma_{\text{PR}} - c_1 \sin \gamma_{\text{PR}} \\ S_2 &= s_2 \cos(2\gamma_{\text{PR}}) - c_2 \sin(2\gamma_{\text{PR}}). \end{aligned} \quad (2.97)$$

Note that if the sample is static, only the  $C_1$  and  $C_2$  terms remain. These terms, it can be shown, are those that give a static powder pattern, identical to the terms in Equation (2.73) except that  $\alpha$ ,  $\beta$  and  $\gamma$  have different definitions.

## 2.6 Further aspects of experimental SS-NMR

In this section, some more ideas are introduced to build upon the simple pulse–acquire experiment described in Section 2.2. By intricate control of the rf field, one is able to manipulate the spins into behaving as if certain nuclear spin interactions were absent or enhanced. This may be done in order to improve resolution or the signal-to-noise ratio, or to open the way to the measure of a parameter that was previously unavailable.

### 2.6.1 Many-pulse NMR sequences

A single  $\pi/2$ -pulse pulse can generate  $(-1)$ -quantum coherence which is then detected in the pulse–acquire experiment. However, it is possible to generate and utilise other coherences by using additional pulses to manipulate the spins. For example, the spin-echo [41], is a common building block for many more complicated experiments, such as those in Chapters 5 and 6. Its pulse sequence, which shows the order and timings of the pulses, is shown in Figure 2.5. After generation of magnetisation along the  $x$ -axis, it consists of two rotor cycles, with a  $\pi$ -pulse pulse in the middle.

The initial  $\pi/2$ -pulse generates  $(+1)$ - and  $(-1)$ -quantum coherences in equal proportions. These coherences evolve for the delay time, which is the first rotor period, during which time they acquire a phase, but do not change their coherence order. The

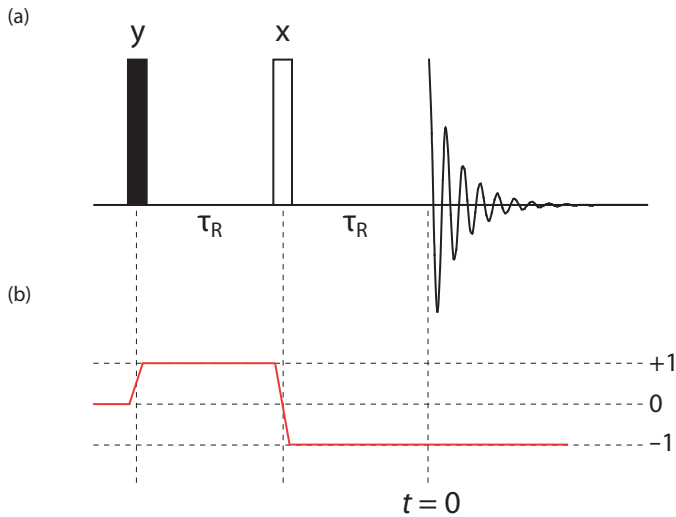


**Figure 2.5** (a) Pulse sequence for a spin-echo experiment. The empty rectangle represents a  $\pi$ -pulse in between two free evolution periods. The length of the delays is the rotor period,  $\tau_R = 2\pi/\omega_R$ . (b) Coherence transfer pathway for the spin-echo experiment, showing the coherence orders which are selected between the pulses. Only the  $(-1)$ -quantum coherence can be recorded in the end, so the pathway that is the mirror image of the red pathway, even though it is present, it is not recorded and is omitted from the diagram.

effect of a  $\pi$ -pulse on the  $(-1)$ -quantum coherence is given by:

$$\begin{aligned}\hat{\rho}(t) &= \exp(-i\pi\hat{I}_x)(\hat{I}_x - i\hat{I}_y)\exp(i\pi\hat{I}_x) \\ &= \hat{I}_x + i\hat{I}_y = \hat{I}_+.\end{aligned}\quad (2.98)$$

So  $(-1)$ -quantum coherence is converted to  $(+1)$ -quantum coherence, which evolves for the second delay time, but does not change coherence order again, so remains as  $(+1)$ -quantum coherence and is undetectable.

It turns out that any  $\pi$ -pulse always flips the sign of the coherence, so the initial  $(+1)$ -quantum coherence becomes  $(-1)$ -quantum coherence, which is detectable. The  $(-1)$ -quantum coherence evolves during the second time period. However,  $(-1)$ -quantum coherence acquires a phase in the second delay which exactly cancels the evolution of the  $(+1)$ -quantum coherence in the first delay. So the net result is that, at the beginning of signal acquisition, magnetisation is as it was right after the initial pulse. In essence, the effect of the chemical shift has been removed for the duration of the spin-echo.

A second  $\pi/2$ -pulse (somewhere after the excitation pulse in the sequence) can have different effects, including generating multiple quantum coherence (MQC),

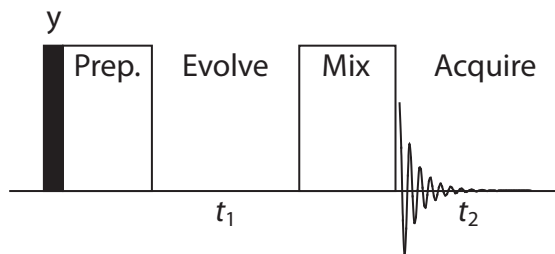


**Figure 2.6** Schematic representation of a two-dimensional experiment, consisting of four parts (preparation, evolution, mixing and acquisition) as described in the text. The experiment is repeated many times, with incremented  $t_1$  values.

which is where spins are correlated on two different nuclei. However, the pulse sequences used in this thesis comprise almost entirely of  $\pi$ -pulses, so  $\pi/2$ -pulses and MQC will not be discussed further.

The changes of coherence over the course of the experiment make up the coherence transfer pathway (CTP). For the spin-echo experiment, the CTP is shown in Figure 2.5(b).

### 2.6.2 Two-dimensional NMR

One-dimensional NMR, even with MAS, often suffers from the problem of overlapping signals from nuclei in different chemical environments. Two-dimensional experiments can help this by separating the signal over a second dimension. Furthermore, two-dimensional NMR can be used to correlate signals that come from nuclei that are close in space to each other, or to recouple nuclear spin interactions that are removed by MAS.

The basic schematic two-dimensional experiment is shown in Figure 2.6, and consists of four phases: (i) preparation of coherence, (ii) evolution of the coherence for time,  $t_1$ , (iii) mixing of the coherences (to convert them to detectable coherences) and (iv) evolution of the  $(-1)$ -quantum coherence for time,  $t_2$ . Using this scheme, it is possible to set up evolution of a different coherence in  $t_1$  to that which is observed in  $t_2$ , which must be  $(-1)$ -quantum coherence.

The FID records the evolution in  $t_2$  in the usual way, and this is known as direct acquisition. To measure the evolution in  $t_1$ , the one-dimensional experiment must be run several times, each with a different incremental value of  $t_1$ . This process is known as indirect acquisition. Since each  $t_1$  point must be recorded as a separate

one-dimensional experiment, the number of  $t_1$  points that it is possible to acquire in a given time is limited. Also, it is often only possible to retain one of the real or imaginary components of the signal (magnetisation), as the other is often lost in the mixing period.

If only the real part of the magnetisation after  $t_1$  is retained, then the recorded signal is cosine modulated:

$$\begin{aligned} S_{\cos}(t_1, t_2) &= \cos(\Omega_1 t_1) \exp(i\Omega_2 t_2) \exp\left(\frac{-t_1}{T_2^{(1)}}\right) \exp\left(\frac{-t_2}{T_2^{(2)}}\right) \\ &= \frac{1}{2} (\exp(i\Omega_1 t_1) + \exp(-i\Omega_1 t_1)) \exp(i\Omega_2 t_2) \exp\left(\frac{-t_1}{T_2^{(1)}}\right) \exp\left(\frac{-t_2}{T_2^{(2)}}\right), \end{aligned} \quad (2.99)$$

where  $T_2^{(1)}$  and  $T_2^{(2)}$  are the  $T_2$  relaxation time constants for the coherences selected in  $t_1$  and  $t_2$ , which are not necessarily the same. A Fourier transform of Equation (2.99) in direct dimension yields:

$$S_{\cos}(t_1, \omega_2) = \frac{1}{2} (\exp(i\Omega_1 t_1) + \exp(-i\Omega_1 t_1)) \exp\left(\frac{-t_1}{T_2^{(1)}}\right) (\mathcal{A}_2 + i\mathcal{D}_2). \quad (2.100)$$

Then a second Fourier transform, this time in the indirect dimension, gives the form of the spectrum:

$$S_{\cos}(\omega_1, \omega_2) = (\mathcal{A}_1^+ + i\mathcal{D}_1^+ + \mathcal{A}_1^- + i\mathcal{D}_1^-)(\mathcal{A}_2 + i\mathcal{D}_2), \quad (2.101)$$

where  $\mathcal{A}_1^+$  and  $\mathcal{A}_1^-$  indicate absorption mode lineshapes at  $\pm\Omega_1$  in the indirect dimension, and  $\mathcal{D}_1^+$  and  $\mathcal{D}_1^-$  indicate the dispersion mode lineshapes similarly. This spectrum shows peak centred at  $(\Omega_1, \Omega_2)$  and  $(-\Omega_1, \Omega_2)$ , so the sign of the offset,  $\Omega_1$ , can not be determined from the cosine-modulated dataset alone. Additionally, the peaks in the real part of the spectrum contain a mixture of double absorption,  $\mathcal{A}_1 \mathcal{A}_2$ , and double dispersion,  $\mathcal{D}_1 \mathcal{D}_2$ , lineshapes, which are shown in Figure 2.7. This is called a phase twist lineshape, also shown in Figure 2.7, and is undesirable.

If the full complex signal is recorded (if possible) by the receiver, then the signal is:

$$S_+(t_1, t_2) = \exp(i\Omega_1 t_1) \exp(i\Omega_2 t_2) \exp\left(\frac{-t_1}{T_2^{(1)}}\right) \exp\left(\frac{-t_2}{T_2^{(2)}}\right). \quad (2.102)$$

After the direct dimension Fourier transform this becomes:

$$S_+(t_1, \omega_2) = \exp(i\Omega_1 t_1) \exp\left(\frac{-t_1}{T_2^{(1)}}\right) (\mathcal{A}_2 + i\mathcal{D}_2), \quad (2.103)$$

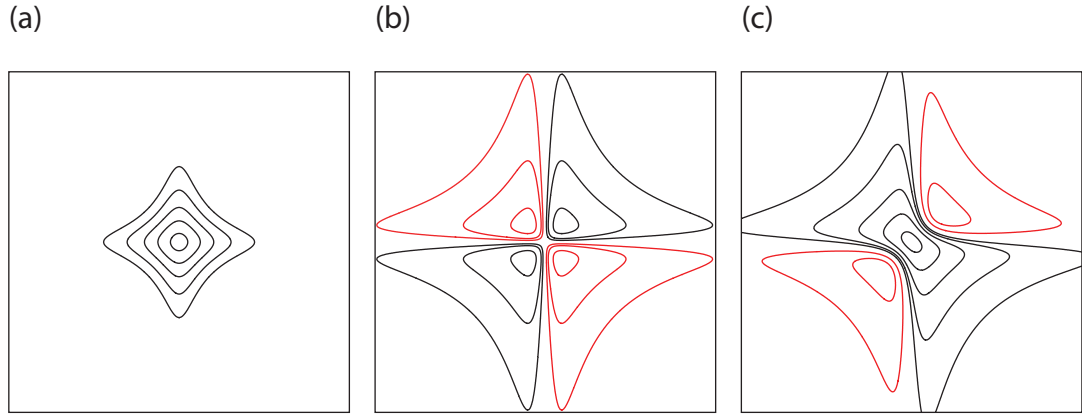


**Figure 2.7** Contour plots showing lineshapes from two-dimensional NMR: (a) double absorption lineshape,  $\mathcal{A}_1\mathcal{A}_2$ ; (b) double dispersion lineshape,  $\mathcal{D}_1\mathcal{D}_2$ ; and (c) the phase twist lineshape,  $\mathcal{A}_1\mathcal{A}_2 - \mathcal{D}_1\mathcal{D}_2$ . The double absorption lineshape is desirable because it has high intensity and no long tails. The contours are  $\pm 0.05$ ,  $\pm 0.1$ ,  $\pm 0.2$ ,  $\pm 0.4$  and  $\pm 0.8$ , of the maximum value of the double absorption mode lineshape. Negative contours are shown in red.

and then after the second Fourier transform:

$$S_+(\omega_1, \omega_2) = (\mathcal{A}_1 + i\mathcal{D}_1)(\mathcal{A}_2 + i\mathcal{D}_2), \quad (2.104)$$

which results in a peak centred at  $\Omega_1$  and  $\Omega_2$  in the two dimensions, and the problem of sign discrimination has been solved. However, the real part of the spectrum still contains a phase twist lineshape.

Now suppose that one is able to record a signal where evolution in the indirect dimension occurs at a frequency,  $-\Omega_1$ :

$$S_-(t_1, t_2) = \exp(-i\Omega_1 t_1) \exp(i\Omega_2 t_2) \exp\left(\frac{-t_1}{T_2^{(1)}}\right) \exp\left(\frac{-t_2}{T_2^{(2)}}\right). \quad (2.105)$$

Taking the Fourier transform in the direct dimension gives:

$$S_-(t_1, \omega_2) = \exp(-i\Omega_1 t_1) \exp\left(\frac{-t_1}{T_2^{(1)}}\right) (\mathcal{A}_2 + i\mathcal{D}_2). \quad (2.106)$$

Taking the complex conjugate of Equation (2.106), which is equivalent to reversing the  $t_1$  evolution, and adding this to (2.103) gives a new dataset:

$$S(t_1, \omega_2) = 2 \exp(i\Omega_1 t_1) \exp\left(\frac{-t_1}{T_2^{(1)}}\right) \mathcal{A}_2. \quad (2.107)$$

Finally, the Fourier transform in the indirect dimension gives:

$$S(\omega_1, \omega_2) = 2(\mathcal{A}_1 + i\mathcal{D}_1)\mathcal{A}_2, \quad (2.108)$$

which is a spectrum with a peak at  $(\Omega_1, \Omega_2)$ , which in the real part has pure absorption mode in both dimensions. This method of getting pure absorption lineshapes is the echo-antiecho method [42] (refering to the normal signal in  $t_1$  as the echo, and that with the reversed  $t_1$  evolution as the antiecho).

An alternative method for avoiding the frequency discrimination and phase-twist lineshape problems in 2D-NMR is the States method [43], which involves measuring the sine-modulated data as well as the cosine-modulated data of Equation (2.99). Another method is time-proportional phase incrementation (TPPI) [44], which is not used extensively in this work.

### 2.6.3 Phase cycling

So far it has been assumed that it is possible to set a  $\pi$ -pulse so that it has exactly the right strength to flip the magnetisation by  $\pi$  about the pulse axis. However, this is often not the case because: (i) the required power of the pulse is not known *a priori* and has to be guessed/optimised, (ii) it is not the same for every site in the sample, and (iii) the rf field strength is not uniform within the sample. If the pulse is not an ideal  $\pi$ -pulse, then it may generate unwanted coherences and allow different coherence pathways to contribute to the signal. To prevent this, a technique called phase cycling is needed.

It has been shown [45] that, if a pulse converts a coherence of order  $m$  into a coherence or order  $n$ , the coherence acquires a phase,  $-\phi\Delta p$ , where  $\phi$  is the phase of the rf pulse, and  $\Delta p = n - m$ :

$$\rho^{(m)} \rightarrow \rho^{(n)} \exp(-i\phi\Delta p). \quad (2.109)$$

The signals from different CTPs acquire different phases since the difference in coherence orders,  $\Delta p$ , for one or more of the pulses is different.

A CTP can be described concisely as  $\mathbf{p} = [0, p_{1,2}, p_{2,3}, \dots, p_{n-1,n}, -1]$ , where  $p_{i,j}$  is the coherence order of the CTP in between the  $i^{\text{th}}$  and  $j^{\text{th}}$  pulse, and  $n$  is the total number of pulses. Any CTPs which do not end with  $(-1)$ -quantum coherence are not detected and do not matter. It has also been assumed that the system has started at equilibrium (i.e. no coherences), otherwise the pulse sequence will act on residual

coherences as well as creating new ones. The total phase,  $\Phi$ , acquired by a CTP after the pulse sequence, where the phase of the  $i^{\text{th}}$  pulse is  $\phi_i$ , is:

$$\Phi(\mathbf{p}) = -\phi_{\text{rec}} - \sum_{i=1}^n \phi_i(p_{i,i+1} - p_{i-1,i}), \quad (2.110)$$

where  $\phi_{\text{rec}}$  is the phase correction applied at the receiver.

In a phase cycle, the experiment is repeated  $N$  times, each with a different combination of phases for the rf pulses in the sequence, with the receiver phase changed so that the phase of the resulting  $(-1)$ -quantum coherence for the required CTP is zero each time. The signal of the desired CTP adds constructively each time, whereas the signals from the unwanted CTPs combine destructively. Mathematically this selection rule can be expressed as:

$$\frac{1}{N} \sum_{m=1}^N \exp(i\Phi(\mathbf{p}; m)) = \begin{cases} 1 & \text{for the desired CTP} \\ 0 & \text{otherwise} \end{cases}, \quad (2.111)$$

where  $\Phi(\mathbf{p}; m)$  is the total phase acquired on the  $m^{\text{th}}$  repetition of the pulse sequence, for which the phases of the pulses will be  $\phi_i^{(m)}$ .

The original way of achieving this is the nested phase cycle [45], where the phase of each pulse is cycled independently. If the phase of a pulse, for which the desired CTP changes by  $\Delta p$ , is cycled through  $N$  steps of  $2\pi/N$ , then the appropriate receiver phase cycles through  $-2\pi\Delta p/N$ . If  $N = 4$ , then a CTP where the coherence changes at that pulse by  $\Delta p'$  has the selection rule:

$$\begin{aligned} \frac{1}{N} \sum_{m=1}^N \exp(i\Phi(\mathbf{p}'; m)) &= \sum_{m=1}^4 \exp\left(\frac{i\pi m}{2}(\Delta p - \Delta p')\right) \\ &= \begin{cases} 1 & \text{if } \Delta p' = \Delta p + 4k, \text{ where } k \text{ is any integer} \\ 0 & \text{otherwise} \end{cases} \end{aligned} \quad (2.112)$$

Thus the desired CTP is accepted, along with any whose change in coherence at the pulse differs by multiples of four from the desired change in coherence at that pulse, whilst all others are rejected. However, high coherence orders are rare and so large changes in coherence order caused by an rf pulse are not usually problematic and a phase cycle of four steps is sufficient in most cases.

With several pulses in a sequence, each needs to be phase cycled in order to select the desired  $\Delta p$  for that pulse. In a nested phase cycle this means that, for each phase cycle step on every pulse, all other pulses have to go around their complete phase cycle. So, for  $n$  pulses, where each pulse is cycled through  $N$  steps, the total number of steps in a phase cycle is  $N^n$ , which increases very rapidly with the number of pulses. This means that for many longer pulse sequences it is not feasible to perform a full phase cycle using the nested phase cycling scheme.

An improved phase cycling scheme for longer pulse sequences is cogwheel phase cycling [46]. In this scheme, rather than cycling the phases of all pulses independently, the phases of all pulses change at the same time, so that the phase of the  $i^{\text{th}}$  pulse on the  $m^{\text{th}}$  step of the phase cycle (out of  $N$  total steps) is:

$$\phi_i^{(m)} = \frac{2\pi m \nu_i}{N}, \quad (2.113)$$

where  $\nu_i$  is the winding number of the  $i^{\text{th}}$  pulse. The total phase acquired over a CTP under this scheme is:

$$\Phi(\mathbf{p}; m) = -\frac{2\pi m}{N} \left( \nu_{\text{rec}} + \sum_{i=1}^n \nu_i (p_{i,i+1} - p_{i-1,i}) \right) \quad (2.114)$$

To select the desired CTP, the receiver must be cycled with winding number:

$$\begin{aligned} \nu_{\text{rec}} &= - \sum_{i=1}^n \nu_i (p_{i,i+1} - p_{i-1,i}) \\ &= \nu_n + \sum_{i=1}^{n-1} \Delta \nu_{i,i+1} p_{i,i+1}, \end{aligned} \quad (2.115)$$

where  $\Delta \nu_{i,i+1}$  is the difference in winding number between the  $i^{\text{th}}$  and  $(i+1)^{\text{th}}$  pulses. For an arbitrary CTP,  $\mathbf{p}'$ , the total phase acquired on the  $m^{\text{th}}$  step of the phase cycle is:

$$\Phi(\mathbf{p}'; m) = \frac{2\pi m}{N} \sum_{i=1}^{n-1} \Delta \nu_{i,i+1} (p'_{i,i+1} - p_{i,i+1}). \quad (2.116)$$

The selection criterion is thus:

$$\frac{1}{N} \sum_{m=1}^N \exp [i\Phi(\mathbf{p}'; m)] = \frac{1}{N} \sum_{m=1}^N \exp \left[ i \frac{2\pi m}{N} \Lambda \right], \quad (2.117)$$

where:

$$\Lambda = \sum_{i=1}^{n-1} \Delta\nu_{i,i+1}(p'_{i,i+1} - p_{i,i+1}). \quad (2.118)$$

Thus, the cogwheel phase cycling scheme accepts the desired pathway, where  $\Lambda = 0$ , and any CTP for which  $\Lambda$  differs by an integer multiple of  $N$ . All other pathways are rejected and so do not contribute to the signal.

The number of steps in the phase cycle does not increase exponentially with  $N$ . The trick though is finding suitable values for the winding numbers, for which all unwanted pathways are rejected. There is no analytical method for doing this [47].

#### 2.6.4 Cross-polarisation

The NMR signal from low  $\gamma$  nuclei is weak because the dipole moment is small and so the equilibrium magnetisation is small (see Equation (2.17)). It is usual to enhance the signal of such nuclei by transferring magnetisation (using dipolar coupling) from a high  $\gamma$  nucleus, usually  $^1\text{H}$ , using a technique called cross-polarisation (CP) [48,49]. This requires simultaneously applying rf pulses at the frequencies of both nuclei. In order to transfer magnetisation from  $^1\text{H}$  to some other spin, X, the pulse amplitudes on the two channels must be set such that,  $\omega_{(1,\text{H})} = \omega_{(1,\text{X})}$ , which is the Hartmann-Hahn condition [50]. The time for which the CP pulses are applied is known as the contact time, and needs to be sufficiently long to allow transfer to the most remote spins, and must be optimised for each sample.

#### 2.6.5 Heteronuclear proton decoupling

The dipolar coupling between  $^{13}\text{C}$  and  $^1\text{H}$  is essential for CP, but can also be a hindrance during data acquisition, since it is responsible for broadening peaks in the  $^{13}\text{C}$  spectrum, even under MAS. This is solved by heteronuclear decoupling, which, in its simplest form involves irradiating the  $^1\text{H}$  spins during acquisition in order to disrupt the dipolar coupling [51], although this is not effective at high MAS rates. More complicated decoupling techniques have been developed for MAS; the two used in this thesis are two-pulse phase modulation (TPPM) [52] and small phase incremental alternation (SPINAL) [53]. A generic pulse sequence for a one-dimensional CP-MAS experiment with CP and proton decoupling is shown in Figure 2.8.

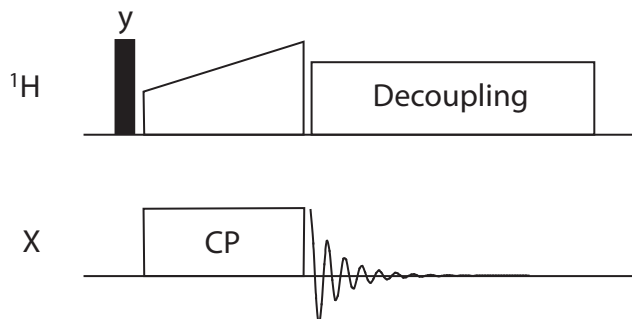


**Figure 2.8** Pulse sequence for simple CP experiment with proton decoupling. Pulses at the proton frequency are shown on the top line, pulses on the other ( $\text{X}$ ) channel are shown on the bottom line. The decoupling block represents a multiple-pulse sequence (TPPM or SPINAL). All experiments in this thesis will use  $^1\text{H}$ - $\text{X}$  CP and  $^1\text{H}$  decoupling, and so the  $^1\text{H}$  channel will not be shown in pulse sequences.

### 2.6.6 NMR simulations

Most calculations performed in this thesis are done using in-house programs, simulating the spectra using formulae that are derived within this thesis. In each case, the relevant equation is simulated for a suitable number of crystallites and the results summed to give the simulated spectrum for a powdered sample<sup>†</sup>.

In the few instances when more advanced simulations are required, where the evolution of the density operator over time is calculated, including the effect of every pulse and delay, the programs SIMPSON [54] and SPIN-EVOLUTION [55] were used. These programs can include the effects of, for example, pulse errors and phase cycling. The choice between the two programs was largely determined by availability on the particular computers used at the time.

---

<sup>†</sup>The number of  $(\alpha, \beta)$  pairs was 233 for sideband patterns in Chapter 4 and 700 for powder patterns in Chapters 5 and 6. These values were chosen as the minimum number of crystallites where the spectrum did not significantly diverge in appearance from one simulated with a very large number of crystallites.

## **Chapter 3**

---

# **Methods and applications of solid-state NMR**

---

MAS, introduced in Section 2.4, leads to the averaging of some nuclear spin interactions, notably the CSA and dipolar coupling, to zero. In many circumstances this is desirable; the exception is when it is the CSA or dipolar coupling that one is trying to measure. This chapter, therefore, introduces some experimental techniques for measuring CSA (Section 3.1) or dipolar coupling (Section 3.2) under MAS. These so-called ‘recoupling’ experiments are required to prevent the averaging under MAS of the particular interaction (and preferably no other interactions). Why it is that we should want to measure CSA or dipolar coupling is demonstrated in Section 3.3, which reviews some examples of these interactions being used as part of structural investigations.

### **3.1 CSA recoupling experiments**

It is possible to measure CSA from a one-dimensional sideband pattern, with methods suggested by Maricq and Waugh [56], Herzfeld and Berger [57] and Fenzke *et al.* [58] being amongst the most popular. This is reliant upon the intensity of at least five sidebands being measurable. The ideal spinning rate for a signal with a particular CSA,  $\Delta_\omega$ , is  $\omega_R = 0.4\Delta_\omega$ , for the most accurate and reliable determination of the CSA,

and slightly slower for the best determination of the asymmetry [39,40]. Additionally, sidebands must be fully resolved from sidebands from other signals that may be present in the spectrum [39]. It may be possible that one can select carefully the MAS rate such that no sidebands are overlapping with other signals (i.e. the separation in isotropic shift is not a multiple of the MAS rate). If there is not a single spinning rate available that is capable of resolving all the sidebands from all the signals, it may be feasible to record sideband spectra at a number of different spinning rates, where all sideband manifolds appear completely resolved for at least one of the spinning rates.

However, there are limits to the range of MAS rates available. For instance, a standard Bruker 4mm MAS probe has a limited range in which the spinning rate is both stable and safe, which is between 2-15 kHz, or thereabouts. Low spinning rates are also unfavourable as dipolar coupling becomes significant, broadening the peaks. High spinning rates may be unfavourable if the sample is temperature or pressure sensitive, since rapid MAS often raises the temperature of the sample to 40-50°C, and leads to enormous pressures at the boundaries of the rotor.

If a spectrum is particularly crowded, it is quite possible that there is not a suitable spinning rate available for a particular signal, where the signal is fully resolved from the sidebands of all other signals and the MAS rate is appropriate for accurate determination of the CSA of that signal. A possible solution (and one which is frequently used where there are problems of overlapping sideband manifolds) is to uniformly isotope label the site of interest (or a few sites at a time), so that its sideband manifold stands out above all others. If the labelled compound can be made, this is the most reliable method for tensor determination. Labelling strategies are common for proteins, and so labelled peptides can be purchased or synthesised relatively inexpensively, but for other materials the manufacture of isotopically labelled compounds require expensive and time-consuming custom synthesis. For many applications, such as high-throughput screening, this is unrealistic.

If isotope labelling is not feasible, one will need to resort to a more advanced experiment than the simple one-dimensional CP-MAS. The featured techniques in the following review are based on the two-dimensional NMR idea from Section 2.6.2. In such experiments, one of the dimensions contains a spectrum where the different signals are well-resolved, such as by isotropic shift (this is *usually* the direct dimension, and is achieved by fast MAS). The second dimension contains the

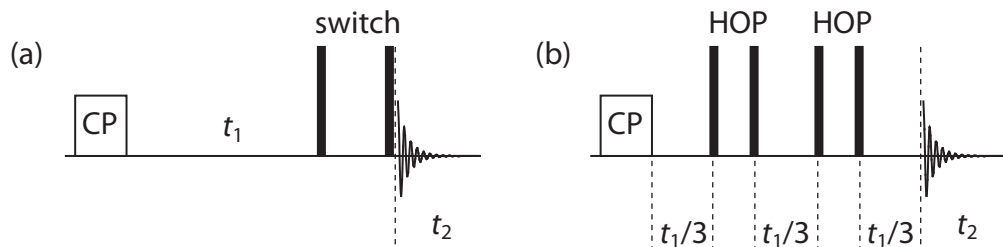


**Figure 3.1** Pulse sequences for the rotationally-controlled experiments: (a) a switching experiment [59–61], where the rotor spinning frequency or angle is altered whilst the magnetisation is stored along the  $z$ -axis in between the two  $\pi/2$ -pulses, and (b) a hopping experiment [62], where the magnetisation evolves during three equal time periods, in between which the rotor hops between different orientations.

anisotropic components (*usually* in the indirect dimension), from which the CST can be calculated. How this isotropic–anisotropic correlation is achieved, and how the anisotropic data is presented differs between the techniques. The techniques can be roughly split into three categories: (i) those where the anisotropic component is presented as a sideband pattern type spectrum; (ii) those where the anisotropic component is presented as a static-type powder pattern spectrum; and (iii) those where the anisotropic component is presented in an unfamiliar form that is neither of the above.

### 3.1.1 Rotationally-controlled sequences

Before the development of complex multiple-pulse experiments for recoupling CSA, a number of attempts were made to attain the anisotropic–isotropic correlation by carefully controlling the sample spinning during the experiment. An early example actually switched the MAS rate from slow to fast in between the  $t_1$  and  $t_2$  evolution periods [59] (Figure 3.1(a)), so that anisotropic components were averaged out only during the  $t_2$  period. The direct dimension therefore contains the isotropic spectrum, with each peak correlated with a sideband pattern appropriate for the lower spinning rate in the indirect dimension. Alternatively, if the sample is actually static during  $t_1$ , the anisotropic information is presented as powder patterns [60]. Although this seems powerful and simple, most commercial hardware takes a considerable amount of time to stabilise the MAS rate, during which time a lot of signal is lost through relaxation.

If the sample is spun away from the magic angle (OMAS), then CSA is not fully averaged out, even at high OMAS rates. In a two-dimensional experiment though, where the rotor angle is switched between OMAS and MAS in between

the  $t_1$  and  $t_2$  evolution periods [61], the CSA is removed in the  $t_2$  period, giving the isotropic spectrum in the direct dimension. The correlated anisotropic component is not presented as a sideband pattern or powder pattern, but as a complex function of the CSA, which can be derived from Equation (2.76), with setting  $d_{00}^{(2)}$  to the appropriate value. It turns out that flipping the rotor angle is less demanding on the hardware than altering the speed.

Another variation on this theme is the ‘hopping’ experiment [62]. During the  $t_1$  and  $t_2$  evolution of this experiment, the rotor is static. However, the  $t_1$  evolution period is split into three equal periods, in between which the rotor orientation hops between three orientations related by a rotation of a third of a rotor cycle about the magic angle (see Figure 3.1(b)). It has been shown that the evolution of the anisotropy in these three position cancels, leaving solely the evolution under the isotropic shift in  $t_1$ . The isotropic peaks are correlated with static powder patterns in the direct dimension.

None of these techniques are possible without specialist equipment, and are no longer considered as realistic alternatives to the multiple-pulse sequences that will follow. However they do nicely demonstrate how the isotropic–anisotropic correlation is set-up, and how the anisotropic component can be presented in a number of different ways.

### 3.1.2 Magic-angle turning

Magic-angle turning (MAT) is distinguished from MAS by the smaller magnitude of the sample rotation rate (typically 30–600 Hz). In a two-dimensional MAT experiment for correlating isotropic and anisotropic chemical shift components, the direct dimension shows a sideband pattern, and the anisotropic component must be ‘decoupled’ in  $t_1$  (contrary to the equivalent MAS experiments, where the direct dimension shows the isotropic spectrum and the anisotropic component must be ‘recoupled’ in  $t_1$ ).

The isotropic–anisotropic correlation experiments using MAT take advantage of the fact that the instantaneous anisotropic frequency at three positions, separated by one third of a rotation about the magic angle, average to zero, in the same way as the ‘hopping’ experiment. However, in MAT experiments, the sample rotates continuously and the necessary orientations are selected using pulses synchronised with one third of a rotor period [63–65].

The problem with using the indirect dimension for the isotropic shift is one of resolution. Good resolution requires acquisition of points at long  $t_1$ . A large

spectral width requires the acquisition of points that are closely spaced in  $t_1$ . So good resolution and spectral width requires a large number of  $t_1$  data points, and a correspondingly lengthy experiment. Also, in MAT, the maximum  $t_1$  is limited by the rotor period. The more recent development of FIREMAT [66] goes towards solving this problem, by artificially recreating the longer  $t_1$  evolution from rotor-synchronised  $t_2$  data. Problems still remain, however, with difficulty in decoupling protons and poor spinning rate stability below 1 kHz without specialist equipment.

### 3.1.3 Multiple-pulse CSA recoupling giving powder patterns

A series of rotor-synchronous  $\pi$ -pulses can be used to recouple CSA interactions otherwise removed by fast MAS. Each  $\pi$ -pulse switches the signs of coherences, and thus the direction of the evolution in between successive pulses, and so interrupts the averaging of the CSA interaction caused by MAS.

The earliest ways of achieving this were developed by Alla *et al.* [67] and Yarim-Agaev *et al.* [68], but these early methods do not produce patterns that resemble conventional static powder patterns. Tycko *et al.* developed the first multiple-pulse CSA recoupling sequence giving undistorted static powder patterns [69]. This experiment, which shall be referred to as MAS-CSA, uses blocks of four or six  $\pi$ -pulses in one rotor cycle, as shown in Figure 3.2(a). The terms,  $C_1$  and  $C_2$ , in Equation (2.97) (i.e. those that remain when  $\omega_R = 0$  and so give rise to a static powder pattern) must be recoupled. By appropriate timing of the  $\pi$ -pulses, which is derived in Chapter 4, the isotropic shift can be removed and the anisotropic components ( $C_1$  and  $C_2$ ) can be recoupled, albeit with a magnitude reduced by a scaling factor,  $\chi_a$ . Using four  $\pi$ -pulses in one rotor cycle there is one possible combination of pulse timings, which gives a scaling factor of  $\chi_a = 0.393$ , whereas with six  $\pi$ -pulses there are many possibilities which give scaling factors in the range,  $-0.393 < \chi_a < 0.393$ .

To construct the  $t_1$  evolution then, the experiment is repeated with increasing numbers of four or six  $\pi$ -pulse blocks, with the spins evolving under the Hamiltonian,  $\chi_a(C_1 + C_2)$ , for time,  $t_1 = n\tau_R$ , where  $n$  is the number of pulse sequence blocks. An alternative way of thinking about  $\chi_a$  is, rather than scaling the anisotropy, it scales the effective  $t_1$  evolution time, so that:

$$t_{1,\text{eff}} = \chi_a n \tau_R. \quad (3.1)$$

The apparent indirect dimension spectral width is therefore  $\omega_R/\chi_a$ . The powder

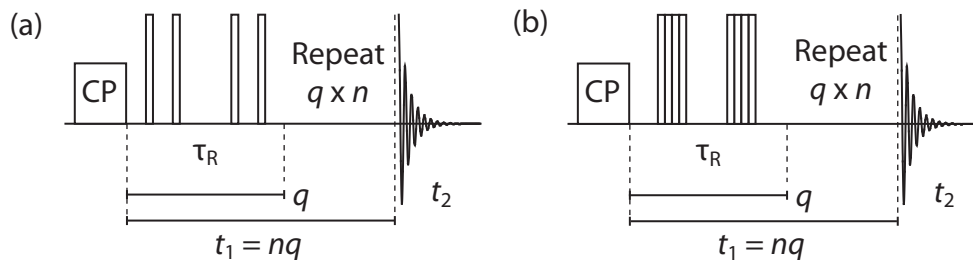


**Figure 3.2** Pulse sequences for powder pattern recoupling experiments: (a) MAS-CSA [69]; and (b) SUPER [70]. In each case, the pulse sequence unit shown, which is one rotor period long, must be repeated to get the different values of  $t_1$ .

patterns in the indirect dimension can have their CST principal values relative to the isotropic shift evaluated (in principle) by inspection, and the isotropic shift is given by the chemical shift in the direct dimension.

A major problem with long sequences of  $\pi$ -pulses is that they are sensitive to accumulation of small pulse imperfections, which severely distorts the powder pattern lineshape of MAS-CSA. Also, the powder pattern lineshapes are broadened by heteronuclear dipolar coupling, since the dipolar coupling, which is averaged out by MAS, is recoupled by MAS-CSA in exactly the same way as CSA. Finally, MAS-CSA is unsuitable for measuring very large or very small anisotropies. Very large anisotropies are problematic because at the high MAS rates required the pulse lengths become significant compared to the pulse spacing (although this can be partially solved by placing the six  $\pi$ -pulses over three rotor periods rather than one [71]). Very small anisotropies are problematic because in order to set an appropriate indirect dimension spectral width, the MAS rate must be very slow (since  $\chi_a < 0.393$ ).

The range of scaling factors available by using six  $\pi$ -pulses allows for some improved variations in the experimental design, such as a constant time implementation [72], where the number of pulse sequence units is kept constant for successive  $t_{1,\text{eff}}$  values, varying  $\chi_a$  instead. This reduces the linebroadening, as the relaxation during the  $t_1$  evolution is the same for every value of  $t_{1,\text{eff}}$ , as the actual  $t_1$  value is fixed. However, this sacrifices a lot of signal, as the number of pulse sequence blocks used for any  $t_{1,\text{eff}}$  time must be the maximum number required for the longest  $t_{1,\text{eff}}$  time; all recorded points therefore lose a lot of signal to relaxation and pulse errors. As a compromise, an optimised version was developed [72], whereby both the number of pulse sequence units,  $n$ , and the scaling factor,  $\chi_a$ , are altered to give the values of  $t_{1,\text{eff}}$

required for the desired spectral width. Also, cogwheel phase cycling [46] is included to reduce the effect of pulse errors.

An alternative approach recouples CSA powder patterns under MAS using two  $(4\pi)$ -pulses placed symmetrically in the rotor cycle, in an experiment known as SUPER [70], shown in Figure 3.2(b), which builds upon earlier experiment by Bax and co-workers [73]. The  $(4\pi)$ -pulses leave magnetisation unchanged; the only difference compared to not having the  $(4\pi)$ -pulses is that the spins have not evolved under their chemical shift Hamiltonian during the finite length of the pulse. It turns out that this ‘missing’ evolution prevents the complete averaging of the anisotropy over the rotor period, and so the anisotropy is recoupled. SUPER also has an anisotropic frequency scaling factor,  $\chi_a$ , which is realistically limited to  $\chi_a < 0.15$ . The isotropic shift evolution in  $t_1$  is not removed by SUPER, which is compensated for by shearing the resulting spectrum.

SUPER is superior to MAS-CSA (in its original version) in that it is less susceptible heteronuclear dipolar coupling, since it is not recoupled by the  $(4\pi)$ -pulses, therefore giving greater signal intensity. It is also relatively insensitive to pulse errors, and does not require high pulse amplitudes, so does suffer from the same lineshape distortion as MAS-CSA. SUPER is inappropriate for use at high MAS rates, however, since the maximum  $\chi_a$  value available is not as large as the maximum  $\chi_a$  for MAS-CSA. The constant time and optimised versions of MAS-CSA, by reducing the number of increments of pulse sequence blocks in  $t_1$ , manage to reduce the effect of linebroadening and in many cases can offer sharper powder pattern lineshapes than SUPER.

Neither the MAS-CSA experiment, nor SUPER, are applicable at very high spinning rates. For high MAS rates, Ishii and Terao have developed a method using amplitude or phase-modulated pulses to recouple the CSA (or dipolar coupling) [74]. Additionally their method is insensitive to rf inhomogeneity and requires no critical adjustment of experimental parameters (unlike MAS-CSA, where accurate calibration of the  $\pi$ -pulse is essential).

For systems with significant homonuclear dipolar coupling, such as uniformly labelled proteins, the ROCSA pulse sequence may be more applicable [75]. This uses a symmetry-based pulse sequence unit [76] to recouple CSA whilst strongly suppressing the homonuclear dipolar interaction. ROCSA is also applicable to higher

MAS rates than SUPER and MAS-CSA, but not to sites with small CSA, like methyl carbons.

### 3.1.4 Multiple-pulse CSA recoupling giving sideband patterns

Powder patterns have a distinct disadvantage compared to sideband patterns, in that their signal intensity is smeared over a continuum of frequencies, whereas in sideband patterns it is concentrated in a few sidebands, rendering it more conspicuous against the background noise. Also, in two-dimensional experiments, recoupling a sideband pattern is particularly useful as one only needs to sample as many points in  $t_1$  as the number of sidebands.

Many techniques in this category are based upon the PASS sequence [77], although PASS does not correlate isotropic–anisotropic frequencies, or recouple CSA, itself. In PASS, a series of well-timed  $\pi$ -pulses prior to acquisition gives a sideband of order,  $k$ , a phase shift of  $k\Theta$ , where  $\Theta$  is called the pitch and is a property of the set of pulse timings. By combining spectra from sequences with different pitch, each order of sideband can be isolated in turn, allowing the sideband intensities to be measured. The experiment suffers from distortion due to relaxation during the pulse sequence, which are of differing length for different  $\Theta$ . This problem was initially solved by putting the  $t_1$  period in between two TOSS [78] sequences, to give the pulse sequence a fixed length (although discarding half of the signal) [79]. This was improved upon again after the discovery of some five  $\pi$ -pulse sequences with fixed length but pitch varying with pulse timings [80], avoiding the need for TOSS. Using these five  $\pi$ -pulse sequences, a 2D-PASS experiment allows for very successful separation of sideband manifolds, provided that the MAS rate is small enough to generate sidebands in the first place.

The class of experiments that correlate isotropic shift (brought about by fast MAS) with a sideband pattern appropriate for a reduced (by a factor  $\chi_a$ ) spinning rate, is known as CSA amplification [81], since this is equivalent to amplifying the CSA during  $t_1$ . An early example of this (not based on PASS) is XCS [82] (shown in Figure 3.3(a)), which uses three  $\pi$ -pulses in four rotor cycles to give an anisotropic scaling factor of  $\chi_a = 4$ . The isotropic shift, however, is not removed from the indirect dimension, which removes the advantage that only as many points as the number of sidebands needs to be sampled in  $t_1$ . Also, the maximum  $t_1$  value is limited to the rotor period, which leads to truncation artefacts (see Section 2.3). An advance on this,

SPEED, uses data replication techniques, similar to those used in FIREMAT, to solve the truncation problem [83], but does not solve the problems of the presence of the isotropic shift in  $t_1$ .

The isotropic shift is removed in the CSA-amplified variants of 2D-PASS [84–87]. The method of Crockford *et al.* [84, 85] (Figure 3.3(b)) places a period where magnetisation is stored along  $z$  for a time,  $t_1$ , in between two identical sequences of a small number of  $\pi$ -pulses in a whole number of rotor cycles, where the pulse timings are chosen to scale CSA by  $\chi_a$  and eliminate the isotropic shift. Scaling factors up to  $\chi_a = 12$  are readily available, but the storage period loses half of the signal.

Orr *et al.* [86] avoid the storage period by using a range of five  $\pi$ -pulse sequences with varied pitch (in the same way as the original 2D-PASS [80]), but with CSA scaled by  $\chi_a$  (Figure 3.3(c)). Scaling factors up to  $\chi_a = 3.4$  can be achieved with one rotor cycle and five  $\pi$ -pulses; larger scaling factors can be achieved by placing multiple blocks together, with scaling factors up to  $\chi_a = 27$  successfully demonstrated [88]. The cost of this is that the number of pulses used is increased, so problems exist with accumulation of pulse errors (although these errors are minimised by the inclusion of cogwheel phase cycling [46]).

The most recent CSA-amplified PASS implementation of Shao *et al.* [87] improves on this by reducing the number of pulses required, so that a scaling factor  $\chi_a$  requires only  $\chi_a - 1$   $\pi$ -pulses, at the expense of limiting the number of  $t_1$  increments to  $\chi_a/2$ . This is particularly handy for high scaling factors, as it avoids having to resort to concatenating many pulse sequence units together. It is less useful for small scaling factors since the number of  $t_1$  increments available is small.

A final alternative for CSA-amplification is ROSES [89], which uses two pulses per pulse sequence unit (see Figure 3.3(d)), but the number of pulse sequence units must be incremented to get the different values of  $t_1$ , so ROSES actually requires a large number of  $\pi$ -pulses for long  $t_1$  values. This can achieve high scaling factors, however it fails to suppress the isotropic shift in  $t_1$ , and does not give standard sideband intensities.

It is desirable for a pulse sequence to have as few  $\pi$ -pulses as possible for a given scaling factor, to limit the accumulation of pulse errors. Out of the experiments included here, XCS, SPEED and the Shao *et al.* CSA-amplified PASS experiment use the fewest  $\pi$ -pulses for a given scaling factor [81]. The Crockford *et al.* CSA-

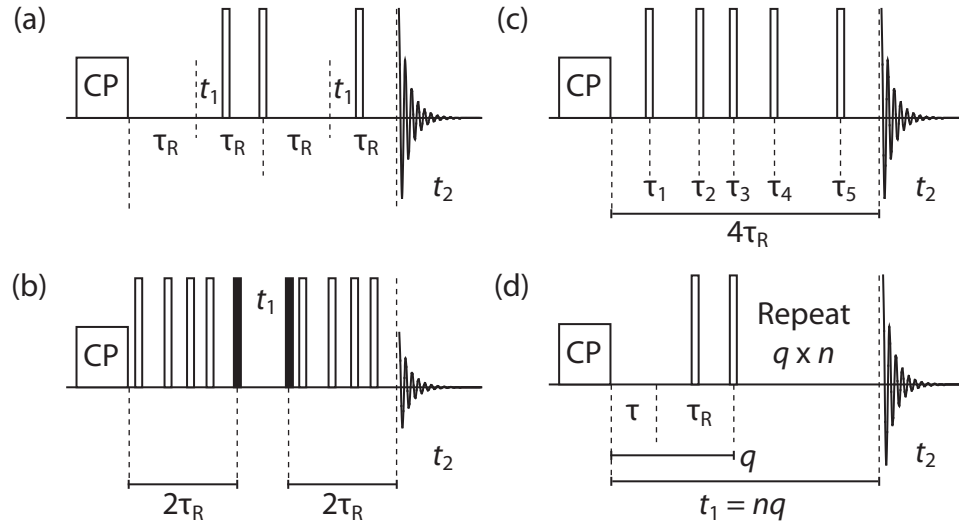


**Figure 3.3** Pulse sequences for CSA-amplification experiments: (a) XCS [82], with three  $\pi$ -pulses in four rotor cycles, which gives  $\chi_a = 4$ , with the  $t_1$  running from 0 to  $\tau_R$ ; (b) the Crockford *et al.* CSA-amplified PASS [84], with a  $t_1$  period where the magnetisation is stored along the  $z$ -axis sandwiched between two identical PASS sequences; (c) the Orr *et al.* CSA-amplified PASS [86], where  $t_1$  is determined by the timings of the five pulses; and (d) ROSES [89], with a unit with two pulses, that is repeated a whole number of times to get different  $t_1$  values.

amplified PASS experiment also has some particularly efficient solutions in terms of the number of pulses, such as a three  $\pi$ -pulse sequence with a scaling factor of  $\chi_a = 6$ . The Orr *et al.* CSA-amplified PASS experiment and ROSES require the most pulses.

It is also advantageous to minimise the number of rotor cycles, to reduce the amount of signal lost to relaxation. In this respect, the Crockford *et al.* CSA-amplified PASS experiment requires the fewest, then XCS, SPEED and the Shao *et al.* CSA-amplified PASS. The Orr *et al.* CSA-amplified PASS and ROSES require the most [81].

There are many factors to consider when determining the optimum choice of experiment for a particular sample and probe. The presence of isotropic shift evolution during  $t_1$  generally disfavours the use of XCS, SPEED and ROSES, reducing the options to the three CSA-amplified PASS variants. If sensitivity is an issue, the Orr *et al.* or the Shao *et al.* experiments might be best as they do not lose signal in a storage period, unlike the Crockford *et al.* experiment. The Crockford *et al.* version will be best in situations where there is fast relaxation, since it is the shortest pulse sequence. The Shao *et al.* version will be best in situations where pulse errors are problematic,

such as large scaling factors or where the probe quality is poor, since it requires the fewest pulses.

### 3.1.5 Overlapping isotropic shifts

None of the techniques described above provide the necessary resolution if two signals share the same isotropic shift. It has been demonstrated that the reliability of tensor determination for sideband methods falls to zero when two signals have an isotropic shift that is the same, or that is separated by a multiple of the spinning rate [39] (i.e. overlapping sideband manifolds). With powder patterns there is more hope; the principal values of the two CSTs can be extracted from overlapping powder patterns, unless the two sites share a principal value to within the limits of the linebroadening (which is often severe in MAS-CSA and SUPER spectra). Various attempts have been made to measure CST parameters from such overlapped signals.

For example, Mou *et al.* measure the CSA of unresolved carbonyl sites in polypeptides by correlation of carbonyl powder patterns with the chemical shift of neighbouring  $C_\alpha$ , which are better resolved [90]. Wylie *et al.* use a three-dimensional experiment to measure  $^{15}\text{N}$  CSA in peptides, resolving the overlapping  $^{15}\text{N}$  powder patterns by correlation to each of  $^{15}\text{N}$ ,  $^{13}\text{C}_\alpha$  and carbonyl  $^{13}\text{C}$  isotropic chemical shifts [91]. An alternative approach is a CSA-filter experiment, where the CSA-filter is a sequence of pulses that preferentially destroys the magnetisation on signals with large CSA [92]. Decay curves, showing the relative intensity with the length of CSA-filter for different CSA values, have been made. Correlating these decay curves for  $^{13}\text{C}$  with  $^{15}\text{N}$  correlation via dipolar coupling to provide resolution, has enabled backbone CSA to be measured in a protein. All these studies, however, have required uniform isotope labelling of the sites of interest, as the magnetisation is transferred between them.

A method is sought after which does not rely on isotope labelling. Recent developments of this nature include the Nishiyama *et al.* OMAS experiment [93]. Rather than recoupling the CSA for all the terms in Equation (2.76), which would give the standard sideband spectrum, the Nishiyama experiment manages (using a symmetry-based pulse sequence [76]) to only recouple the terms with  $n = 2$ . With OMAS, this leads to unusual two-dimensional powder patterns in both dimensions (where neither is a standard static powder pattern). The overall two-dimensional lineshape is in the form of a parallelogram, shown in Figure 3.4. The positions of the apices of the parallelogram are related to the principal values of the CST. However,

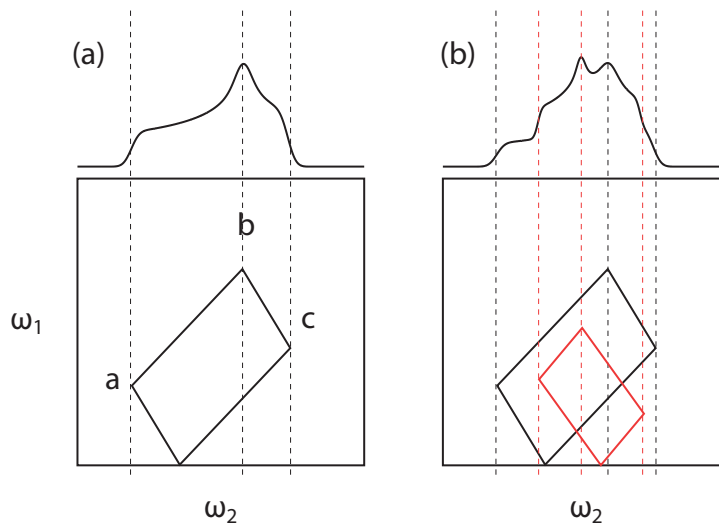


**Figure 3.4** Schematic representations of spectra from the Nishiyama *et al.* experiment [93]. The signal from a particular CST appears as a two-dimensional parallelogram powder pattern, with ridges marked by the lines, as in (a). The principle values of the CST can be determined from the  $\omega_2$  co-ordinates of the corners of the parallelogram. With the overlapped signals, as in (b), even though the two parallelograms powder patterns are overlapped, the ridges should still be visible, allowing the positions of the corners, and thus the CST principal values to be determined.

since the powder pattern is now spread over two dimensions, even if two overlapping signals share a principal value, they are now separated in the second dimension and principal values for both sites can be determined accurately. It does however rely on OMAS, which suffers a severe penalty in terms of resolution.

De Swiet's solution to the problem of overlapping isotropic shifts is a three-dimensional experiment, performed under MAS [94]. The direct dimension contains the information of the isotropic shift. In one of the indirect dimensions, a standard MAS-CSA experiment recouples the traditional powder pattern. In the other indirect dimension, a complementary powder pattern is recorded which, rather than containing  $C_1 + C_2$  terms from Equation (2.97) (as in the normal powder pattern), has the  $S_1 - S_2$  terms recoupled instead. The experiment therefore gives two-dimensional powder patterns correlated with their isotropic shift. The two-dimensional powder patterns can be simulated and fitted to CSA and asymmetry values, or the singularities in the powder pattern, projected onto the  $\omega_1$  axis (that of the conventional powder pattern) to give the CST principal values.

However, the de Swiet experiment goes one step further. A transformation

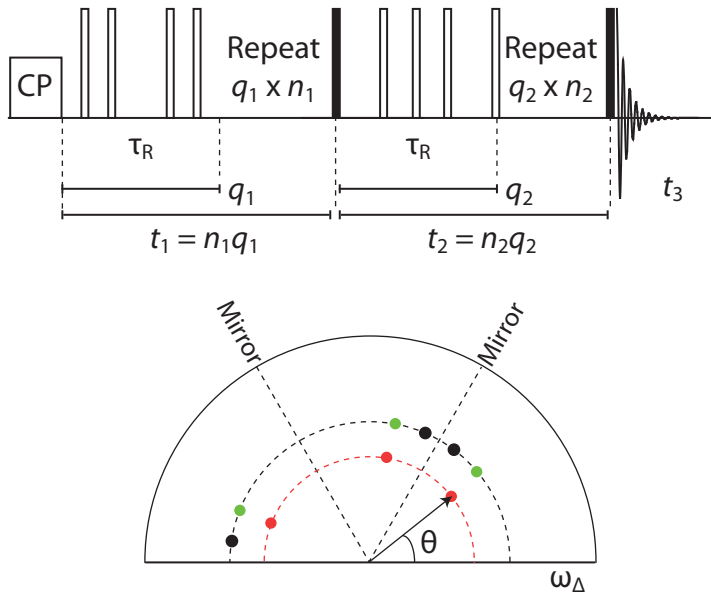


**Figure 3.5** (a) Pulse sequence for three-dimensional de Swiet experiment. (b) Schematic diagram of output of de Swiet experiment after two-dimensional transformation. Each chemical site appears as one peak in each  $60^\circ$  wedge. The principal values for the CST are given by the  $\omega_\Delta$ -axis projection of the peak and its mirror image peaks in the other  $60^\circ$  wedges. Alternatively, the radius and angle of the peak (marked on for the red peak) are simply related to the CSA and asymmetry (see Chapter 6). The red, green and black signals all share principal values, however they are separated by the de Swiet experiment, either by radius or angle.

exists that will convert the powder pattern into a one-dimensional spectrum with one delta-function per chemical site, at a position that is related to the CSA and asymmetry. A different transformation exists that will convert the powder pattern into a two-dimensional spectrum with three delta-functions per chemical site, which directly give the principal values of the CST [95], as shown in Figure 3.5. The overlapping signals have essentially been separated according to their isotropic shift and CSA. The de Swiet experiments will be described in much greater depth in Chapter 6.

A two-dimensional experiment correlating isotropic shift with CST principal values (i.e. three peaks, one at each principal value of the CST for each site) is also possible [96]. This experiment makes use of the fact that, for the three orientations where the PAF is aligned with the rotor frame (but no other orientations), the terms  $C_1^2 + S_1^2$  from Equation (2.97), are zero. The  $C_1^2 + S_1^2$  terms are recoupled under fast MAS by rotary resonance [97], causing all orientations other than the three where the

PAF is aligned to ‘dephase’. The chemical shift of the orientations that have surviving magnetisation can then be measured by a number of common techniques, such as MAS-CSA. Rather than resulting in a powder pattern though, only the principal values are retained; so long as the principal values are unique, the problem of overlap has been solved. This experiment suffers from sensitivity issues, as only a tiny fraction of the sample contributes to the signal.

Another attempt at achieving this separation by CSA involves recording one-dimensional sideband spectra at a range of MAS rates [98]. Spectra from high MAS rates have most signal from the small CSA component concentrated in the centreband; spectra from low MAS rates have the signal from the large CSA smeared out over many sidebands so contributes little to any individual sideband. This approach was used with a modicum of success to measure CSA for overlapping sites, but only if they differ significantly.

One paper quotes  $^{13}\text{C}$  chemical shift parameters for overlapping signals apparently using a single sideband pattern recorded using a FIREMAT experiment [99]. The parameters are measured for four heterosubstituted polycyclic aromatic compounds, three of which are found to have overlapping signals. Separate parameters are assigned to signals which only differ in CSA by 3 ppm (the CSAs of the two overlapping sites in carbazole, for instance, are 110 ppm and 113 ppm), with errors of  $\pm 2$  ppm. This seems somewhat unrealistic. However, it perhaps should be noted that, the reliability of chemical shift parameters determined from one-dimensional sideband patterns is low, but not actually zero. This suggests that if the signal-to-noise ratio is really very high, it may be possible that these claims could be justified. From inspection of their experimental spectra, however, this does not appear to be the case.

### 3.2 Recoupling dipolar interactions

The strength of the dipolar coupling between two spins varies inversely with the cube of the distance between the spins. Hence, measurement of the dipolar coupling gives the distance between the coupling spins, directly giving useful structural information. Dipolar coupling also varies with the angle of the vector connecting the two spins with the magnetic field vector, with an angular dependence of  $3\cos^2\theta - 1$ . Like CSA, therefore, it is averaged out by MAS. To measure the dipolar coupling constant between two spins, experiments are required to recouple the dipolar interaction. A

number of dipolar recoupling methods exist [100, 101], which must be split into the categories of those that recouple dipolar coupling between two spins of the same type (homonuclear), and those that recouple dipolar coupling between spins of different types (heteronuclear).

Since dipolar coupling relates so directly to structure, it often plays a vital role in structural investigations using NMR, as will be seen in Section 3.3. However, it does not play such a major part in this thesis only the few dipolar coupling techniques that are used are briefly introduced here.

### 3.2.1 Heteronuclear dipolar recoupling

One common method for recoupling heteronuclear dipolar coupling, which is used extensively in Chapter 7, is the rotation-echo double resonance (REDOR) experiment [102]. In REDOR, a spin-echo experiment is performed on the observed spin, to give a reference spectrum, followed by a second experiment which is equivalent except for a series of rotor-synchronised  $\pi$ -pulses during the spin-echo evolution period, on the channel of the spin whose dipolar coupling to the observed spin is to be recoupled. In the spectrum from the second experiment, some signals from the observed spins are dephased (reduced in intensity) due to dipolar coupling to the non-observed spins. The ratio of the intensity of a particular signal in the dephased spectrum to the reference spectrum depends on the dipolar coupling strength (and thus on the internuclear distance). In practice, the experiment is repeated for different dephasing times (that is the length of the spin-echo, which must be an integer multiple of the rotor period) to build up a dephasing curve, which is used to calculate the dipolar coupling strength by the REDOR transform [103], or by comparison with simulations using programs such as SPIN-EVOLUTION [55].

A variant of REDOR is transfer-echo double resonance (TEDOR) [104, 105]. The TEDOR experiment is similar except that magnetisation is transferred between the coupling nuclei, and it records the component of the signal that is dephased in the REDOR experiment. This is useful where there are only a small fraction of spins which are close in space to the dephasing spin, whilst most are remote and so unaffected by the REDOR pulses.

A heteronuclear correlation experiment (HETCOR) is a different approach. In such an experiment, magnetisation is allowed to evolve on a spin during  $t_1$  and then transferred via dipolar coupling (perhaps by CP) to another spin, which is observed.

The resulting spectrum shows a cross peak at the isotropic shifts of two spins that are coupled. By observing the build-up of the intensity of a cross-peak over magnetisation transfer time, it is sometimes possible to determine the distance between the two correlated sites, although data analysis can be complex.

### 3.2.2 Homonuclear dipolar recoupling

There is also a wide range of homonuclear dipolar recoupling pulse sequences, which vary in their rf pulse power requirements, excitation bandwidths, tolerance of pulse imperfections, high MAS rates and large CSA [101].

The only homonuclear dipolar recoupling sequence used in this thesis is POST-C7 [106], which is one of the best for moderate MAS rates (under 15 kHz). It is used to excite/de-excite double quantum coherence in DQ–SQ correlation experiments.

An interesting possibility is rotational resonance (RR), where the MAS rate is an integer multiple of the difference in chemical shift between the two spins, which can be shown to recouple the dipolar coupling without any rf pulses [107]. By controlling the MAS rate, it allows recoupling of specific spins pairs, which can be very useful.

### 3.2.3 Problems with using dipolar coupling

Using dipolar coupling to obtain interatomic distances typically runs into one of two key problems. For low  $\gamma$ , low natural abundance nuclei (i.e.  $^{13}\text{C}$  and  $^{15}\text{N}$ ), the probability of finding two close enough together to be able to couple is very low. This means that, particularly for proteins, isotopic labelling schemes have to be employed to selectively enrich the sites of interest. For high  $\gamma$ , high natural abundance nuclei (i.e.  $^{31}\text{P}$  and  $^1\text{H}$ ), then there are often so many interactions that it is impossible to break them down into pairwise interactions, making the determination of individual interatomic distances more difficult. The chemical shift, and CSA, provide an important alternative approach for accessing structural information for occasions when methods involving dipolar coupling fail.

For  $^1\text{H}$ , the homonuclear dipolar coupling is so strong it is not fully averaged out by moderate spinning rates. This leads to very poor signal resolution. Therefore, any HETCOR experiments involving  $^1\text{H}$  must include homonuclear dipolar decoupling, such as combined rotation and multiple pulse spectroscopy (CRAMPS) [108].

### 3.3 SS-NMR in structural investigations

Liquid-state NMR is a very useful tool for molecular identification. The chemical shift, by comparison with chemical shifts of known molecules, gives clues as to what types of nuclear environments are present. Two-dimensional correlation spectroscopy using  $J$ -coupling is used to work out the connectivity of the different nuclear environments and so build up the structure of the whole molecule. Use of NMR in this way is very commonplace.

Whilst solid-state NMR can also be used for molecular identification, it is often also used for studying molecular conformation. If the chemical species (molecules, polymers, ions etc.) present have already been identified, NMR can be used to determine something of the three-dimensional shape of the molecules and polymers (looking particularly at weak interactions such as hydrogen bonds), or packing with respect to other molecules or ions. This section forms a brief review of the current state of ‘NMR crystallography’: the determination of the structure of solids using NMR (either alone or in conjunction with other techniques). Each study utilises one or more of the internal nuclear spin interactions to identify the local environment of the spins. The scope of this review shall be limited to powdered samples and spin-1/2 nuclei.

#### 3.3.1 Using heteronuclear dipolar coupling

Dipolar coupling provides a direct route to internuclear distances, so has found many uses in structural studies. For example, Middleton *et al.* use  $^{13}\text{C}$ – $\{^{15}\text{N}\}$  REDOR (where the nucleus outside the curly braces is the observed spin, and the nucleus inside the curly braces is the spin to which the observe nucleus is recoupled) to determine C–N distances in labelled cimetidine, which were then used as constraints in PXRD structure determination [109]. Cimetidine is sufficiently large and flexible that the probability of successfully locating the global energy minimum using PXRD data alone is low. REDOR results have also been used as constraints in energy minimisation, as has been done with the  $^{13}\text{C}$ – $\{^{15}\text{N}\}$  REDOR of methoxycarbonylurea [110]. In this particular study, the REDOR distances allow the conformation of a single molecule of methoxycarbonylurea to be determined, and then the intermolecular arrangement found by molecular modelling.

An inorganic layered material, chiolite ( $\text{Na}_5\text{Al}_3\text{F}_4$ ), has had its structure deter-

mined by a combination of  $^{23}\text{Na}$ - $^{19}\text{F}$  and  $^{27}\text{Al}$ - $^{19}\text{F}$  HETCOR, PXRD and force field calculation [111]. In this case the NMR data was used to identify atomic connectivities and then to construct initial building block units to use as initial conditions for structural refinement.

For non-crystalline systems,  $^{13}\text{C}$ -{ $^{31}\text{P}$ } REDOR has been used for applications including locating and identifying the secondary structure of the membrane-active antibiotic peptide, magainin, in phospholipid bilayers [112], and identifying sugar molecules that are close to the mineral interface in bone [113]. Also common is  $^{13}\text{C}$ -{ $^{15}\text{N}$ } REDOR, used for the study of proteins, particularly determination of their secondary structure [114].

### 3.3.2 Using homonuclear dipolar coupling

A  $^1\text{H}$ - $^1\text{H}$  correlation experiment is a common way of obtaining distance constraints, by measuring the rate of proton spin diffusion (PSD). The rate of spin diffusion over time can be modelled, and so proton positions can be determined by fitting experimental data to the model. In combination with a force field calculation, this has been used to determine the crystal structure of aspartylalanine [115]. This structure can then be refined using DFT with periodic boundary conditions, which can include calculation of  $^{13}\text{C}$  chemical shifts to give additional parameters for comparison with experiment, allowing greater confidence in the result [116].

With low  $\gamma$  nuclei, Nomura *et al.* use RR to recouple homonuclear dipolar coupling and measure distances between different homonuclear spin pairs in turn in the uniformly  $^{13}\text{C}$ ,  $^{15}\text{N}$ -labelled short peptide, glycylisoleucine [117]. By doing so, they were able to determine all dihedral angles and so construct the full three-dimensional structure of the peptide, in good agreement with XRD.

### 3.3.3 Using isotropic chemical shift

The isotropic chemical shift can be measured easily under MAS without the need for recoupling pulse sequences. However, the chemical shift can not be directly linked to structure in the same way that dipolar coupling leads to interatomic distances. There are two approaches therefore to using chemical shift in structural investigation: the empirical approach, whereby chemical shifts are compared to those from known structures and it is presumed that similar chemical shifts result from similar structures; or the first principles quantum chemical calculation approach, where computer simu-

lations are used to calculate chemical shifts for a given structure and the results can be compared to the experimental structure.

A particularly pertinent example of the use of isotropic chemical shifts is in determining the secondary structure of proteins and peptides [118]. It was reported that  $\alpha$ -protons (in the liquid-state) vary by up to 0.8 ppm in their isotropic shifts (a large difference for protons) for helical peptides compared to random coil arrangements [119]. This discovery lead to the development of the chemical shift index [120], which assigns blocks of residues to helices or sheets if a sufficient number of  $\alpha$ -proton chemical shifts from that block deviate from the random coil chemical shift in the appropriate direction for a helix or a sheet.

Proton NMR is less useful in the solid-state, due to strong homonuclear dipolar coupling, but the  $^{13}\text{C}_\alpha$ ,  $^{13}\text{C}_\beta$  and amide  $^{15}\text{N}$  chemical shifts are also found to vary with backbone torsion angles,  $\phi$  and  $\psi$ . Surfaces have been plotted of chemical shift deviation (from random coil values) against a range of values of these torsion angles [121, 122]. Iwadate *et al.* have built up an extensive database of  $^{13}\text{C}_\alpha$  and  $^{13}\text{C}_\beta$  chemical shifts for proteins with known solution-state structures [123], with a view to a more comprehensive understanding of the structural effects governing their chemical shift differences.

The chemical shifts can be calculated using *ab initio* methods introduced in Section 1.4. Assuming sufficient accuracy can be obtained in the calculations, they can be useful for structure determination where a suitable reference for empirical judgment is not available. Attempts have been made at reproducing the empirical data for isotropic shifts in peptides [121] using *ab initio* methods [124]. However, the complexity of a calculation increases rapidly with the size of the system, so computer simulations are better suited to smaller molecules.

For example, Harris *et al.* use chemical shift calculations of the crystal structure two polymorphs of 4-methyl-2-nitroacetanilide (MNA) [125] using DFT with plane-wave pseudopotentials (to take advantage of the periodic nature of crystals) [22, 23]. They track the change in isotropic shift of the ring carbons with variation of a particular torsion angle to find the torsion angle where the chemical shifts match best their values from CP-MAS experiment. Meanwhile, Smith *et al.* have utilised  $^{13}\text{C}$  and  $^{15}\text{N}$  chemical shifts to distinguish between trial crystal structures for the pharmaceutical, theophylline [126], which were indistinguishable by PXRD fits or

lattice energy calculations.

### 3.3.4 Using chemical shift anisotropy

The isotropic shift contains only one piece of data, the average of the three principal values of the CST. The information available from measuring the full CST (or equivalently the isotropic shift, CSA and asymmetry) can provide superior structure determination compared to the isotropic shift alone [127]. CSA can be used in the same way as isotropic shift, by empirical comparisons or quantum chemical calculation. The CSA can be recoupled under MAS using one of the experiments described in Section 3.1.

Initially, CSA was used in another way; to aid assignment of isotropic chemical shifts. An example for this is for cortisone acetate, with five high  $^{13}\text{C}$  chemical shift signals and seven known polymorphs, where the assignments of the peaks, which have similar isotropic chemical shift, is made by the distinctly different CSA values [128]. Shao *et al.* use CSA amplification to measure the CST of some carbohydrates, using comparison with DFT calculation to aid signal assignment [129].

The superiority of CSA over isotropic shift alone has been demonstrated in a study of some carbohydrates with known structure [130]. This study used rapid energy optimisation techniques to form a range of trial structures, for which the full  $^{13}\text{C}$  CST was calculated using HF methods, and trial structures were eliminated when the calculated CST is a poor match for experimental values. In each of the four carbohydrates tested, the known crystal structure was found amongst the top five structures ranked by fit to the full CST. However, when using isotropic shift alone, for two of the four carbohydrates the correct structure was ranked significantly below the best fit structure and was thus eliminated as a possible solution.

A similar approach to that used on MNA with isotropic shifts [125], is adapted for use with anisotropies [131, 132]. The effect on  $^{13}\text{C}$  CSAs of changing a particular torsion angle between two aromatic rings in 5-methyl-2-[(2-nitrophenyl)amino]3-thiophenecarbonitrile (known as ROY) is investigated by isolated molecule DFT calculations. The torsion angle between the aromatic rings in each of three polymorphs of ROY are determined by comparing their experimental CSA to the calculated values. The  $^{13}\text{C}$  CSTs polymorphs of dimethyl-3,6-dichloro-2,5-dihydroxyterephthalate have also been compared to HF and DFT calculated values for three-molecule clusters, although this study warned that the absolute agreement between experiment and

calculation was moderate [133]. Ma *et al.* also warn about reliance on DFT calculation of CST for small clusters, finding large differences (23 ppm) between experimental and theoretical CST principal values for some substituted naphthalenes [134].

In a separate study on polymorphism,  $^{13}\text{C}$  CSTs was used to detect which part of the molecule 10-deacetyl baccatin III changes conformation between the major (fully characterised by XRD) polymorph, and the minor polymorph (not fully characterised by XRD) [135]. They find that the conformational change, as seen by  $^{13}\text{C}$  CST is confined to one cyclohexenyl ring and any ring substituents.

More recently,  $^{29}\text{Si}$  chemical shifts have been used in an iterative process for geometry optimisation of the structure of a zeolite, silica-ZSM-12 [136]. Partial differentials of the CST (from *ab initio* quantum chemical calculations) with respect to small perturbations in atomic co-ordinates, are combined with distance restraints from PXRD to compute a change in the structure for the next iteration. The CST proves to be extremely sensitive to changes in atomic co-ordinates on the order of 0.1 Å.

Secondary structure in proteins also affects the CSA, as shown empirically [137] and by computer simulations [138–140]. The calculated  $^{13}\text{C}_\alpha$  CST dependency on  $\phi$  and  $\psi$  torsion angles has been put to use for determining the secondary structure of proteins such as melanostatin [141], with good agreement with the X-ray structure, except for at glycine and proline residues.

The CSA is also highly sensitive to hydrogen-bonding. It has been used in combination with PSD, for instance, to study the hydrogen-bonding pattern of *N*-benzoyl(-DL-)L-phenylalanine polymorphs [142].

Other nuclei for which CST measurements have been used (for structure determination, molecule identification, signal assignment or otherwise), include  $^{15}\text{N}$  in azobenzene dyes [143] and peptides [144] and  $^{31}\text{P}$  in DNA [145] and phospholipids [146]. Examples can also be found involving  $^{119}\text{Sn}$  in crystalline trialkyltin functionalised octameric spherasilicates [147],  $^{113}\text{Cd}$  bound to biological ligands [148], and most other spin-1/2 nuclei.

### 3.3.5 Correlation of dipolar and chemical shielding tensors

If dipolar coupling and chemical shielding can both be determined, this provides two excellent sources of data for structural determination. Even better, if the orientation of the dipolar coupling tensor (aligned with the internuclear vector) with respect to the CST can be determined, this fixes the orientation of the CST in the molecular

frame. The orientation of the CST can also be used, empirically or by first principles calculation, as another constraint that narrows the range of feasible structures.

A typical example of this is the orientation of the  $^{13}\text{C}_\alpha$  CST in peptides, which is found to be dependent on the  $\phi$  and  $\psi$  backbone torsion angles [124, 138]. To measure this orientation, an experiment is needed that provides good site resolution, high angular precision and high sensitivity. A good example of such an experiment is the dipolar-modulated SUPER technique of Yao and Hong [149], using  $^{15}\text{N}$ - $^{13}\text{C}$  dipolar coupling (and therefore requiring isotope labelling), but was later shown to be also possible to utilise the  $^{14}\text{N}$ - $^{13}\text{C}$  dipolar coupling [150].

## Chapter 4

---

# Sideband–sideband correlation

---

It has been demonstrated in Section 3.3 how measurements of CSA have been used as part of a structural investigation. It is therefore desirable to be able to measure the CSA as accurately as possible and in as many situations as possible. This chapter, therefore, explores some developments for measuring CSA with improved accuracy, and a situation where CSA measurement was previously considered challenging, namely where two signals share the same isotropic chemical shift.

The CSA-amplified PASS experiments [84–87] described in Section 3.1 are able to recouple CSA under fast MAS in the form of a sideband pattern that is equivalent to a sideband pattern for a spinning rate that is scaled down by a factor,  $\chi_a$ . This one-dimensional sideband pattern can be fitted to give CST principal values, but only if the signals are fully resolved by their isotropic chemical shift [39].

At intermediate MAS rates sidebands also appear in the direct dimension. The two-dimensional CSA-amplified PASS spectrum therefore shows a correlation pattern between sidebands at two spinning rates, the form of which shall be derived in Section 4.1. In this chapter it is explained how the data available from the two-dimensional sideband–sideband correlation pattern is not currently used to its full potential. Currently it is usually converted to a one-dimensional sideband pattern by a process known as projection. This process of projection loses some of the detail of the spectrum, reducing the accuracy of the CST principal values determined from it.

Additionally, the correlation pattern can, in some situations, be used to determine

CST principal values even when two signals share the same isotropic shift. This possibility is demonstrated on a mixture of phosphates, which share the same  $^{31}\text{P}$  isotropic shifts, but can have their CST principal values determined separately as an independent test. It is then applied to a real life problem, the overlapping  $^{13}\text{C}$  signals in the antibiotic, ampicillin.

#### 4.1 Peak intensities in CSA-amplified experiments

In a CSA-amplification experiment, in  $t_1$  it is desired that the magnetisation evolves under the anisotropic chemical shift that is scaled by  $\chi_a$  (and an isotropic chemical shift that is scaled by  $\chi_i$ , which, in CSA-amplified PASS is conveniently set to zero). The signal from a particular crystallite, with orientation given by the Euler angles,  $\Omega_{\text{PR}} = (\alpha_{\text{PR}}, \beta_{\text{PR}}, \gamma_{\text{PR}})$ , after evolution under the scaled anisotropy for  $t_1$  and the normal MAS Hamiltonian for  $t_2$ , is given by an extension of Equation (2.83) [81]:

$$\begin{aligned} S_c(t_1, t_2; \gamma_{\text{PR}}) &= \exp\{i\chi_a[\xi(t_1; \gamma_{\text{PR}}) - \xi(0; \gamma_{\text{PR}})]\} \\ &\quad \times \exp\{i[\omega_{\text{iso}}t_2 + \xi(t_2; \gamma_{\text{PR}}) - \xi(0; \gamma_{\text{PR}})]\}. \end{aligned} \quad (4.1)$$

The sideband intensity factors,  $C_c^{(j)}$ , which are the equivalent of  $F_c^{(k)}$  in Equation (2.86), but for the scaled anisotropy are:

$$C_c^{(j)}(\gamma_{\text{PR}}) = \frac{1}{\tau_{\text{R}}} \int_{t=0}^{\tau_{\text{R}}} \exp(i\chi_a \xi(t; \Omega_{\text{PR}})) \exp(-ij\omega_{\text{R}}t) dt. \quad (4.2)$$

By a change of variables,  $t' = \chi_a t$ , these  $C_c^{(j)}$  values can be shown to be equivalent to the intensities of the  $j^{\text{th}}$  sideband for the CST at an effective reduced spinning rate,  $\omega_{\text{R}}/\chi_a$ .

Equation (4.1) can then be expressed in terms of the Fourier components,  $C_c^{(j)}$  and  $F_c^{(k)}$ :

$$\begin{aligned} S_c(t_1, t_2; \gamma_{\text{PR}}) &= \sum_{j'} \sum_{k'} \sum_j \sum_k C_c^{(j)}(\gamma_{\text{PR}}) [C_c^{(j')}(\gamma_{\text{PR}})]^* F_c^{(k)}(\gamma_{\text{PR}}) [F_c^{(k')}(\gamma_{\text{PR}})]^* \\ &\quad \times \exp\{i(j\omega_{\text{R}}t_1 + \omega_{\text{iso}}t_2 + k\omega_{\text{R}}t_2)\}. \end{aligned} \quad (4.3)$$

Using the relationship between the signal of different members of a carousel, given in

Equation (2.91), this can be re-expressed as:

$$\begin{aligned} S_c(t_1, t_2; \gamma_{\text{PR}}) &= \sum_{j'} \sum_{k'} \sum_j \sum_k C_c^{(j)}(0) [C_c^{(j')}(0)]^* F_c^{(k)}(0) [F_c^{(k')}(0)]^* \\ &\times \exp\{i(j\omega_R t_1 + \omega_{\text{iso}} t_2 + k\omega_R t_2)\} \\ &\exp\{i(k - k' + j - j')\gamma_{\text{PR}}\}. \end{aligned} \quad (4.4)$$

Integrating over a carousel (i.e. over  $\gamma_{\text{PR}}$ ), only terms with  $k - k' + j - j' = 0$  survive. The intensity,  $I_c$ , of the two-dimensional cross peak that is the  $j^{\text{th}}$  sideband in  $\omega_1$  and the  $k^{\text{th}}$  sideband in  $\omega_2$ , from a particular carousel, is therefore given by:

$$I_c(j, k) = \sum_{j'} C_c^{(j)}(0) [C_c^{(j')}(0)]^* F_c^{(k)}(0) [F_c^{(k+j-j')}(0)]^*. \quad (4.5)$$

The total intensity of the cross peak is then found by integrating Equation (4.5) over  $\alpha_{\text{PR}}$  and  $\beta_{\text{PR}}$  angles. A simulated spectrum from a CSA-amplified PASS experiment is shown in Figure 4.1.

If the MAS rate is fast, only the  $k = 0$  sideband in  $\omega_2$  is significant. In this case, the intensities of the sidebands in  $\omega_1$  are:

$$I_c(j) = C_c^{(j)}(0) [C_c^{(j)}(0)]^* = |C_c^{(j)}(0)|^2, \quad (4.6)$$

which is identical to Equation (2.91), and are the intensities of the sidebands that would be seen in a simple one-dimensional experiment where the MAS rate was reduced to  $\omega_R/\chi_a$ .

Alternatively, the one-dimensional sideband pattern can be created by projecting the two-dimensional pattern onto the  $\omega_1$ -axis [84]. In this case:

$$I_c(j) = \sum_k I_c(j, k) = \sum_k \sum_{j'} C_c^{(j)}(0) [C_c^{(j')}(0)]^* F_c^{(k)}(0) [F_c^{(k+j-j')}(0)]^*. \quad (4.7)$$

However, the Fourier components have the following property:

$$\sum_k F_c^{(k)}(0) [F_c^{(k+j-j')}(0)]^* = \begin{cases} 1, & \text{if } j = j' \\ 0, & \text{otherwise} \end{cases}, \quad (4.8)$$

therefore:

$$I_c(j) = C_c^{(j)}(0) [C_c^{(j)}(0)]^* = |C_c^{(j)}(0)|^2, \quad (4.9)$$

which is again the one-dimensional sideband pattern characteristic of the reduced MAS rate.

The projection of the correlation pattern onto the  $\omega_2$ -axis yields the sideband pattern for the actual MAS rate, although there is little experimental point to this. The sideband pattern for the actual MAS rate could be obtained much more quickly, and with fewer experimental errors, by a simple one-dimensional CP-MAS experiment.

How the CSA-amplified PASS experiments obtain a signal of the form given in Equation (4.1) differs between the Crockford *et al.*, Orr *et al.* and Shao *et al.* variants, and is not of vital importance here. The discussion of the rest of the chapter applies equally to all these variants, although the experimental examples use Orr's version for a matter of convenience. The CSA recoupling experiments other than CSA-amplified PASS, such as ROSES, give a signal that is similar to, but not identical to Equation (4.1), and so do not give true sideband patterns, but distorted ones. These distorted sideband patterns can be simulated and used to determine the CST, but this option has not been explored further here.

#### 4.1.1 Two-dimensional correlation spectra

The projection of the two-dimensional sideband–sideband correlation pattern to make a one-dimensional sideband pattern discards some useful information in going from Equation (4.5) to Equation (4.9), specifically the correlation between  $F_c$  and  $C_c$  terms. With the correlation pattern, there is greater potential for determining the CST principal values more accurately and, in particular, in cases where there are two sideband patterns that are overlapping. The price to pay is reduced signal-to-noise ratio since the signal intensity is spread over more points. This sacrifice is not a severe as one might initially think, as the sidebands in the two-dimensional correlation pattern can have both positive and negative phases; when the projection is taken there is some cancellation of signal, and so the signal-to-noise ratio does not increase as much as expected.

For resolved signals, the reason why the correlation approach can sometimes give improved accuracy in fitting chemical shift parameters, is that, for a small change in one of the CST parameters, say  $\zeta$ , there is a larger change in the appearance of the two-dimensional sideband–sideband correlation pattern than there is in the appearance of the projected one-dimensional sideband pattern (as measured by the sum of the squared differences between the two spectra, see Figure 4.2). From the point of view of

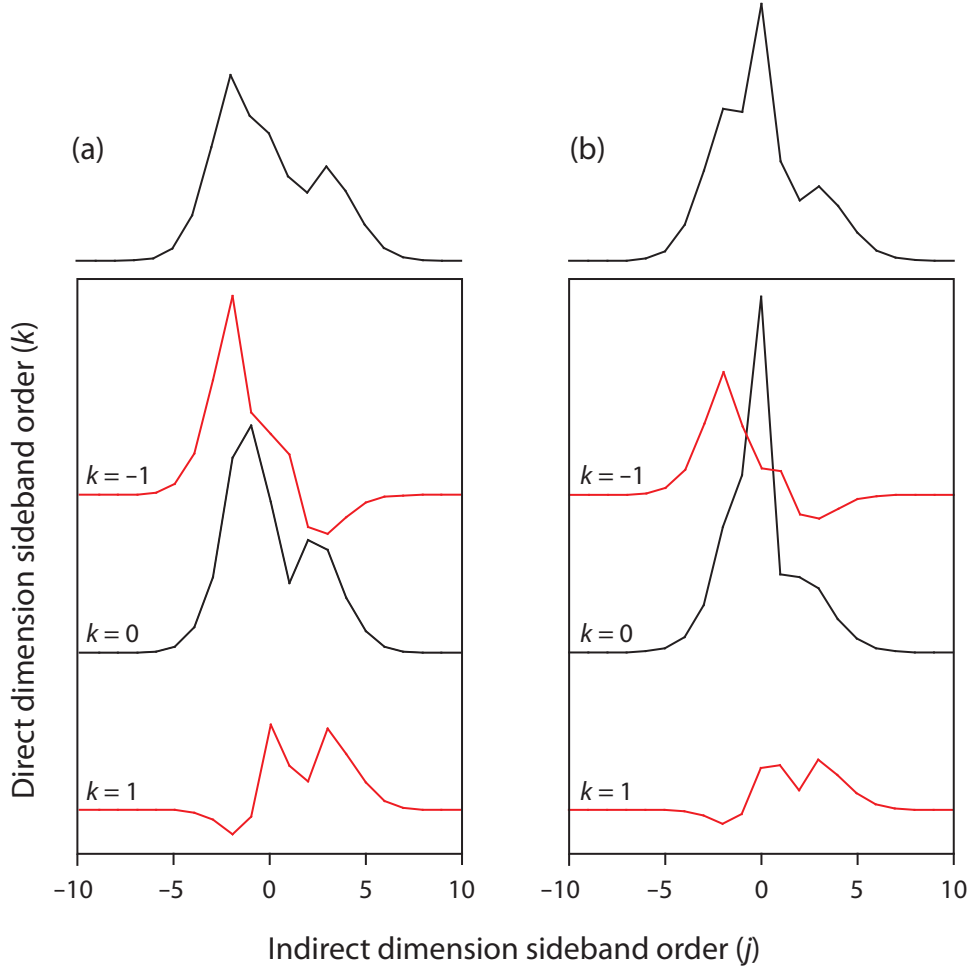


**Figure 4.1** (a) Simulated two-dimensional sideband correlation pattern from a CSA-amplified PASS experiment, with  $\Delta_\omega/\omega_R = 2$ ,  $\eta = 0.5$ , and  $\chi_a = 3$ , such that the apparent spinning rate for the sideband pattern in the indirect dimension is  $\chi_a \Delta_\omega/\omega_R = 6$ . The slices show the sideband intensity envelope in  $\omega_1$  (presented in the same fashion as the one-dimension sideband intensity envelopes in Figure 2.4), correlated with the sideband order from the direct dimension sideband spectrum. The sideband envelope at the top is the projection on the  $\omega_1$ -axis, which is a faithfully-reproduced sideband pattern corresponding to the scaled spinning rate. (b) Simulated two-dimensional sideband correlation pattern from a CSA-amplified PASS experiment, with overlapping signals from two components with,  $\Delta_\omega/\omega_R = 2$ ,  $\eta = 0.5$ , and  $\Delta_\omega/\omega_R = 0.5$ ,  $\eta = 0.8$ . The scaling factor for the spinning rate in the indirect dimension is unchanged,  $\chi_a = 3$ , and the projection on the  $\omega_1$ -axis is also shown. It is clearly visible that the  $k = \pm 1$  sidebands (in red) are largely unaffected by the addition of the second component, whereas the  $k = 0$  sideband and projection (in black) are severely changed.

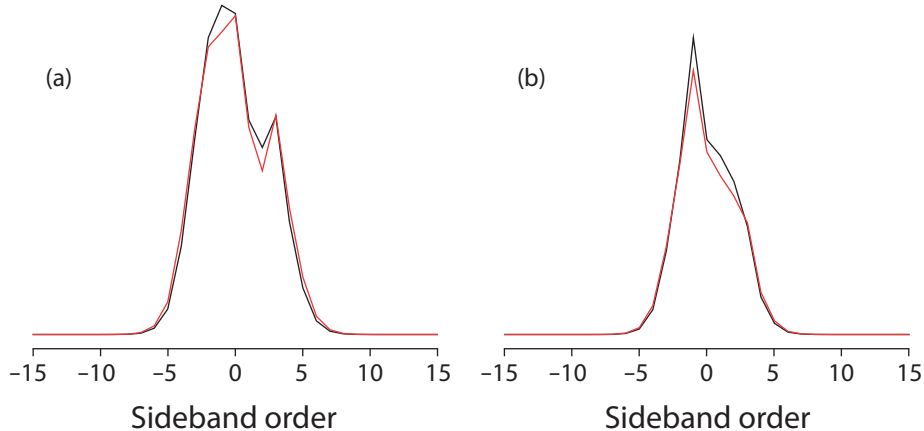


**Figure 4.2** Change in sideband manifold appearance caused by a 5% change in the CSA parameter for (a) one-dimensional sideband pattern and (b) a slice in the two-dimensional correlation pattern, through the  $k = 0$  sideband in the direct dimension. These two have a very similar change in terms of the sum of squared differences. However, the correlation pattern is supplemented by the changes in the slices correlated with the outer direct dimension sidebands (not shown), giving a greater total change in the appearance of the spectrum, measured by  $\chi^2$ .

the least squares fitting procedure analysing a noisy spectrum, this is very important; the confidence limits on the best fit parameters are determined by the limits of the fitted parameters where the change in the appearance of the spectrum is insignificant compared to the noise level. If the same change in a parameter causes a greater change in the appearance of the spectrum, then the confidence limits are going to be narrower.

If a projection is used, the root mean square (rms) noise level is increased in the projected sideband pattern by a factor of  $\sqrt{N}$ , where  $N$  is the number of direct dimension sidebands over which the projection is taken. This means that the confidence limits for the fitted CST parameters will be widened.

Now consider overlapping signals in the extreme case of a system where the one of the overlapping components with identical isotropic shift has very much larger CSA than the other, exemplified by spectrum (b) in Figure 4.1. In the two-dimensional correlation pattern, the component with the small CSA is almost entirely contained in the  $k = 0$  sideband in the direct dimension, as the actual MAS rate is large compared to the CSA of this component. This means that the outer direct dimension sidebands result almost entirely from the component with the larger CSA. The slices through the indirect, reduced spinning rate, dimension, for the  $k \neq 0$  sidebands from the direct dimension, can then be analysed to reveal the chemical shift parameters of

the component with the larger CSA. The contribution of the component with the larger CSA to the reduced spinning rate sideband envelope correlated with  $k = 0$  sideband in the direct dimension can be calculated and subtracted from the spectrum, leaving only the sideband envelope for the component with the smaller CSA. This can now be fitted to reveal the chemical shift parameters for the second site, and so the parameters for both sites have been determined, essentially by separating the two overlapping sideband patterns according to their CSA. This separation is not possible in a one-dimensional sideband pattern (such as the projections shown in Figure 4.1).

In the more general case, where the CSA of the two components are more similar, the slices in the two-dimensional spectrum, correlated with each sideband in the direct dimension, will contain contributions from both components, in proportions determined by the populations of the two sites and intensity of the direct dimension sideband which is turn is determined by the size of the CSA. Unless the CSAs are very similar (i.e. their sideband patterns are indistinguishable within the level of noise), there is still scope for determining the chemical shift parameters by least squares fitting of the correlation pattern as a whole.

This principle is the basis for accurate determination of CSA that is pursued in this chapter. Some questions raised, which will be answered in the sections that follows, include:

- What are the optimal correlated spinning rates (for resolved signals and overlapping signals)?
- Can one determine how many overlapping components are present in a given spectrum? What is the maximum number of overlapping components for which the CSA can be measured?
- How different must two CSAs be if they are to be distinguished?
- How weak can one signal be before it is swamped by a stronger one?

These issues and others will be investigated extensively by computer simulations in Section 4.2, and then the concept is demonstrated experimentally in Section 4.3.

#### 4.1.2 Extension to the third dimension

The CSA-amplified PASS experiment can be readily extended to a three-dimensional experiment. This might be necessary if the actual MAS rate is restricted, for reasons of

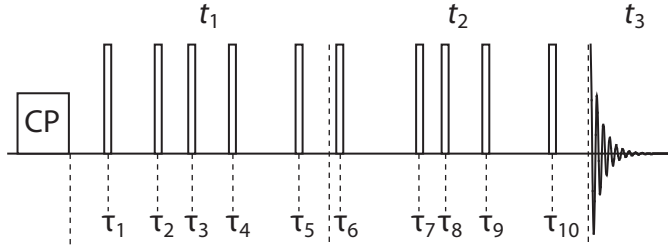


**Figure 4.3** Recommended pulse sequence for a three-dimensional CSA-amplified PASS sequence. Each of the  $t_1$  and  $t_2$  evolution periods contain a PASS sequence with a different scaling factor. The pitch of each of the two PASS sequences is cycled independently by adjusting the pulse timings. The sequence shown here is based upon the two-dimensional version of Orr *et al.* [86], although this is not an essential feature of the three-dimensional experiment.

resolution, to speeds where only the  $k = 0$  sideband is visible in the direct dimension. In such circumstances a correlation pattern would not be formed by a two-dimensional experiment, as the spectrum would be of the form given in Equation (4.9).

By inserting a second PASS sequence with a different scaling factor to the first, and cycling through the different pitches of each PASS sequence (which determine the effective  $t_1$  and  $t_2$  times) independently, a three-dimensional experiment is created. The pulse sequence for this experiment is shown in Figure 4.3. The resulting spectrum contains two-dimensional sideband correlation patterns, characteristic for the two reduced spinning rates, separated by their isotropic shifts in the third dimension. The form of these correlation patterns is the same as Equation (4.5), except that now the  $C_c$  terms are given by:

$$C_c^{(j)}(\gamma_{\text{PR}}) = \frac{1}{\tau_R} \int_{t=0}^{\tau_R} \exp(i\chi_{a,1}\xi(t; \Omega_{\text{PR}})) \exp(-ij\omega_R t) dt, \quad (4.10)$$

and the  $F_c$  terms by:

$$F_c^{(k)}(\gamma_{\text{PR}}) = \frac{1}{\tau_R} \int_{t=0}^{\tau_R} \exp(i\chi_{a,2}\xi(t; \Omega_{\text{PR}})) \exp(-ik\omega_R t) dt, \quad (4.11)$$

where  $\chi_{a,1}$  and  $\chi_{a,2}$  are the anisotropic scaling factors during  $t_1$  and  $t_2$  respectively, and  $\chi_{a,1} > \chi_{a,2}$ .

Such an experiment need not be prohibitively lengthy. The faster of the two reduced spinning rates needs only to be slow enough to show a few sidebands in  $\omega_2$ . The number of increments of the pitch needed for this dimension, which is equal to the maximum number of sidebands, is also small. The three-dimensional experiment

is therefore only equivalent to running a two-dimensional experiment a few times, which is eminently feasible. Although it is not *anticipated* to be overly problematic to implement this experiment, it has not yet been attempted. As shall be uncovered by the investigations of Section 4.2, the potential useful applications of the three-dimensional CSA-amplified PASS will in fact be rather limited.

## 4.2 Investigation by computer simulations

As a first step to determine whether this correlation approach is useful for measuring CSA, two-dimensional correlation patterns were simulated by calculating Equation (4.5) explicitly, for a range of values of the anisotropies and asymmetries, and the actual and reduced spinning rates, with a view to find the optimal choices of the correlated spinning rates for the most accurate determination of the CSA. Random noise was generated with a Gaussian distribution and added to the spectra. The reliabilities of  $\zeta$  and  $\eta$  values obtained from least-squares fitting of these simulated spectra are calculated using the Cramér–Rao lower bounds method [151], which uses the partial derivatives of the intensities of each point in the spectrum with respect to each fitted variable,  $\zeta$  and  $\eta$ . The reliabilities of  $\zeta$  and  $\eta$  values obtained from least-squares fitting of the one-dimensional sideband patterns that are the projections of these two-dimensional sideband correlation spectra are also calculated for comparison. The projected sideband patterns are made by summing over the sidebands in the higher spinning rate dimension, taking the sum over as many sidebands in the high spinning rate dimension as were clearly visible above the noise. An enormous amount of data of this nature has been collected; only the most relevant points have been summarised here.

If the noise level is low, and if the intensities of the correlated sidebands change significantly for a small change in  $\zeta$  and  $\eta$ , then the values of  $\zeta$  and  $\eta$  are likely to be accurate and the reliability is high. If changes in the intensities of the correlated sidebands caused by a small change in  $\zeta$  and  $\eta$  are small compared to the noise level, then there is likely to be significant error in  $\zeta$  and  $\eta$  values determined from fitting the spectrum, and the reliability is low. Relative error is proportional to the inverse of the reliability. A reliability,  $r = 1$ , means that the fitted  $\zeta$  or  $\eta$  value to which it refers is completely random (the error is as large in magnitude as the measured value).

The noise level per point in a two-dimensional spectrum depends on a number

of experimental features, in particular the total time for which the experiment is run [152]. In order to compare the reliabilities that could be obtained in a certain total experimental time, the noise level per point of the correlation pattern is kept constant at an arbitrary value (so the signal-to-noise ratio is not constant, as when the spinning rates are lower, the signal is spread out over more points).

The absolute reliability depends (inversely) upon the arbitrary noise level. Therefore, the reliabilities for each parameter are scaled by the maximum reliability for that parameter for any combination of spinning rates. This relative reliability (rr) does not depend on the arbitrary noise level. The desired absolute reliability depends on the intended application of the fitted parameters.

#### 4.2.1 Resolved signals

Figure 4.4 shows how the reliability of  $\Delta_\omega$  (the CSA in angular frequency units) and  $\eta$ , depend upon the correlated spinning rates for resolved signals. Figure 4.5 shows the same for projections of the correlation patterns. The reliability of the chemical shift parameters determined from the two-dimensional pattern is always greater than or equal to the reliability of the chemical shift parameters determined from the projected pattern. The cases where they are equal are those where the actual MAS rate is so high that the only significant direct dimension sideband is  $k = 0$  and the two-dimensional pattern is identical to the projection pattern. Figure 4.6 shows the relative reliabilities of fitting parameters from the projection pattern compared to those from the correlation pattern as a function of the correlated spinning rates.

The optimum combination of spinning rates for reliable determination of the CSA is found to be  $\omega_R/\Delta_\omega = 0.4$  and  $\omega_R/\chi_a\Delta_\omega = 0.4$ . This is in fact the conditions for a 2D-PASS experiment (no CSA amplification), with the optimal MAS rate [39]. Such a spectrum shows a one-dimensional sideband pattern with five visible sidebands into which the signal intensity is concentrated. In this circumstance the deleterious effects of the projection are avoided, and the so the advantage of the stronger signal outweighs the smaller change in the form of the pattern for a given change in a parameter. Under 2D-PASS conditions, the errors from one-dimensional and two-dimensional analyses are obviously equal.

The optimal MAS rate for 2D-PASS may not always be experimentally obtainable, as it may be too slow for stable spinning. However, there is a wide range of correlated spinning rates that allow determination of the chemical shift parameters that is almost

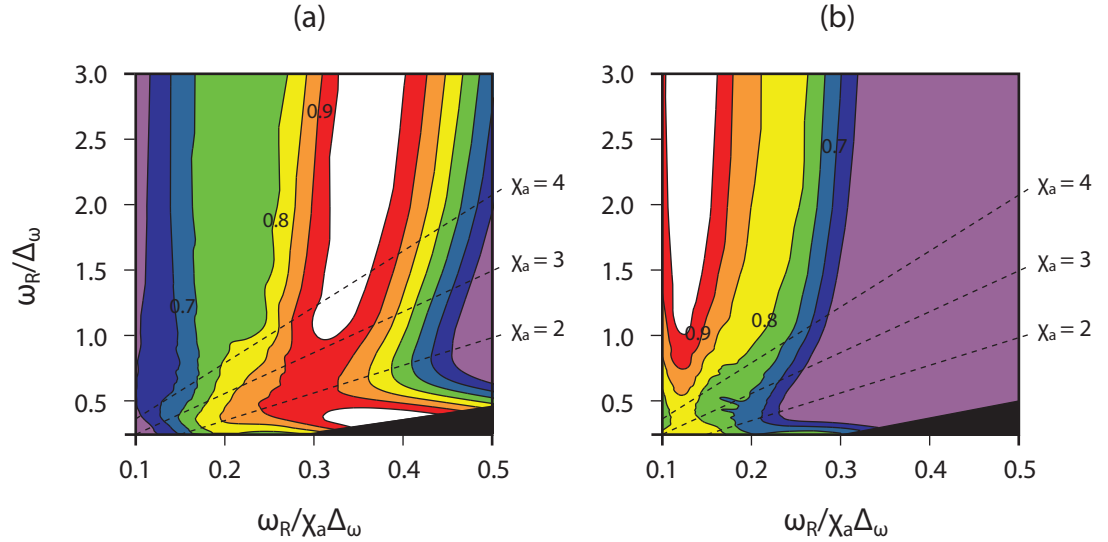


**Figure 4.4** Contour plots showing how the reliability of (a)  $\Delta_\omega$  and (b)  $\eta$ , scaled to the maximum reliability of each parameter, depend upon the ratio of the actual MAS rate to the CSA ( $\omega_R/\Delta_\omega$ ) and ratio of the reduced MAS rate to the CSA ( $\omega_R/\chi_a\Delta_\omega$ ), for fitting of two-dimensional correlation patterns. The contour levels are every 0.05 in relative reliability (the white region is  $rr > 0.95$ , the violet region is  $rr < 0.65$ ). Also marked are the dashed lines showing some different values of  $\chi_a$ . The blacked-out region marks the non-sensical region corresponding to  $\chi_a < 1$ .

as reliable as the 2D-PASS. These spinning rates are identified by the ‘L’-shaped ridge in Figure 4.4(a). This includes the regime where the actual MAS rate is high and the reduced rate is slightly less than  $\omega_R/\chi_a\Delta_\omega = 0.4$ , which requires one of the CSA-amplification experiments. Unless the actual spinning rate is very large, the spectrum shows a correlation pattern from which the CSA can be measured more accurately as a whole rather than a projection.

The reliability of the asymmetry,  $\eta$ , depends slightly differently on the correlated spinning rates. The highest reliabilities here are seen where the reduced spinning rate is around  $\omega_R/\chi_a\Delta_\omega = 0.15$ , and the actual MAS rate is high. However, this is for a particular value of  $\eta = 0.5$ ; different values of  $\eta$  have different optimal spinning rates for determination from one-dimensional sideband patterns [39]. As a general trend, the larger the asymmetry, the larger the optimal reduced spinning rate.

There is a valley of low reliability in Figure 4.4 in both  $\zeta$  and  $\eta$  that corresponds approximately to a scaling factor,  $\chi_a = 2$ . This suggests that larger scaling factors, perhaps  $\chi_a > 4$ , should be used wherever possible. The reason for the appearance of this valley is unknown.

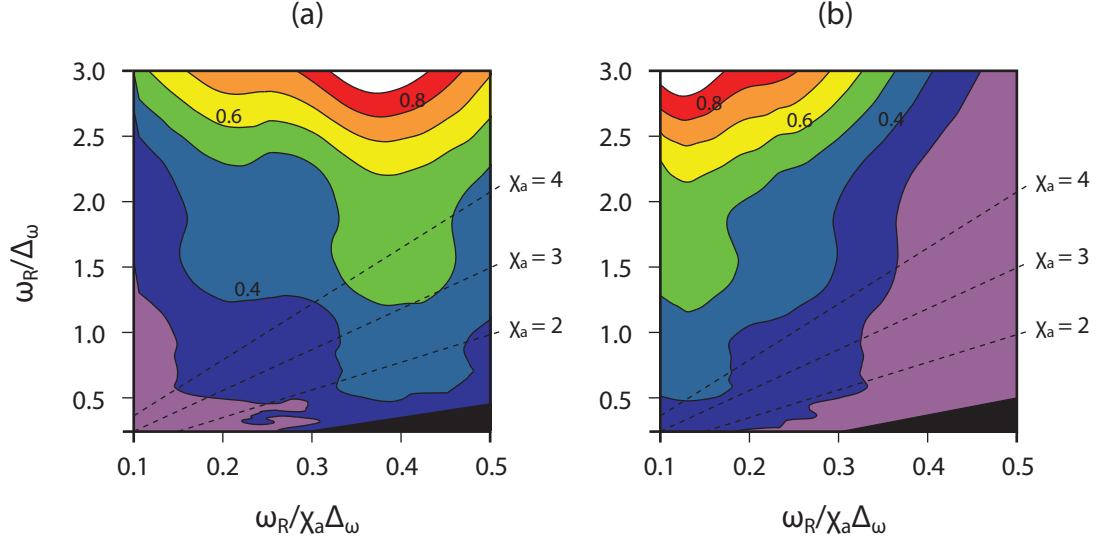


**Figure 4.5** Contour plots showing how the reliability of (a)  $\Delta_\omega$  and (b)  $\eta$ , scaled to the maximum reliability of each parameter, depend upon the ratio of the actual MAS rate to the CSA ( $\omega_R/\Delta_\omega$ ) and ratio of the reduced MAS rate to the CSA ( $\omega_R/\chi_a \Delta_\omega$ ), for fitting of one-dimensional projected sideband patterns. These patterns were created by summing a two-dimensional pattern over as many sidebands with a predetermined minimum intensity. The contour levels are every 0.1 in relative reliability (the white region is  $rr > 0.9$ , the violet region is  $rr < 0.3$ ). Also marked are the dashed lines showing some different values of  $\chi_a$ . The blacked-out region marks the non-sensical region corresponding to  $\chi_a < 1$ . Note that for the  $\chi_a = 1$  diagonal, which corresponds to 2D-PASS without CSA amplification, the experiment will present a one-dimensional sideband pattern without the need for projection, so the reliability here will be greater than determined in this analysis.

For the projection patterns, the dependency of the reliability of  $\zeta$  and  $\eta$  shown in Figure 4.5 is rather simpler to explain. An effective spinning rate of  $\omega_R/\chi_a \Delta_\omega = 0.4$ , as predicted by Hodgkinson and Emsley [39] is best for  $\zeta$  and  $\omega_R/\chi_a \Delta_\omega = 0.15$  is best for  $\eta$ . The reliability increases with actual MAS rate, as there are fewer significant direct dimension sidebands over which the sum of the indirect dimension sideband envelopes must be taken in order to create the projection pattern, and so there is no  $\sqrt{N}$  increase in the noise level. The exception to this trend is the 2D-PASS condition (which is not shown in Figure 4.5), where a one-dimensional sideband pattern occurs naturally on the diagonal of the 2D-PASS spectrum.

The ratio of the reliability parameters from correlation and projection pattern fits (Figure 4.6), shows that they are equal at fast MAS rate and 2D-PASS conditions, but everywhere in between favours the use of the correlation pattern. The major reason for this appears to be mostly due to the number of sidebands required in the projections, with the corresponding increase in the noise level. This greatly outweighs

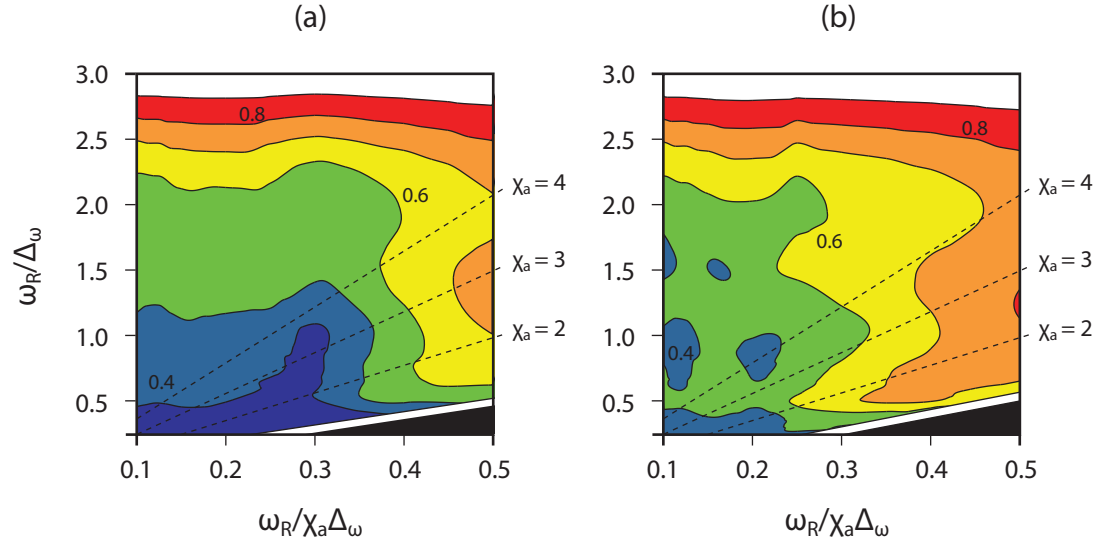


**Figure 4.6** Contour plots showing the ratio of reliability of (a)  $\Delta_\omega$  and (b)  $\eta$ , as determined from a projection plot (Figure 4.5) compared to a correlation pattern (Figure 4.4). The contour levels are every 0.1 in ratio of reliability (the white region is  $r > 0.9$ , the indigo region is  $r < 0.4$ ). Also marked are the dashed lines showing some different values of  $\chi_a$ . The blacked-out region marks the non-sensical region corresponding to  $\chi_a < 1$ . The white regions are where projection and correlation fits have equal reliability, and correspond to fast MAS and 2D-PASS conditions.

the importance of the greater sensitivity of the two-dimensional pattern to changes in  $\zeta$  and  $\eta$ . The variation of Figure 4.6 with reduced spinning rate, seen almost equivalently in the graphs for  $\zeta$  and  $\eta$ , is unexplained.

All the discussion in this section does not apply to one-dimensional sideband patterns that are actually recorded as a one-dimensional experiment (i.e. simple CP-MAS). In circumstances where sufficient resolution can be obtained in a one-dimensional sideband pattern at a low spinning rate, then this is far superior to the two-dimensional correlation since the experiment time is very much shorter (or for the same experiment time, much more signal can be acquired).

#### 4.2.2 Overlapping signals

Regarding overlapping sideband spectra, a similar analysis can be performed, except in this case five parameters need to be determined; the two anisotropies,  $\zeta_1$  and  $\zeta_2$ , two asymmetries,  $\eta_1$  and  $\eta_2$ , and the ratio of the overall intensities of the two components. Of these, the ratio of the intensities is not often of interest, as the intensity of the peaks is not only dependent on the population density of the nuclear environment that causes

it, but also on other factors, such as CP efficiency. A low reliability of the intensity ratio can therefore be tolerated, so long as it does not reduce the reliabilities of the other parameters. The reliabilities of the parameters depend upon the relative sizes of the CSAs being measured, the correlated spinning rates, the proportions of the two components and the noise level.

The optimal choice of correlated spinning rates, assuming a 1:1 mixture of the two components, varies with the ratio of CSAs,  $\zeta_1/\zeta_2$ , as shown in Figure 4.7. If  $\zeta_1$  and  $\zeta_2$  are very different (Figure 4.7(a), 60% difference), the optimum correlated spinning rates for determination of  $\zeta$  are different from the resolved case. The 2D-PASS condition with  $\omega_R/\Delta_\omega = 0.4$  is no longer suitable for determination of the chemical shift parameters. However, there are spinning rates where it is possible to determine the chemical shift parameters accurately. The optimum is found to be with an actual spinning rate around  $\omega_R/\Delta_\omega = 0.5$  and reduced spinning rate around  $\omega_R/\chi_a\Delta_\omega = 0.2$  (i.e. much slower spinning than for resolved signals). The maximum value for the reliability in Figure 4.7(a) is about one sixth of the maximum for the resolved signals; the reliability is significantly reduced by overlapping signals, but is not eliminated entirely. Determination of the chemical shift parameters for overlapping signals is most definitely possible, but may require more scans in an experiment (in order to ensure that the signal-to-noise level is sufficiently high to give a reliability,  $r \gg 1$ ).

If the two CSAs are more similar in value (Figure 4.7(b), 40% difference), the optimal reduced spinning rate is reduced slightly compared to the previous example where the CSAs differed by 60%, and the maximum reliability is also reduced. This is because high order sidebands are required to distinguish between the two components, whose sideband patterns are otherwise very similar. When the CSAs become even more similar (Figure 4.7(c), 20% difference), the reliability of the parameters that could be determined from the correlation pattern falls off dramatically; the sideband patterns are too similar (compared to the level of noise).

Figures 4.7 (a) and (b) show ridges of high reliability that are independent of the actual spinning rate. The ridges extend up to high actual spinning rate, where there are no direct dimension sidebands visible, and the spectrum is a one-dimensional sideband spectrum. This suggests that in fact a correlation pattern is not required for determination of chemical shift parameters from overlapping signals, but merely a sideband pattern for much lower spinning rate than the  $\omega_R/\Delta_\omega = 0.4$  suitable for

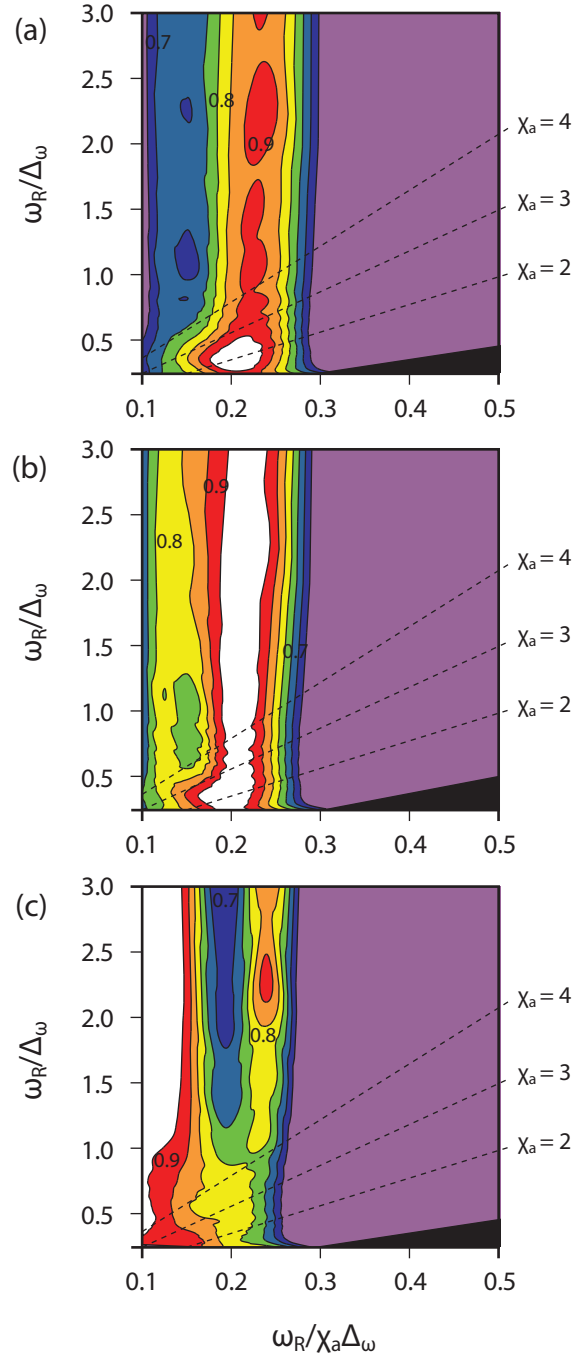


**Figure 4.7** Contour plots showing the reliability of  $\Delta_\omega$  for a signal that is overlapped with another that has an anisotropy of (a)  $0.4\Delta_\omega$ , (b)  $0.6\Delta_\omega$ , and (c)  $0.8\Delta_\omega$ . The contour levels are every 0.05 in relative reliability (the white region is  $rr > 0.95$ , the violet region is  $rr < 0.65$ ).

resolved signals. This is perhaps not a surprise, since as  $\omega_R \rightarrow 0$ , the sideband pattern begins to resemble a powder pattern, for which it is known that principal values for two overlapping components can be determined. Looking back at the work of Hodgkinson and Emsley, this possibility does not appear to have been examined in their analysis. This discovery does not rule out the usefulness of the CSA-amplified PASS sideband–sideband correlation pattern method pitched here; the spinning rate required for a one-dimensional sideband pattern from which it is possible to accurately determine CSA for overlapping components may well be too slow for the hardware to achieve as a direct CP-MAS experiment.

For a fixed combination of anisotropies, it was also investigated as to how the relative proportions of the two components affects the reliability of the fitted parameters. As the overall intensity of one component increases relative to the other, keeping the noise level constant relative to the total intensity of both components, it is understandable that the reliabilities of the chemical shift parameters for the major component become greater, whilst the reliabilities of the parameters for the minor component are reduced. The optimal correlated spinning rates for each particular component are found not to depend strongly upon the intensity ratio of the two signals, however, the optimum correlated spinning rates for the system as a whole move towards the optimum conditions for the minor component.

It has also been investigated whether it is possible to determine CSA for three overlapping components. This has had a modicum of success, provided that: (i) low noise level; (ii) intensities of all components are comparable; and (iii) all three CSAs are very different. Although the first problem can be reduced simply by increasing the number of scans, the latter ones place a severe restriction on the possibility of CSA determination for multiple overlapping signals. Beyond three components in a signal and there is little hope for determining all the CSAs.

It may also be the case that, rather than two distinct environments, there is a degree of disorder, so that one environment has a continuous distribution of CSA values in different parts of the sample. Fitting the sideband pattern of such a system, assuming two components, may result in what looks to be a successful two component fit, whereas in reality both fitted components have CSA values within the distribution of the CSA values of the single, disordered, site. It may be possible to model a Gaussian distribution of CSA values with unknown width (which is an additional parameter for

fitting) to the sideband spectrum. This has not been investigated further – whether or not a Gaussian distribution of CSA is a sensible model remains to be seen, as asymmetry could vary too, and there is the possibility that the variation in CSA and asymmetry may be correlated.

#### 4.2.3 How many components are there?

A key aspect of this work is determining the number of components that comprise a signal, which is not always known *a priori*. Allowing a greater number of variable parameters (by assuming extra components in the signal) in a fitting process will always reduce the goodness of fit parameter,  $\chi^2$ . The chemical shift parameters for components above and beyond the actual number of components present adjust themselves so that they ‘fit’ some of the noise in the spectrum. Even though  $\chi^2$  is reduced, the extra components are false. This problem is not unique to fitting these two-dimensional correlation patterns, but common to all fitting procedures that rely on fitting a model of the spectrum.

Probably the safest way of avoiding this trap is looking at the reduction in  $\chi^2$  caused by adding the extra parameters to the fit; if the reduction is smaller than the noise level, then the extra component should be rejected, as the data is insufficiently clear as to be confident of its presence. The best possible fit is where  $\chi^2$  is equal to the noise level (squared); any further reduction in  $\chi^2$  should be viewed with suspicion by the user.

Another sensible way of weeding out false components is common sense, or chemical intuition. A false component is likely to have improbable chemical shift parameters, such as a very large CSA (for  $^{13}\text{C}$  the largest CSAs are around 130 ppm) or really small intensity. A component should also be rejected if its chemical shift parameters lie within the error bounds of the parameters for another component, since these are likely to be one and the same site (or possibly a part of distribution of similar environments). The reliability of parameters of a false components are likely to be low, and so can be rejected on these grounds too.

The values of chemical shift parameters of a false component should also change if the random noise is changed; if the experiment is repeated, or if simulated noise is added, the values of real parameters may be affected slightly (and their reliabilities will change), but the values of false parameters will be completely different as they are fitting different noise features.

All these methods may fail if there is significant systematic error in the spectrum (which is quite possible in sequences with a long train of  $\pi$ -pulses), as in this case there might still be a major drop in  $\chi^2$  by adding an extra component that results for fitting features caused by the systematic error. The intensity of this false component may be significant and it will not change parameters if the random noise is changed. The best check for this would be to run a completely separate experiment, such as a different scaling factor, a different CSA-amplified PASS variant, XCS, FIREMAT or even MAS-CSA or SUPER, as any systematic errors are likely to affect each one differently.

An open mind should always be kept though – it is possible that the extra minor component, with poorly defined chemical shift parameters, may in fact be real, low intensity component. Its signal is so shrouded in noise and the other signals that the reliability in its parameters is low. The only way to tell for sure whether it is real, is to repeat the experiment a large number of times so that there sufficient signal intensity from this minor component to be able to confidently identify it as a real component.

### 4.3 Experimental examples

The determination of chemical shift parameters from two-dimensional correlation patterns has been demonstrated to be possible using computer simulations. In circumstances where the signals are resolved, a one-dimensional sideband pattern is sufficient to determine the chemical shift parameters, but wherever this has been constructed by projection of a two-dimensional correlation pattern, the parameters could have been determined more accurately by analysing the correlation pattern. This is demonstrated on fumaric acid monoethyl ester, for which the chemical shift parameters for the six  $^{13}\text{C}$  environments have been determined previously using a projection of a correlation pattern produced by the Orr *et al.* CSA-amplified PASS experiment [86].

The determination of chemical shift parameters for overlapping signals is then demonstrated on, first a mixture of phosphates that share the same  $^{31}\text{P}$  isotropic chemical shift, but can have their chemical shift parameters determined accurately from the pure samples. This is followed by an application of the technique to a real-life problem. The antibiotic, ampicillin, contains two  $^{13}\text{C}$  signals that have overlapping chemical shift and so did not have their chemical shift parameters determined in a previous study [153]. The parameters have been determined by DFT calculation

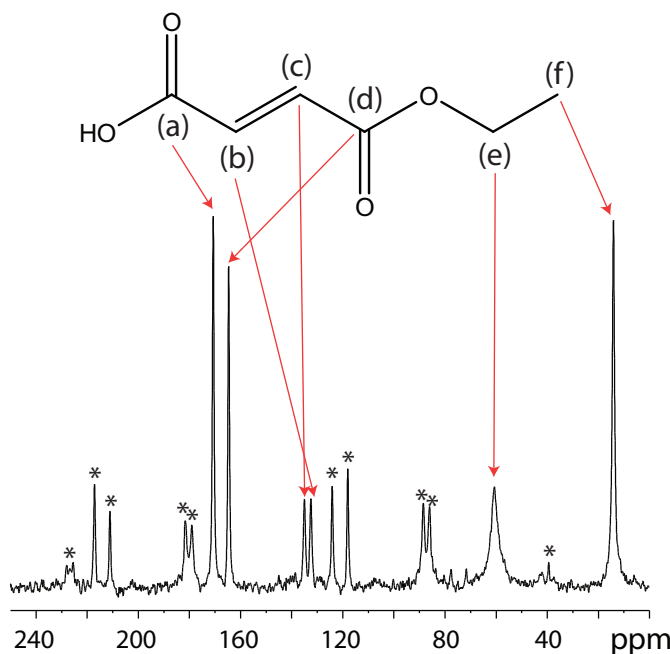


**Figure 4.8** Structure of FAME showing the labelling of the carbon atoms, and one-dimensional <sup>13</sup>C CP-MAS spectrum. Signals marked an asterisk are sidebands.

[154], which show the two overlapping signals should theoretically have significantly different CSA, and so ampicillin presents a potential example for experimental determination of parameters from overlapping signals.

#### 4.3.1 Fumaric acid monoethyl ester

Fumaric acid monoethyl ester (FAME, Figure 4.8) contains six <sup>13</sup>C environments covering a range of anisotropies, and so provides a good test of the scope of a new CSA determination technique. The values of chemical shift parameters for these sites, determined from one-dimensional projected sideband patterns are given in Table 4.1. The values determined from sideband–sideband correlation patterns are given in Table 4.2.

The errors in the chemical shift parameters determined from the correlation patterns are noticeably lower than those for chemical shift parameters determined from the projection pattern, in one case four times lower. The sites with the greatest advantage for the correlation method are those with the larger CSA, since these have more direct dimension sidebands.

$^{13}\text{C}$ site	$\delta_{\text{iso}}$ / ppm	This study		Orr's study	
		$\zeta$ / ppm	$\eta$	$\zeta$ / ppm	$\eta$
(f)	14.8	$13.8 \pm 0.2$	$0.54 \pm 0.04$	13	0.5
(e)	61.6	$-41.2 \pm 0.6$	$0.71 \pm 0.03$	41	0.73
(b)	133.6	$98.9 \pm 1.4$	$0.71 \pm 0.02$	97	0.71
(c)	136.2	$104.0 \pm 1.6$	$0.72 \pm 0.02$	103	0.69
(d)	165.5	$86.9 \pm 0.6$	$0.25 \pm 0.01$	86	0.25
(a)	171.6	$-68.5 \pm 1.0$	$0.99 \pm 0.03$	67	1.0

**Table 4.1** Best fit values for  $^{13}\text{C}$  chemical shift parameters for FAME using one-dimensional sideband patterns. The effective spinning rate for the sideband patterns, which were created by projection of a CSA-amplified PASS experiment, was either 564 Hz or 846 Hz, which ever gave the most accurate parameters for each particular site. Also included for comparison are the values found by Orr *et al.* [86], though he does not quote errors.

$^{13}\text{C}$ site	$\delta_{\text{iso}}$ / ppm	MAS: 5750–564 Hz		MAS: 5750–846 Hz	
		$\zeta$ / ppm	$\eta$	$\zeta$ / ppm	$\eta$
(f)	14.8	$14.1 \pm 0.2$	$0.51 \pm 0.03$	$14.9 \pm 0.2$	$0.43 \pm 0.04$
(e)	61.6	$-42.3 \pm 0.4$	$0.71 \pm 0.01$	$-41.4 \pm 0.4$	$0.71 \pm 0.02$
(b)	133.6	$99.9 \pm 0.6$	$0.72 \pm 0.01$	$101.2 \pm 0.6$	$0.70 \pm 0.01$
(c)	136.2	$105.9 \pm 0.4$	$0.72 \pm 0.01$	$106.9 \pm 0.6$	$0.72 \pm 0.01$
(d)	165.5	$87.8 \pm 0.4$	$0.25 \pm 0.01$	$87.6 \pm 0.2$	$0.25 \pm 0.01$
(a)	171.6	$-69.0 \pm 0.4$	$1.00 \pm 0.01$	$-69.3 \pm 0.4$	$1.00 \pm 0.02$

**Table 4.2** Best fit values for  $^{13}\text{C}$  chemical shift parameters for FAME using two-dimensional sideband correlation patterns, with actual spinning rate of 5750 Hz, and scaling factors of  $\chi_a = 10.2$  (giving a reduced spinning rate of 564 Hz) and  $\chi_a = 6.8$  (giving a reduced spinning rate of 846 Hz).

The CSA determined from the two-dimensional patterns is, in every instance, larger than that determined from the projection pattern, even where the same experimental data has been used. The difference is often greater than the random errors. A possible explanation for this is that the first sidebands that were rejected from the projection and from correlation pattern fitting because they are too weak (compared to the noise level) contain intensity contributions from crystallites that, over the course of a rotor cycle, go through a series of orientations with respect to the magnetic field that have a large variation in frequency. Since these are missed from the projection, the resultant pattern is lacking some of its highly anisotropic components, and so appears narrower (smaller CSA) than it should\*. Although the outer sidebands are also omitted

\*This proposition has since been tested with simulated data, which showed that the effect described

from the fitting of the correlation pattern, their omission does not affect the fitting of the remaining sidebands.

In some cases, the difference between the fitted parameters (for a given chemical site in the two experiments with different correlated spinning rates) is greater than the estimated errors. This may be indicative of the presence of systematic errors in the pulse sequences, that, in this case (where the signal is strong) outweigh the random errors caused by noise.

Not unexpectedly, there was no evidence that any of the signals contained two components. The reduction in  $\chi^2$  by allowing two components rather than one was minimal, and the best fit intensity ratio was close to zero, indicating that one of the two components is not real.

#### 4.3.2 Mixtures of phosphates

Two phosphate compounds were chosen, hydroxyapatite and sodium dihydrogen phosphate, which both have  $^{31}\text{P}$  isotropic shifts of 2 ppm, but crucially have very different CSAs. In a physical mixture of the two compounds, therefore, a CP-MAS spectrum shows a sideband manifold that corresponds to the sum of the sideband manifolds of the two compounds.

First of all, the spectra of the isolated compounds were recorded and used to determine the chemical shift parameters of the  $^{31}\text{P}$  nuclei in each. The values were determined from a two-dimensional sideband correlation pattern, with an actual spinning rate of  $\omega_R/2\pi = 4.08 \text{ kHz}$ , and a scaling factor of  $\chi_a = 6.8$  to give a reduced spinning rate of  $\omega_R/2\pi\chi_a = 0.6 \text{ kHz}$ . Just for comparison, the chemical shift parameters were also determined from the projection of these spectra onto the  $\omega_1$ -axis. The parameters determined in this way, and their lowest bound errors (accounting only for random errors), are given in Table 4.3.

Note that, since there are no other  $^{31}\text{P}$  signals in the spectra, a vastly superior method for determining the CSA of these *resolved* signals would be a simple, one-dimensional, CP-MAS at a suitable low MAS rate. This might not be possible for hydroxyapatite, however, since the CSA is small and so the MAS rate required would be slower than the spectrometer's capabilities.

For five physical mixtures of the two phosphates, in ratios of 1:4, 1:2, 1:1, 2:1

---

is real but might not be strong enough to account for the experimental differences of 1–2 ppm.

	Fitted parameters from projection pattern	Fitted parameters from correlation pattern
Hydroxyapatite	$\zeta = 9.4 \pm 0.2$ ppm $\eta = 0.79 \pm 0.05$	$\zeta = 9.7 \pm 0.1$ ppm $\eta = 0.77 \pm 0.02$
Sodium dihydrogen phosphate	$\zeta = -79.6 \pm 0.7$ ppm $\eta = 0.46 \pm 0.02$	$\zeta = -79.9 \pm 0.2$ ppm $\eta = 0.46 \pm 0.01$

**Table 4.3** Best fit chemical shift parameters for resolved  $^{31}\text{P}$  sites in hydroxyapatite and sodium dihydrogen phosphate, from a CSA-amplified PASS [86] correlation pattern with spinning rate  $\omega_R/2\pi = 4.08$  kHz and scaling factor,  $\chi_a = 6.8$ , and from a projection of this spectrum onto the  $\omega_1$ -axis, which gives a sideband pattern corresponding to a spinning rate of 0.6 kHz. Errors are Cramér–Rao lower bounds estimates of random error [151]. For hydroxyapatite, 3 sidebands are used from the direct dimension and for sodium dihydrogen phosphate, 9 sidebands are used.

Volume ratio	$\zeta_1$ / ppm	$\eta_1$	$\zeta_2$ / ppm	$\eta_2$	Intensity ratio
1:4	$9.4 \pm 0.2$	$0.88 \pm 0.10$	$-79.8 \pm 0.3$	$0.45 \pm 0.02$	1:28.4
1:2	$9.4 \pm 0.2$	$0.82 \pm 0.08$	$-79.7 \pm 0.3$	$0.45 \pm 0.01$	1:15.9
1:1	$9.4 \pm 0.2$	$0.79 \pm 0.05$	$-79.6 \pm 0.3$	$0.46 \pm 0.01$	1:8.5
2:1	$9.4 \pm 0.1$	$0.77 \pm 0.03$	$-79.4 \pm 0.3$	$0.46 \pm 0.01$	1:4.4
3:1	$9.4 \pm 0.1$	$0.76 \pm 0.02$	$-79.2 \pm 0.4$	$0.46 \pm 0.01$	1:3.0

**Table 4.4** Best fit chemical shift parameters for  $^{31}\text{P}$  sites for the hydroxyapatite and sodium dihydrogen phosphate mixtures described in the text, with different volume ratios of phosphate. The best fits are found using the two-dimensional correlation pattern analysis. The parameters  $\zeta_1$  and  $\eta_1$  refer to hydroxyapatite and  $\zeta_2$  and  $\eta_2$  to sodium dihydrogen phosphate. The fitted intensity ratios of hydroxyapatite to sodium dihydrogen phosphate are also listed. Errors are Cramér–Rao lower bounds estimates of random error [151]. In each case 9 direct dimension sidebands were used for fitting. Note that these results are different to those in the reference [155], which are in error due to an inappropriate choice of spinning rate.

and 3:1 hydroxyapatite to sodium dihydrogen phosphate (approximately, by volume), the same CSA-amplified PASS experiment was repeated, and the best fit chemical shielding parameters were determined, fitting five parameters as mentioned previously. These fitted parameters are recorded in Table 4.4. Parameters found from the one-dimensional projections are shown in Table 4.5, and have noticeably higher error bounds.

These results show that the CSA parameters can be determined for the two components using the correlation pattern, even when one component, the hydroxyapatite, contributes only 5% of the total signal. Naturally the errors in the parameters increase as the component to which that parameter refers comprises a smaller fraction of the signal. With the projection pattern, the errors (particularly in  $\eta$  for hydroxyapatite)

Volume ratio	$\zeta_1$ / ppm	$\eta_1$	$\zeta_2$ / ppm	$\eta_2$	Intensity ratio
1:4	$-8.9 \pm 1.7$	$0.9 \pm 0.5$	$-79.5 \pm 0.8$	$0.46 \pm 0.01$	1:26.5
1:2	$8.7 \pm 1.1$	$1.0 \pm 0.3$	$-79.4 \pm 0.8$	$0.46 \pm 0.02$	1:15.6
1:1	$8.8 \pm 1.2$	$0.88 \pm 0.16$	$-79.3 \pm 0.8$	$0.46 \pm 0.02$	1:8.3
2:1	$9.0 \pm 0.3$	$0.83 \pm 0.10$	$-78.9 \pm 1.0$	$0.47 \pm 0.02$	1:4.5
3:1	$9.0 \pm 0.2$	$0.81 \pm 0.08$	$-78.7 \pm 1.1$	$0.48 \pm 0.02$	1:3.1

**Table 4.5** Best fit chemical shift parameters for  $^{31}\text{P}$  sites for the hydroxyapatite and sodium dihydrogen phosphate mixtures described in the text, with different volume ratios of phosphate. The best fits are found using the one-dimensional projection of the two-dimensional correlation pattern analysis. The parameters  $\zeta_1$  and  $\eta_1$  refer to hydroxyapatite and  $\zeta_2$  and  $\eta_2$  to sodium dihydrogen phosphate. The fitted intensity ratios of hydroxyapatite to sodium dihydrogen phosphate are also listed. In each case 9 direct dimension sidebands were used for projection.

become prohibitive much sooner, about when the hydroxyapatite signal comprises around 10% of the total signal. Note that the low intensity of hydroxyapatite is probably tolerated more because it has a low CSA, so the intensity is focused in only a few points. If it were the broader signal that was weaker then the analysis would be likely to fail much sooner.

#### 4.3.3 Ampicillin

The structure of the antibiotic, ampicillin, is shown in Figure 4.9. In a previous study, Antzutkin *et al.* measured using 2D-PASS the chemical shift parameters of all but two of the  $^{13}\text{C}$  sites [153]. The exceptions are C-6 and C-16, both of which have an isotropic shift of 57 ppm, and so their sideband manifolds are overlapping. The signal at 129 ppm also contains two overlapping components, but their CSAs are assumed to be very similar, and no concrete evidence has been produced to say otherwise.

Table 4.6 gives the best fit chemical shift parameters for the resolved ampicillin  $^{13}\text{C}$  sites from this study and the previous one [153]. There is a good agreement between the values from the two studies, except for at sites where the carbon is directly bonded to a nitrogen. The  $^{14}\text{N}$  atom that is in this neighbouring position dipole couples with the carbon, with a coupling constant,  $D$ , of the order of 500–1000 Hz. This distorts the sideband pattern and makes fitting inaccurate. Neither this study, nor that of Antzutkin *et al.*, attempt to factor in  $^{14}\text{N}$  in the sideband pattern fitting procedure.

At the actual MAS rate chosen (6.2 kHz), which was optimised for the CSA of the 57 ppm signal, the peaks around 65 ppm and 127 ppm are separated by the spinning rate, so the sideband manifolds are overlapped (but offset by one sideband order). The

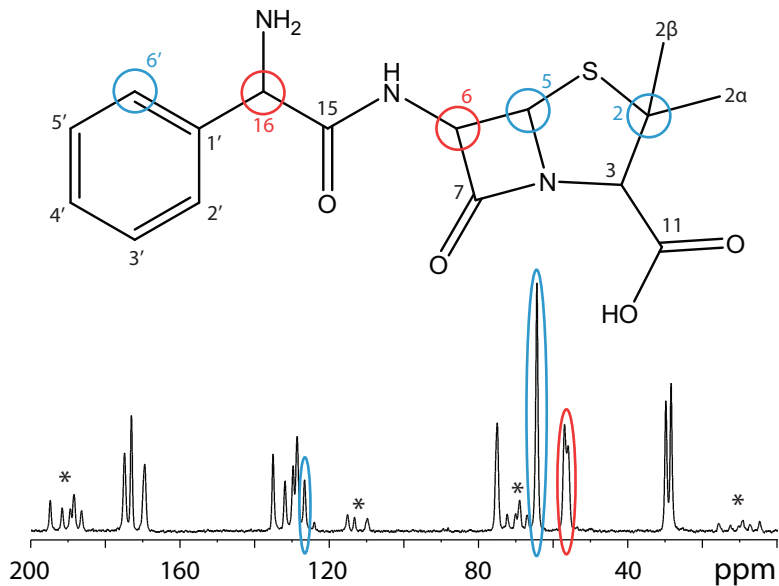


**Figure 4.9** Structure of ampicillin, showing the atom labelling scheme that is used in Table 4.6. The  $^{13}\text{C}$  CP-MAS spectrum is shown. The sites marked in red have the same isotropic chemical shift as each other. Those marked in blue have isotropic chemical shifts that are separated by the MAS rate of the experiment, and so are carelessly overlapped. Assignments were made by Clayden [156] and updated by Antzutkin [153]. Sidebands are marked with an asterisk.

correlation pattern fitting procedure can be adapted to account for this. Fitting two sets of parameters to this data (that is assuming that the two signals around 65 ppm have the same CST), the chemical shift parameters so determined at  $\zeta = -116.9$  ppm and  $\eta = 0.65$  for the signal with the isotropic shift at 127 ppm, and  $\zeta = 39.9$  ppm and  $\eta = 0.72$  for the signals with the isotropic shift at 65 ppm. The intensity of the 65 ppm signal is approximately double that of the 127 ppm one. This is a very good match for the data from the previous study where the signals were properly resolved. Fitting three sets of parameters to this data was unsuccessful, presumably because the CSA of C-2 and C-5 are too similar to be determined by this method. Notice that the fitted parameters assuming these two sites are the same are approximately the average of the two sites.

Now the overlapping C-6 and C-16 sites have not had their chemical shift parameters determined previously by experiment. A DFT study has calculated values for these sites though [154], finding values of  $\zeta = 28$  ppm and  $\eta = 0.52$  for C-6, and  $\zeta = -15$  ppm and  $\eta = 0.83$  for C-16. Fitting the experiment sideband–sideband

Carbon site		This study		Antzutkin's study	
	$\delta_{\text{iso}} / \text{ppm}$	$\zeta / \text{ppm}$	$\eta$	$\zeta / \text{ppm}$	$\eta$
2 $\beta$ -Me	28.9	$-27.9 \pm 0.1$	$0.67 \pm 0.01$	$-28.6 \pm 0.5$	$0.56 \pm 0.08$
2 $\alpha$ -Me	30.2	$-24.4 \pm 0.1$	$0.81 \pm 0.01$	$-22.9 \pm 0.5$	$0.94 \pm 0.06$
C-6, C-16	57.0	Overlapping with each other			
C-2	64.8	Overlapping with C-6'		$42.0 \pm 0.3$	$0.76 \pm 0.02$
C-5 *	65.3	Overlapping with C-6'		$36.5 \pm 2.9$	$0.66 \pm 0.29$
C-3 *	73.4	$22.2 \pm 0.2$	$0.78 \pm 0.03$	$-31.6 \pm 0.7$	$0.60 \pm 0.11$
C-6'	127.1	Overlapping with C-2 and C-5		$-116.9 \pm 1.3$	$0.64 \pm 0.02$
C-3', C-5'	129.2	$-116.2 \pm 1.2$	$0.71 \pm 0.02$	$-115.3 \pm 0.4$	$0.72 \pm 0.01$
C-2'	130.0	$-105.6 \pm 0.8$	$0.77 \pm 0.03$	$-104.6 \pm 1.0$	$0.79 \pm 0.02$
C-4'	132.3	$-121.2 \pm 0.5$	$0.65 \pm 0.02$	$-121.9 \pm 1.5$	$0.68 \pm 0.02$
C-1'	135.5	$-114.8 \pm 2.1$	$0.67 \pm 0.04$	$-115.5 \pm 1.0$	$0.61 \pm 0.02$
C-15 *	170.1	$82.0 \pm 0.9$	$0.79 \pm 0.02$	$89.1 \pm 2.0$	$0.73 \pm 0.04$
C-11	173.3	$67.6 \pm 0.4$	$0.94 \pm 0.01$	$67.1 \pm 0.7$	$0.93 \pm 0.02$
C-7 *	175.2	$87.5 \pm 0.9$	$0.54 \pm 0.01$	$93.2 \pm 1.5$	$0.53 \pm 0.04$

**Table 4.6** Best fit values for  $^{13}\text{C}$  chemical shift parameters for ampicillin. Assignments from Clayden *et al.* except the methyl groups [153, 156]. Those marked with a \* are directly bonded to  $^{14}\text{N}$ , which causes distortion in the sideband pattern by dipolar coupling. In this study, the spinning rate chosen for the experiment was set accidentally so the signals at 65 ppm and 127 ppm where separated by the spinning rate and so are unresolved.

correlation pattern for these sites, however, gives values of:

$$\zeta_1 = -10.3 \text{ ppm}, \eta_1 = 0.56, \zeta_2 = 22.9 \text{ ppm}, \eta_2 = 0.93,$$

which is not a good match for the DFT values. Although it is possible that the DFT results are inaccurate, there is a major source of error in the experimental procedure: the coupling with nitrogen.

Attempts were made to take the dipolar coupling into account during fitting. This required a couple of assumptions: (i) the strength of the dipolar coupling was 700 Hz (corresponding to a typical C–N single bond length), and (ii) the C–N internuclear vector is aligned with one of the principal axes of the CST in both sites (for simplicity). The best fit CST parameters were determined for each orientations of the C–N internuclear vector with the CSTs. The lowest  $\chi^2$  fit occurred when the internuclear vectors were aligned with the principal axis in the Cartesian frame where the value of the shielding is intermediate between the two extremes (i.e.  $\sigma_{yy}$ ). This fit was:

$$\zeta_1 = -10.6 \text{ ppm}, \eta_1 = 0.42, \zeta_2 = 24.8 \text{ ppm}, \eta_2 = 0.89,$$

which is similar to the best fit without  $^{14}\text{N}$  coupling.

Unfortunately, it has not been possible to determine confidently the chemical shift parameters for these sites using a correlation pattern. The presence of  $^{14}\text{N}$  coupling means the CSA values determined here are liable to be inaccurate. These signals are also difficult because their CSAs are very small, which requires a very slow effective spinning rate (thus a large scaling factor, long pulse sequence and plenty of pulse errors). It is unclear, therefore, whether they should be trusted over and above the DFT results.

#### 4.4 Experimental procedure

Anhydrous D[-]- $\alpha$ -aminobenzylpenicillin (ampicillin), fumaric acid monoethyl ester, hydroxyapatite and sodium dihydrogen phosphate monohydrate were purchased from Sigma and used without further purification or recrystallisation. Experiments were performed on a Bruker Avance 400 spectrometer, operating at a phosphorus frequency of 161.9 MHz or a carbon frequency of 100.5 MHz, and a proton frequency of 399.9 MHz, using a double resonance 4 mm MAS probe. The experiments use the Orr *et al.* version of CSA-amplified PASS [86], more for convenience than any experimental advantage it may have over other CSA-amplified PASS variants.

The  $^{31}\text{P}$  CSA-amplified PASS spectra were recorded of both the pure phosphates and mixtures in approximate volumetric ratios of phosphate (of hydroxyapatite to sodium dihydrogen phosphate) of 1:3, 1:2, 1:1, 2:1 and 4:1. For the all spectra, an actual spinning rate of 4080 Hz was used. The scaling factor used was  $N = 6.8$ , giving a reduced spinning rate of 600 Hz, recording 50  $t_1$  points with 26 acquisitions per point using a cogwheel phase cycling scheme [46]. The recycle delay was 10 s. The  $^1\text{H}$ – $^{31}\text{P}$  cross-polarisation contact time was 8 ms. High-power TPPM proton decoupling [52] was applied with a field strength of 78 kHz. The two-dimensional sideband intensity patterns used for fitting were generated by integrating the slices in the indirect dimension over the sideband peak-width in the direct dimension. No linebroadening or zero-filling is required. The one-dimensional sideband patterns were calculated by summing intensities over all visible sidebands in the direct dimension of the above experiment, giving a projected sideband pattern corresponding to the reduced spinning rate,  $\omega_R/\chi_a$ .

The  $^{13}\text{C}$  CSA-amplified PASS spectra of ampicillin were recorded at an actual

spinning rate of 6.2 kHz with  $\chi_a = 5.0$  to achieve an effective spinning rate of 1240 Hz, with  $\chi_a = 6.7$  to achieve an effective spinning rate of 930 Hz and with  $\chi_a = 10.2$  to achieve an effective spinning rate of 608 Hz. A further experiment was recorded with an actual spinning rate of 3.3 kHz and with  $\chi_a = 6.8$  to achieve an effective spinning rate of 485 Hz. The recycle delay was 5 s. The  $^1\text{H}$ – $^{13}\text{C}$  cross-polarisation contact time was 3 ms, and 32  $t_1$  points were recorded with 40 acquisitions per point using a cogwheel phase cycling scheme [46]. High-power SPINAL [53] proton decoupling was applied with a field strength of 83 kHz.

The  $^{13}\text{C}$  CSA-amplified PASS spectra of fumaric acid monoethyl ester were recorded at an actual spinning rate of 5750 Hz, with  $\chi_a = 6.8$  to achieve an effective spinning rate of 846 Hz (recording 32  $t_1$  data points with 156 scans per point) and with  $\chi_a = 10.2$  to achieve an effective spinning rate of 564 Hz (recording 44  $t_1$  data points with 152 scans per point). The recycle delay was 10 s. High power TPPM proton decoupling [52] was applied with a field strength of 96 kHz. The  $^{13}\text{C}$   $\pi$ -pulse length was 6  $\mu\text{s}$ , and the  $^1\text{H}$ – $^{13}\text{C}$  cross-polarisation contact time was 2.5 ms.

#### 4.4.1 Numerical simulations

Numerical simulations of two-dimensional sideband spectra were performed using a procedure written in the PV-Wave environment [157]. Equation 4.5 was evaluated and summed for 233  $\alpha$  and  $\beta$  angles generated by a REPULSION algorithm [34]. Best fits were found using a least squares fitting routine [158] to minimise  $\chi^2$ . Initial estimates of chemical shielding parameters were generated randomly within usual ranges of these parameters for  $^{31}\text{P}$ . For fitting of simulated spectra, random noise was generated with a standard deviation of 1/200 of the total signal intensity under all of the sidebands, and added to the simulated spectrum prior to fitting. As many sidebands in  $\omega_2$  were used as were visible above the noise level, and all  $\omega_1$  points were used in the fits.

## 4.5 Conclusions

The two-dimensional sideband–sideband correlation has shown some promise for accurate determination of CSA and asymmetry, but its use is not applicable in all situations. It appears that the reason the two-dimensional approach fares better is not because of the additional information present in the correlation pattern, as was

originally anticipated. The advantage comes from the lack of the projection that is required to create a one-dimensional sideband pattern from a two-dimensional correlation pattern, which increases the noise level by a factor of  $\sqrt{N}$ .

If it is possible to obtain a CP-MAS spectrum at a suitable spinning rate, then this will always be superior to any CSA-amplified PASS method. A one-dimensional spectrum can also be obtained, without the need for projection, from a fast MAS CSA-amplified PASS, where there are no direct dimension sidebands. However, in practice, such an experiment will require a large scaling factor and a lengthy pulse sequence, leading to large systematic errors that are not taken into account in the error estimates by the analysis in this chapter.

These limitations mean that moderate MAS rate CSA-amplified PASS is frequently used for CSA determination, in which case a two-dimensional sideband–sideband correlation pattern results. If this is the case, it costs nothing to analyse the correlation pattern itself, and this is better than analysing its one-dimensional projection.

It has been found that, in fact, overlapping signals can have their chemical shift parameters determined from a one-dimensional sideband pattern, contrary to the findings of Hodgkinson and Emsley. The difference is that the spinning rate must be reduced below the optimum for resolved signals, which their study does not investigate. Even so, experimental constraints (particularly the slowest stable spinning rate of the spectrometer) may invoke the use of CSA-amplified PASS anyway. Table 4.7 attempts to summarise the circumstances where the CSA-amplified PASS experiment is applicable and where it is not.

Of course, prior to determining the CSA, it is unknown, and so the optimal experimental procedure is unknown. A simple CP-MAS experiment should always be used first to determine the isotropic shifts and also to get an idea of the range of CSAs present, and so to decide whether a two-dimensional experiment is needed and what the spinning rates should be. It is also likely that there are several sites with different CSAs in one sample; the same experiment might not be able to determine CSAs accurately for all sites present. In this case, more than one experiment may be necessary.

The sideband approaches are particularly limited where the CSAs are very similar, since the sideband patterns will be very similar. A different method is required for

System description	Optimal CSA determination
One component, large CSA	CP-MAS at spinning rate, $\omega_R/\Delta\omega = 0.4$ .
One component, small CSA	CSA-amplified PASS, using correlation pattern if direct dimension sidebands visible.
Many resolved components, all large CSA	CP-MAS, finding a spinning rate where signals are resolved. Possibly several CP-MAS experiments if a single value of the MAS rate is not suitable for all sites.
Many resolved components, some small CSAs	CSA-amplified PASS, using correlation pattern for those sites with visible direct dimension sidebands. Possibly separate CP-MAS spectrum for determination of larger CSAs.
Overlapping components, very different CSA	CP-MAS, or CSA-amplified PASS. See Section 4.2 for spinning rate suggestion.
Overlapping components, similar CSA	Sideband patterns not suitable.

**Table 4.7** General suggestions for which method is best for CSA determination for different systems. ‘Large CSA’ implies one where the appropriate MAS rate for CSA analysis is experimentally obtainable, and ‘small CSA’ is where the appropriate MAS rate is too slow for the hardware. The operator must use their judgment, as in many cases the choice may be affected by other factors, such as experimental time available, maximum rotor speed, required accuracy and the like.

these situations, which shall be investigated in the next chapter.

## Chapter 5

---

# Sideband–powder correlation

---

In the previous chapter, it was shown that a two-dimensional sideband–sideband correlation pattern can be used to determine CSA from overlapping signals. It has been previously been shown that, in fact, a one-dimensional powder pattern is sufficient to determine the CST for overlapping signals [39], but only if they do not share a principal value.

The experimental recording of powder patterns almost always necessitates the use of a two-dimensional technique, as if there are many sites in the sample, in a one-dimensional spectrum the powder patterns are superimposed, resulting in an indeterminable mess. Powder patterns can be recoupled under MAS using the MAS-CSA [69] or SUPER [70] experiments described in Section 3.1, correlating isotropic shift with the powder pattern.

It has been suggested that, in order to perform these experiments robustly, the MAS rate can not be greater than around  $0.8 \Delta_\omega$ , since faster MAS rates require larger CSA recoupling scaling factors, which in turn require a large number of pulses leading to larger errors. In other words, there will inevitably be direct dimension sidebands present, so that the two-dimensional spectrum consists of a sideband–powder correlation pattern. Currently, this situation is dealt with by projection of the powder pattern, taking the sum over all direct dimension sidebands. In this chapter it is revealed that, in an analogous manner to sideband–sideband correlation spectra, analysis of the full sideband–powder correlation pattern can yield more accurate CSA values than

analysis of the projection pattern. In particular this enables accurate determination of the CST in cases where two signals have the same isotropic shift *and* CSAs that differ by only a few percent, where the previous sideband–sideband correlation technique is weak.

## 5.1 MAS-CSA correlation patterns

The pulse sequence for Tycko *et al.* original MAS-CSA experiment was shown in Figure 3.2. Each  $\pi$ -pulse switches the sign of the coherence; this is represented by a stepped function,  $f(t)$ , which switches between values of +1 and -1 at every  $\pi$ -pulse. The total phase acquired over one rotor cycle with the four  $\pi$ -pulses is:

$$\Phi(\tau_R/2, -\tau_R/2; \Omega_{PR}) = \int_{-\tau_R/2}^{\tau_R/2} \omega(t; \Omega_{PR}) f(t) dt. \quad (5.1)$$

If the timings of the pulses obey the following relationships:

$$\begin{aligned} \int_{-\tau_R/2}^{\tau_R/2} f(t) \cos(\omega_R t) dt &= \int_{-\tau_R/2}^{\tau_R/2} f(t) \cos(2\omega_R t) dt \\ \int_{-\tau_R/2}^{\tau_R/2} f(t) \sin(\omega_R t) dt &= \int_{-\tau_R/2}^{\tau_R/2} f(t) \sin(2\omega_R t) dt = 0, \end{aligned} \quad (5.2)$$

then, over the whole rotor period, the terms in Equation (2.97) with  $\sin(\omega_R t)$  and  $\sin(2\omega_R t)$  dependence (that is  $S_1$  and  $S_2$ , those not wanted for a static powder pattern) are averaged to zero, whilst those with  $\cos(\omega_R t)$  and  $\cos(2\omega_R t)$  dependence ( $C_1$  and  $C_2$ , which are those which remain in Equation (2.97) when  $\omega_R = 0$ ), are recoupled in equal proportions. This situation is achieved if the pulses are placed symmetrically about  $t = 0$ , as shown in Figure 5.1. In this case:

$$\Phi(\tau_R/2, -\tau_R/2; \Omega_{PR}) = \tau_R \left( \chi_i \omega_{iso} + \omega_0 \sqrt{\frac{2}{3}} \chi_a [C_1(\Omega_{PR}) + C_2(\Omega_{PR})] \right), \quad (5.3)$$

where,  $\chi_a$  and  $\chi_i$  are scaling factors for the anisotropic and isotropic frequencies respectively, given by:

$$\chi_a = \frac{1}{\tau_R} \int_{-\tau_R/2}^{\tau_R/2} f(t) \cos(\omega_R t) dt \quad (5.4)$$

$$\chi_i = \frac{1}{\tau_R} \int_{-\tau_R/2}^{\tau_R/2} f(t) dt. \quad (5.5)$$

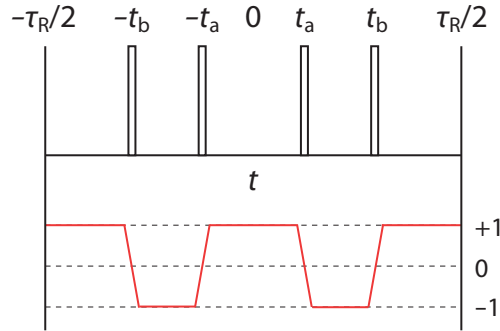


**Figure 5.1** Pulse timings for one pulse sequence unit of MAS-CSA that recouples the cosine-dependent terms of Equation (2.97), which requires four pulses symmetrically placed about the middle of the rotor period, which is at  $t = 0$ . The red line shows the CTP, or equivalently the stepped function,  $f(t)$ , that gives the sign of the evolution frequency between successive pulses.

It is helpful if the isotropic frequency is removed from the indirect dimension, since if it is present, it would require an increased spectral width (more data points). All the necessary information about the isotropic shift is contained in the direct dimension anyway. Given the restriction that  $\chi_i = 0$ , there is one solution to Equation (5.2), that is a sequence with pulses at timings of  $t_a = 0.197\tau_R$  and  $t_b = 0.447\tau_R$ . The anisotropic scaling factor for this sequence is  $\chi_a = 0.393$ .

The available values of  $t_{1,\text{eff}}$  are given by Equation (3.1), interpreting  $\chi_a$  as a scaling factor of the  $t_1$  time rather than anisotropic frequency. The apparent spectral width in the indirect dimension is  $1/\tau_R\chi_a$ . In order to obtain an attractive powder pattern, this spectral width should be around double the largest anisotropy in the sample. This is the origin of the limitation of the actual MAS rate to  $0.8\Delta_\omega$ , with visible direct dimension sidebands, and thus a sideband–powder correlation pattern in the two-dimensional spectrum.

The Tycko *et al.* original MAS-CSA, as mentioned in Section 3.1, suffers problems of artefacts and linebroadening, due to the long train of  $\pi$ -pulses required for long  $t_1$  times. Using six  $\pi$ -pulses in three rotor cycles, there are a number of solutions to Equation (5.2) with different  $\chi_a$  values. Orr and Duer take advantage of this to create optimised and constant time versions of MAS-CSA [72]. In the optimised version,  $t_{1,\text{eff}}$  is varied between successive slices by varying both  $\chi_a$  and  $n$  (the number of six  $\pi$ -pulse blocks), reducing the problems with artefacts and linebroadening. However, the maximum  $\chi_a$  is still limiting on the MAS rate; Orr himself suggests that  $\chi_{a,\text{opt}}$ , which is the apparent  $\chi_a$  for the optimised sequence as a whole (as if it were a normal

Tycko MAS-CSA incrementing the number of pulse sequence units with fixed  $\chi_{a,\text{opt}}$ ), should take a value around 0.18, which requires a slower MAS rate and more direct dimension sidebands than the original Tycko experiment [159]. If a larger value of  $\chi_{a,\text{opt}}$  is used, a faster MAS rate can be used, but the advantage of the optimised version over the original version is lost, as more increments of  $n$  are needed. So it is inevitable in MAS-CSA experiments, even in the most modern implementations, that a two-dimensional sideband–powder correlation pattern will exist.

The full signal for the two-dimensional experiment is:

$$\begin{aligned} S_c(t_1, t_2; \Omega_{\text{PR}}) = & \exp \{ i[\chi_a(C_1(\Omega_{\text{PR}}) + C_2(\Omega_{\text{PR}}))t_1 + \omega_{\text{iso}}t_2 \\ & + \xi(t_2 + \tau_R/2; \Omega_{\text{PR}}) - \xi(\tau_R/2; \Omega_{\text{PR}})] \}. \end{aligned} \quad (5.6)$$

The time offset of  $\tau_R/2$  appears because during the MAS-CSA pulse sequence, the recoupled CSA takes on the values of  $C_1$  and  $C_2$  for the orientation half way through the rotor cycle, which are offset by half a rotor cycle from the corresponding orientations that give rise to the evolution in  $t_2$ . Unfortunately, Equation (5.6) can not be integrated over  $\gamma_{\text{PR}}$  in the same manner as Equation (2.86), as  $C_1(\Omega_{\text{PR}}) + C_2(\Omega_{\text{PR}})$  is also dependent upon  $\gamma_{\text{PR}}$ . The spectrum must therefore be calculated by numerical integration of Equation (5.6) over three Euler angles, followed by Fourier transformation in two dimensions. This is computationally more time consuming, although with fast modern computers this is not problematic.

## 5.2 Simulations

Simulated two-dimensional correlation patterns can be fitted to experimental ones in a least squares fitting procedure. One difference compared to the sideband–sideband correlation is the presence of an extra parameter for each site,  $T_2^{(1)}$ , the relaxation time constant in the indirect dimension. This additional parameter is sometimes of interest, but can impede the fitting routine. It is recommended therefore, that the fitting procedure is repeated several times with different values for  $T_2^{(1)}$  which are fixed each time. The  $T_2^{(1)}$  value that leads to the solution with the lowest  $\chi^2$  is chosen manually at the end. Note that  $T_2^{(1)}$  is not necessarily the same for all sites in one sample.

The number of components present is often clearly visible by eye in powder patterns. If it is not, then the same arguments for determination of the number of components in a sideband–sideband correlation spectrum, detailed in Section 4.2, also

hold true to determining the number of components in a sideband–powder correlation pattern.

### 5.2.1 Resolved signals

The reliabilities of best fit parameters that would be obtained from fitting MAS-CSA spectra have been investigated for simulated spectra with random noise for fitting a correlation pattern and a projection pattern, in similar way to the previous investigation of sideband–sideband correlation patterns. In each case the indirect dimension spectral width was fixed to be much greater than the CSA. The relaxation time constant, noise level, and the number of data points was the same in each case. The only variation between the tests was the actual MAS rate (and therefore  $\chi_a$ ), which controls the number of direct dimension sidebands that are visible.

In general it is found that two-dimensional sideband–powder correlation patterns can provide more accurate chemical shift parameters than projected powder patterns, as shown in Figure 5.2. The two methods are equivalent at very fast MAS rates, but as the MAS rate is decreased, the reliabilities of parameters determined from the correlation pattern are not majorly affected, but reliabilities of parameters determined from the projection patterns drop significantly as more direct dimension sidebands appear.

For reasons discussed previously, the very fast MAS rates are not practical for MAS-CSA experiments (the simulations did not take into account the pulse errors). So, inevitably the two-dimensional correlation pattern fitting will be superior for resolved signals due to the presence of a significant number of direct dimension sidebands.

With resolved signals, however, if sidebands with orders up to  $k = \pm 2$  are visible and fully resolved, then a two-dimensional MAS-CSA experiment is a waste of time. A CP-MAS, one-dimensional sideband pattern would be sufficient to determine accurate chemical shift parameters (far more accurately than any two-dimensional experiment with a long pulse train). Therefore, MAS-CSA is not going to be of great use for determining chemical shift parameters for resolved signals, and so this will not be discussed further.

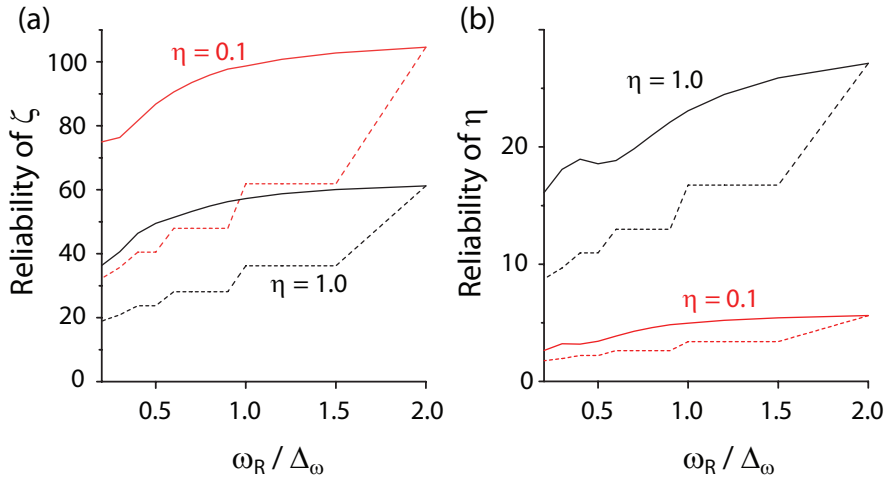


**Figure 5.2** Graphs showing how the reliability of (a)  $\zeta$ , and (b)  $\eta$ , depend upon the actual spinning rate for resolved signals, for a simulated two-dimensional sideband–powder correlation pattern (solid lines) and the one-dimensional powder pattern (dashed lines) which is a projection of the correlation pattern. Two values of the asymmetry,  $\eta = 0.1$  (red lines) and  $\eta = 1.0$  (black lines), were tested. The stepped nature of the plots for the one-dimensional powder patterns results from the number of sidebands that must be summed over to create the projection, and the corresponding increase in noise level that this causes.

### 5.2.2 Overlapping signals

For the same reasons as for resolved signals, a two-dimensional sideband–powder correlation pattern can be used to determine more accurate chemical shift parameters for overlapping signals than its projection. Since the sideband manifolds are overlapped in a CP-MAS spectrum, a one-dimensional sideband pattern is not likely to be an alternative for parameter determination. Since ultra-fast MAS rates are not recommended for MAS-CSA, then a one-dimensional powder pattern without projection can not be accurately measured either. And if the CSAs of the overlapping sites are similar, the sideband–sideband correlation pattern is unlikely to be of much use either. This is not a problem to sideband–powder correlation, since, as with overlapping one-dimensional sideband patterns, the parameters can be determined in many situations so long as principal values are not shared. Therefore there is a niche in which the sideband–powder correlation pattern is useful for determining chemical shift parameters for overlapping signals.

An extensive investigation by simulation of overlapping systems was not performed, due to the obscene number of parameters to investigate (which is more than with sideband–sideband correlation due to the inclusion of relaxation constants, spec-

tral width, number of data points acquired and the like). A simulated comparison with CSA-amplified PASS was also not performed, as the signal-to-noise level obtainable in a given experimental time is not comparable between the two types of experiment. The comparison is therefore left to the experimental examples that follow.

### 5.3 Experimental examples

Three systems were used as tests of the sideband–powder pattern correlation method. First of all, the mixture of hydroxyapatite and sodium dihydrogen phosphate, used for testing the sideband–sideband correlation approach was re-used, where it is found that the sideband–powder correlation does not perform so well. Secondly, mixtures of some short peptides were used, which have many  $^{13}\text{C}$  signals in a small range of isotropic shifts. Moreover, these signals tend to have similar CSAs, rendering them ineligible for analysis by sideband–sideband correlation. Finally, pamidronate, a small drug molecule, is a real-life example with genuinely overlapping signals in the  $^{31}\text{P}$  spectrum. It demonstrates that, even when the spectrum contains only two signals, it is still possible to have accidental degeneracy isotropic shifts. The chemical shift parameters for the  $^{31}\text{P}$  environments are determined via the sideband–powder correlation pattern and also by a one-dimensional powder pattern and the sideband–sideband correlation pattern methods for comparison.

#### 5.3.1 Mixtures of phosphates

For the example used in Chapter 4, a physical mixture of hydroxyapatite and sodium dihydrogen phosphate, CST determination is less successful using the sideband–powder correlation pattern. The best fit parameters for the two  $^{31}\text{P}$  environments using the sideband–sideband correlation method were given in Table 4.3, for the resolved signals and Table 4.4 when they were overlapped. These showed a good match between the parameters determined from the overlapping signals and those for the resolved signals. However, using a MAS-CSA experiment, the best fit parameters determined from overlapping signals are found to be in error (see Table 5.1). The CSA for the hydroxyapatite is underestimated by some 10–20%, and the uncertainty in  $\eta$  for hydroxyapatite is of the same magnitude as its value.

The most likely reason for this is that the large difference in CSA actually disfavours finding an accurate fit for sideband–powder correlation experiments. In

Volume ratio	$\zeta_1$ / ppm	$\eta_1$	$\zeta_2$ / ppm	$\eta_2$
1:3	$8.8 \pm 0.7$	$0.8 \pm 0.5$	$-79.3 \pm 0.2$	$0.44 \pm 0.01$
1:1	$8.1 \pm 0.5$	$0.6 \pm 0.6$	$-79.5 \pm 0.4$	$0.43 \pm 0.01$
2:1	$8.5 \pm 0.2$	$0.7 \pm 0.2$	$-79.4 \pm 0.7$	$0.44 \pm 0.02$

**Table 5.1** Best fit chemical shift parameters for  $^{31}\text{P}$  sites for the hydroxyapatite and sodium dihydrogen phosphate mixtures described in the text, with different volumetric ratios of phosphate, found using the 2D analysis described in the text.  $\zeta_1$  and  $\eta_1$  refer to hydroxyapatite and  $\zeta_2$  and  $\eta_2$  to sodium dihydrogen phosphate. The values found in Table 4.3 are  $\zeta = 9.7$  ppm and  $\eta = 0.77$  for hydroxyapatite, and  $\zeta = -79.9$  ppm and  $\eta = 0.46$  for sodium dihydrogen phosphate. The errors are the Cramér–Rao lower bounds estimates of random error. In each case, a two-dimensional correlation pattern incorporating 7 direct dimension sidebands were used for fitting.

order to obtain the full lineshape for the larger CSA, a large spectral width is required, meaning that the  $t_1$  data points must be closely spaced. In order to obtain sufficient resolution on the lineshape for the smaller CSA, long  $t_1$  times must be recorded. However, the requirements of both sites can not be met simultaneously except by an extremely long and impracticable experiment. Whilst the same is still true for the sideband–sideband correlation spectrum, since the signal is concentrated into sidebands, the inherent sensitivity is higher. In the same experiment time, therefore, the signal-to-noise is superior in the CSA-amplified PASS spectrum, and so CST parameter determination is more accurate.

### 5.3.2 Mixtures of peptides

The  $^{13}\text{C}$  CP-MAS spectra of a number of short peptides (with 2-4 residues) were recorded, and the CSAs measured for the signals with isotropic shifts between 30-60 ppm, which are mostly due to  $^{13}\text{C}_\alpha$ . The chemical shift parameters measured for these (resolved) carbons are given in Table 5.2.

A suitable pair of signals to perform an analysis on unresolved signals are the signals at isotropic shifts of 51 ppm in Ala-Ala and Gly-Phe-Ala. To this end, the two peptides were mixed in equal proportions by volume, and a sideband–powder correlation pattern was recorded.

The best fit values for this spectrum were:

$$\zeta_1 = -18.2 \text{ ppm}, \eta_1 = 0.41, \zeta_2 = 21.3 \text{ ppm}, \eta_2 = 0.93.$$

The parameters  $\zeta_1$  and  $\eta_1$  are assigned to Ala-Ala, and  $\zeta_2$  and  $\eta_2$  to Gly-Phe-Ala. Neither of these is a particularly great match for the parameters measured for the re-

Peptide	Assignment	$\delta_{\text{iso}} / \text{ppm}$	$\zeta / \text{ppm}$	$\eta$
Ala-Ala	Ala	51.0	$-20.6 \pm 0.4$	$0.63 \pm 0.04$
Ala-Ala	Ala	49.3	$-21.3 \pm 0.4$	$0.45 \pm 0.04$
Ala-Gly	Ala	49.6	$-22.3 \pm 0.2$	$0.47 \pm 0.04$
Ala-Gly	Gly	44.5	$25.7 \pm 0.4$	$0.96 \pm 0.04$
Gly-Phe-Ala	Phe	54.1	$-18.4 \pm 0.4$	$0.98 \pm 0.08$
Gly-Phe-Ala	Ala	51.3	$23.8 \pm 0.4$	$0.81 \pm 0.04$
Gly-Phe-Ala	Gly	40.4	$-21.1 \pm 0.4$	$0.61 \pm 0.08$
Gly-Phe-Phe	Phe	60.0	$-22.0 \pm 0.6$	$0.80 \pm 0.08$
Gly-Phe-Phe	Phe	57.0	$-17.1 \pm 1.2$	$1.0 \pm 0.2$
Gly-Phe-Phe	Gly	40.5	$-20.3 \pm 0.8$	$0.72 \pm 0.12$
Gly-Pro-Gly-Gly	Pro	60.4	$-20.8 \pm 0.6$	$0.57 \pm 0.14$
Gly-Pro-Gly-Gly	Gly	46.4	$-22.3 \pm 1.0$	$0.86 \pm 0.12$
Gly-Pro-Gly-Gly	Gly	43.5	$-27.5 \pm 1.2$	$0.98 \pm 0.04$
Gly-Pro-Gly-Gly	Gly	42.0	$-26.0 \pm 0.6$	$0.87 \pm 0.04$

**Table 5.2** Best fit values for  $^{13}\text{C}$  chemical shift parameters for some short peptides, and tentative assignments to residues.

spective sites in the resolved spectrum (at least not within the calculated errors, which are of the order of 0.5 ppm for the anisotropies and 0.05 for the asymmetries). Both anisotropies are underestimated by about 3 ppm. A sideband–sideband correlation technique also fails with this example, as the anisotropies are very similar.

It should be noted that this is a particularly tough example for CSA determination because of the fact that the CSAs are very similar, small in magnitude and the sensitivity is so low. Also, the carbon atoms involved are directly bonded to  $^{14}\text{N}$ , the dipolar coupling with which can distort the powder patterns significantly when the CSAs are small.

Unfortunately, it has not been demonstrated here that it is possible to determine chemical shift parameters for overlapping  $^{13}\text{C}_{\alpha}$  signals in peptides, which was anticipated as a possible application of this technique. However, it may be possible to improve the experimental procedure to tolerate  $^{14}\text{N}$  dipolar coupling; in this respect SUPER would be preferable to MAS-CSA, but the low maximum scaling factor for SUPER means it is unsuitable for measuring the small CSAs of  $^{13}\text{C}_{\alpha}$  signals.

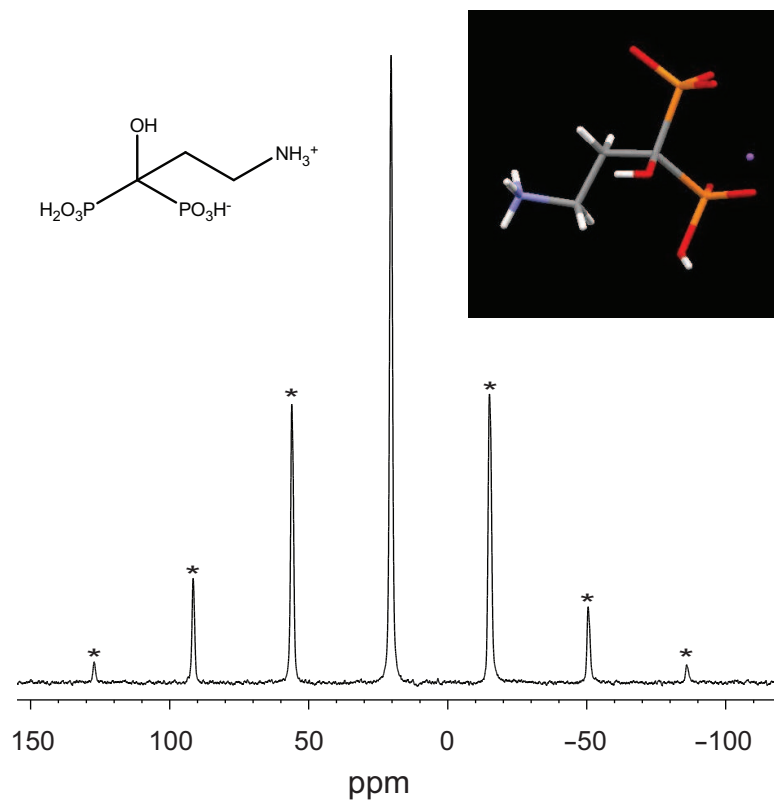


**Figure 5.3**  $^{31}\text{P}$  CPMAS spectrum of disodium pamidronate hydrate, at 8 kHz spinning rate, showing only one isotropic signal. Those peaks marked with a \* are spinning sidebands. Inset left: structure of pamidronate acid molecule. Inset right: conformation of pamidronate ion in its disodium salt form [160], showing that the two phosphorus atoms (shown in orange) are crystallographically distinct due to their different protonation states and so need not necessarily have similar shielding tensors.

### 5.3.3 Pamidronate

Pamidronate is a bis-phosphonate drug molecule used for the treatment of bone diseases, such as osteoporosis, which will appear again in Chapter 7. This molecule contains two  $^{31}\text{P}$  environments, which have been previously shown by XRD to be crystallographically dissimilar [160]. Both of the  $^{31}\text{P}$  sites have an isotropic shift of 20.5 ppm relative to 85%  $\text{H}_3\text{PO}_4$ , and so are overlapping in the MAS spectrum (Figure 5.3). The chemical shift parameters can be determined using a powder pattern from a one-dimensional spectrum generated from a static sample, since there are no other  $^{31}\text{P}$  signals from pamidronate to overlap with.

Attempts were made to measure the chemical shift parameters for the two  $^{31}\text{P}$  sites in pamidronate using sideband–sideband and sideband–powder correlation pat-

	$\zeta_1$ / ppm	$\eta_1$	$\zeta_2$ / ppm	$\eta_2$	Intensity ratio
Static	$68.0 \pm 0.1$	$0.24 \pm 0.01$	$-83.2 \pm 0.2$	$0.99 \pm 0.01$	1:1.0
Powder Pattern Projection	$69.0 \pm 1.3$	$0.41 \pm 0.03$	$-83.8 \pm 2.0$	$0.94 \pm 0.04$	1:1.0
Sideband–Powder	$68.9 \pm 0.2$	$0.27 \pm 0.01$	$-82.4 \pm 0.3$	$0.97 \pm 0.01$	1:1.3
CP-MAS	$67.7 \pm 2.4$	?	$82.2 \pm 1.4$	$0.97 \pm 0.06$	1:2.0
Sideband Projection	$71.6 \pm 0.8$	$0.44 \pm 0.06$	$-90.2 \pm 3.8$	$0.85 \pm 0.04$	1:0.9
Sideband–Sideband	$71.5 \pm 0.4$	$0.48 \pm 0.02$	$-89.8 \pm 1.4$	$0.86 \pm 0.02$	1:0.8

**Table 5.3** Best fit chemical shift parameters for the two  $^{31}\text{P}$  sites in disodium pamidronate hydrate, using a powder–sideband correlation pattern and its one-dimensional projection, a sideband–sideband correlation pattern and its one-dimensional projection, a CP-MAS spectrum and the powder pattern recorded on a static sample. Errors are Cramér–Rao lower bounds estimates of random error, but do not include systematic errors. In each case 7 direct dimension sidebands were used for fitting or for summing to make the projection.

tern methods, with results compared to the parameters found from fitting the one-dimensional static spectrum (which are presumed to be the most accurate). Additionally, the parameters were measured from projections of the two-dimensional correlation patterns. The best fit parameters in each case are listed in Table 5.3.

Clearly the best match for the values determined from the static spectrum are those from the sideband–powder correlation pattern. This was the only other method to accurately determine the small value of  $\eta_1$  with any sort of accuracy. The worst matching parameter is the intensity ratio, but this might not be significant since the CP efficiency may be different for a static sample than a rotating one. The quoted errors appear to be unrealistically small, perhaps because there are large systematic errors that the Cramér–Rao approach does not take into account.

All methods involving sideband patterns alone do not find the fit accurately and the errors in general are higher than the equivalent methods involving powder patterns. The sideband pattern methods all fail to find an accurate  $\eta_1$ , and  $\zeta_2$  is also wildly overestimated.

One additional advantage of the sideband–powder correlation approach, that can not be seen in the table, is the confidence in the number of components that make up the spectrum. For the sideband–powder correlation pattern, a reduction in  $\chi^2$  of two orders of magnitude is seen upon fitting two components to the data rather than one, but no reduction in  $\chi^2$  with the addition of a superfluous third component. For the sideband–sideband methods or the projection of the sideband–powder correlation

pattern, a significant reduction in  $\chi^2$  is seen when adding a third component.

The best fits of the sideband–sideband and sideband–powder correlation patterns are shown in Figure 5.4. It is found that using the best fit parameters found from fitting the sideband–sideband correlation pattern to simulate the sideband–powder correlation pattern clearly results in a mis-match with the experimental spectrum. However, using the best fit parameters found from fitting the sideband–powder correlation pattern to simulate the sideband–sideband correlation pattern gives a pattern that is, by eye at least, indistinguishable from the experimental pattern. This is also seen when comparing simulated one-dimensional powder patterns using these parameters with the actual static pattern, as shown in Figure 5.5. This is a clear indication that the fitted parameters from the sideband–powder correlation pattern are more trustworthy than those determined from the sideband–sideband correlation pattern, because the appearance of the sideband–powder correlation pattern is more sensitive to small changes in the chemical shift parameters.

## 5.4 Experimental procedure

Disodium pamidronate hydrate, sodium dihydrogen phosphate, hydroxyapatite and the five short peptides were purchased from Sigma and used without further purification or recrystallisation. Experiments were performed on a Bruker Avance 400 spectrometer, operating at a  $^{31}\text{P}$  frequency of 161.9 MHz or a  $^{13}\text{C}$  frequency of 100.5 MHz, and a  $^1\text{H}$  frequency of 400.1 MHz, using a standard Bruker double resonance 4 mm MAS probe. Orr and Duer's optimised MAS-CSA experiment was used to produce all the sideband–powder correlation patterns [72], and the Orr *et al.* CSA-amplified PASS for the sideband–sideband correlation patterns [86].

The  $^{31}\text{P}$  MAS-CSA spectrum of pamidronate, sodium dihydrogen phosphate and hydroxyapatite were recorded at an actual spinning rate of 5750 Hz and with an anisotropic scaling factor of  $\chi_a = 0.1797$ , giving an  $\omega_1$  spectral width of 32 kHz. The basic CSA-recoupling pulse unit consisted of six  $\pi$ -pulses in three rotor periods. There were 20  $t_1$  complex data points collected, with 150 scans per point using a cogwheel phase cycling scheme [46]. The recycle delay was 6 s. The  $^1\text{H}$ – $^{31}\text{P}$  ramped cross-polarisation [161] contact time was 5 ms with a  $^1\text{H}$  field strength of 78 kHz. The  $^{31}\text{P}$   $\pi$ -pulse length was  $5.85\ \mu\text{s}$  and the  $^1\text{H}$   $\pi/2$ -pulse length was  $3.2\ \mu\text{s}$ . High-power TPPM proton decoupling [52] was applied throughout with a field strength of 78 kHz.

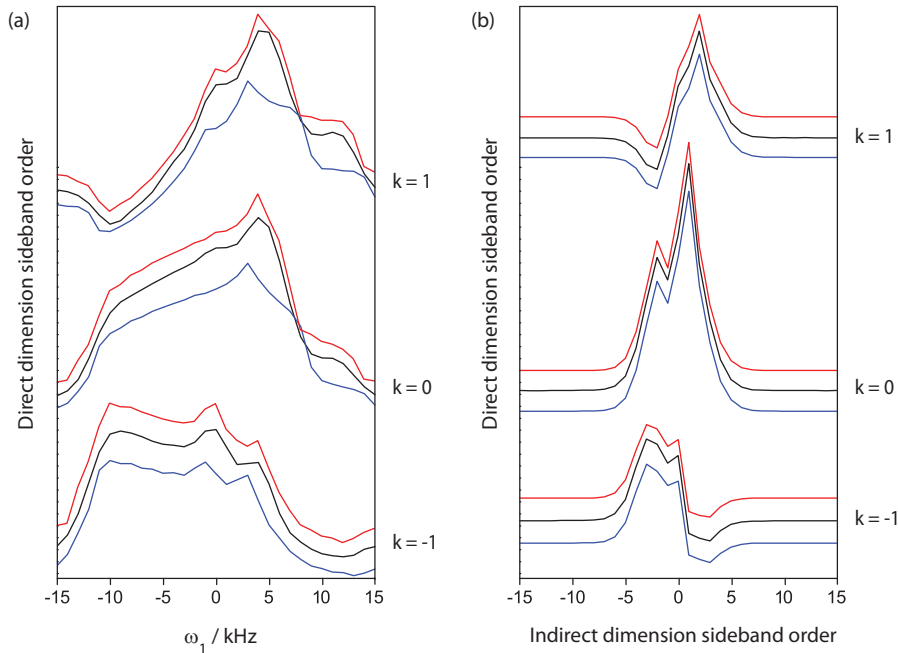


**Figure 5.4** (a) Experimental  $^{31}\text{P}$  MAS-CSA spectrum of disodium pamidronate hydrate (black lines), the simulation using best fit parameters determined from MAS-CSA given in Table 5.3 (red lines) and simulation using best fit parameters determined from sideband–sideband correlation using CSA-amplified PASS (blue lines). Shown are the powder patterns in  $\omega_1$  that are correlated with the centreband and  $k = \pm 1$  sidebands from the  $\omega_2$  dimension. (b) Experimental  $^{31}\text{P}$  CSA-amplified PASS spectrum of pamidronate (black lines) and simulated lineshapes using parameters determined from MAS-CSA (red lines) and CSA-amplified PASS (blue lines), showing the sideband intensity envelopes in  $\omega_1$  that are correlated with the centreband and  $k = \pm 1$  sidebands from the  $\omega_2$  dimension. Only three slices are shown in each case for clarity, although seven  $\omega_2$  sidebands were used to determine the fit, with 32  $t_1$  points for each.

The two-dimensional correlation pattern is formed by Fourier transforming in both dimensions. Zero-filling was applied to 32 points in  $t_1$ , but no artificial line-broadening was used. The one-dimensional powder pattern is created by summing the correlation pattern over the seven visible sidebands in the  $\omega_2$  dimension. The experiment time is approximately 5 hours each.

The  $^{31}\text{P}$  CSA-amplified PASS spectrum of pamidronate was recorded at an actual spinning rate of 8 kHz, with a scaling factor of  $N = 3.4$ , giving an effective indirect dimension spinning rate of 2353 Hz. There were 32  $t_1$  data points collected, with 64 scans per point using a cogwheel phase cycling scheme [46]. Other experimental parameters are the same as for the MAS-CSA. The two-dimensional correlation pattern is formed by Fourier transforming in both dimensions. No zero-filling or

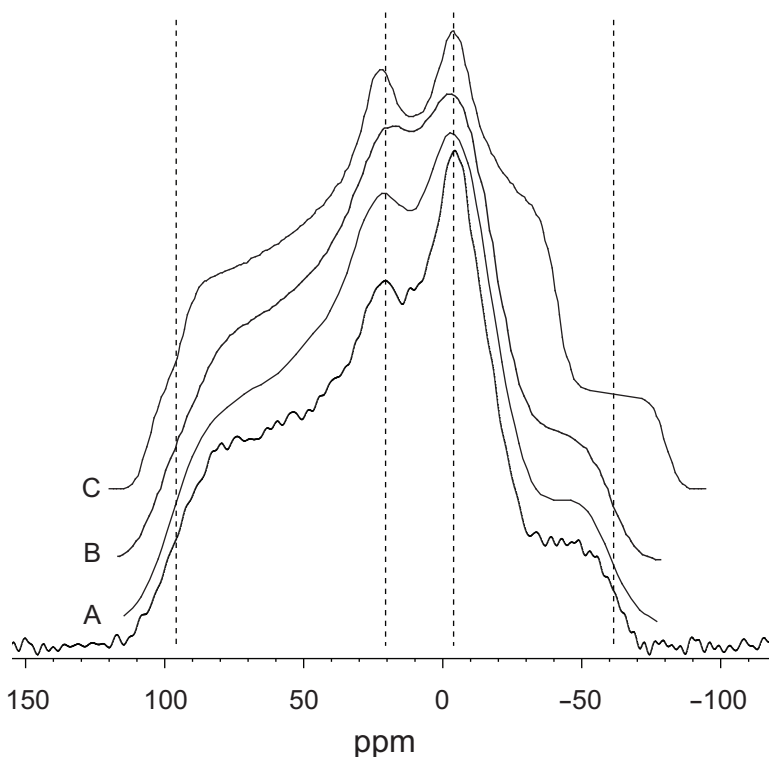


**Figure 5.5** Experimental static  $^{31}\text{P}$  powder pattern for disodium pamidronate hydrate. Overlaid are (A) the projection of the MAS-CSA spectrum onto the  $\omega_1$ -axis, (B) the best fit simulation simulation of the static powder pattern lineshape and (C) simulation of powder pattern lineshape using best fit parameters found from the sideband–sideband correlation experiment, CSA-amplified PASS. The best fit chemical shift parameters found from the static powder pattern are given in Table 5.3.

line-broadening were applied in  $t_1$ . The one-dimensional sideband pattern is created by summing the correlation pattern over the seven visible sidebands in the direct dimension. The experiment time is approximately 3.5 hours.

The  $^{31}\text{P}$  spectrum of the static sample of pamidronate was recorded at an using the same cross-polarisation parameters as for MAS-CSA. The recycle delay was 7 s and 64 scans were recorded. The spectral width was 60 kHz. The experiment time is approximately 7 minutes.

The  $^{13}\text{C}$  MAS-CSA experiments on the peptides were recorded under a mixture of conditions optimised for each peptide individually. Specifically the MAS rate ranged from 2.3–2.95 kHz, and the indirect dimension effective spectral width from 7.5–10 kHz, with 32 complex  $t_1$  data points recorded with 200–400 scans per point.

The recycle delay was 4–5 s, the cross polarisation contact time was 2.5 ms and the  $^{13}\text{C}$   $\pi$ -pulse length was  $5.8\ \mu\text{s}$ . The decoupling field strength was 100 kHz.

#### 5.4.1 Numerical simulations

Numerical simulations of two-dimensional powder–sideband pattern correlation spectra were performed using a procedure written in the PV-Wave environment [157]. The evolution of the magnetisation vector under pseudo-static conditions in  $t_1$  followed by spinning conditions in  $t_2$  was calculated using Equation (5.6) and summed for 700  $\alpha$  and  $\beta$  angles generated by the REPULSION algorithm [34] and 96 evenly-spaced  $\gamma$  angles, to produce a simulated free induction decay (FID). The simulated FID is line-broadened (choosing the amount of line-broadening applied to give a similar appearance to the experimental lineshapes by eye), and then Fourier transformed to give the two-dimensional correlation pattern. The one-dimensional simulated powder patterns were formed by summing the two-dimensional simulated patterns over all visible sidebands. Best fits were found using a least squares fitting routine to minimise  $\chi^2$ . Initial estimates of chemical shielding parameters were generated randomly within usual ranges of these parameters for  $^{31}\text{P}$ . For fitting of simulated spectra, random noise was generated with a standard deviation of 1/200 of the total signal intensity under all the sidebands, and added to the simulated spectrum prior to fitting. As many sidebands in  $\omega_2$  were used in the fitting process as were visible above the noise level, and all  $\omega_1$  points were used in the fits. Fitting of the sideband–sideband correlation patterns is done as is described in the reference [155].

### 5.5 Conclusions

The analysis of a two-dimensional sideband–powder correlation pattern has been found to be capable of determining chemical shift parameters in an additional case where the sideband–sideband correlation approach of the previous chapter failed. This case is where the spectrum has contribution from two components with overlapping isotropic chemical shift and where the anisotropies of the two components are similar. This has been demonstrated with the phosphorus spectrum of pamidronate, where the CSAs of the two overlapping components differ by less than 20%. It also confidently shows that the number of components in the signal is two (based on the reduction in  $\chi^2$ , although also seen by eye), whereas the sideband–sideband technique applied to

the same problem is less deterministic.

The advantage of analysis of a sideband–powder correlation pattern over its projection is due to the increase in noise level caused by summing over direct dimension sidebands. However, restrictions on the MAS rate for the experiments mean that direct dimension sidebands, usually up to second order, are inevitable. If signals are resolved, then a one-dimensional sideband analysis is sufficient to determine chemical shift parameters. If there are overlapping signals with different CSAs, then analysis of the two-dimensional sideband–sideband correlation pattern, or a one-dimensional CP-MAS with very low spinning rate, will be better than analysis of the sideband–powder correlation pattern, as it has superior signal-to-noise. This was demonstrated in the example of the mixture of hydroxyapatite and sodium dihydrogen phosphate. This new sideband–powder correlation pattern analysis is useful in the circumstance of overlapping signals with similar CSAs. This is likely to be a common occurrence for  $^{13}\text{C}_\alpha$  signals in peptides, for instance, though in this particular case our experiments show that dipolar coupling to  $^{14}\text{N}$  needs to be taken into account for accurate results.

## Chapter 6

---

# The de Swiet experiment

---

The sideband–sideband and sideband–powder correlation pattern approaches introduced in the previous two chapters both rely on fitting a model to the experimental data. In both cases, trial spectra are generated by numerical integration of the relevant equations over a finite crystallite set. The number of components that comprise a particular signal must be assumed. The determination of chemical shift parameters from overlapping spectra using the correlation patterns has been described as resolving the signals by their CSA, but in fact the signals are never truly resolved. This leads to the difficulty in deciding with confidence the number of distinct components that comprise the signal, as discussed in Section 4.2.

A better approach would be to actually resolve the signals according to their CSA so that they are no longer overlapped at all. Ideally, in such an experiment each nuclear environment will lead to a  $\delta$ -function peak in a three-dimensional spectrum, where the three co-ordinates of the peak give directly the isotropic chemical shift,  $\delta_{\text{iso}}$ , the CSA,  $\zeta$ , and the asymmetry,  $\eta$ . Each chemical environment of a nucleus would give a separate, resolved peak, separated by the CSA in the second dimension, from which the chemical shift parameters, and thus the principal values can be read straight from the spectrum, without requiring any model fitting or assumptions about the number of components present in the spectrum. The distribution and errors in the CST would be easily visible from the shape of its corresponding peak, and the signal-to-noise ratio gives a clear measure of the confidence that should be placed in the result.

This ideal experiment is not currently possible, but a number of attempts have been made to produce its vital feature: that signals are somehow resolved by their CSA. Some of these methods were briefly introduced in Section 3.1. In this chapter, the method of de Swiet [94, 95] will be examined in greater detail. The potential of this experiment for accurate determination of CSTs has not been reflected in the level of usage it has received in the ten years since its conception (the relevant papers have received just seven citations in ten years, none of which appear to have actually implemented the experiment in any practical problem). There are two likely reasons for this:

- The theory behind the experiment is very complex, making the original papers difficult to understand.
- The experimental examples are disappointing, as they suffer from linebroadening and lineshape distortion as an inevitable consequence of the pulse sequences used.

Hopefully by addressing these problems, the de Swiet experiment may become more widespread in its application in the future.

## 6.1 Basic theory

The anisotropic components of the CST in the rotor frame can be split, according to Equation (2.76), into five complex components that are given by:

$$A_{2n}^R = \sum_{m=-2}^2 A_{2m}^{\text{PAF}} D_{mn}^{(2)}(\Omega_{\text{PR}}), \quad (6.1)$$

where  $n$  runs from  $-2$  to  $2$ . Those components with opposite  $n$  are related by:

$$A_{2n}^R = (-1)^n (A_{2-n}^R)^*, \quad (6.2)$$

so they can be conveniently transformed into a purely real basis:

$$\begin{aligned}
 \hat{A}_1 &= A_{20}^R \\
 \hat{A}_2 &= \frac{A_{2-1}^R - A_{21}^R}{\sqrt{2}} \\
 \hat{A}_3 &= i \frac{A_{2-1}^R + A_{21}^R}{\sqrt{2}} \\
 \hat{A}_4 &= \frac{A_{2-2}^R + A_{22}^R}{\sqrt{2}} \\
 \hat{A}_5 &= i \frac{A_{22}^R + A_{2-2}^R}{\sqrt{2}}.
 \end{aligned} \tag{6.3}$$

The anisotropic CST,  $\hat{\mathbf{A}}$ , is thus represented as a vector in five-dimensional space, the value of which depends upon  $\zeta$  and  $\eta$  and the Euler angles,  $\alpha_{PR}$ ,  $\beta_{PR}$  and  $\gamma_{PR}$ . A different crystallite, with its different Euler angles, will have a different CST in the rotor frame, but crucially all crystallite orientations have the same length of  $\hat{\mathbf{A}}$ , which is:

$$\begin{aligned}
 |\hat{\mathbf{A}}| &= \sqrt{\hat{A}_1^2 + \hat{A}_2^2 + \hat{A}_3^2 + \hat{A}_4^2 + \hat{A}_5^2} \\
 &= \zeta \sqrt{(3 + \eta^2)/2}.
 \end{aligned} \tag{6.4}$$

If the probability of the CST of a spin having a particular value,  $\hat{\mathbf{A}}$ , is  $P(\hat{\mathbf{A}})$ , then for each chemical site, the probability is only non-zero on a spherical shell (in five dimensions) with radius  $|\hat{\mathbf{A}}|$ . The non-zero probability region does not cover the whole shell in five dimensions, as not all rotations in five dimensions can be achieved with a physical rotation in three dimensions. The remainder of the five-dimensional spherical surface would correspond to tensors with the same value of  $|\hat{\mathbf{A}}|$ , but a different combination of  $\zeta$  and  $\eta$ .

If it were possible to measure a spectrum of  $P(\hat{\mathbf{A}})$ , for all  $\hat{\mathbf{A}}$ , and integrate over shells of fixed radius, this would result in a one-dimensional spectrum of  $P(|\hat{\mathbf{A}}|)$ . The peaks in this spectrum could be read off as values of  $\zeta \sqrt{(3 + \eta^2)/2}$  for each chemical site, without needing any simulations or model fitting. The isotropic shift information would be contained in a separate dimension of the experiment, so in fact each spin environment leads to a peak in a two-dimensional spectrum, of the CSA-related parameter,  $|\hat{\mathbf{A}}|$ , correlated with isotropic shift.

This is not quite everything that was desired from the ideal experiment, which was a three-dimensional pattern, where the three co-ordinates of a peak give directly the isotropic chemical shift,  $\delta_{\text{iso}}$ , the CSA,  $\zeta$ , and the asymmetry,  $\eta$ . The measurement of  $P(\hat{\mathbf{A}})$  can be transformed to give a two-dimensional spectrum of  $\zeta$  against  $\eta$ , which when correlated with the isotropic shift gives a three-dimensional spectrum of the kind described [95]. However, the transform of  $P(\hat{\mathbf{A}})$  required to achieve this is considerably more complicated than the integration over shells of fixed radius required for the measurement of  $|\hat{\mathbf{A}}|$ . If our main aim is the separation of signals with the same isotropic chemical shift, then the only instances where the additional transform will be necessary are where two chemical sites have tensors with the same  $\delta_{\text{iso}}$  and  $|\hat{\mathbf{A}}|$ , but different  $\zeta$  and  $\eta$ ; such situations are likely to be rare. For now, therefore, the simpler measurement of  $|\hat{\mathbf{A}}|$  will be settled for.

### 6.1.1 Measurement of $P(\hat{\mathbf{A}})$

The most obvious way that one might attempt to measure  $P(\hat{\mathbf{A}})$  is by using a five-dimensional experiment (six including the isotropic shift). In each of the five evolution periods, the Hamiltonian is constructed so that the spins evolve under one of the five components of  $\hat{\mathbf{A}}$ . This approach has two rather serious drawbacks.

First of all, under MAS, the all-important  $A_{20}^{\text{lab}}(t)$  term, given by Equation (2.76), expressed in terms of the components of  $\hat{\mathbf{A}}$  from Equation (6.3), is:

$$\begin{aligned} A_{20}^{\text{lab}}(t) = & d_{00}^{(2)}(\beta_{\text{RL}})\hat{A}_1 - \sqrt{2}d_{10}^{(2)}(\beta_{\text{RL}})\hat{A}_2 \cos(\omega_{\text{R}}t) \\ & - \sqrt{2}d_{10}^{(2)}(\beta_{\text{RL}})\hat{A}_3 \sin(\omega_{\text{R}}t) + \sqrt{2}d_{20}^{(2)}(\beta_{\text{RL}})\hat{A}_4 \cos(2\omega_{\text{R}}t) \\ & + \sqrt{2}d_{20}^{(2)}(\beta_{\text{RL}})\hat{A}_5 \sin(2\omega_{\text{R}}t). \end{aligned} \quad (6.5)$$

Now, the terms containing  $\hat{A}_2$  through to  $\hat{A}_5$  can be identified with the terms  $C_1$ ,  $S_1$ ,  $C_2$  and  $S_2$  in Equation (2.97) respectively, and are, in principle, measurable. However,  $d_{00}^{(2)}(\beta_{\text{RL}})$  is zero, where  $\beta_{\text{RL}}$  is the magic angle, and so the term with  $\hat{A}_1$  can never be recoupled under MAS. Thus, it is impossible to measure  $\hat{A}_1$  at the magic angle, and so direct measurement of  $|\hat{\mathbf{A}}|$  is also prohibited\*.

The second problem with this approach is that a five- or six-dimensional experiment is likely to be severely time consuming, and lead to significant signal decay

---

\*The  $d_{00}^{(2)}(\beta_{\text{RL}})$  is non-zero with OMAS, so  $\hat{A}_1$  could be recoupled. However, MAS is desirable as it is required for resolution in the isotropic shift dimension.

through relaxation during the presumably lengthy pulse sequence. High dimensional experiments, however, are becoming increasingly common, particularly in liquid-state NMR. The problem of the length of the experiment is avoided by not actually recording the full  $N$ -dimensional spectrum, but by recording only a small number lower-dimensional slices, which are projections of the  $N$ -dimensional spectrum. A number of techniques exist to ‘reconstruct’ the missing data [162], creating the full  $N$ -dimensional spectrum from a fraction of the experimental time. This sounds risky, but the reason that this can be done is that in a high dimensional spectrum, a large proportion of the parameter space is unoccupied, so a large amount of time is wasted in recording data for these regions. By careful selection of the projections to record, a real  $N$ -dimensional spectrum can be recorded in a fraction of the time.

### 6.1.2 Projection reconstruction and the inverse Radon transform

Projection reconstruction is a technique for reconstructing a full  $N$ -dimensional spectrum from a limited number of lower-dimensional projections [162]. It is probably best explained using the reconstruction of a two-dimensional experiment from three one-dimensional projections, as shown in Figure 6.1.

If the projection onto all vectors is known, then the projection reconstruction leads to the exact spectrum, but then this requires measuring an infinite number of projections; hardly a short-cut. If only a subset of the projections are known, then there is the possibility for some ambiguities in the reconstructed spectrum, but the experimental time is reduced.

Now, the Radon transform [163],  $P^*$ , of  $P(\hat{\mathbf{A}})$ , gives the projection of the full  $P(\hat{\mathbf{A}})$  shell onto an arbitrary unit vector,  $\hat{\mathbf{n}}$ :

$$P^*(z, \hat{\mathbf{n}}) = \int \delta(\hat{\mathbf{A}} \cdot \hat{\mathbf{n}} - z) P(\hat{\mathbf{A}}) d^5\hat{\mathbf{A}}, \quad (6.6)$$

where  $z$  is a distance from the origin along the vector,  $\hat{\mathbf{n}}$ . The full spectrum can be reconstructed using the inverse Radon transform (providing the projections onto all unit vectors are known), which is the same as projection reconstruction of the five-dimensional pattern.

Now consider the task of measuring the projections onto particular unit vector. Direct measurement of the projection onto  $\hat{\mathbf{n}} = (1, 0, 0, 0, 0)$ , which is parallel to  $\hat{\mathbf{A}}_1$ , for instance, is known to be impossible. The projection of  $P(\hat{\mathbf{A}})$  onto  $\hat{\mathbf{n}} = (0, \sqrt{2/3}, 0, \sqrt{1/3}, 0)$ , on the other hand, is common place. This amounts to recoupling

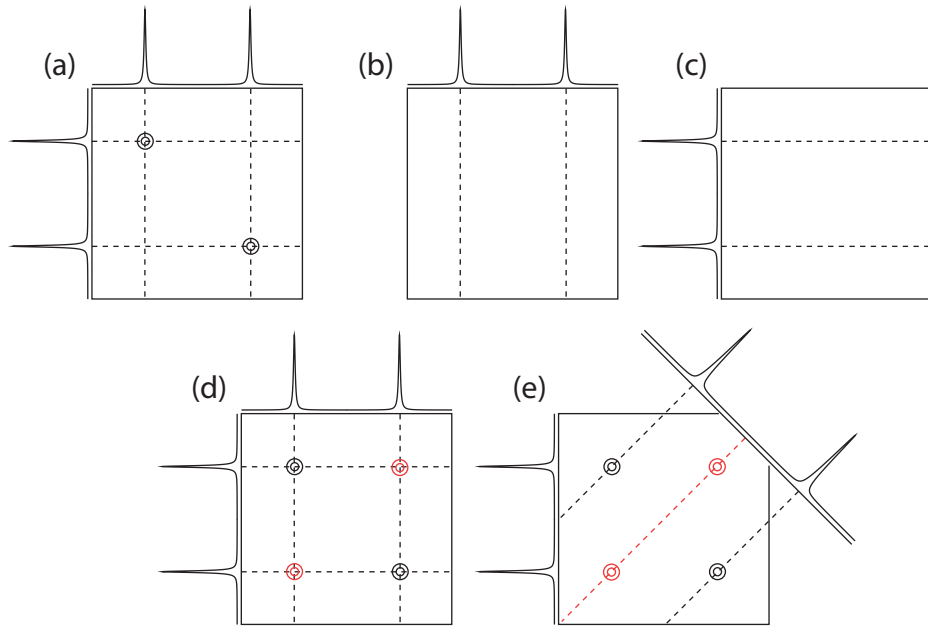


**Figure 6.1** Diagram showing the reconstruction of a full two-dimensional spectrum from three one-dimensional projections, by the process of projection reconstruction. (a) The full two-dimensional spectrum (the desired end-point), and its projection onto two perpendicular axes. (b) Record the first projection (on the horizontal axis). The dashed line shows all the positions where peaks could be to cause that projection. (c) Record the second projection (on the vertical axis). Again the dashed lines shows the possible peak locations in the two-dimensional spectrum. (d) The possible peaks are where these lines cross, and include the real peaks (in black) and some fake peaks (in red). (e) Record a third projection on an axis oriented at 45° to the other two. The absence of a peak at the position of the red dotted line marks these out as fake peaks, whilst the peaks at the position of the black dotted line confirms the presence of these two peaks. Overall then, the full two-dimensional spectrum has been recorded; if the spectrum is  $N$  points by  $N$  points, it would require  $N^2$  measurements to record it directly, but only  $3N$  using projection reconstruction.

the  $C_1 + C_2$  terms from Equation (2.97), which was successfully achieved by Tycko *et al.* [69] (amongst others), and was the subject of the discussion in Chapter 5. This one projection though is insufficient to reconstruct the full five-dimensional  $P(\hat{\mathbf{A}})$  spectrum.

### 6.1.3 Equivalence of projections for disordered powders

In the case of a completely disordered powder, it is known that  $P(\hat{\mathbf{A}})$  is rotationally invariant, since any sample rotation does not change the overall distribution of orientation angles, as all orientations are equally populated. Thus  $P(\hat{\mathbf{A}})$  is unchanged by any physical three-dimensional rotation, represented by the rotation matrix,  $R_{ij}$ . In other

words:

$$P(\hat{\mathbf{A}}') = P(\hat{\mathbf{A}}), \quad (6.7)$$

where  $\hat{A}'_i = R_{ij}\hat{A}_j$ .

The Radon transform,  $P^*$ , is therefore also rotationally invariant, so:

$$P^*(z, \hat{\mathbf{n}}) = P^*(z, \hat{\mathbf{n}}'), \quad (6.8)$$

where  $\hat{n}'_i = R_{ij}\hat{n}_j$ . This means that many projections of  $P(\hat{\mathbf{A}})$  are equivalent.

For a crystallite with orientation angles,  $\alpha_{\text{PR}}$ ,  $\beta_{\text{PR}}$  and  $\gamma_{\text{PR}}$ , there must exist a physical rotation that takes the PAF back to the orientation,  $\alpha_{\text{PR}} = 0$ ,  $\beta_{\text{PR}} = 0$  and  $\gamma_{\text{PR}} = 0$  (i.e. the rotor frame and chemical shift PAF are co-incident). In this frame, the CST is found, using Equation (6.3), to be  $\hat{\mathbf{A}} = (\zeta\sqrt{3/2}, 0, 0, \zeta\eta\sqrt{1/2}, 0)$ . Thus it must also true that any unit vector in  $\mathbf{A}$ -space, that is parallel to  $\hat{\mathbf{A}}$  for a crystallite with chemical shift parameters,  $\zeta$  and  $\eta$ , and orientation angles,  $\alpha_{\text{PR}}$ ,  $\beta_{\text{PR}}$  and  $\gamma_{\text{PR}}$ , can be rotated by the same physical rotation to a unit vector parallel to  $\hat{\mathbf{n}} \propto (\zeta\sqrt{3/2}, 0, 0, \zeta\eta\sqrt{1/2}, 0)$ . It will be convenient to write this as:

$$\hat{\mathbf{n}} = (\cos \phi, 0, 0, \sin \phi, 0), \quad (6.9)$$

where  $\tan \phi = \eta/\sqrt{3}$ . The projection onto this unit vector is still impossible to record under MAS because of the non-zero  $\hat{A}_1$  component.

However, a further rotation through Euler angles  $\alpha_{\text{PR}} = 45^\circ$ ,  $\beta_{\text{PR}} = 54.7^\circ$  and  $\gamma_{\text{PR}} = 180^\circ$  transforms this vector to:

$$\hat{\mathbf{n}} = (0, \sqrt{2/3} \cos \phi, \sqrt{2/3} \sin \phi, \sqrt{1/3} \cos \phi, -\sqrt{1/3} \sin \phi). \quad (6.10)$$

This can be seen by inputting the Euler angles for this rotation into Equation (6.3), and substituting for  $\cos \phi$  and  $\sin \phi$ .

A physical rotation can always be found, therefore, that rotates an arbitrary unit vector  $\hat{\mathbf{n}}$  to a unit vector in the plane defined by the unit vectors:

$$\hat{\mathbf{n}}^{(x)} = (0, \sqrt{2/3}, 0, \sqrt{1/3}, 0), \quad \hat{\mathbf{n}}^{(y)} = (0, 0, \sqrt{2/3}, 0, -\sqrt{1/3}). \quad (6.11)$$

In other words:

$$\hat{n}'_i = R_{ij}(\cos(\phi)\hat{n}_j^{(x)} + \sin(\phi)\hat{n}_j^{(y)}), \quad (6.12)$$

where  $\phi$  is the polar angle for the orientation in the  $\hat{\mathbf{n}}^{(x)}-\hat{\mathbf{n}}^{(y)}$  plane onto which the particular vector,  $\hat{\mathbf{n}}$ , can be rotated. Equation (6.8) shows that all the projections of  $P(\hat{\mathbf{A}})$  onto arbitrary  $\hat{\mathbf{n}}$ , are related to a projection in the  $\hat{\mathbf{n}}^{(x)}-\hat{\mathbf{n}}^{(y)}$  plane.

### 6.1.4 Recording of the projections

So, by recording all projections onto vectors in the  $\hat{\mathbf{n}}^{(x)}-\hat{\mathbf{n}}^{(y)}$  plane, the projection on every vector in five dimensions (i.e.  $P^*(z, \hat{\mathbf{n}})$ ) can be determined. The inverse Radon transformation of  $P^*(z, \hat{\mathbf{n}})$  produces the desired  $P(\hat{\mathbf{A}})$ . The experiment is thus reduced to two-dimensions, and, crucially, neither  $\hat{\mathbf{n}}^{(x)}$  or  $\hat{\mathbf{n}}^{(y)}$  contain any contribution from  $\hat{A}_1$ , and so the projections are experimentally accessible under MAS. In particular, the projection onto  $\hat{\mathbf{n}}^{(x)}$  is already well-known; this is the MAS-CSA experiment [69]. The projection onto  $\hat{\mathbf{n}}^{(y)}$  is less familiar. This requires recoupling the  $S_1 - S_2$  terms from Equation (2.97), which gives what shall be known as the *complementary* powder pattern.

All the necessary projections in the  $\hat{\mathbf{n}}^{(x)}-\hat{\mathbf{n}}^{(y)}$  plane can therefore be recorded using a three-dimensional experiment, recoupling  $C_1 + C_2$  in  $t_1$  using the Tycko *et al.* pulse sequence,  $S_1 - S_2$  in  $t_2$ , using a new pulse sequence [94], and normal evolution under MAS in  $t_3$  to obtain the isotropic dimension. Such an experiment correlates the conventional and complementary powder patterns in the  $\omega_1-\omega_2$  plane (see, for example, Figure 6.2). The projections of this pattern onto any vector at an angle  $\phi$  to the  $\omega_1$ -axis can easily be calculated (see, for example, Figure 6.3).

The  $S_1 - S_2$  terms in Equation (2.97), those required for evolution during  $t_2$  of this experiment, can be recoupled using an experiment that is very similar to the Tycko *et al.* experiment. The difference is that now:

$$\begin{aligned} \int_{-\tau_R/2}^{\tau_R/2} f(t) \cos(\omega_R t) dt &= \int_{-\tau_R/2}^{\tau_R/2} f(t) \cos(2\omega_R t) dt = 0 \\ \int_{-\tau_R/2}^{\tau_R/2} f(t) \sin(\omega_R t) dt &= \int_{-\tau_R/2}^{\tau_R/2} f(t) \sin(2\omega_R t) dt. \end{aligned} \quad (6.13)$$

This can be achieved with four pulses, except with different timings to the Tycko *et al.* MAS-CSA experiment. Specifically,  $f(t)$  must be odd, which requires pulses at  $t = 0$  and  $t = \tau_R/2$ , with additional pulses at  $t = \pm 0.143\tau_R$ , which is shown in Figure 6.4. The isotropic scaling factor for this sequence is  $\chi_i = 0$ , and the anisotropic scaling factor is  $\chi_a = 0.393$  (the same as for the MAS-CSA sequence).

### 6.1.5 Six-fold symmetry of powder pattern and projections

There are six different ways in which the PAF can be aligned with the rotor frame, which are related by further rotations in multiples of  $90^\circ$  about any of the principal

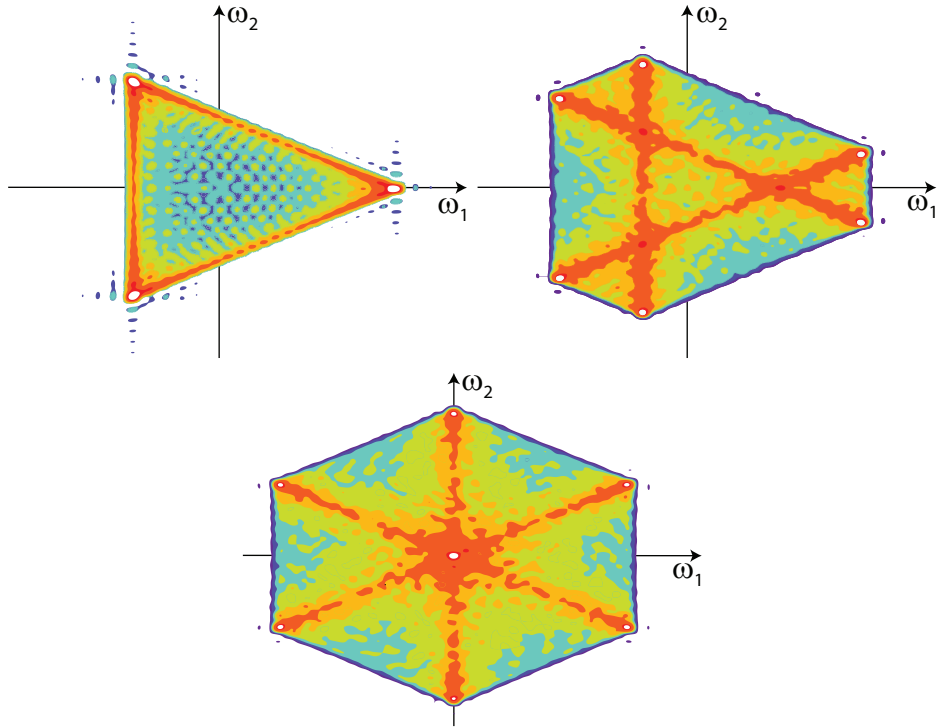


**Figure 6.2** Simulated example correlation powder patterns in the  $\hat{\mathbf{n}}^{(x)}-\hat{\mathbf{n}}^{(y)}$  plane, that result from the CSA recoupling experiment described in the text. The examples shown have the same anisotropy, but different asymmetries,  $\eta$ , of (a) 0, (b) 0.5, (c) 1. The white contours show the highest peaks.

axes. For example, a rotation through  $\alpha_{\text{PR}} = 90^\circ$  is equivalent to swapping the  $x$ - and  $y$ -axes of the PAF, maps the CST to  $\hat{\mathbf{A}} = (\zeta\sqrt{3}/2, 0, 0, -\zeta\eta\sqrt{1/2}, 0)$ . The unit vector parallel to this  $\hat{\mathbf{A}}$  can be written as:

$$\hat{\mathbf{n}} = (\cos \phi, 0, 0, \sin \phi, 0), \quad (6.14)$$

as in Equation (6.9), except now  $\tan \phi = -\eta/\sqrt{3}$ . A projection on a vector in the  $\hat{\mathbf{n}}^{(x)}-\hat{\mathbf{n}}^{(y)}$  plane at an angle  $\phi$  to the  $\hat{\mathbf{n}}^{(x)}$ -axis is therefore equivalent to the projection on a unit vector at an angle  $-\phi$  to the  $\hat{\mathbf{n}}^{(x)}$ -axis, as the projections are related by this physical rotation. This also implies that the  $\hat{\mathbf{n}}^{(x)}$ -axis is a mirror plane in the two-dimensional powder pattern.

Another possible rotation (which leaves the PAF aligned with the rotor frame) is by  $\beta_{\text{PR}} = 90^\circ$ , which can be shown to rotate the vector  $\hat{\mathbf{n}} = (\cos \phi, 0, 0, \sin \phi, 0)$  to:

$$\hat{\mathbf{n}} = \left( \frac{\sqrt{3}}{2} \sin \phi - \frac{1}{2} \cos \phi, 0, 0, \frac{\sqrt{3}}{2} \cos \phi + \frac{1}{2} \sin \phi, 0 \right). \quad (6.15)$$

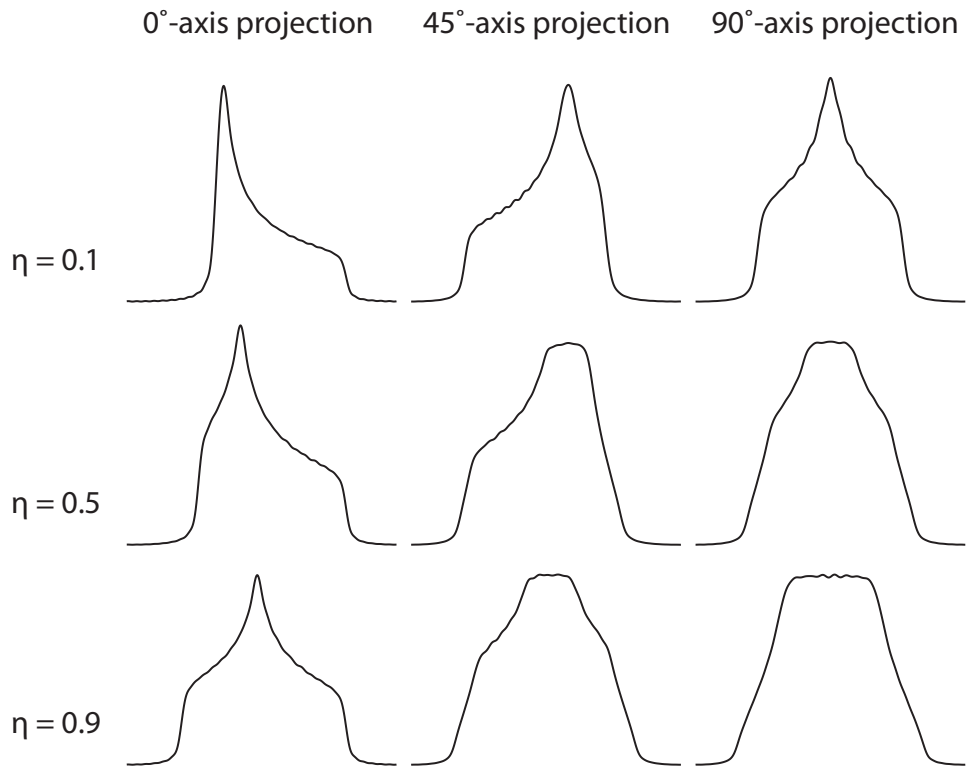


**Figure 6.3** Projections of the two-dimensional powder patterns in Figure 6.2 onto various axes in the  $\hat{\mathbf{n}}^{(x)}-\hat{\mathbf{n}}^{(y)}$  plane. All examples are for the same anisotropy. The top row has asymmetry,  $\eta = 0.1$ , the middle row,  $\eta = 0.5$ , and the bottom row,  $\eta = 0.9$ . The first column shows the projection onto  $\hat{\mathbf{n}}^{(x)} = (0, \sqrt{2/3}, 0, \sqrt{1/3}, 0)$ , which is the conventional one-dimensional powder pattern. The third column shows the projection onto  $\hat{\mathbf{n}}^{(y)} = (0, 0, \sqrt{2/3}, 0, -\sqrt{1/3})$ , which is the complementary powder pattern, formed by recoupling  $S_1 - S_2$  terms in Equation (2.97). The middle column shows the projection onto an axis at  $45^\circ$  between the two.

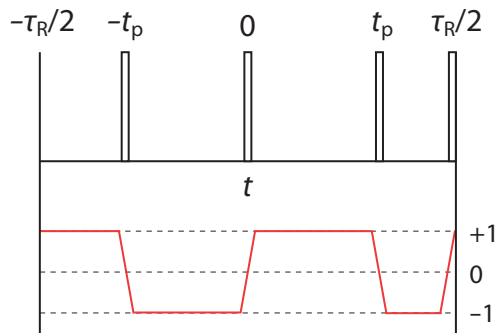


**Figure 6.4** Pulse sequence unit for the de Swiet experiment, and the CTP (or equivalently,  $f(t)$ ) shown in red.

By equating the co-efficients of  $\hat{A}_1$  and  $\hat{A}_4$  with  $\cos \phi$  and  $\sin \phi$ , this can be shown to be equivalent to a vector,  $\hat{\mathbf{n}}$ , with  $\phi \rightarrow 2\pi/3 - \phi$ . Thus projections onto vectors at these angles in the  $\hat{\mathbf{n}}^{(x)}-\hat{\mathbf{n}}^{(y)}$  plane are also equivalent. Additional rotations can be found that relate tensors and unit vectors with at angles  $\phi$  to those with angles  $\phi \rightarrow 2\pi/3 + \phi$ . This explains the six-fold symmetry that is seen in Figure 6.2. The two-dimensional powder pattern, or its projections, are therefore completely determined by a  $60^\circ$  wedge.

#### 6.1.6 Applying the inverse Radon transform

The probability distribution of  $|\hat{\mathbf{A}}|$ ,  $P(|\hat{\mathbf{A}}|)$ , can be calculated from the multiple projections of the two-dimensional powder pattern integrated over shells of fixed radius, using the inverse Radon transform:

$$P(|\hat{\mathbf{A}}|) = \mathcal{R}^{-1} \int P^*(z, \hat{\mathbf{n}}) d\hat{\mathbf{n}}, \quad (6.16)$$

where  $\mathcal{R}^{-1}$  is the inverse Radon transform operator.

Now,  $P^*(z, \hat{\mathbf{n}})$  for arbitrary  $\hat{\mathbf{n}}$  has been shown to possess an equivalent projection in the  $\hat{\mathbf{n}}^{(x)}-\hat{\mathbf{n}}^{(y)}$  plane, so Equation (6.16) becomes:

$$P(|\hat{\mathbf{A}}|) = \mathcal{R}^{-1} \int P^*(z, \hat{\mathbf{n}}^{(x)} \cos(\phi(\hat{\mathbf{n}})) + \hat{\mathbf{n}}^{(y)} \sin(\phi(\hat{\mathbf{n}}))) d\hat{\mathbf{n}}, \quad (6.17)$$

where  $\phi(\hat{\mathbf{n}})$  is the appropriate angle for the vector in the  $\hat{\mathbf{n}}^{(x)}-\hat{\mathbf{n}}^{(y)}$  plane to which the particular vector,  $\hat{\mathbf{n}}$ , can be rotated.

The different projections in the  $\hat{\mathbf{n}}^{(x)}-\hat{\mathbf{n}}^{(y)}$  plane are not equally weighted. The number density of five-dimensional vectors that can be rotated to a particular vector at an angle  $\phi$  in the  $\hat{\mathbf{n}}^{(x)}-\hat{\mathbf{n}}^{(y)}$  plane has been shown to be proportional to  $\sin(3\phi)$ , which was evaluated numerically by de Swiet [94]. Therefore the change of integration variable, from  $\hat{\mathbf{n}}$  to  $\phi$ , leads to:

$$P(|\hat{\mathbf{A}}|) = \mathcal{R}^{-1} \int_{\phi=0}^{\pi/3} P^*(z, \hat{\mathbf{n}}^{(x)} \cos(\phi) + \hat{\mathbf{n}}^{(y)} \sin(\phi)) \sin(3\phi) d\phi. \quad (6.18)$$

The restriction for  $\phi$  between 0 and  $\pi/3$  is due to the known symmetry of the powder pattern and its projections. Writing out the inverse Radon transform explicitly gives the equation for the spectrum of  $|\hat{\mathbf{A}}|$  values as:

$$P(|\hat{\mathbf{A}}|) = \left[ z^2 \frac{d}{dz^2} - z \frac{d}{dz} \right] \int_{\phi=0}^{\pi/3} P^*(z, \hat{\mathbf{n}}^{(x)} \cos(\phi) + \hat{\mathbf{n}}^{(y)} \sin(\phi)) \sin(3\phi) d\phi. \quad (6.19)$$

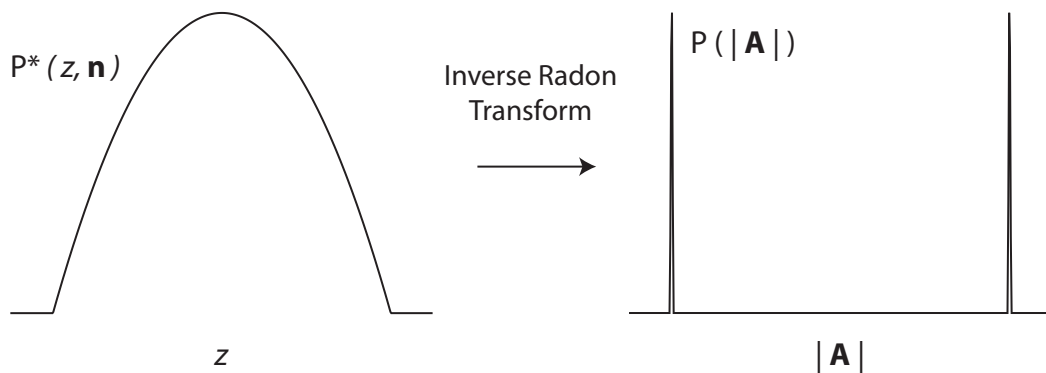


**Figure 6.5** Idealised form of  $P^*(z, \hat{n})$  with a single component, integrated over all  $\hat{n}$ , (left), and its inverse Radon transform (right). Both are symmetrical and so it is usual to only display half of the spectrum.

The peaks in this spectrum (i.e.  $P(|\hat{A}|)$ ) are the values of  $|\hat{A}| = \zeta \sqrt{(3 + \eta)/2}$  for each site. The number of peaks gives the number of components and the broadness of the peaks shows something of the distribution of  $|\hat{A}|$  values for a particular peak. Figure 6.5 shows the effect of the inverse Radon transform on an idealised data set.

## 6.2 Improved implementations

In his own paper [95], de Swiet uses the three-dimensional experiment described to obtain the two-dimensional powder patterns for  $^{13}\text{C}$  in methyl- $\alpha$ -D-glucopyranoside (MAGP). The powder patterns he obtains are not of good quality. There are a number of possible reasons for this, many of which can be avoided using a combination of techniques that were unavailable ten years ago when the original experiment was published. By applying some of these modern techniques to the de Swiet experiment, coupled with the improvement in spectrometer hardware, it is hoped that sufficient improvement in the quality of spectra can be seen in order to make the de Swiet experiment a viable technique for measurement of CST in crowded spectra.

The efforts that have been made in this work have included aiming to reduce pulse errors, both by reducing the total number of pulses, or improving the phase cycling scheme. Also, the adverse effects of relaxation during the lengthy pulse sequence need to be minimised. Finally, anything that would improve the sensitivity would not go amiss.

### 6.2.1 Constant time version

The constant time version of the de Swiet experiment eliminates the linebroadening inherent in a variable  $t_1$  delay experiment by fixing the length of the pulse sequence so the magnetisation decays by the same amount in all  $t_1$  slices. This was shown to make a major improvement on the MAS-CSA experiment on which the de Swiet experiment is based [72].

In the constant time version, the  $t_{1,\text{eff}}$  of a particular slice must be controlled by changing  $\chi_a$  rather than the number of pulse sequence units,  $n$ . Like MAS-CSA, the only four  $\pi$ -pulse block available that recouples  $S_1 - S_2$  whilst removing the isotropic shift, is one with an anisotropic scaling factor,  $\chi_a = 0.393$ . However, by placing six  $\pi$ -pulses in one rotor cycle, a range of scaling factors can be obtained between  $\chi_a = -0.393$  and  $\chi_a = 0.393$  (i.e. the same range as for MAS-CSA). Unlike MAS-CSA, however, no solutions for Equation (6.13) were found for recoupling  $S_1 - S_2$  using six  $\pi$ -pulses in three rotor periods, although there is no proof that this is fundamentally the case.

The drawback of the constant time version is that a significant amount of signal is sacrificed. Since the length of the pulse sequence in  $t_1$  is constant throughout the experiment, all  $t_1$  and  $t_2$  data points must use as many pulse sequence blocks as required for the longest  $t_1$  and  $t_2$  times, causing signal loss through relaxation and pulse errors.

### 6.2.2 Optimised version

The optimised version of the de Swiet experiment allows manipulation of both  $\chi_a$  and  $n$ . This is a compromise between the constant time version, which removes linebroadening in  $t_1$  but suffers from low sensitivity, and the original experiment which has better sensitivity but poor line shapes. For each effective  $t_1$  and  $t_2$  value, the minimum number of pulse sequence units (with the appropriate value of  $\chi_a$ ) are used to build up the  $t_1$  and  $t_2$  periods. This is exactly analogous to the optimised version of MAS-CSA.

The relative merits of the optimised, constant time and original variants of the de Swiet experiment are seen in Figure 6.6, which shows the projection on the  $\hat{\mathbf{n}}^{(y)}$ -axis of the two-dimensional pattern for the three different implementations of the de Swiet experiment. It is clear that both the constant time and optimised versions are considerable improvements upon the original version, which shows artefacts that

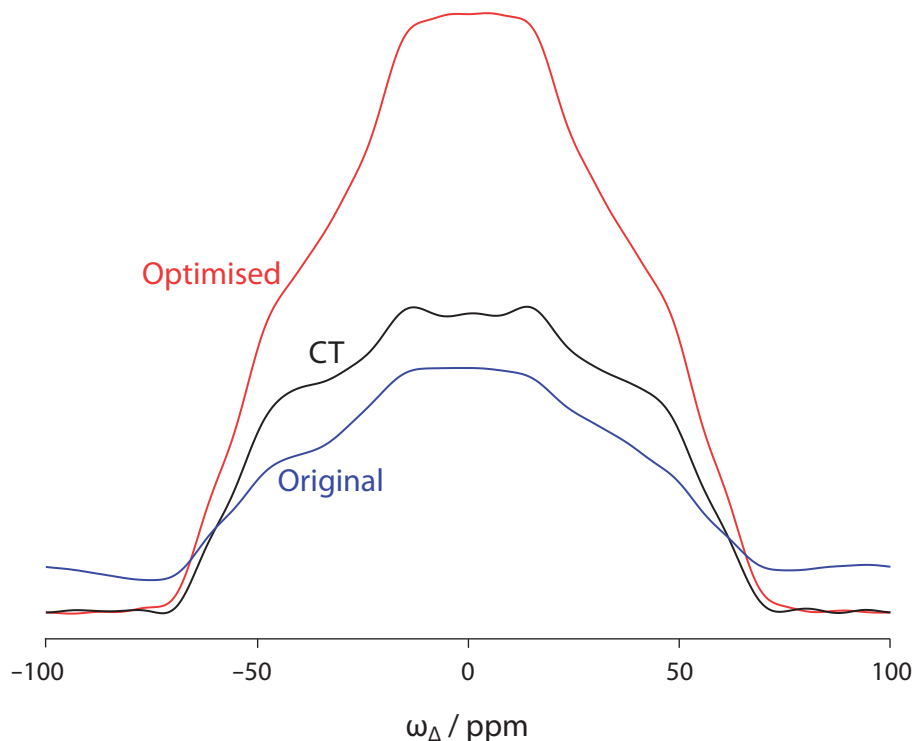


**Figure 6.6** Comparison of experimental lineshapes for the  $\hat{n}^{(y)}$ -axis projection of a de Swiet powder pattern, for a  $^{31}\text{P}$  site in the bis-phosphonate drug molecule, neridronate. Three different approaches are used: the original version (blue), the constant time version (black) and the optimised version (red). The experimental parameters and pulse sequences used are described in Section 6.5.

are almost identical to those reported in MAS-CSA [72]. The differences between the constant time and optimised versions is as expected; the constant time version gives a sharper lineshape, but considerably less intense than the optimised version. It is therefore anticipated that the constant time version might be used when the sensitivity is inherently high and linebroadening is problematic, but otherwise the optimised version will probably prove to be the superior approach.

### 6.2.3 Five-pulse units

In the pulse sequence units that comprise  $t_2$  (i.e. those that recouple the complementary powder pattern), the final pulse in each unit comes right at the very end of the rotor period unit. The purpose of this pulse is to return the coherence to the same coherence order as there was present at the start of the pulse sequence unit. If this were not the case, then the following pulse sequence unit would begin with the opposite sign of

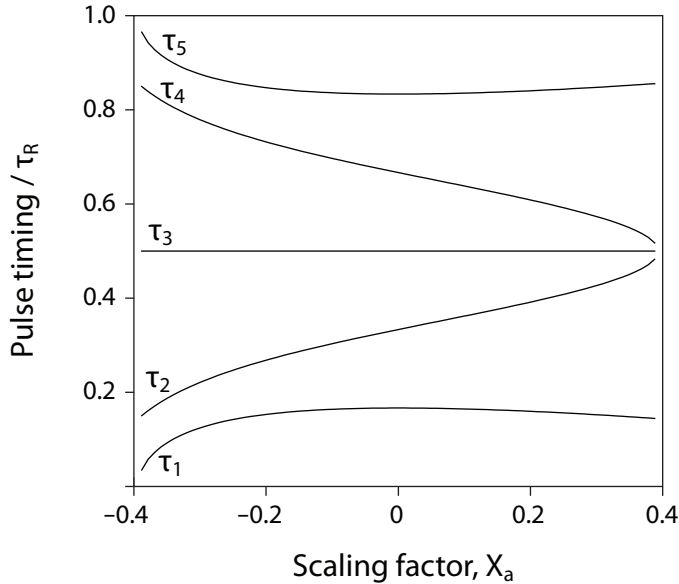


**Figure 6.7** Pulse timings, as fractions of a full rotor cycle, for recoupling  $S_1 - S_2$  with five pulses for the range of scaling factors  $-0.393 < \chi_a < 0.393$ .

coherence order, and so evolution in this second pulse sequence unit would exactly cancel the evolution in the first pulse sequence unit. This is the only purpose of this pulse; it does not have any affect on the scaling factors of the individual pulse sequence units, as shown by Equation (6.13).

For a six  $\pi$ -pulse unit, with pulse timings which give an anisotropic scaling factor of  $\chi_a$ , there also exists a different set of pulse timings which give an anisotropic scaling factor of  $-\chi_a$ . This leads to the possibility of removing the final pulse of the six-pulse unit. To prevent the evolution in the next pulse sequence unit from cancelling the previous evolution, alternating blocks must be swapped with sequences that have the opposite sign of  $\chi_a$ . The opposite sign of  $\chi_a$  and the opposite sign of the coherence order at the start of the pulse sequence unit cancel out, and therefore the evolution in the second unit is in the same direction as the first unit.

The effect of this change is to miss out every sixth pulse of the overall pulse sequence in  $t_2$ . By reducing the number of pulses, it is hoped that losses due to pulse errors are minimised. The pulse timings for the five  $\pi$ -pulse units are shown in Figure 6.7.

The same argument can not be applied to the  $t_1$  pulse sequence units that recouple

$C_1 + C_2$ , since every pulse affects  $\chi_a$  for that sequence. Recoupling  $C_1 + C_2$  requires  $f(t)$  in Equation (5.2) to be even, which can not be achieved with an odd number of  $\pi$ -pulses.

#### 6.2.4 Cogwheel phase cycling

Another easily implemented improvement to the original scheme is the inclusion of cogwheel phase cycling [46]. In the original experimental example, de Swiet uses a basic nested phase cycle, which, due to the enormous number of steps required to do a full phase cycle (assuming a nested four-step phase cycle for each pulse, with 32 blocks of four pulses in  $t_1$  and  $t_2$ , the total length of the phase cycle is an stonking  $1.3 \times 10^{154}$  steps for each  $t_1-t_2$  point; many orders of magnitude higher than the number of seconds since the universe began!) he understandably cut it back a bit to just a 16 step phase cycle per point. Though this can cancel for some phase errors, others can still creep through.

A cogwheel phase cycling scheme is ideal for this situation. Since phases of all pulses are cycled simultaneously, the total pulse sequence length does not increase exponentially with the number of pulses. The details of the cogwheel phase cycling scheme applied to the three-dimensional de Swiet experiment (any variant) are shown in Figure 6.8. For the same number of pulses as the original experiment, which required  $1.3 \times 10^{154}$  steps for a full nested phase cycle, a complete cogwheel phase cycle requires only 260 steps – still a large number, but with a reasonably short recycle delay (say 2 s), eminently feasible on the timescale of a week for a full 32 points in  $t_1$  and  $t_2$ . If the information that comes out of the experiment is sufficiently valuable, then a week of spectrometer time is a worthwhile sacrifice.

The use of cogwheel phase cycling gives another motivation for reducing the total number of pulses in the experiment; for each pulse that is removed, the total length of the phase cycle can be reduced by two, with the corresponding reduction in experiment time.

#### 6.2.5 Echo-antiecho

De Swiet used the States method [43] for obtaining the high dimensional data set without phase twist lineshapes. The phase cycling required in the States method to select the cosine or sine modulated components is trickier than that for the echo-antiecho component, since, in the States scheme, for each CTP that is allowed, its

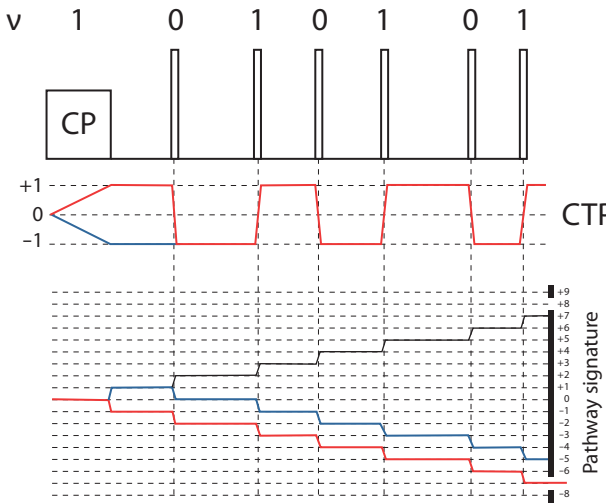


**Figure 6.8** Cogwheel phase cycling scheme for de Swiet experiment. Shown is the pulse sequence (top), with the winding number,  $v$ , for each pulse, and the desired CTP in red. The behaviour of  $\Lambda$  over the course of the pulse sequence is shown (bottom), for the desired pathway (red), its mirror image CTP (black) and an alternative wrong pathway (blue). The black bar at the right indicates the values of  $\Lambda$  that are let through the filter, for a 16 step phase cycle. No CTP is allowed other than the desired one.

mirror image must also be allowed. To let both through the phase cycle, the number of steps in the phase cycle must be equal to the separation in  $\Lambda$  (see Equation (2.118)) for the two pathways. However, for the optimised version and the original version, this is difficult since the separation between the two pathways increases with the number of pulses in the sequence. Thus the number of steps in the cogwheel phase cycle (which determines the spacing between allowed pathways) is different for each data point, and so the points would not easily be sampled evenly. With echo-antiecho this is not a problem as the CTP for the echo and antiecho are recorded separately. The number of steps in the cogwheel phase cycle can then be chosen to be just large enough to block out all unwanted CTPs for the data point requiring the most pulses; for all points requiring fewer pulses, the maximum separation between CTPs is smaller, and so all unwanted CTPs can still be blocked. This argument does not apply to the constant time version, since the number of pulses is constant.

Theoretically, four experiments need to be recorded to get the pure absorption lineshapes in three dimensions, since the  $t_1$  and  $t_2$  dimensions both need the echo-antiecho treatment independently. However, because of the known symmetry of the two-dimensional powder pattern, only the data set that has the real component in  $t_1$  and

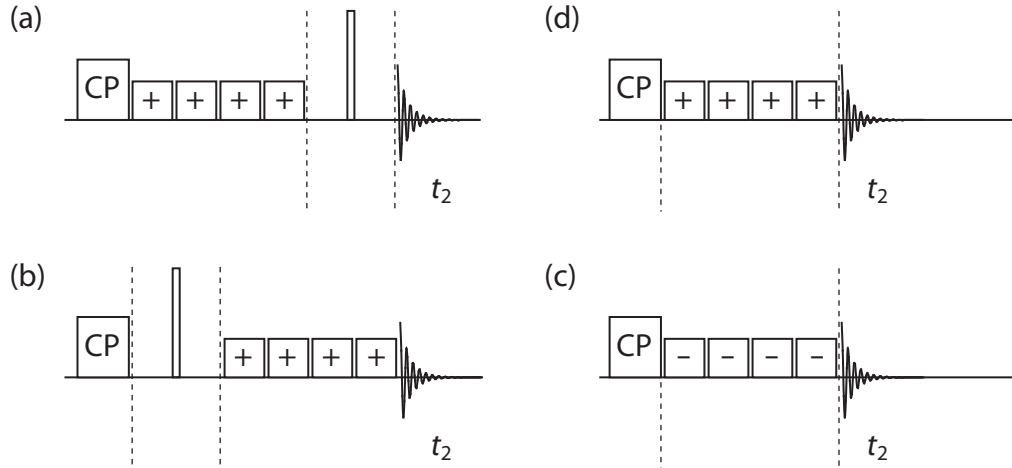


**Figure 6.9** Example pulse sequences for recording the echo (a), and antiecho (b), for the de Swiet experiment, using a spin-echo approach. The improved method switches the sign of the scaling factor of each pulse sequence block rather than the coherence that passes through it, giving the echo (c), and antiecho (d). A block containing a '+' indicates a six-pulse de Swiet block with positive  $\chi_a$ , and a block containing a '-' indicates a six-pulse de Swiet block with negative  $\chi_a$ . The new approach saves one pulse and two rotor cycles compared to the original.

$t_2$  is required. Using the States method this requires only one experiment, retaining the cosine-modulated component after  $t_1$  and  $t_2$ . Using the echo-antiecho, two data sets (those where  $t_1$  and  $t_2$  are both positive, or both negative) are required, which must be combined to give the doubly cosine-modulated data set.

The most basic implementation of the echo-antiecho involves placing a spin-echo either before or after the rest of the pulse sequence to obtain the antiecho and echo respectively (Figure 6.9). The spin-echo changes the sign of the coherence, but does not allow any evolution under either isotropic or anisotropic chemical shift Hamiltonians. If the spin-echo is before the main body of the pulse sequence, the coherence order at the start of the CSA recoupling is opposite to the coherence order at the start of CSA recoupling when the spin-echo is after the main body. The CTP through the CSA recoupling sequence is inverted between these two cases, and so the evolution in one case will be in the opposite sense to evolution in the other case. This makes up the echo and antiecho.

However, using the flexibility in  $\chi_a$  with five or six-pulse unit blocks, the echo and antiecho can be set up in a different, more efficient manner (Figure 6.9). The antiecho, with the direction of evolution reversed compared to the echo, can easily be

constructed by switching the sign of  $\chi_a$  of every block in the pulse sequence for the echo. The CTP then does not have to be altered, and the spin-echo can therefore be omitted.

The advantages of this technique over the inclusion of the spin-echo are that there is one fewer pulse, and the pulse sequence is one rotor cycle shorter, so there is less time for relaxation. One small problem is that for the evolution under  $C_1 + C_2$  recoupling, no solutions have been found for large negative  $\chi_a$  when there are six pulses in three rotor periods. This restriction necessitates the use of six pulses in one rotor period (for which the range of negative  $\chi_a$  is equal to the range of positive  $\chi_a$ ), and loses the advantage of the larger (positive)  $\chi_a$  available with the six pulses in three rotor periods pulse sequence units.

#### 6.2.6 Ultra-optimised version

Whilst the flexibility in  $\chi_a$  for five and six  $\pi$ -pulse units has been put to good use in the constant time and optimised versions of MAS-CSA and the de Swiet experiment, there are some features of the original four  $\pi$ -pulse units that make them attractive. The four  $\pi$ -pulse units recouple CSA with  $\chi_a = 0.393$ , whereas the five and six  $\pi$ -pulse units require more pulses and only have smaller or equal scaling factors available ( $\chi_a \leq 0.393$ ). Additionally, the pulses in the four  $\pi$ -pulse units are evenly spread throughout the rotor period, whereas with five and six  $\pi$ -pulse units, the pulses can be very close together (particularly at the outer limits of the range of scaling factors, see Figure 6.7), which causes problems since the pulses have a finite width. Ideally we would like to use the beneficial properties of the four  $\pi$ -pulse units, whilst retaining the flexibility in  $\chi_a$  provided by the five and six  $\pi$ -pulse units, which is the motivation behind this ‘ultra’-optimised version.

Consider the previous optimised version of the pulse sequence that recouples  $S_1 - S_2$ . In it, to obtain an effective  $t_2$  time,  $t_{2,\text{eff}}$ ,  $n$  pulse sequence units (each with five  $\pi$ -pulses) are used with a scaling factor,  $\chi_a$ , so that:

$$t_{2,\text{eff}} = \chi_a n \tau_R. \quad (6.20)$$

In the ultra-optimised version, the same  $t_{2,\text{eff}}$  value is obtained using as many four  $\pi$ -pulse blocks with  $\chi_a = 0.393$  as needed to get close to  $t_{2,\text{eff}}$ , then one five pulse unit tagged on the end, with the  $\chi_a$  chosen to exactly select  $t_{2,\text{eff}}$ . The  $t_{2,\text{eff}}$  time in this case

is given by:

$$t_{2,\text{eff}} = (0.393(n - 1) + \chi_a)\tau_R, \quad (6.21)$$

where  $n$  is the total number of pulse sequence units (which is unchanged from the optimised version), and  $\chi_a$  is the anisotropic scaling factor of the final five  $\pi$ -pulses block. This approach still has full control over the  $t_{2,\text{eff}}$  times, like the optimised version, but requires  $(n - 1)$  fewer pulses.

Another advantage of this relates to the  $\chi_a$  required for the longest  $t_{2,\text{eff}}$  point recorded. It is this point that determines the maximum number of pulses in any one  $t_2$  slice, and thus the total number of phase cycle steps for all  $t_2$  points (since all points must be recorded by the same number of scans). It is common to try and set this point with  $\chi_a$  as close to 0.393 as possible, to get the maximum  $t_{2,\text{eff}}$  possible without having to introduce another pulse sequence unit, with the extra pulses and therefore steps in the phase cycle that this entails. However, the five pulse sequences with  $\chi_a$  approaching 0.393 suffer from pulses becoming close together, and so the finite pulse width becomes problematic. With the mixed four and five-pulse units, this problem is reduced, since the pulses in the four-pulse units are more evenly distributed, and also since  $\chi_a$  for the four-pulse unit is exactly the maximum possible every time, so the same  $t_{2,\text{eff}}$  can be achieved with the  $\chi_a$  for the five-pulse unit can be reduced away from the maximum, which spreads the pulses out more.

In fact, anywhere  $t_{2,\text{eff}}$  is just less than a multiple of  $0.393\tau_R$ , this new approach is beneficial. Rather than pushing  $\chi_a$  for the five-pulse sequence too close to 0.393, it is better to use four-pulse units (which for this  $\chi_a$  have reasonably well-spaced pulses) plus a single five-pulse unit with smaller  $\chi_a$ , which, compared with the five-pulse units with  $\chi_a$  closer to 0.393, has more widely-spaced pulses. Another option for such situations is to get the same  $t_{2,\text{eff}}$  by adding one extra four-pulse unit than is required, so  $t_{2,\text{eff}}$  slightly overshoots the desired value, and then a five-pulse unit with a small negative  $\chi_a$  to compensate.

This same improvement can be applied to the pulse units that recouple  $C_1 + C_2$  that appear in the  $t_1$  evolution period. The saving in this case, replacing the six  $\pi$ -pulse units with four  $\pi$ -pulse units, is  $2(n - 1)$  fewer pulses. There is a slight difference here in that if the six  $\pi$ -pulses in three rotor cycles units are being used, then the maximum available  $\chi_a$  for these units is higher than the four  $\pi$ -pulse units, and so no advantage is served by using the four-pulse units (unless relaxation during the three rotor cycles

is a problem).

### 6.2.7 Improved constant time version

A similar improvement to that discussed in the previous section for the optimised version can be applied to the constant time version. Some of the five or six  $\pi$ -pulse units can again be replaced with four  $\pi$ -pulse units. However, there is an additional difficulty for improving the constant time version which needs to be addressed. In order to generate small  $t_{1,\text{eff}}$  or  $t_{2,\text{eff}}$ , some of the four  $\pi$ -pulse units must be arranged so that their evolution cancels that of other four-pulse units, as the only scaling factor available is  $\chi_a = 0.393$

The solution to this (with regards recoupling  $S_1 - S_2$ ) is to place an odd number of five  $\pi$ -pulse units in between an even number of four  $\pi$ -pulse units. This way, the five-pulse unit(s) switch the sign of the evolving coherence, so the evolution through the second group of four-pulse units is in the opposite sense to the evolution through the first group of four-pulse units. For larger values of  $t_{2,\text{eff}}$ , the four-pulse blocks are placed asymmetrically, so that the evolution through the four-pulse units does not cancel entirely. For the very largest  $t_{2,\text{eff}}$  values, all the four-pulse units appear on the same side of the five-pulse unit(s), so there is no cancellation.

To make this a little clearer, Table 6.1 shows how the ordering of pulse sequence units should change for different  $t_{2,\text{eff}}$ , using six four-pulse units and three five-pulse units<sup>†</sup>. Note how there are redundancies; some values of  $t_{2,\text{eff}}$  are covered by two arrangements of pulses. This allows the large values of  $\chi_a$  for the five-pulse unit to be avoided for all but the very longest  $t_{2,\text{eff}}$  times.

For the pulse blocks that recouple  $C_1 + C_2$ , there are no five  $\pi$ -pulse units available, and so the same trick can not be repeated. The switching of the sign of the coherence in order to make the evolution under the four  $\pi$ -pulse units cancel for short  $t_{1,\text{eff}}$  must be achieved by inclusion of a spin-echo.

### 6.2.8 Diagonals

In order to record the data point,  $(t_1, t_2)$ , it has so far been necessary to recouple the  $C_1 + C_2$  terms of the Hamiltonian for time  $t_1$ , then the  $S_1 - S_2$  terms for time  $t_2$ .

---

<sup>†</sup>It has also been investigated as to whether further improvement could be made by omitting the final pulse of the four  $\pi$ -pulse units that recouple  $S_1 - S_2$ , and a pulse sequence constructed out of three and five-pulse units. The advantage this provided was minimal, so it was not taken further.

$t_{2,\text{eff}}$ range	1	2	3	4	5	6	7	8	9
$-9\chi_{a,\text{max}}\tau_R$ to $-6\chi_{a,\text{max}}\tau_R$	5(−)	5(+)	5(−)	4	4	4	4	4	4
$-7\chi_{a,\text{max}}\tau_R$ to $-4\chi_{a,\text{max}}\tau_R$	4	5(−)	5(+)	5(−)	4	4	4	4	4
$-5\chi_{a,\text{max}}\tau_R$ to $-2\chi_{a,\text{max}}\tau_R$	4	4	5(−)	5(+)	5(−)	4	4	4	4
$-3\chi_{a,\text{max}}\tau_R$ to 0	4	4	4	5(−)	5(+)	5(−)	4	4	4
0 to $3\chi_{a,\text{max}}\tau_R$	4	4	4	5(+)	5(−)	5(+)	4	4	4
$2\chi_{a,\text{max}}\tau_R$ to $5\chi_{a,\text{max}}\tau_R$	4	4	4	4	5(+)	5(−)	5(+)	4	4
$4\chi_{a,\text{max}}\tau_R$ to $7\chi_{a,\text{max}}\tau_R$	4	4	4	4	4	5(+)	5(−)	5(+)	4
$6\chi_{a,\text{max}}\tau_R$ to $9\chi_{a,\text{max}}\tau_R$	4	4	4	4	4	4	5(+)	5(−)	5(+)

**Table 6.1** The sequencing of pulse sequence units for the improved constant time version, for  $t_2$  evolution of the de Swiet experiment, using nine blocks in total. The numbers in the table represent whether each block should be a four-pulse unit, ‘4’, a five-pulse unit with positive  $\chi_a$ , ‘5(+)’, or a five-pulse unit with negative  $\chi_a$ , ‘5(−)’. The range of  $t_{2,\text{eff}}$  that can be obtained with each arrangement is given in the left hand column, and is related to the maximum value of  $\chi_a$ , which is 0.393, and the rotor period,  $\tau_R$ . The total number of pulses is 39. Remember that after every five-pulse unit, the sign of the coherence is switched, so the evolution during the following block is reversed.

An alternative to this, that de Swiet himself suggests but does not investigate further, is to recouple the Hamiltonian,  $\hat{\mathcal{H}} \propto (\cos \phi(C_1 + C_2) + \sin \phi(S_1 - S_2))\hat{I}_z$ , for a time,  $t = \sqrt{t_1^2 + t_2^2}$ , where  $\phi = \tan^{-1}(t_2/t_1)$ .

It turns out that this ‘diagonal’ Hamiltonian, parallel to a vector at an angle  $\phi$  in the  $\hat{\mathbf{n}}^{(x)}-\hat{\mathbf{n}}^{(y)}$  plane, can be recoupled with four  $\pi$ -pulse units with an anisotropic scaling factor of  $\chi_a = 0.393$ , or five  $\pi$ -pulse units, with anisotropic scaling factors available between  $-0.393 < \chi_a < 0.393$ . This is the same range as is available for recoupling  $C_1 + C_2$  (parallel to  $\hat{\mathbf{n}}^{(x)}$ ) and  $S_1 - S_2$  (parallel to  $\hat{\mathbf{n}}^{(y)}$ ).<sup>‡</sup>

Now if you imagine trying to ‘walk’ to an arbitrary point in  $(t_1, t_2)$  space, the size of the steps you can take in any direction is the same, and you need to get to the point in as few steps as possible. It is obvious that, rather than taking a number of steps,  $i$ , along the  $t_1$  direction, followed by a number of steps,  $j$ , along  $t_2$ , a quicker way of getting to the given point would be stepping directly towards it (i.e. along a diagonal). Thus, rather than recording a  $(t_1, t_2)$  data point by applying  $i$  blocks of  $C_1 + C_2$  recoupling sequence followed by  $j$  blocks of  $S_1 - S_2$  recoupling sequence, one can apply  $k$  blocks of the diagonal recoupling sequence. Since  $k^2 = i^2 + j^2$ , then  $k < i + j$ , then a shorter pulse sequence is required. Figure 6.10(a) indicates where advantage can be taken of diagonal Hamiltonian recoupling sequences.

<sup>‡</sup>Excluding for now the possibility of six  $\pi$ -pulse units in three rotor cycles for recoupling  $C_1 + C_2$ .

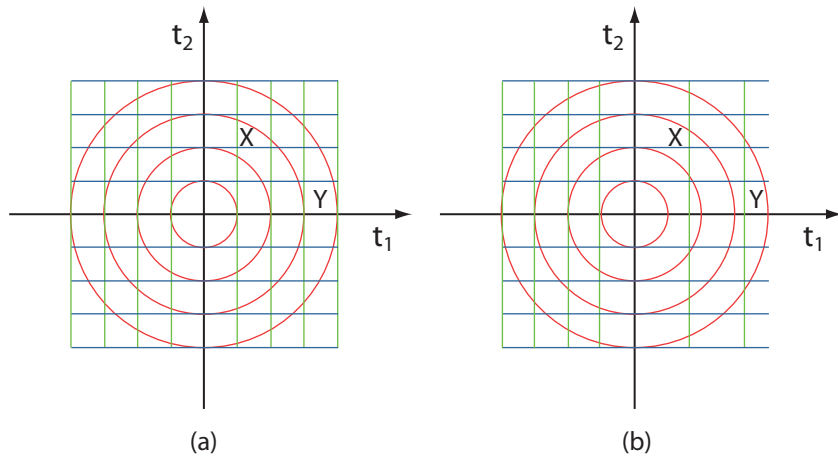


**Figure 6.10** Diagrams to show the number of pulse sequence units required to record a point at  $(t_1, t_2)$  using the recoupling diagonal Hamiltonians or separate  $t_1$  and  $t_2$  evolutions. The red, green and blue lines indicate the maximum step size in each direction. To work out the number of pulse sequence units required to measure any point using the diagonal Hamiltonians, each red contour that is passed between the origin and the  $(t_1, t_2)$  point necessitates an extra pulse block, recoupling the diagonal Hamiltonian. For X in (a), three pulse sequence units are required, whereas for Y, four pulse sequence units are needed. With separate  $t_1$  and  $t_2$  evolution periods, each time a green contour is crossed, an extra block of  $C_1 + C_2$  recoupling is added, whilst for every blue contour that is crossed, an extra block of  $S_1 - S_2$  recoupling is added. So X in (a) requires two blocks of  $C_1 + C_2$  and three blocks of  $S_1 - S_2$ , whilst Y requires four blocks of  $C_1 + C_2$  and one block of  $S_1 - S_2$ . In both cases, five blocks are required in total, which can be reduced using diagonal Hamiltonians. Diagram (b) includes the option of using six pulses in three rotor period blocks for  $t_1$  evolution, with the higher limit of  $\chi_a$  in the positive  $t_1$  region. X now requires one block of  $C_1 + C_2$  and three of  $S_1 - S_2$  (still beaten by the diagonal Hamiltonian), whilst Y requires two blocks of  $C_1 + C_2$  and one of  $S_1 - S_2$  (so three blocks in total, which is less than for the diagonal Hamiltonian).

By using six  $\pi$ -pulses in three rotor periods, the maximum step size in the  $t_1$  direction is larger, due to the larger  $\chi_a$  available for  $C_1 + C_2$  recoupling. This means that for  $(t_1, t_2)$  points close to the  $t_1$ -axis, it is better (requires fewer pulses) to use the six pulses in three rotor cycles sequence units for  $C_1 + C_2$ , followed by the normal five-pulse units for  $S_1 - S_2$ , rather than the diagonal units that are restricted to  $\chi_a < 0.393$ . This is demonstrated in Figure 6.10(b). It may be desirable, however, to have sequences with the same efficiency (i.e. number of pulses and rotor cycles) in  $t_1$  and  $t_2$ , which rules out the use of six  $\pi$ -pulses in three rotor periods to recouple  $C_1 + C_2$ , as it does not have an equivalent sequence that recouples  $S_1 - S_2$ .

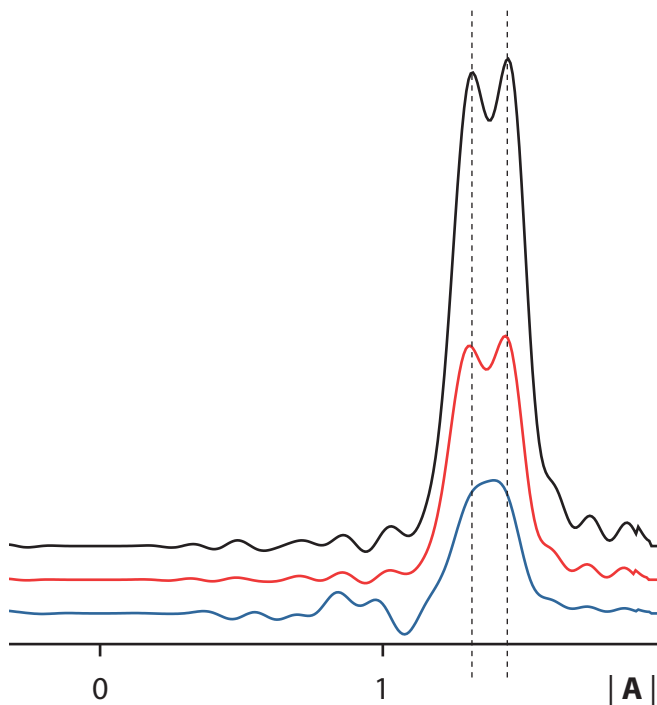


**Figure 6.11** Simulation of de Swiet experiment  $P(|\hat{\mathbf{A}}|)$  spectra with different number of projections: 3 (blue), 6 (red) and 12 (black). The angles of the projections are evenly distributed. The system has two components with  $|\hat{\mathbf{A}}| = 1.27$  and  $|\hat{\mathbf{A}}| = 1.38$ . Two resolved peaks are seen in the spectra with 6 and 12 projections (although in that with 6 projections, the positions of the peaks is slightly out), but 3 projections are insufficient to provide resolution here.

### 6.2.9 Recording projections

The full two-dimensional powder pattern itself is never actually used, as only the projections onto some vectors in the two-dimensional plane are required to construct  $P(|\hat{\mathbf{A}}|)$ . In practise, in this work, these projections are recorded directly as one-dimensional powder patterns.

Experiments were undertaken to determine what the minimum number of projections that should be recorded to obtain accurate peak positions in the  $P(|\hat{\mathbf{A}}|)$  spectrum. Figure 6.11 shows how the spectrum of  $P(|\hat{\mathbf{A}}|)$  changes with increasing number of projections. It shows that approximately six projections is sufficient to obtain an accurate measurement of the peak position.

The  $\phi$ -angles for the projections can be chosen so that the  $\sin 3\phi$  factor is included

in the sampling density, so a greater density of  $\phi$ -angles are taken where  $\sin 3\phi$  is large, and less where it is small. This avoids the use of a weighting factor and improves the sampling efficiency.

Additionally, the projections need only be measured within a  $30^\circ$  wedge. This is because, according to the symmetry of the two-dimensional powder pattern, for a projection on a vector at angle  $\phi$  with respect to the  $t_1$ -axis, there is an equivalent projection on a vector at angle  $\phi' \rightarrow -2\pi/3 - \phi$ . The projection on a vector is the mirror image of the projection on the reverse of the same vector (i.e. on a vector rotated  $180^\circ$  in the  $\hat{\mathbf{n}}^{(x)}-\hat{\mathbf{n}}^{(y)}$  plane). Therefore, the projection on the vector at angle  $\phi$  is the mirror image of the projection on the vector at angle  $\phi' \rightarrow \pi/3 - \phi$ . Thus projections on vectors with angles in the range  $30^\circ < \phi < 60^\circ$  are related to the reversed projections on vectors with angles in the range  $0^\circ < \phi < 30^\circ$ .

In fact the best wedge to record projections is that between  $30^\circ < \phi < 60^\circ$ . This is because the calculated five  $\pi$ -pulse timings for these pulse sequence units have the most evenly-spaced pulses. The five-pulse units with large  $\chi_a$  and  $\phi < 30^\circ$  have a pulse that is very late in the rotor cycle, and so, the finite width of this pulse means that it finishes somewhere in the beginning of the next block, which causes problems with pulse programming and with the start of the acquisition.

#### 6.2.10 Summary of improvements

Each of the sections above details a small improvement that can be made to the implementation of the de Swiet experiment. With a combination of these suggestions, the sensitivity can be increased and the effects of linebroadening and pulse errors reduced. The effects of each are summarised in Table 6.2.

By combining some of these improvements, a difference can be made that will improve the de Swiet experiment significantly, so that it may find more widespread use in the future. For example, using the ultra-optimised version, combined with diagonal Hamiltonians, the maximum number of pulses for any  $(t_1, t_2)$  point is reduced from 256 (for a  $32 \times 32$  experiment by the original method) to sixty-five<sup>§</sup>. With cogwheel phase cycling included as well, some of the pulse errors for these 65 pulses will be compensated for, resulting in a much improved lineshape.

---

<sup>§</sup>Calculated for  $\chi_{a,\text{opt}} = 0.2$ . The maximum number of pulses for the ultra-optimised version depends upon  $\chi_{a,\text{opt}}$ ; the smaller  $\chi_{a,\text{opt}}$ , the fewer pulses required.

Improvement	Effects
<b>Constant time:</b> select $(t_1, t_2)$ by fixing $n$ and varying $\chi_a$ .	Removes the effects of linebroadening, at expense of signal intensity.
<b>Optimised:</b> select $(t_1, t_2)$ by varying both $n$ and $\chi_a$ , choosing minimum $n$ for each point.	With $\chi_{a,\text{opt}} < 0.2$ , significantly improves lineshapes compared to original de Swiet experiment, and sensitivity compared to constant time version.
<b>Five <math>\pi</math>-pulse units:</b> remove final pulse from the six-pulse units that recouple $S_1 - S_2$ in $t_2$ .	Number of pulses decreases by one sixth, reducing effects of pulse errors.
<b>Cogwheel phase cycling.</b>	Number of steps in full phase cycle reduced. Enables full phase cycle to be completed in realistic timescale, removing effects of pulse errors.
<b>Echo-antiecho acquisition.</b>	No genuine advantage on its own, but works well with cogwheel phase cycle.
<b>Ultra-optimised version:</b> same as optimised version, except uses four $\pi$ -pulse units, with their fixed $\chi_a$ for all but the final unit, which is a five $\pi$ -pulse unit with flexibility in $\chi_a$ .	Reduces number of pulses by $n - 1$ . Reduces problems with finite pulse widths, as pulses are more evenly spread in the rotor cycle.
<b>Improved constant time version:</b> uses mixture of four and five-pulse units in the constant time version.	Similar to ultra-optimised version. More tricky to implement, however, particularly for recoupling $C_1 + C_2$ .
<b>Diagonals:</b> use pulse sequence units that recouple a mixture of $C_1 + C_2$ and $S_1 - S_2$ .	A particular $(t_1, t_2)$ point can be recorded with fewer pulse sequence units. The number of pulses and rotor cycles is reduced, improving signal-to-noise and reducing pulse errors.
<b>Recording projections:</b> as opposed to recording the full two-dimensional powder pattern.	The minimum number of projections is recorded that gives an accurate $P(\hat{\mathbf{A}})$ spectrum.

**Table 6.2** Summary of the improvements to the de Swiet experiment, and their effects on the resulting spectrum.

### 6.3 Simulated examples

De Swiet spectra were simulated for a signal with a particular CST (typical of one of the bis-phosphonates experimented upon in Chapter 7). Randomly distributed Gaussian noise was added at various noise levels prior to the de Swiet transform, to see how the transform handles noise (Figure 6.12). Noise appears to have most severe effects at large  $|\hat{\mathbf{A}}|$ , owing to the  $z^2 \frac{d}{dz^2}$  term in Equation (6.19). Additionally, at high noise levels, the peak appears weaker (and possibly broader) as well as the noise level appearing higher; perhaps this is because the noise hides the features of the projected powder patterns, so the first and second derivatives in Equation (6.19) do not pick out

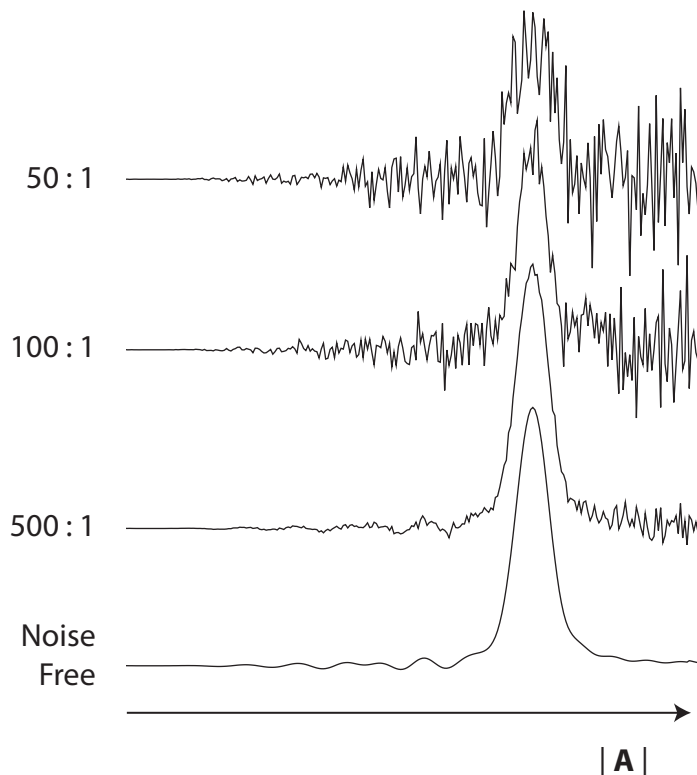


**Figure 6.12** Simulated de Swiet spectra of  $P(|\hat{\mathbf{A}}|)$ , with randomly generated noise with signal-to-noise ratios of 500:1, 100:1 and 50:1, added to the simulated spectrum prior to the de Swiet calculation. The bottom spectrum contains no added noise, but still contains some wiggles caused by incomplete sampling.

these features so successfully. So the de Swiet experiment is sensitive to noise, and as much effort should be made as practicable to reduce this. The apparent noise can be reduced by applying a smoothing function to the first and second derivatives, at the expense of resolution.

Figure 6.13 shows the effect of having more than one component in the spectrum, with different  $|\hat{\mathbf{A}}|$ . This shows that, even with a large number of overlapped components, the peaks in the  $P(|\hat{\mathbf{A}}|)$  spectrum can still easily be seen. The CSA differences between the signals in the figure is about 10%, so, even with only two components, the sideband–sideband correlation method would struggle to find accurate chemical shift parameters, and with four components it would most certainly fail. With two components, the sideband–powder correlation method may succeed (depending on whether the principal values are resolved), but with four components it too will

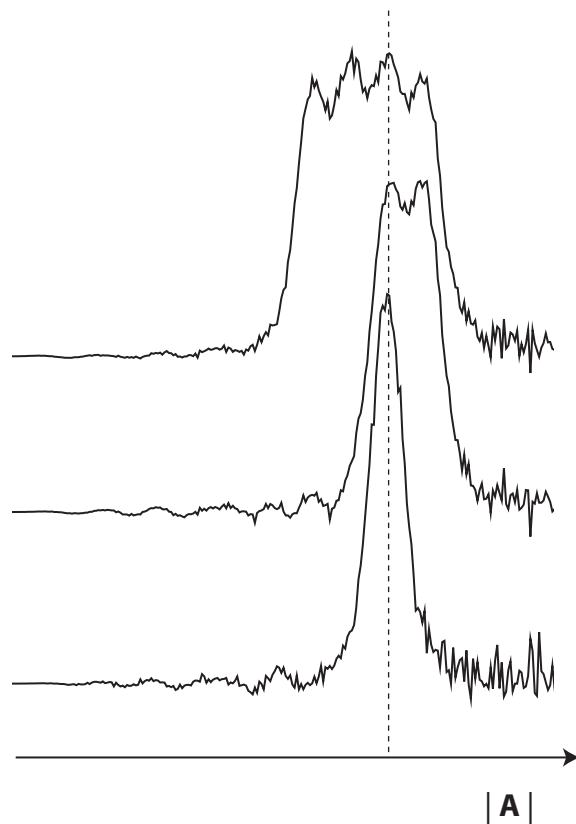


**Figure 6.13** Simulated de Swiet spectra of  $P(|\hat{A}|)$ , with one, two and four signals sharing the same isotropic shift, and with  $|\hat{A}|$  values of 0.8, 0.9, 1.0 and 1.1.

certainly fail. The de Swiet method is superior therefore where there is multiple overlap.

How close two signals can be in terms of  $|\hat{A}|$  before they are indistinguishable by the de Swiet experiment depends upon the linewidths of the peaks in the  $P(|\hat{A}|)$  spectrum. The linewidths in turn depend upon a number of experimental and analytical parameters. Sharp powder pattern projections will lead to a sharp transformed  $P(|\hat{A}|)$  spectrum, but will most likely suffer from noise and artefacts.

#### 6.4 Experimental examples

Two examples from previous chapters are repeated here to demonstrate experimentally the value of the de Swiet experiment. Firstly, the  $^{13}\text{C}$  spectrum of FAME (see Chapter 4) is used, where all signals are resolved and have had their CSA measured,

	de Swiet	Sideband fit
$\delta_{\text{iso}} / \text{ppm}$	$ \hat{\mathbf{A}}  / \text{ppm}$	$ \hat{\mathbf{A}}  / \text{ppm}$
14.8	22	17 – 19
61.6	60	54 – 56
133.6	133	128 – 134
136.2	138	136 – 142
165.5	107	106 – 109
171.6	97	95 – 98

**Table 6.3** Values of  $|\hat{\mathbf{A}}|$  for  $^{13}\text{C}$  sites in FAME as determined from the de Swiet experiment, and the range of values given the  $\zeta$  and  $\eta$  values determined by fitting sideband patterns and sideband–sideband correlation patterns, given in Tables 4.1 and 4.2.

both by fitting a sideband–sideband correlation pattern, and one-dimensional sideband patterns. Secondly, the  $^{31}\text{P}$  spectrum of pamidronate (see Chapter 5) is used, which has genuinely overlapping signals that had their CSAs determined by fitting a sideband–powder correlation pattern. The de Swiet experiment may prove to be a useful independent check of the CSA values measured for pamidronate.

#### 6.4.1 Fumaric acid monoethyl ester

The  $^{13}\text{C}$  de Swiet spectrum of FAME was used to determine values for  $|\hat{\mathbf{A}}|$  for the six  $^{13}\text{C}$  environments, which are given in Table 6.3 alongside values calculated from the  $\zeta$  and  $\eta$  values determined from fitting the sideband patterns in Section 4.3. Except for the methyl and methylene groups, the results are an excellent match with previous results. The inaccuracies in the methyl and methylene groups are caused by the experimental set-up, in particular the spectral width, which was optimised for the signals with the largest CSAs.

The  $^{13}\text{C}$  signals in FAME are well-resolved by their isotropic shifts. However, if the peaks for all the signals are summed, prior to the inverse Radon transform, this is equivalent to removing the resolution by isotropic shift and provides a test of resolution by  $|\hat{\mathbf{A}}|$ . The  $P(|\hat{\mathbf{A}}|)$  spectrum for this is shown in Figure 6.14, which shows that four out of six signals are resolved. The difference in  $|\hat{\mathbf{A}}|$  must be somewhat greater than 10 ppm to achieve resolution by CSA.

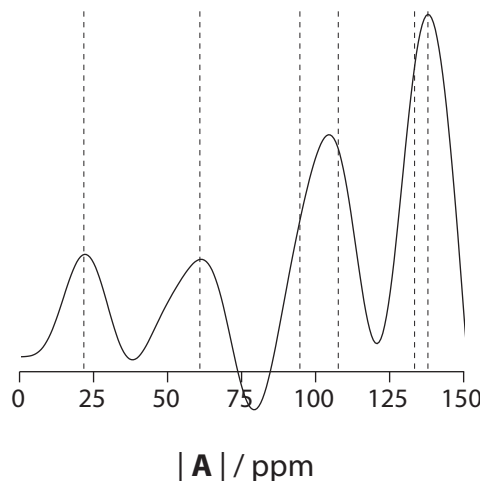


**Figure 6.14** Experimental  $^{13}\text{C}$  de Swiet spectrum of FAME, recorded using the ultra-optimised version. The six  $^{13}\text{C}$  environments are deliberately overlapped by summing their powder patterns prior to the inverse Radon transform. The dashed lines show the positions of the peaks when the peaks are not overlapped.

#### 6.4.2 Pamidronate

The chemical shift parameters for the two  $^{31}\text{P}$  environments in pamidronate, determined from overlapping powder patterns, were given in Table 5.3. The spectrum of  $P(|\hat{\mathbf{A}}|)$  for pamidronate was recorded using the ultra-optimised version of the de Swiet experiment, and is shown in Figure 6.15. The particular experimental details can be found in Section 6.5.

Figure 6.15 shows, as expected, two peaks, indicating, without the need for further calculation or model fitting, that there are two chemical environments present. The values of  $|\hat{\mathbf{A}}|$  for these sites, are 88.4 ppm and 116.7 ppm. Using the chemical shift parameters determined from the static spectrum in Table 5.3, the expected values of these parameters are 84.1 ppm and 117.4 ppm. Using the chemical shift parameters determined from the sideband–powder correlation pattern, also in Table 5.3, the expected values of these parameters are 85.4 ppm and 115.7 ppm.

The values for  $|\hat{\mathbf{A}}|$  found for this study are within the error estimates for the component with the larger CSA, but out by a few ppm for the component with the smaller CSA. This difference may be partially accounted for in the uncertainty in the position of the maximum of the  $P(|\hat{\mathbf{A}}|)$  spectrum, which is about  $\pm 2$  ppm.

In order to calculate  $\zeta$  and  $\eta$  separately, a more challenging de Swiet experiment

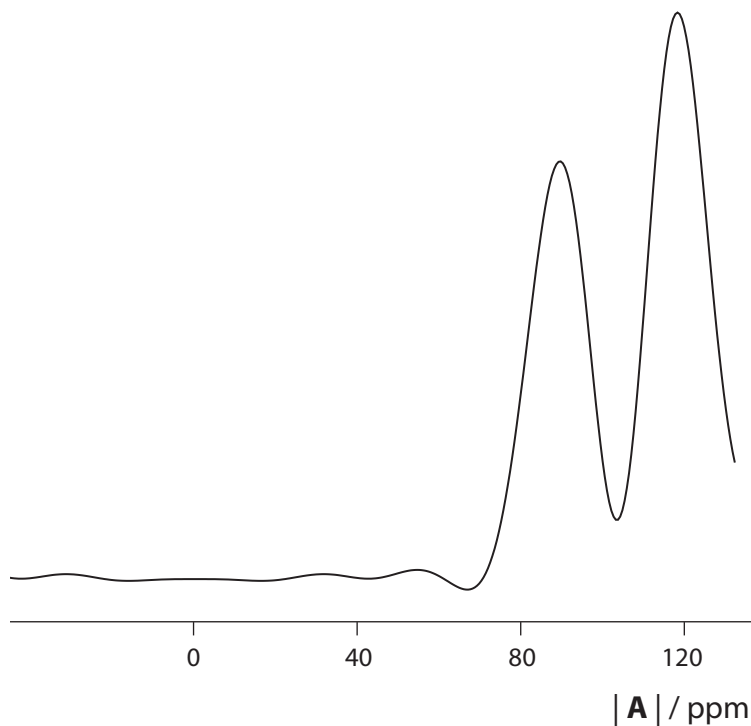


**Figure 6.15** Experimental  $^{31}\text{P}$  de Swiet spectrum of pamidronate.

is required, where the full two-dimensional powder pattern must be recorded. This is likely to be extremely time consuming. However, since the parameter,  $\zeta \sqrt{(3 + \eta^2)/2}$ , has been measured, it could be used as a constraint in the fitting of the conventional powder pattern in Chapter 5. So, rather than fitting five parameters (two anisotropies, two asymmetries and the intensity ratio of the two signals), now only three parameters are required, since the asymmetry and anisotropy are no longer independent. The projection onto the  $\hat{\mathbf{n}}^{(x)}$ -axis (i.e. the conventional powder pattern) can be used for this purpose, as can any of the other projections in the  $\hat{\mathbf{n}}^{(x)}-\hat{\mathbf{n}}^{(y)}$  plane. It can be shown that, alone, the projection onto the  $\hat{\mathbf{n}}^{(x)}$ -axis is best for determining the chemical shift parameters (since, for example, the projection onto the  $\hat{\mathbf{n}}^{(y)}$ -axis is symmetrical about  $\omega = 0$ , and so some of the spectral width is wasted as it does not provide additional information to aid the fitting). However, the  $\hat{\mathbf{n}}^{(x)}$ -projection is not normally recorded in a de Swiet experiment, since the weighting factor of  $\sin 3\phi$  eliminates it from the

inverse Radon transform.

Rather than recording extra data, the projections that have been acquired can be recycled in this fitting process. In this case, the projection on the  $\hat{\mathbf{n}}^{(x)}$ -axis has already been recorded in the previous chapter, so this can be included as well. The best fit chemical shift parameters found using the constraints from the de Swiet  $P(|\hat{\mathbf{A}}|)$  spectrum were:

$$\zeta_1 = 71.4 \text{ ppm}, \eta_1 = 0.26, \zeta_2 = -82.5 \text{ ppm}, \eta_2 = 1.00,$$

with an intensity ratio of 1.2:1. The values found previously from the static spectrum without constraints were:

$$\zeta_1 = 68.0 \text{ ppm}, \eta_1 = 0.24, \zeta_2 = -83.2 \text{ ppm}, \eta_2 = 0.99,$$

with an intensity ratio of 1.0:1. The appearance of the projections onto the  $\hat{\mathbf{n}}^{(x)}$ -axis are compared in Figure 6.16.

Note though, that this procedure for recovering  $\zeta$  and  $\eta$  has reverted to model fitting, with the problems that this brings. Although the number of components is no longer a problem, the distribution of  $\zeta$  and  $\eta$  is unknown. For instance, if the de Swiet experiment shows a component within a range of  $|\hat{\mathbf{A}}|$ , the variation could be entirely caused by variation in  $\zeta$ , by variation in  $\eta$ , by some coherent variation of  $\zeta$  and  $\eta$  at the same time, or by a random incoherent distribution of both parameters.

## 6.5 Experimental procedure

The  $^{31}\text{P}$  ultra-optimised de Swiet experiment of pamidronate was recorded as five two-dimensional experiments, recording projections onto unit vectors at angles of  $\phi = 31.9^\circ, 35.8^\circ, 40.0^\circ, 44.8^\circ$  and  $51.4^\circ$ . Pulse timings were calculated to recouple diagonal Hamiltonians,  $\hat{\mathcal{H}} = (\cos \phi(C_1 + C_2) + \sin \phi(S_1 - S_2))\hat{I}_z$ , for each  $\phi$ -angle, for both four-pulse sequences with  $\chi_a = 0.393$  and for five-pulse sequences with a range of  $\chi_a$ . The MAS rate was 6470 Hz, and the overall scaling factor for the experiment was 0.1797, giving an indirect dimension spectral width of 36 kHz. The largest number of pulse sequence units was seven, leading to a phase cycle of 64 steps. Fifteen complex data points were recorded in  $t_1$ , with 64 scans per point. The spectra were zero-filled out to 512 points, and relatively severe linebroadening was applied (since noise features are amplified by the inverse Radon transform). Otherwise, experimental

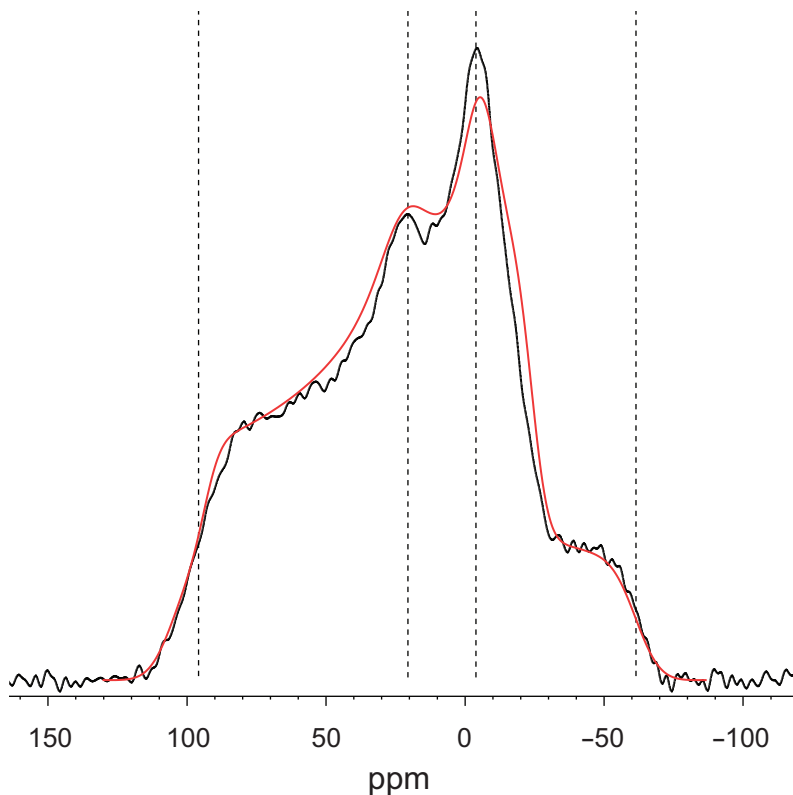


**Figure 6.16** Simulated best fit lineshape (red) of the experimental pamidronate  $^{31}\text{P}$  powder pattern lineshape (black), constraining the parameters to the values found for  $|\hat{\mathbf{A}}|$  found from Figure 6.15. The absolute best fit is shown in Figure 5.5. Both look like equally plausible fits to the powder pattern, although the parameters for each differ by more than the error estimates.

details are identical to the  $^{31}\text{P}$  MAS-CSA experiments of the previous chapter. In total, the experiment took approximately 35 hours.

The inverse Radon transform was applied to the data using Equation (6.16), to obtain the spectrum of  $P(|\hat{\mathbf{A}}|)$ . The scale on the resulting spectrum must be multiplied by  $\sqrt{3}/2$  to account for the factor of  $\sqrt{2/3}$  in Equation (2.69).

For neridronate, the projection onto the  $\hat{\mathbf{n}}^{(y)}$ -axis has been recorded for the original, constant time and optimised versions. Experimental parameters were the same as for pamidronate except: the actual spinning rate was 5750 Hz; (b) the indirect dimension spectral width was 32 kHz; (c) the number of scans per point was different for each experiment, due to different phase cycle lengths, within the range of 150–160 scans per point.

The  $^{13}\text{C}$  ultra-optimised de Swiet experiment of FAME was recorded as five two-

dimensional experiments, recording the same angled projections as the pamidronate experiment. The MAS rate was 4672 Hz, and the overall scaling factor for the experiment was 0.1797, giving an indirect dimension spectral width of 26 kHz. The largest number of pulse sequence units was seven, leading to a phase cycle of 64 steps. Fifteen complex data points were recorded in  $t_1$ , with 128 scans per point. The  $^{13}\text{C}$   $\pi$ -pulse length was  $6.0\ \mu\text{s}$ , and the CP contact time was 2.5 ms. The spectra were zero-filled out to 512 points, and relatively severe linebroadening was applied. In total, the experiment took approximately 42 hours.

### 6.5.1 Numerical simulations

Numerical simulations of the de Swiet spectra were performed using a procedure written in the PV-Wave environment [157], in an almost identical fashion to that used to simulate sideband–powder correlation patterns. The evolution of the magnetisation vector under pseudo-static conditions in  $t_1$  followed by spinning conditions in  $t_2$  was calculated and summed for 700  $\alpha$  and  $\beta$  angles generated by the REPULSION algorithm [34] and 96 evenly-spaced  $\gamma$  angles, to produce a simulated free induction decay (FID). The simulated FID is line-broadened (choosing the amount of line-broadening applied to give a similar appearance to the experimental lineshapes by eye), and then Fourier transformed to give the two-dimensional correlation pattern.

## 6.6 Conclusions

The de Swiet experiment has been improved using a number of changes, that were detailed in Table 6.2. In particular, the ultra-optimised version, with diagonal Hamiltonians and cogwheel phase cycling has been tested on pamidronate and FAME with promising results. It is now possible, in a reasonable amount of time (much less than a week) to record enough projections to produce a useful spectrum of  $P(|\hat{\mathbf{A}}|)$ , from which the quantity,  $|\hat{\mathbf{A}}| = \zeta \sqrt{(3 + \eta^2)/2}$ , can be determined. This can then be used, if desired, as a constraint for  $\zeta$  and  $\eta$  in fitting a sideband or powder pattern.

The de Swiet method is superior to model fitting in many ways. First of all, no assumptions are required about the number of components in the spectrum. In the  $P(|\hat{\mathbf{A}}|)$  spectrum, multiple components appear as separate peaks, unless they share the same value of  $|\hat{\mathbf{A}}|$  as well as isotropic chemical shift. Additionally, the de Swiet experiment gives a clear indication of the accuracy and reliability of the results it gives,

from the noise level and linewidths of the peaks in the  $P(\hat{\mathbf{A}})$  spectrum.

The de Swiet experiment (particularly the ultra-optimised version), may now hopefully find uses as an alternative to fitting of sideband or powder patterns for determining CSA. In order to avoid model fitting completely, the more complicated, two-dimensional de Swiet transform of the full two-dimensional powder pattern is required [95]. The investigation of the optimal procedure for this advance de Swiet experiment is left as a subject for further study.

## **Chapter 7**

---

# **Application to bis-phosphonates bound to bone-mineral**

---

To conclude this thesis, the techniques that have been developed in the previous three chapters, shall be used, in conjunction with other NMR techniques and non-NMR techniques, such as PXRD, to see what can be achieved in a real-life, difficult, structural problem. What are the practical limits of these techniques? Where is there room for further development?

The example chosen to showcase the techniques is a series of small molecule drugs, called bis-phosphonates. Bis-phosphonates are characterised by having two phosphonate groups attached to a single carbon atom, and are now the world-leading treatment for degenerative bone diseases such as osteoporosis. Additionally, owing to their propensity for binding to bone mineral, they are used to carry radioisotopes to bone for imaging and therapy, and they are currently being investigated as vehicles for bone-targetting of antibacterials or antineoplastics [164]. This is a particularly hopeful example for study by NMR because of the presence of two phosphorus atoms;  $^{31}\text{P}$  has 100% natural abundance and has high  $\gamma$  (gyromagnetic ratio).

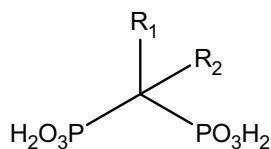


**Figure 7.1** Generalised structure of a bis-phosphonate drug molecule.

## 7.1 Bis-phosphonates

Bis-phosphonates were first studied as calcification inhibitors, mimicking the body's own pyrophosphate in binding strongly to bone and preventing crystal growth [165]. However, their value to clinical medicine was realised later when it was discovered that bis-phosphonates could also inhibit bone resorption [166]. The generalised structure of a bis-phosphonate is shown in Figure 7.1. The central carbon atom is joined to two phosphonate groups: this is the key feature of a bis-phosphonate, and any alteration to this moiety dramatically reduces the drug's bone mineral binding affinity and potency [167].

The nature of  $R_1$  and  $R_2$  affect the biological activity of the bis-phosphonate. One of the groups,  $R_1$ , is usually a small polar group, such as  $-OH$  or  $-NH_2$ . A wide variety of  $R_2$  group variants has been tested for potency as bone resorption inhibitors. Figure 7.2 shows a selection of bis-phosphonates that have been approved for clinical use.

The fact that these molecules bind strongly to bone has considerable pharmacological advantages because it limits side effects caused by action of the drug in other parts of the body. It also means that the release of adsorbed drug from the bone surface is slow, improving the persistence of the drug *in vivo*, thereby prolonging its action and reducing the frequency of repeat treatments. The strength of the binding is largely attributed to the two phosphonate groups and the  $R_1$  group with calcium ions in bone mineral [168], although the  $R_2$  group also has an effect on binding [169].

There are other factors that affect the binding of bis-phosphonates. The surface of bone can become saturated with bis-phosphonate; the total binding capacity of a particular bis-phosphonate does not appear to be related to the binding affinity [170]. Also, bis-phosphonates tend to localise in regions of bone deposition or bone resorption, with different bis-phosphonates distributing themselves differently between the two regions [171].

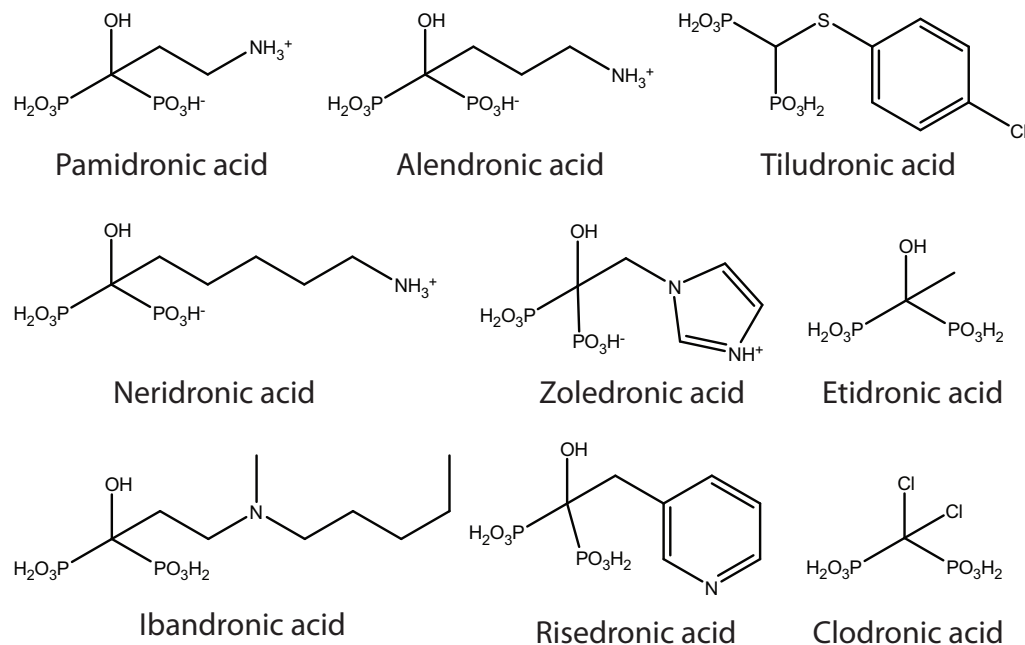


**Figure 7.2** Structures of the nine bis-phosphonates (in their free acid form) that are currently, or have been in the past, used for medicinal purposes. The first five (pamidronate, alendronate, tiludronate, neridronate and zoledronate) were used in this study.

However, simply binding to the bone mineral does not in itself bring about a significant protection of the bone from demineralisation. The second function of a bis-phosphonate drug is to interfere with the osteoclasts, the cells responsible for bone resorption. Nitrogen-containing bis-phosphonates achieve this by the inhibition of the enzyme farnesyl diphosphate synthase (FPPS) [172], an important enzyme in the functioning of osteoclasts, and can cause osteoclast apoptosis [173]. This pharmacological action by modulating local cellular activities is strongly dependent on the nature of the  $R_2$  group [174], although also influenced by  $R_1$  [175]. Other bis-phosphonates (those which do not contain a nitrogen atom) act in a slightly different way, being incorporated into an adenosine triphosphate (ATP) analogue, which also prevents the functioning of osteoclasts, albeit less effectively than FPPS inhibition [176].

There is another beneficial effect of bis-phosphonates *in vivo*: the protection from apoptosis of osteocytes (bone cells) and osteoblast (bone deposition cells). The mechanism for this is poorly understood [177]. The effectiveness of certain bis-phosphonates at protecting osteocytes has been measured and found to be somewhat

Bis-phosphonate	Binding affinity	FPPS inhibition	Medicinal uses
Pamidronate	Medium	Weak	Paget's disease, brittle bones
Alendronate	Strong	Medium	Osteoporosis
Neridronate	Weak	Weak	Uncommon
Zoledronate	Very strong	Very strong	Paget's disease, metastatic cancer
Tiludronate	Weak	None	Navicular syndrome in horses
Clodronate	Very weak	None	Antiquated
Etidronate	Weak	None	Calcification disorders
Risedronate	Medium	Strong	Osteoporosis
Ibandronate	Medium	Strong	Vertebral fractures

**Table 7.1** Summary of the properties and clinical uses of nine bis-phosphonates. The information is summarised from the references [181, 182], and should not be considered as a detailed clinical review of the different bis-phosphonates.

independent of the other effects [178].

Their properties as regards binding affinity towards bone and effectiveness at FPPS inhibition are summarised in Table 7.1. Both these properties influence the clinical uses of these drugs and the dosage required. For instance, alendronate and risedronate have very similar uses and dosages, although their profile is quite different; alendronate binds more strongly to bone and risedronate inhibits FPPS more strongly [179]. Some bis-phosphonates with relatively low binding affinity but effective osteoclast inhibition are still useful as clinical antiresorptioin drugs where it might be undesirable for the drug to remain *in vivo* for a long period, such as in children [180].

In designing new bis-phosphonate drugs, one needs to consider the effects of the choices of  $R_1$  and  $R_2$  groups on both the binding affinity to the bone mineral surface and on the pharmacological activity in inhibiting FPPS. It would be useful therefore to understand what specific structural features of  $R_1$  and  $R_2$  are important for giving rise to these properties. To this end, a number of recent studies have attempted to gain an insight into impact of three-dimensional bis-phosphonate conformation on the interactions of the various bis-phosphonate molecules with (i) the mineral surface of bone [183–186] and (ii) the enzyme, FPPS [187, 188]. It is the former of these, the interactions with the mineral surface of bone, that will be focused upon here.

One structural feature that has already been identified as being important in this respect, for example, is an optimum distance of a nitrogen atom in  $R_2$  from the

phosphonate head group in order to be well-positioned for strong hydrogen bonding with the phosphates or hydroxyls in the bone mineral surface [182]. This has identified alendronate as having the optimum distance and having strong binding, whereas binding is weaker for the similar pamidronate and neridronate, which differ only in the length of the carbon chains. Also important for the strength of this hydrogen-bonding is the partial charge on the amine nitrogen [169].

Mukherjee *et al.* [186] recently conducted a detailed study of isotopically labelled bis-phosphonates using the SS-NMR techniques, TEDOR [105], double cross-polarisation (DCP) [189] and <sup>2</sup>H quadrupole echo NMR [190]. They find that the *R*<sub>2</sub> sidechain of pamidronate is bent into a *gauche* conformation when bound to bone, such that NH<sub>3</sub><sup>+</sup> group is in contact with the mineral surface, presumably to attain additional electrostatic attractions to the surface. They also find that there is significant sidechain motion on the NMR timescale (although the bis-phosphonate headgroup is fixed). The nature of this motion is dependent on the exact identity of the bis-phosphonate in question, but could be hopping of the NH<sub>3</sub><sup>+</sup> between two binding sites on the bone surface (i.e. pamidronate), a crank-handle twisting of the carbon chain (i.e. alendronate) or a ring wobble (i.e. zoledronate).

The approaches used by these authors required custom synthesis of <sup>2</sup>H, <sup>13</sup>C and <sup>15</sup>N labelled bis-phosphonates, to a large extent in order to render the drug signals conspicuous against the background of signals from collagen and other bone matrix biopolymers. Powerful as they are, these approaches require specialist isotope synthesis skills and lengthen study timelines, neither of which is always acceptable to a drug discovery organisation, especially a small one. Also it precludes quick screening of a large range of compounds in systematic studies of structure-affinity relationships, as each member of a homologous series must be specifically synthesised in an isotopically enriched form.

By looking at <sup>31</sup>P-NMR, which has 100% natural abundance, and crucially has a different isotropic chemical shift in bis-phosphonate to that in bone or hydroxyapatite, Grossmann *et al.* avoided the need for isotope labelling [183]. They look at how the isotropic shift for the bis-phosphonate <sup>31</sup>P changes upon binding to mineral. They find that the free bis-phosphonates have a range of isotropic shifts that are affected by the conformation of the P–O and P–C bonds. All adsorbed bis-phosphonates, however, have very similar isotropic shifts, presumably because the torsion angles adjust to

	$\delta_{\text{iso}}$	$\zeta$	$\eta$
Bis	23 ppm	-56 ppm	0.77
Mono	15 ppm	-69 ppm	0.98
De	Not investigated		

**Table 7.2** Average  $^{31}\text{P}$  chemical shift parameters for phosphonate groups in fully (bis) protonated, singly (mono) deprotonated and fully (de) deprotonated states, as determined by quantum chemical calculation by Zhang and Oldfield [184]. The estimated errors are around 7%.

create the same, optimal binding configuration.

Zhang and Oldfield [184], on the other hand, use quantum chemical calculation to determine the CSA of bis-phosphonate  $^{31}\text{P}$ , and in particular how it depends upon the protonation state of the phosphonate group. The average values they find for fully (bis) protonated and singly (mono) protonated phosphonate groups are given in Table 7.2, and are significantly different. This CSA approach is not unprecedented; the  $^{31}\text{P}$  CSA had previously been used to study the hydration state of crystalline and amorphous clodronate [191].

In this study, the  $^{31}\text{P}$  CSTs were measured for a selection of bis-phosphonates, both in their crystalline form and when bound to the mineral surface, to see if information about protonation state and/or conformation could be determined. This CSA measurement can be done using the techniques described in previous chapters, although only for one bis-phosphonate, pamidronate, are they found to be necessary (see Section 5.3), because for other bis-phosphonates all signals were well resolved.

In addition,  $^{13}\text{C}-\{^{31}\text{P}\}$  REDOR [102] was performed (prior to the publication of Mukherjee's work) to attempt to determine the conformation of the carbon backbone of the bis-phosphonates. These experiments were performed on natural abundance materials. In order to render the  $^{13}\text{C}$  signals from bis-phosphonate visible above the  $^{13}\text{C}$  signals from bone collagen, the essential step of this new method is the chemical stripping (by caustic soda and bleach) of organic material from bone, to leave just bone mineral with a much reduced  $^{13}\text{C}$  background signal. The hope is that the bone mineral structure, including the hydrated surface layer, of this treated bone is very similar to that of the mineral in native bone, and so the binding configuration of the bis-phosphonate molecule to the treated bone is identical to natural bone. If this can be shown to be the case, this provides a practicable alternative for studying bis-phosphonates to isotope labelling.

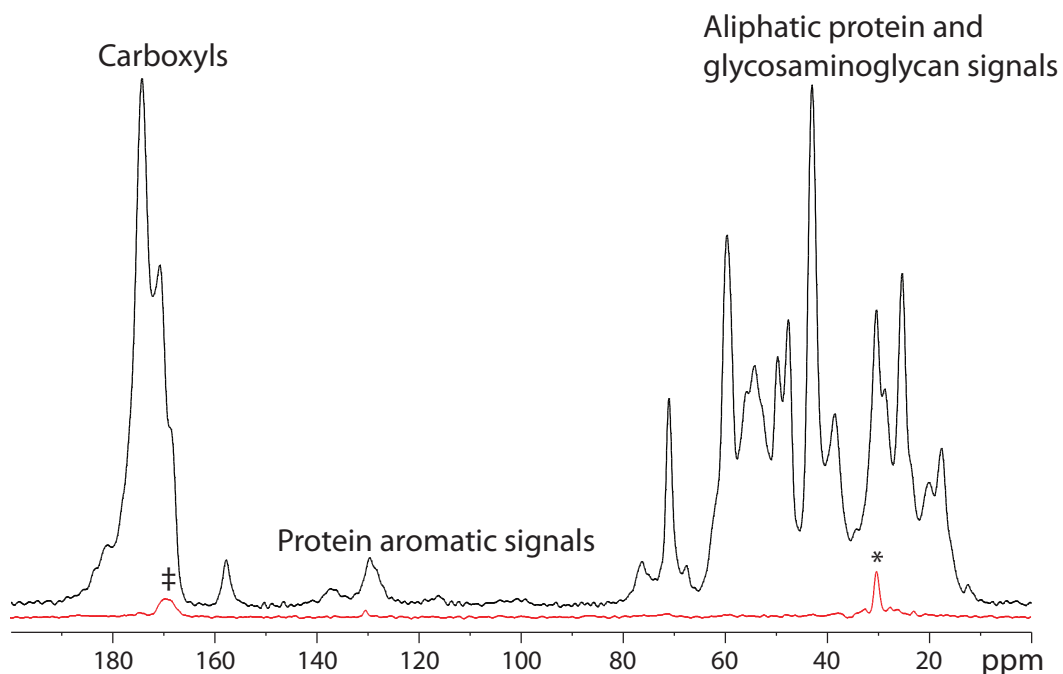


**Figure 7.3**  $^{13}\text{C}$  CP-MAS spectra on natural bone (black) and digested bone that has undergone the treatment described in the text (red). Most of the  $^{13}\text{C}$  signal is gone from the digested sample. The two exceptions, that remain even after the most extreme and prolonged treatment are around 170 ppm (‡), which is assigned to inorganic mineral carbonate, and 30 ppm (\*), which is assigned to phospholipid vesicles. The spectrum of natural bone was kindly provided by Dr Erica Wise.

## 7.2 Digested bone mineral

The organic components (collagen, glycosaminoglycans, etc.) were stripped chemically from bone by prolonged treatment with caustic soda and then bleach, before the resulting mineral was washed and dried in air (the treated bone was prepared by Dr David Reid). The white powder that results from this treatment has a carbon signature that is greatly reduced from the natural bone. Figure 7.3 compares the  $^{13}\text{C}$  CP-MAS spectra of treated bone with natural bone.

The treatment is found to have been successful at removing most of the organic components from bone, including all the protein signals of collagen. There are two  $^{13}\text{C}$  signals that persist even under the most severe treatment. These are around 170 ppm,

which corresponds to mineral carbonate, which is an integral part of carbonated apatite in bone and was not expected to be removed by the treatment. The more surprising signal that persists is the one around 30 ppm. This is in the region from aliphatic signals from proteins such as collagen, and glycosaminoglycans, but since no other signals from these compounds persist upon digestion, then the 30 ppm signal can not be assigned to these. It is instead assigned to phospholipid vesicles that are buried deep within the mineral and are therefore protected from the chemical attack of caustic soda and bleach.\*

These remnants give two regions of the  $^{13}\text{C}$  spectrum where the bone treatment does not help bring about complete removal of spectral overlap with bound bis-phosphonates. This limits the usefulness of  $^{13}\text{C}$  NMR of bis-phosphonates within these regions, most significantly in the 30 ppm region, where a number of  $^{13}\text{C}$  signals from bis-phosphonates appear.

A diagnostic test to see how the bone mineral has been affected by the treatment is by  $^{31}\text{P}-^{1}\text{H}$  HETCOR, shown in Figure 7.4. There are three types of proton identified: hydroxide and hydrogen phosphate (which are known to be contained within the mineral) and water that is near the mineral surface. The strongest  $^{31}\text{P}-^{1}\text{H}$  cross peak, corresponding to hydroxide in the bulk material, is unchanged by the digestion treatment. However, the high frequency proton chemical shift tail, shown in Figure 7.4, though still present, is greatly reduced in intensity. This indicates that the surface is less hydrated than natural bone, or that the total surface area is smaller. If the former is true, it could affect the binding of bis-phosphonates to the surface, and so results of studies using the digested material then must be validated by comparison with studies on natural bone material.

\*The evidence for this is that the lipid signals show almost no dephasing in the  $^{13}\text{C} - \{^{31}\text{P}\}$  REDOR, indicating that the carbons are remote from the phosphorus of the bone mineral or in the lipids themselves. The presence of lipid vesicles may be significant in its own right: Dr David Reid also found that when mineralised atherosclerotic plaque (a hard substance that blocks arteries) was subjected to a similar chemical treatment, the leftover mineral also retains a  $^{13}\text{C}$  signal around 30 ppm, which is also assigned to phospholipid vesicles. It has been postulated that these vesicles, buried deep within the mineralised structure, are a relic of the original mineralisation process; they may be involved in templating the initial formation of mineral crystals, thereby playing a vital role in both bone formation and pathological mineral deposition.

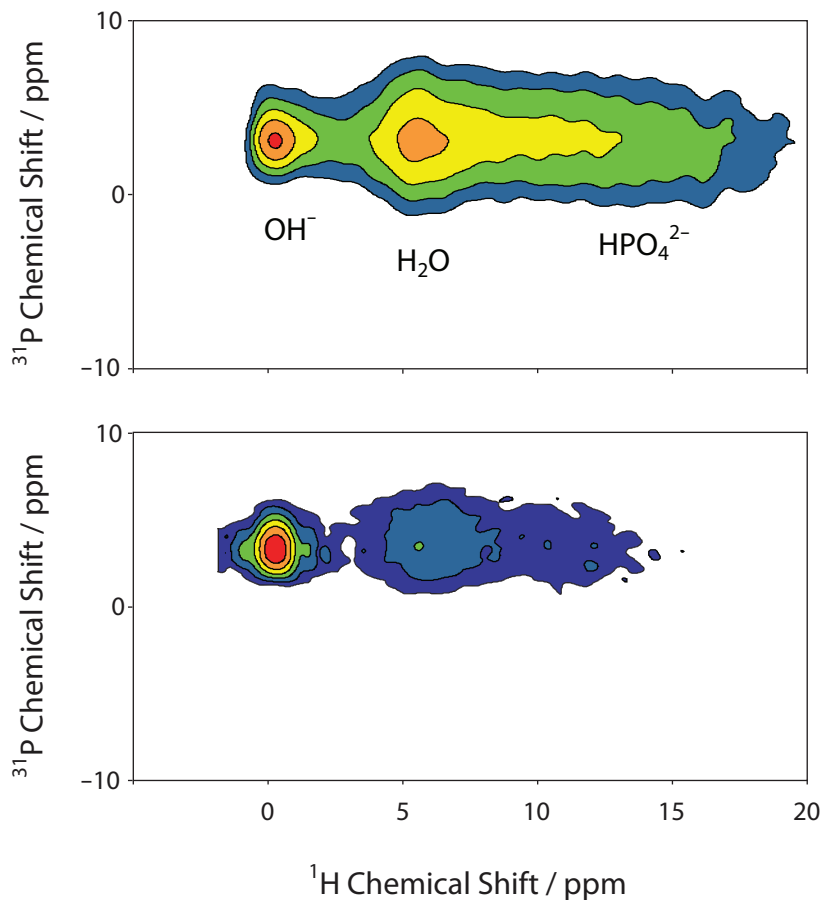


**Figure 7.4**  $^{31}\text{P}$ - $^1\text{H}$  HETCOR of natural equine bone (top, courtesy of Dr Erica Wise) and of the bone mineral after bleach and caustic soda treatment (bottom). The cross-polarisation contact time was 2 ms in both cases. The assignments of the protons are suggested by Cho [192].

### 7.3 $^{31}\text{P}$ CST measurements

In solution at physiological pH, the bis-phosphonate drugs exist as equilibrium mixtures of, predominantly, bis-protonated ( $-\text{PO}(\text{OH})_2$ ) and mono-protonated ( $-\text{PO}(\text{OH})\text{O}^-$ ) phosphonate groups [185]. In the crystalline sodium salts used in this study there are also present some fully deprotonated ( $-\text{PO}_3^{2-}$ ) phosphonate groups. Table 7.3 lists the  $^{31}\text{P}$  chemical shift parameters found for disodium pamidronate, sodium alendronate, disodium zoledronate, neridronic acid and disodium tiludronate in their crystalline form, and when the bis-phosphonates are complexed with bone mineral, measured using spinning sideband patterns at 4–6 kHz MAS rates, except for crystalline disodium pamidronate, for which the chemical shift parameters were

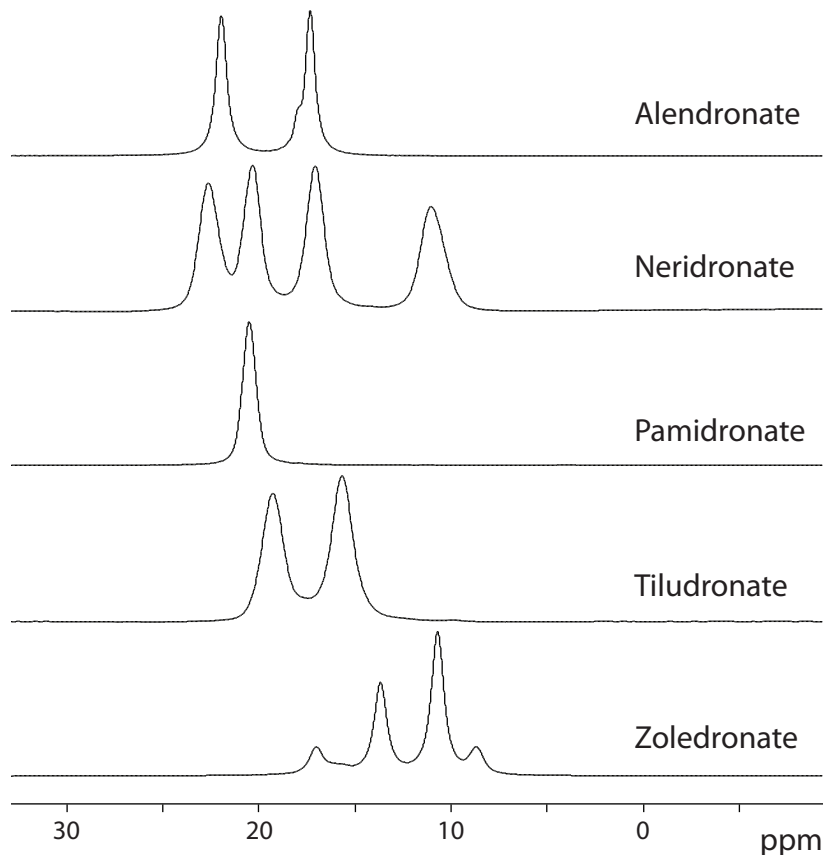


**Figure 7.5** Isotropic  $^{31}\text{P}$  spectra for five bis-phosphonates in their crystalline form.

determined in Section 5.3. The  $^{31}\text{P}$  isotropic spectra for the five bis-phosphonates are shown in Figure 7.5, and the sideband envelopes for alendronate and neridronate, are shown in Figure 7.6.

In their crystalline forms, each bis-phosphonate shows at least two distinct  $^{31}\text{P}$  environments, corresponding to phosphonate groups in different protonation states and/or different conformations. Using the chemical shift parameters measured for these  $^{31}\text{P}$  sites, they are assigned to their protonation states, using the work of Zhang and Oldfield [184]. The differences in conformation cause smaller changes in the CST, and so signals for phosphonate groups with the same protonation state are not assigned to particular crystallographic environments.

	Protonation State	$\delta_{\text{iso}}$ / ppm	$\zeta$ / ppm	$\eta$
Pamidronate (crystal)	De	20.5	$68.0 \pm 0.1$	$0.24 \pm 0.01$
	Mono	20.5	$-83.2 \pm 0.2$	$0.99 \pm 0.01$
Pamidronate (complex)		17.5	$64.5 \pm 0.4$	$0.42 \pm 0.04$
Alendronate (crystal)	Mono	22.1	$69.9 \pm 0.2$	$0.72 \pm 0.01$
	Mono	17.4	$-77.4 \pm 0.4$	$0.88 \pm 0.02$
Alendronate (complex)		18.5	$62.2 \pm 0.4$	$0.50 \pm 0.02$
Zoledronate (crystal)	Mono	17.1	$-80.4 \pm 0.8$	$0.99 \pm 0.02$
	Mono	13.8	$78.4 \pm 0.4$	$0.84 \pm 0.01$
	De	10.7	$74.8 \pm 0.4$	$0.35 \pm 0.02$
	De	8.7	$73.5 \pm 0.4$	$0.55 \pm 0.02$
Zoledronate (complex)		15.2	$69.8 \pm 0.6$	$0.41 \pm 0.04$
Neridronate (crystal)	Bis	23.9	$-60.1 \pm 0.2$	$0.54 \pm 0.02$
	Bis	21.6	$-66.9 \pm 0.2$	$0.46 \pm 0.02$
	Mono	18.2	$53.2 \pm 0.2$	$0.83 \pm 0.02$
	Mono	12.1	$64.0 \pm 0.1$	$0.96 \pm 0.01$
Neridronate (complex)		19.1	$61.0 \pm 0.6$	$0.57 \pm 0.04$
Tiludronate (crystal)	Mono	20.8	$-75.3 \pm 0.2$	$0.90 \pm 0.02$
	Mono	17.2	$-71.6 \pm 0.6$	$0.97 \pm 0.02$
Tiludronate (complex)		15.7	$65.8 \pm 0.8$	$0.53 \pm 0.04$

**Table 7.3** Experimental  $^{31}\text{P}$  chemical shift parameters, the isotropic chemical shift,  $\delta_{\text{iso}}$ , chemical shift anisotropy,  $\zeta$ , and asymmetry,  $\eta$ , for the five bis-phosphonates studied in their crystalline form and in their complexes with the bone mineral. Isotropic shifts are referenced to  $\text{H}_3\text{PO}_4$ . Anisotropic parameters are found using basic sideband analysis, except for crystalline pamidronate where the chemical shift parameters for the overlapping sites are resolved using the powder pattern. None of the mineral complexes showed conclusively that there was more than one distinct  $^{31}\text{P}$  site present. Error estimates are Cramér-Rao lower bounds [151].

When bound to mineral, however, each of the bis-phosphonates gives rise to only a single broad peak in the  $^{31}\text{P}$  NMR spectrum (in addition to the peak corresponding to phosphate in the bone mineral at ca. 2 ppm), as also observed by Mukherjee [186]. The  $^{31}\text{P}$  signals from all the bis-phosphonates when bound to bone mineral have CSA values around 60 ppm and asymmetries around 0.5, indicating that they all bind to bone mineral in a similar manner (even tiludronate, which lacks the  $-\text{OH}$  group and therefore the possibility of tridentate binding). A MAS-CSA study, with sideband-powder pattern analysis as proposed in Chapter 5, gives no firm evidence that there is more than one component in any of these signals (insufficient drop in  $\chi^2$  for fits upon

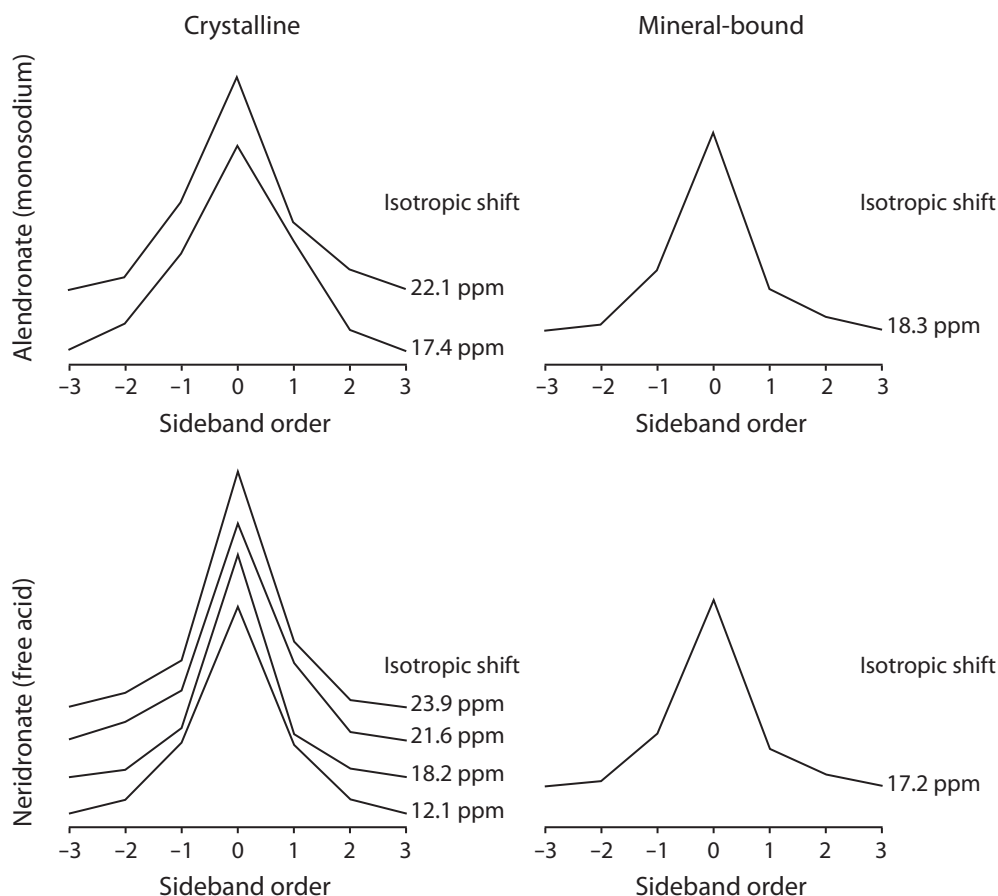


**Figure 7.6** Sideband envelope lineshapes for a spinning rate of 5750 Hz of  $^{31}\text{P}$  signals in alendronate and neridronate in both crystalline and mineral bound forms. Chemical shift parameters, found by fitting these lineshapes, are given in Table 7.3.

assumption of more than one component). Figure 7.6 shows the difference between the appearance of the crystalline and mineral-bound bis-phosphonate  $^{31}\text{P}$  sideband patterns for alendronate and neridronate.

One of the low energy conformations suggested by Robinson *et al.* in their computational study for bis-phosphonate binding to hydroxyapatite (used as a bone model) consists of one phosphonate bound to the mineral and one ‘dangling’ into solution [185]. Our experimental data shows that this is unlikely, as if it were the case one would expect to see different values for  $^{31}\text{P}$  isotropic and anisotropic chemical shifts, and the signal for the ‘dangling’ phosphonate would be sharpened due to dynamics. The fact only one value of CSA is seen suggests all the phosphonate groups

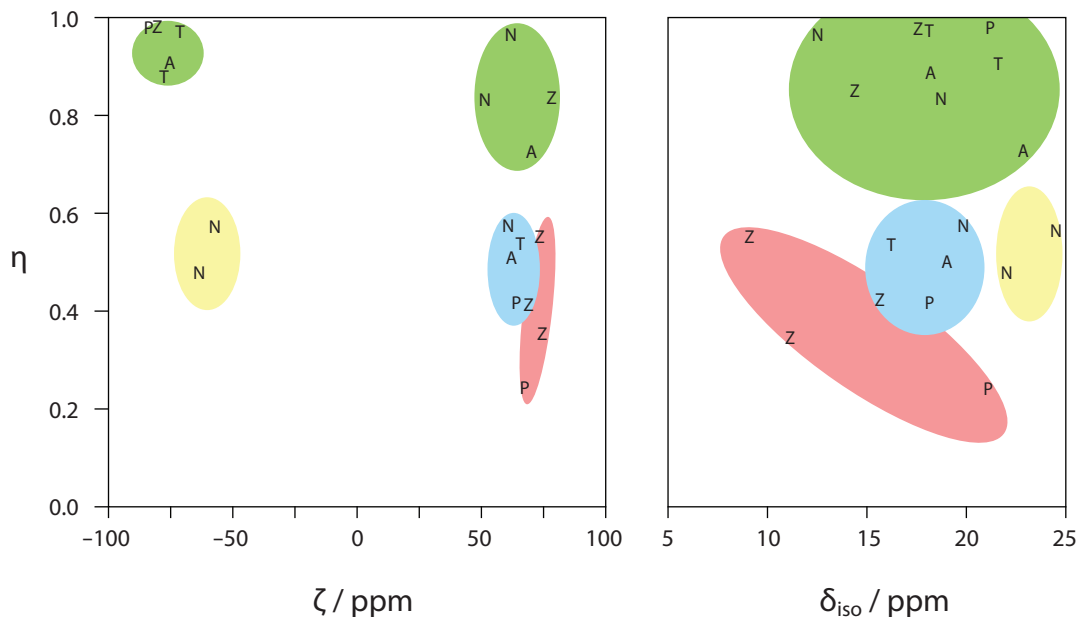


**Figure 7.7** Scatter plots of  $\eta$  against  $\zeta$  (left) and  $\delta_{\text{iso}}$  (right) for  $^{31}\text{P}$  in phosphonate groups. Coloured regions indicate the assigned protonation state: red for fully deprotonated, green for mono-protonated and yellow for bis-protonated. Blue indicates the points for mineral-bound bis-phosphonates. The letters indicate which bis-phosphonate that each point corresponds to: A – alendronate, N – neridronate, P – pamidronate, T – tiludronate and Z – zoledronate.

are in the same protonation state, or possibly that two phosphorus environments are exchanging rapidly.

In order to examine trends in the chemical shift parameters given in Table 7.3, or in the equivalent CST principal values, Figure 7.7 shows the scatter of  $\delta_{\text{iso}}$ ,  $\zeta$  and  $\eta$  for bis-protonated, mono-protonated and deprotonated phosphonate groups, and for the mineral bound bis-phosphonates. It shows that  $\zeta$  and  $\eta$  appear to be far more useful gauges of protonation state than the isotropic shift. Figure 7.8 shows the range of the three principal values of the CSTs of each protonation state of phosphonate.

From Figures 7.7 and 7.8 it appears that the bis-phosphonate head groups in the bound state are in a fully deprotonated state. This is based on the assignment of the phosphonates to their protonation states, based upon the work of Zhang and Oldfield [184]. It assumes that protonation state (rather than bond conformation) is the most significant contributor to the differences in CST, and that the bound bis-phosphonate group is static. In order to verify these results, it would be a good idea to simulate using CASTEP or otherwise, the CST of phosphonates in a fully deprotonated state,

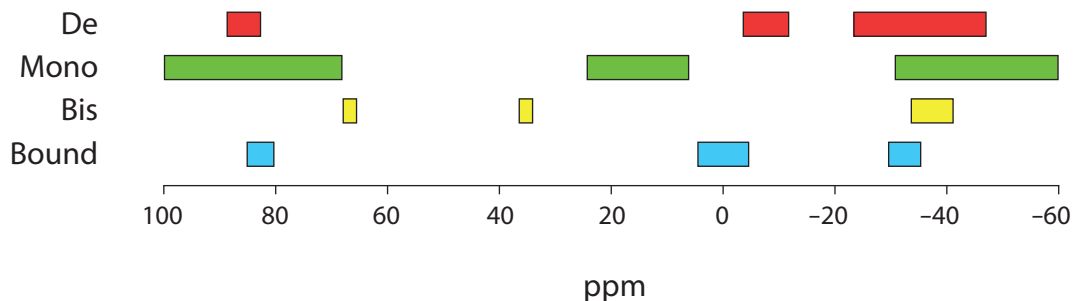


**Figure 7.8** Range of principal values for  $^{31}\text{P}$  CST for the five bis-phosphonates for different protonation states of phosphonate groups, and for the same bis-phosphonates bound to bone mineral, where the protonation state is unknown. Note that the apparently larger range of principal values for mono-protonated phosphonate groups is probably more due to the larger number of examples with this protonation state, rather than any inherently greater variability in CST principal values.

bonding to calcium ions in an appropriate arrangement resembling the surface layer of bone.

### 7.3.1 Natural bone

To ensure that the bone treatment was not significantly affecting the results of this experiment, it was repeated with zoledronate on natural bone. The  $^{31}\text{P}$  CST results were within the error bounds of the measurements for zoledronate on digested bone.

One noticeable difference was that the signal from bis-phosphonates was much stronger. This could indicate superior binding on natural bone compared with digested bone (either from the influence of the organic components or some property of the surface hydration layer), but could equally be due to difference in the sample preparation (possibly a greater mineral surface area).

### 7.3.2 Hydroxyapatite

Some previous studies, for example that of Robinson [185], use hydroxyapatite as a model for bone surface. Tiludronate was bound to hydroxyapatite to compare  $^{31}\text{P}$  CST results with the same compound bound to digested bone, to see which of hydroxyapatite or digested bone were a better model for natural bone.

First of all it was noticed that very little bis-phosphonate was taken up by the hydroxyapatite. This could indicate some feature of the hydroxyapatite surface is less suitable for binding with bis-phosphonates than bone mineral surface, or, less interestingly, could be an indicator of the relatively smaller surface area of hydroxyapatite

crystal particles.

The  $^{31}\text{P}$  CST results found for the tiludronate phosphonate groups show a slight deviation between hydroxyapatite and digested bone, particularly in asymmetry (which here is  $\eta = 0.7$ ), from the region marked out for mineral-bound phosphonate groups in Figure 7.7. This is some initial evidence that hydroxyapatite might not be suitable for a study of bis-phosphonates on bone, as the binding structure might be dissimilar.

### 7.3.3 Variable temperature

The  $^{31}\text{P}$  CST measurements were repeated at 273 K for alendronate, zoledronate and tiludronate bound to digested bone, to determine whether there is any influence of motion on the measured CSA values. The change in the parameters from those in Table 7.3 was smaller than the error bounds, which indicates either: (a) motion does not have a significant influence on the CSA, or, (b) motion is fast, so that reducing the temperature by approximately 30 K does not affect its influence on CSA. For zoledronate, the low temperature experiment was repeated at 223 K, and again no significant difference in CSA parameters was detected. A static bis-phosphonate head-group would be in accordance with the findings of Mukherjee [186].

### 7.3.4 $^{13}\text{C}$ CST measurements

The  $^{13}\text{C}$  CSA-amplified 2D-PASS [86] spectra of tiludronate and zoledronate show that the CSA of the aromatic carbons is greatly reduced upon binding to the bone mineral from about  $-100$  ppm to  $-60$  ppm (Figure 7.9). This could be indicative of a ring wobble (as the motion partially averages the CSA), so any binding between the sidechain and the bone mineral surface must be weak. For the other bis-phosphonates the  $^{13}\text{C}$  CSA-amplified 2D-PASS is not particularly informative, since the  $^{13}\text{C}$  CSAs are very small and difficult to measure accurately.

## 7.4 $^{13}\text{C}-\{^{31}\text{P}\}$ REDOR

The REDOR experiment, described briefly in Section 3.3, is a method for measuring interatomic distances between nuclei, based upon the dephasing of the spectrum caused by coupling between them. With bis-phosphonates, the distances between the  $^{13}\text{C}$  atoms in the  $R_2$  group and the  $^{31}\text{P}$  atoms in the phosphonate groups are measured in order to examine the conformation and/or the dynamics of the  $R_2$  group when bound

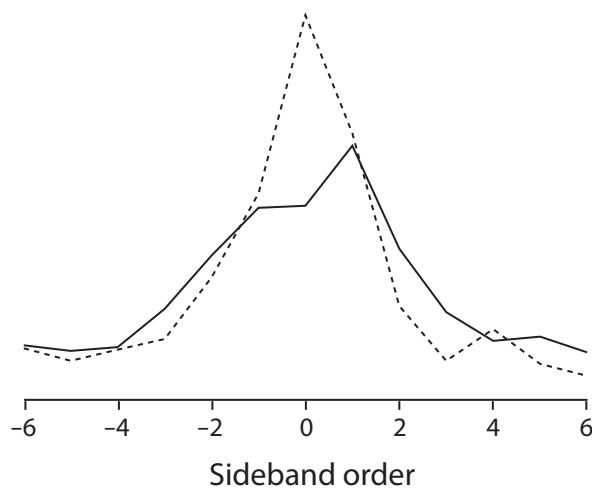


**Figure 7.9** Sideband envelope lineshapes for a spinning rate of 2350 Hz (from a CSA-amplified 2D-PASS experiment with an actual spinning rate of 8 kHz) of  $^{13}\text{C}$  signals in tiludronate as a crystalline disodium salt (solid line) and when bound to bone mineral (dashed line), showing the narrowing of the sideband envelope due to a decrease in CSA upon binding.

to bone. There is an added complication that there are two  $^{31}\text{P}$  atoms in each molecule that the  $^{13}\text{C}$  can couple to, as well as  $^{31}\text{P}$  nuclei in phosphate in the bone mineral, and  $^{31}\text{P}$  nuclei in neighbouring bis-phosphonate molecules. This makes accurate quantitative measurement of individual  $^{13}\text{C}$ - $^{31}\text{P}$  distances very difficult (particularly for those atoms at the far end of the  $R_2$  group), and so results can only be viewed qualitatively. Also, since this experiment is acquired on  $^{13}\text{C}$ , care must be taken to avoid the signals of organic remnants in the digested bone (around 30 ppm), so not all bis-phosphonate  $^{13}\text{C}$  signals can be properly resolved in the mineral bound form.

#### 7.4.1 Alendronate

The crystal structure for alendronate is known [193]. Mukherjee *et al.* conclude that when bound to mineral, the  $-\text{NH}_3^+$  is held in one place on the surface, presumably close to mineral phosphate, whilst the carbons in the chain undergo a rapid concerted motion, like a crankhandle [186]. In the pure crystalline form the carbon chain of alendronate is static. Crystalline and mineral-bound alendronate give rise to good quality  $^{13}\text{C}$  spectra, with well-resolved signals, in particular avoiding the remnant bone-mineral signal at 30 ppm (see Figure 7.10).

The dephasing curves for alendronate are shown in Figure 7.11. Firstly, they agree with the carbon chain being static in the crystalline pure material, as the  $^{13}\text{C}$ - $^{31}\text{P}$

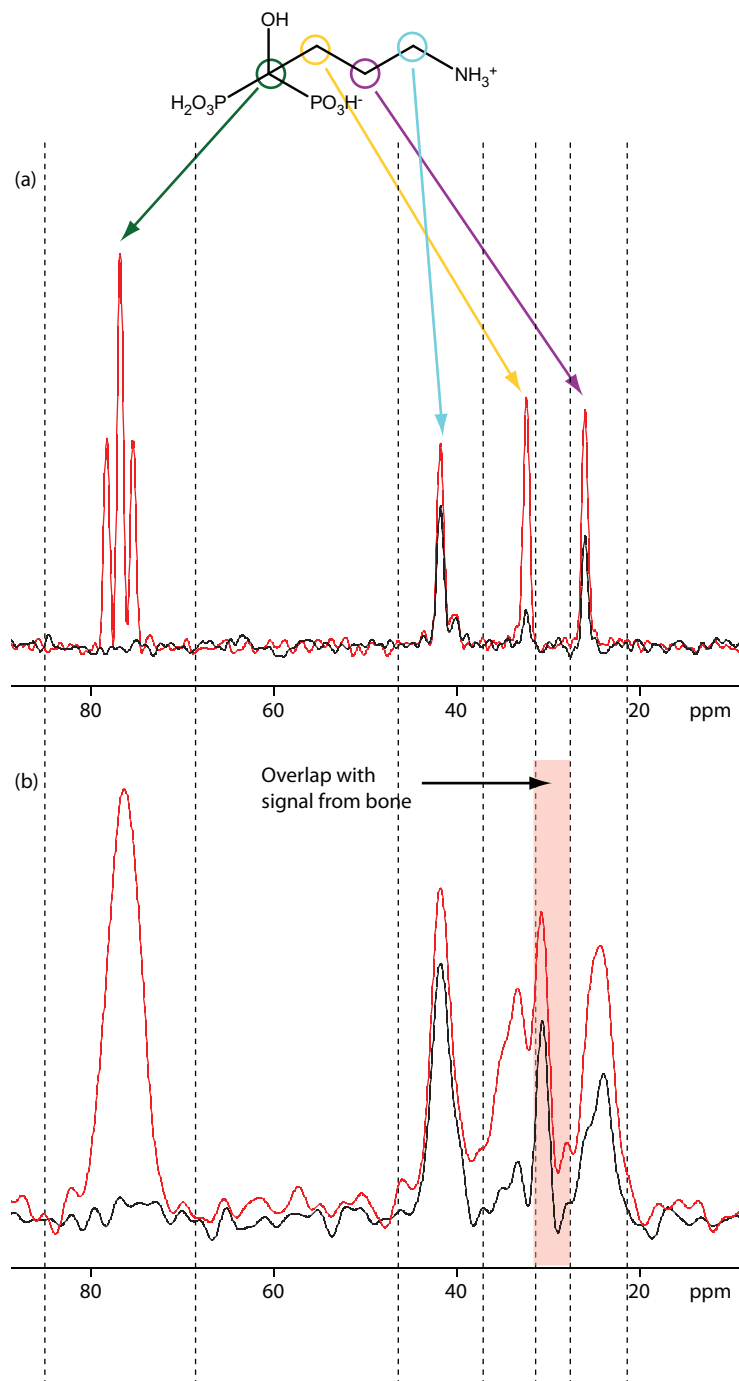


**Figure 7.10**  $^{13}\text{C}$ - $\{^{31}\text{P}\}$  REDOR spectra of (a) crystalline and (b) mineral-bound alendronate, acquired with (black lines - dephased spectra) and without (red lines - reference spectra) refocusing of  $^{13}\text{C}$ - $^{31}\text{P}$  dipolar coupling, for a dephasing time of 2.6 ms. Dashed lines mark the divisions between different  $^{13}\text{C}$  signals.

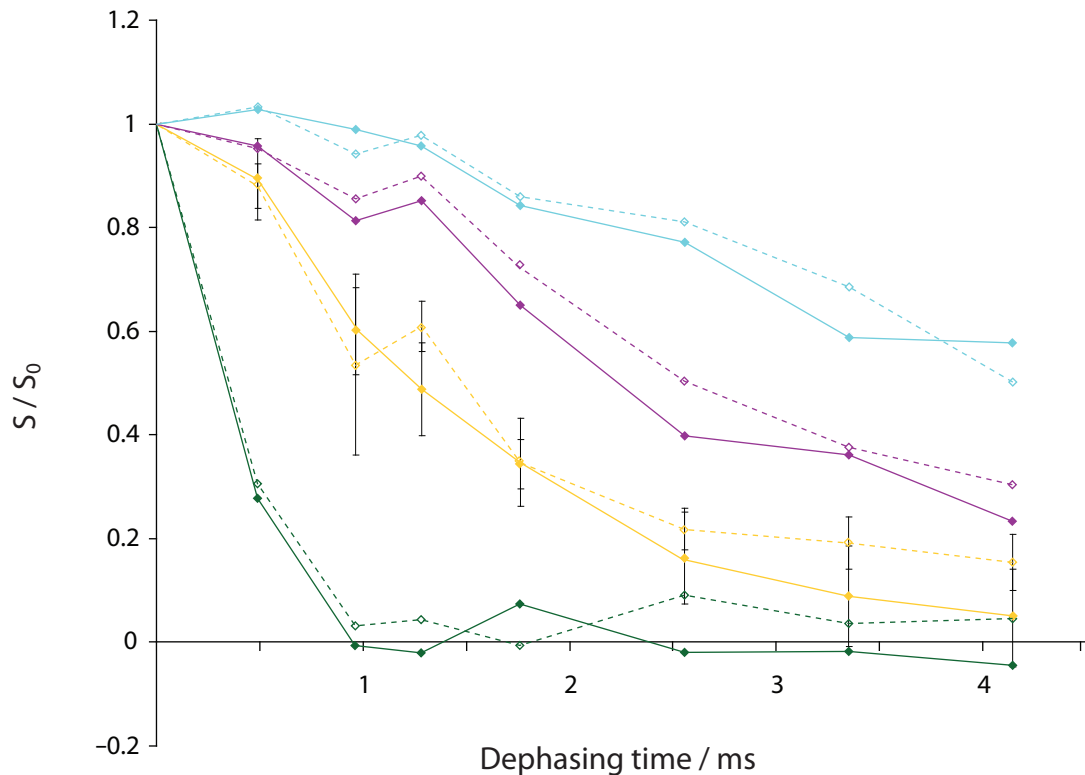


**Figure 7.11** REDOR dephasing curves for  $^{13}\text{C}$  in crystalline (solid lines) and mineral-bound (dashed lines) alendronate. Filled diamonds correspond to actual data points for crystalline alendronate, and open diamonds to those for mineral-bound alendronate. The colours refer to the colours shown in Figure 7.10. An estimate of the errors based on the noise level in the spectra is shown by the error bars on the dephasing curve for the second carbon in the chain (yellow).

distances measured (ignoring intermolecular  $^{13}\text{C}$ - $^{31}\text{P}$  dipolar interactions) by fitting these curves match those in the crystal structure to within  $\pm 0.2\text{ \AA}$ , indicating that the dipolar dephasing is not affected by motion.

For mineral-bound alendronate, if a crankhandle motion is present, this should disrupt the dipolar coupling between the  $^{31}\text{P}$  nuclei and, in particular, the third  $^{13}\text{C}$  in the chain, since this is the carbon which moves most relative to the phosphorus atoms (purple in Figure 7.11). If this is true, the  $^{13}\text{C}$  signal for the third carbon will show slower dephasing. Although the dephasing curve for the third  $^{13}\text{C}$  in the chain does show a slightly slower dephasing compared with the crystalline material, which could be evidence of a crankhandle motion, the error estimates (shown for the second carbon in Figure 7.11) are greater than the change, so the results are inconclusive.

#### 7.4.2 Pamidronate

In a previous study it was found that pamidronate has a carbon chain in a *gauche* conformation when bound to bone, presumably so that the  $-\text{NH}_3^+$  group could interact with the mineral [186]. This means that the  $^{13}\text{C}$ - $^{31}\text{P}$  distances for the terminal carbon are shorter than in the crystalline form, where the chain is in the *trans* conformation. This should make the signal from this carbon dephase quicker in the  $^{13}\text{C}$ - $\{^{31}\text{P}\}$  REDOR experiment. However, it was also found that the tail ‘hopped’ between different binding sites, which should interfere with the dipolar coupling and reduce the dephasing seen in the REDOR experiment.

Figure 7.12 shows the  $^{13}\text{C}$  spectra of pamidronate and the signal assignments, and Figure 7.13 shows the  $^{13}\text{C}$ - $\{^{31}\text{P}\}$  REDOR dephasing curves. The terminal carbon (purple) shows a slightly more rapid dephasing, which could indicate the adoption of a *gauche* conformation, although the change is marginal compared to the noise level. The middle carbon (yellow) shows significantly slower dephasing in mineral-bound compared to crystalline pamidronate, although this signal poorly resolved from the 30 ppm signal from bone (which does not show any dephasing) and the signal from the terminal carbon, so the dephasing curve is unreliable.<sup>†</sup>

#### 7.4.3 Neridronate

The assignments of the  $^{13}\text{C}$  signals in neridronate are made with the aid of several experiments, which are discussed in Chapter 8. There are two molecules per asymmetric unit in the crystalline form, so some signals are split in the spectra of crystalline neridronate (see Figure 7.14). This splitting is obviously not seen in the mineral-bound neridronate spectra.

From the  $^{13}\text{C}$ - $\{^{31}\text{P}\}$  REDOR dephasing curves (Figure 7.15) for crystalline neridronate notice that the slowest dephasing signals (i.e. those from  $^{13}\text{C}$  further in space from  $^{31}\text{P}$ ) are not in fact those at the end of the  $R_2$  group, but from those in the middle. This indicates that either (a) the ends of the  $R_2$  groups are close to the phosphonate groups on neighbouring molecules, or (b) the  $R_2$  chain is looped back towards itself, and so the ends of the  $R_2$  groups are close to the phosphonate groups in the same

<sup>†</sup>The conditions for the pamidronate REDOR spectra differ from the other REDOR experiments due to spectrometer difficulties at the time (see Section 7.5). It has been proposed that these experiments should be repeated to ensure compatibility between spectra, but this has not yet been possible due to a catastrophic equipment malfunction.

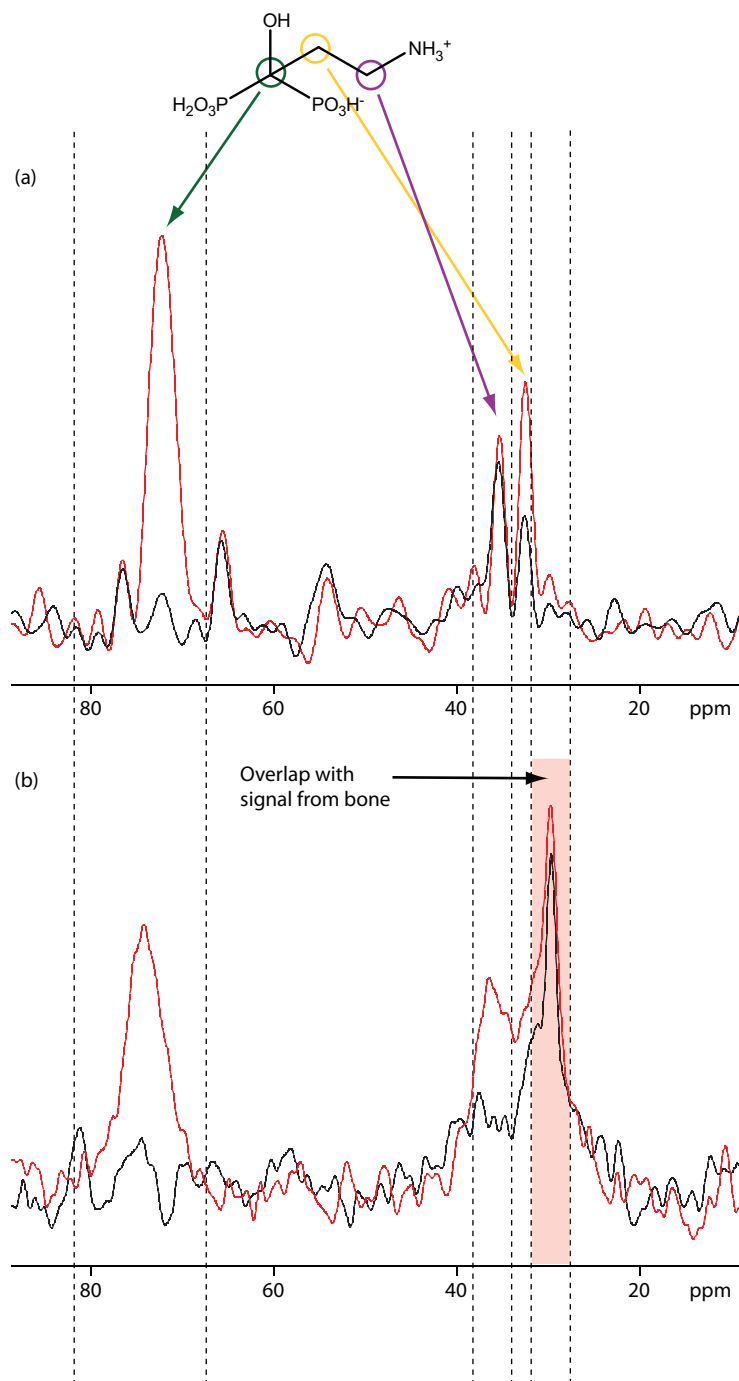


**Figure 7.12**  $^{13}\text{C}$ - $^{31}\text{P}$  REDOR spectra of (a) crystalline and (b) mineral-bound pamidronate, acquired with (black lines - dephased spectra) and without (red lines - reference spectra)  $^{13}\text{C}$ - $^{31}\text{P}$  dipolar coupling, for a dephasing time of 2.0 ms. Dashed lines mark the divisions between different  $^{13}\text{C}$  signals, if they are resolvable.

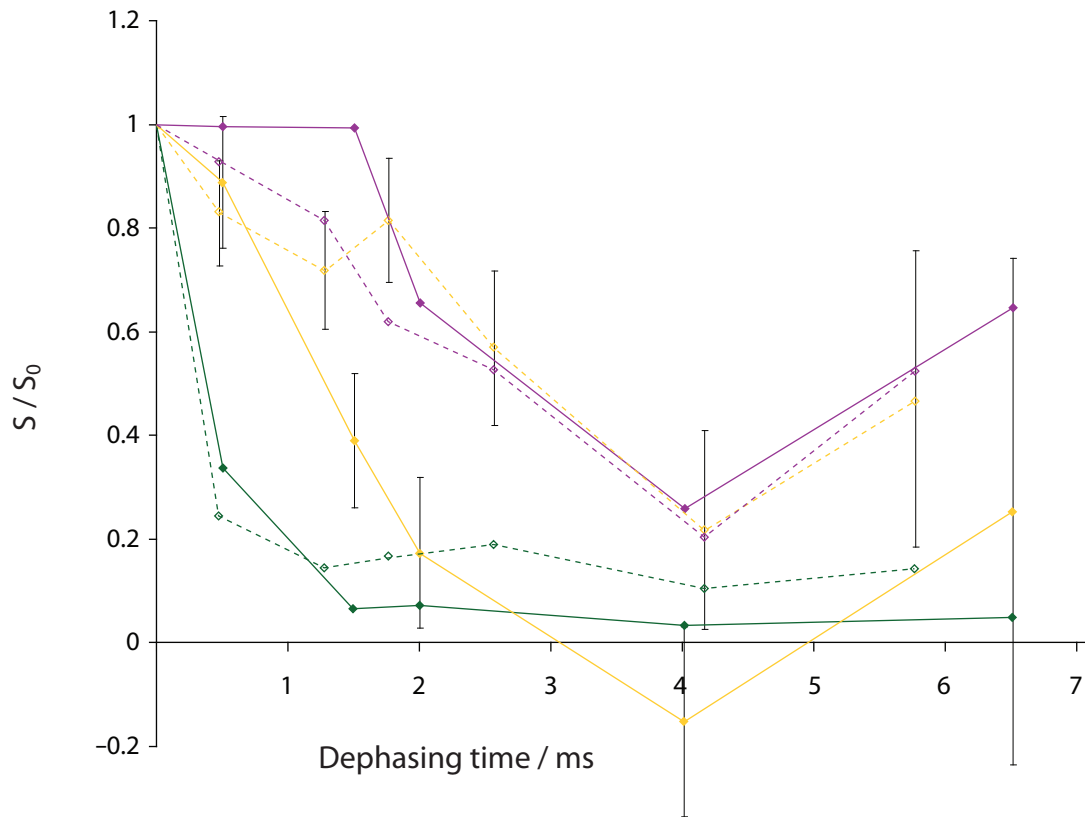


**Figure 7.13** REDOR dephasing curves for  $^{13}\text{C}$  in crystalline (solid lines) and mineral-bound (dashed lines) pamidronate. Filled diamonds correspond to actual data points for crystalline pamidronate, and open diamonds to those for mineral-bound pamidronate. The colours refer to the colours shown in Figure 7.12. An estimate of the errors based on the noise level in the spectra is shown by the error bars on the dephasing curve for the second carbon in the chain (yellow).

molecule.

Comparison of the REDOR dephasing curve for crystalline and mineral-bound neridronate shows some differences. Most notably, the signal from the third and sixth carbons in the chain (purple and blue) dephase significantly more slowly in mineral-bound bis-phosphonate. A possible explanation for this is that the amine end of the chain is not bound tightly to the surface, but it dangles. If the side chain is loose and free to move, this disrupts the dipolar coupling to the  $^{31}\text{P}$  and so reduces the rate of dephasing. This could also explain why neridronate binds much more weakly to the surface than its analogues, alendronate and pamidronate.

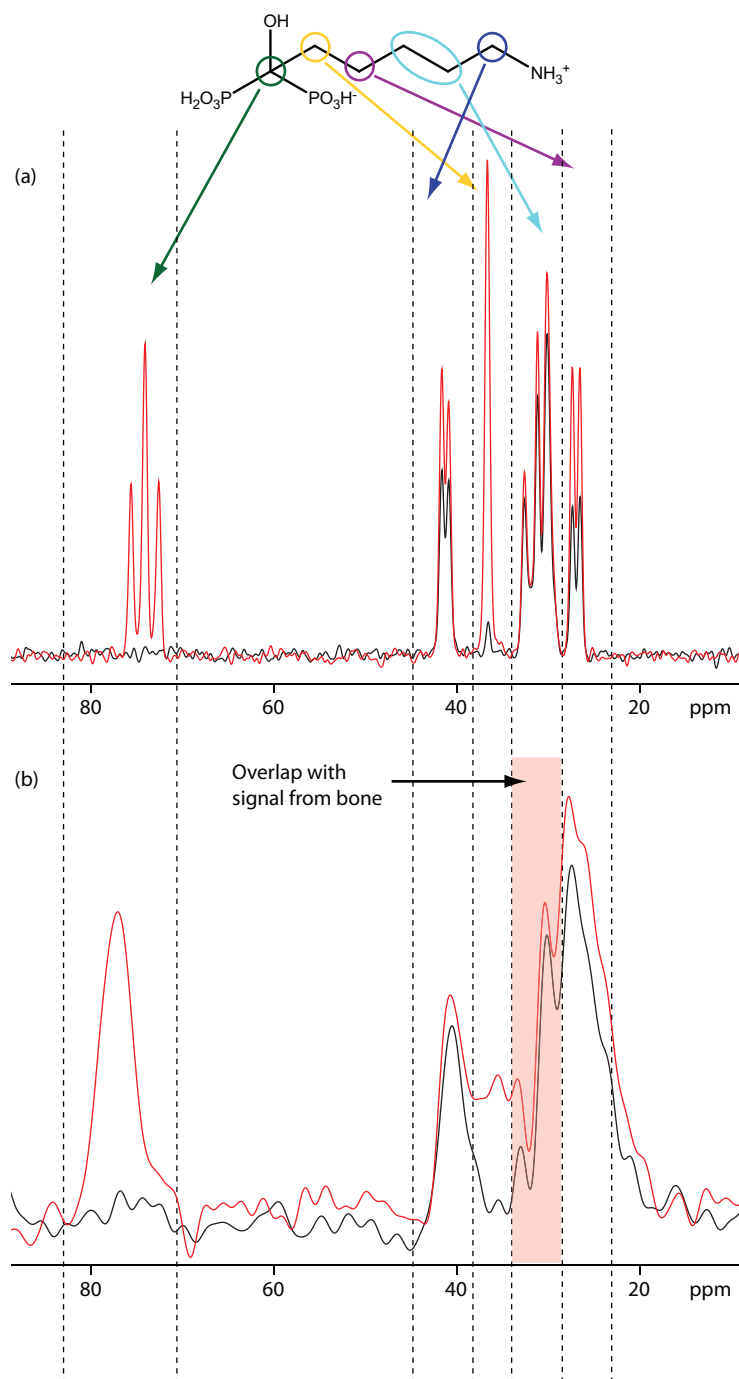


**Figure 7.14**  $^{13}\text{C}-\{^{31}\text{P}\}$  REDOR spectra of (a) crystalline and (b) mineral-bound neridronate, acquired with (black lines - dephased spectra) and without (red lines - reference spectra)  $^{13}\text{C}-^{31}\text{P}$  dipolar coupling, for a dephasing time of 2.6 ms. Dashed lines mark the divisions between different  $^{13}\text{C}$  signals, if they are resolvable.

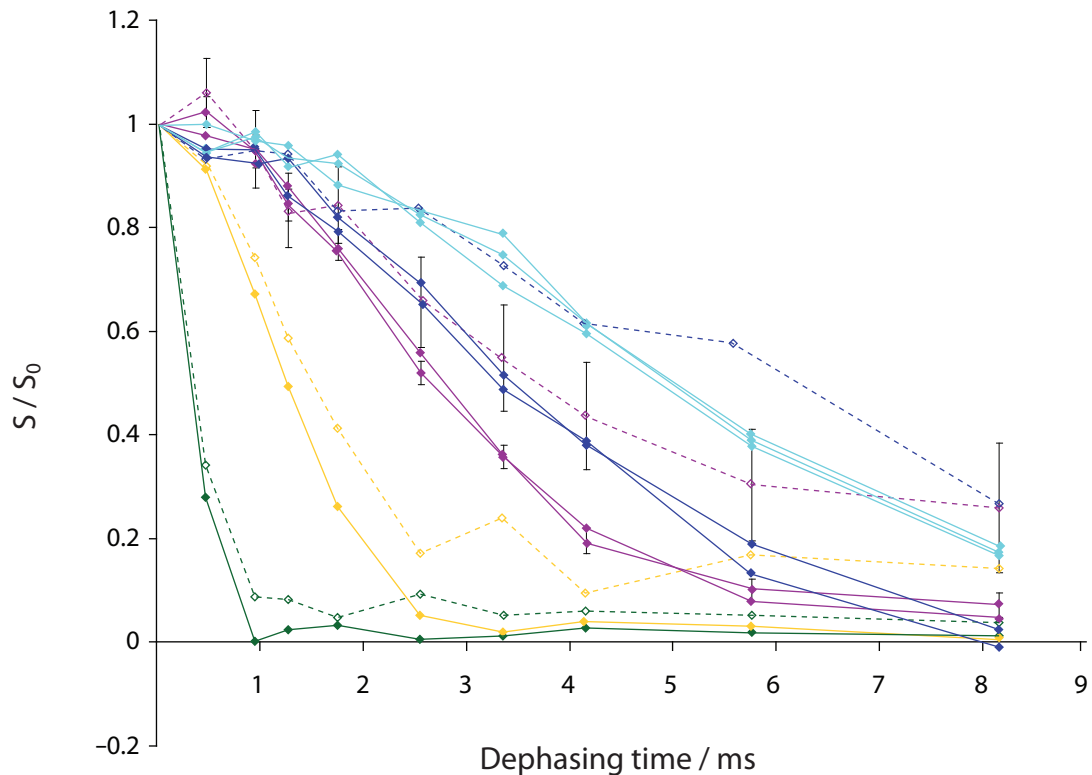


**Figure 7.15** REDOR dephasing curves for  $^{13}\text{C}$  in crystalline (solid lines) and mineral-bound (dashed lines) neridronate. Filled diamonds correspond to actual data points for crystalline neridronate, and open diamonds to those for mineral-bound neridronate. The colours refer to the colours shown in Figure 7.14. An estimate of the errors based on the noise level in the spectra is shown by the error bars on the dephasing curve for the third carbon in the chain (purple). No curves are shown for the fourth and fifth carbons in mineral-bound neridronate, as they are not resolved from the residual bone signal.

#### 7.4.4 Zoledronate

Zoledronate appears to have a ring wobble, as evidenced by the reduction in CSA in the  $^{13}\text{C}$  CSA-amplified PASS spectrum (see Section 7.3). The  $^{13}\text{C}-\{^{31}\text{P}\}$  REDOR experiment (Figures 7.16 and 7.17) shows the signal from the  $\text{CH}_2$  carbon (yellow) dephasing more slowly for mineral-bound zoledronate than for crystalline zoledronate. This change can not be caused by a ring wobble.<sup>‡</sup> The signals for the ring carbons do not confidently show a change in dephasing rate going from crystalline to mineral-bound forms. The dephasing curve for the signal of the carbon bonded

<sup>‡</sup>The dephasing curves for this signal in the crystalline and mineral-bound zoledronate only diverge at long dephasing times, which suggests this difference might be due to more distant  $^{31}\text{P}$  spins.

to both nitrogens in the imidazole ring (shown in light blue) is very different in the mineral-bound compared to the crystalline sample, but not in any systematic manner.

#### 7.4.5 Tiludronate

Very little can be said about tiludronate, due to the poor resolution of the mineral-bound tiludronate  $^{13}\text{C}$  spectrum. The aromatic  $^{13}\text{C}$  signals are overlapped, and the overall dephasing of this overlapped peak, is similar to the dephasing of the individual peaks in the crystalline sample. The signal for the first carbon is absent from the mineral-bound spectrum, except at very short CP contact times; the reason for this is unknown.

### 7.5 Experimental procedure

Monosodium alendronate, disodium pamidronate and neridronic acid were purchased from Sigma. Disodium zoledronate was donated by Novatis, and disodium tiludronate was donated by Sanofi-Aventis. All were used without further purification.

#### 7.5.1 Preparation of bone mineral

Bone was obtained from adult horses used for general purpose exercise and euthanised for humanitarian reasons unconnected with this study. Bone mineral was prepared by removing the organic matrix (primarily collagen and other proteoglycans and glycoproteins) by prolonged digestion (several weeks) in concentrated sodium hydroxide and sodium hypochlorite. Digested mineral was thoroughly washed with distilled water to remove all the solubilised material, until the pH of the water used was neutral. It was then air dried and stored at 4°C; the same batch of mineral was used in all experiments.

Bone mineral/bis-phosphonate complexes were prepared by dissolving ca. 40 mg of bis-phosphonate in 5 ml distilled water, with the addition of dilute NaOH in the case of those supplied as free acids to solubilise them, and mixing the resulting neutral solution with about 200 mg of bone mineral. After standing at 4°C overnight, the mineral was filtered, washed twice with distilled water to remove unbound bis-phosphonate, and air dried at room temperature.

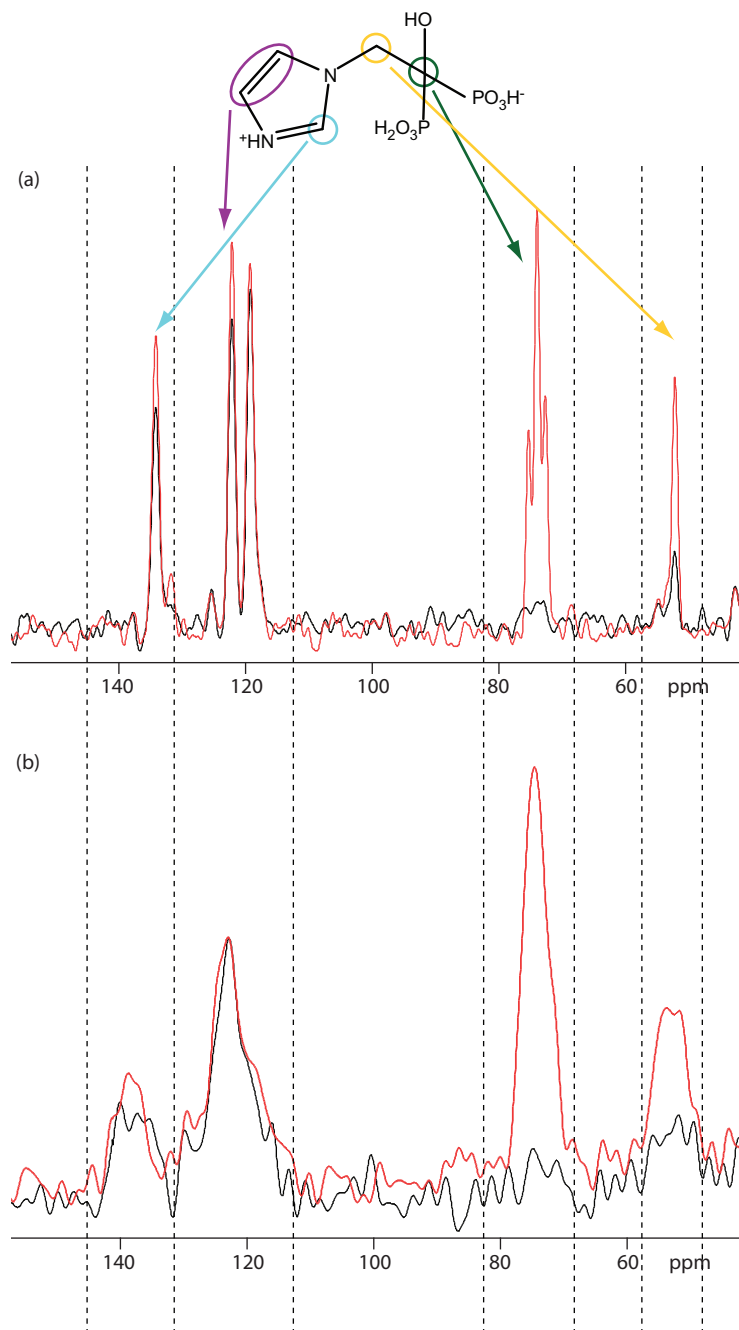


**Figure 7.16**  $^{13}\text{C}$ - $\{{}^{31}\text{P}\}$  REDOR spectra of (a) crystalline and (b) mineral-bound zoledronate, acquired with (black lines - dephased spectra) and without (red lines - reference spectra)  $^{13}\text{C}$ - ${}^{31}\text{P}$  dipolar coupling, for a dephasing time of 2.0 ms. Dashed lines mark the divisions between different  $^{13}\text{C}$  signals, if they are resolvable.

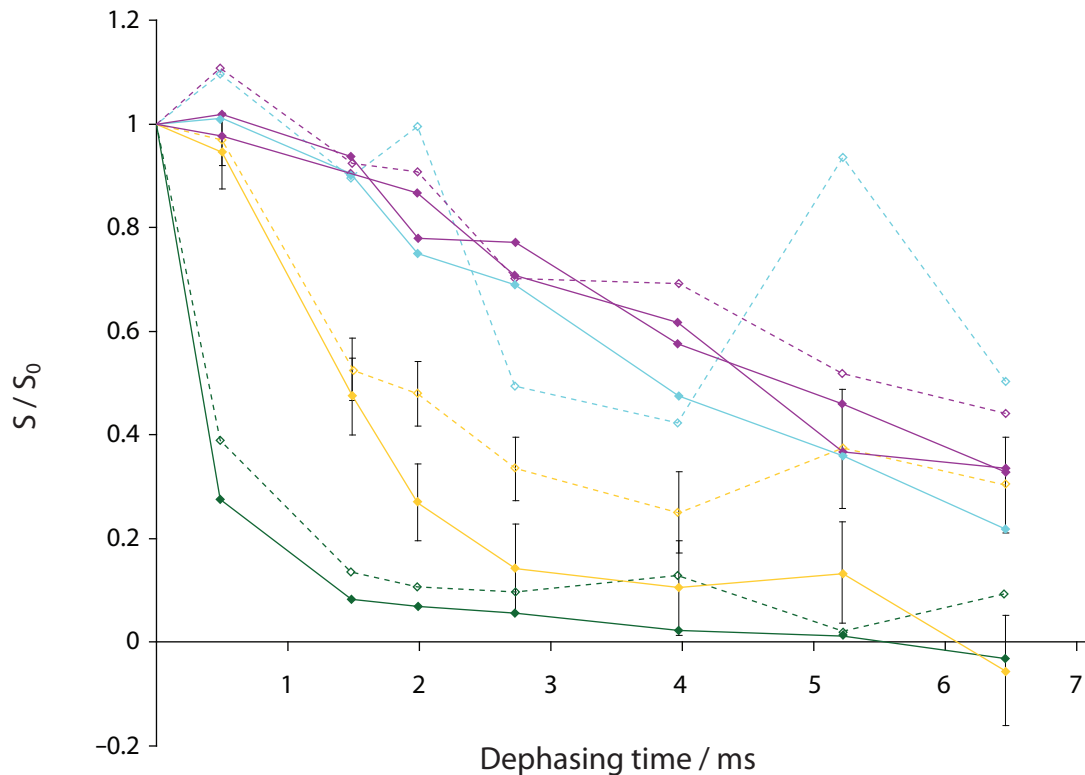


**Figure 7.17** REDOR dephasing curves for  $^{13}\text{C}$  in crystalline (solid lines) and mineral-bound (dashed lines) zoledronate. Filled diamonds correspond to actual data points for crystalline zoledronate, and open diamonds to those for mineral-bound zoledronate. The colours refer to the colours shown in Figure 7.16. An estimate of the errors based on the noise level in the spectra is shown by the error bars on the dephasing curve for the second carbon in the chain (yellow).

### 7.5.2 REDOR

REDOR experiments [102] were performed using a Bruker Avance 400 spectrometer fitted with a 4 mm wide bore broadband triple resonance probe. Samples were packed in the middle half of 4 mm zirconia rotors, with teflon tape occupying the rest of the space.

For alendronate, neridronate and tiludronate (crystalline and mineral-bound) the sample was spun at the magic angle at a rate of 12.5 kHz. For zoledronate and pamidronate the MAS rate was 8 kHz, due to hardware problems. The  $^{31}\text{P}$   $\pi$ -pulse length was  $8.1\ \mu\text{s}$ . The  $^1\text{H}$   $\pi/2$ -pulse length was  $2.5\ \mu\text{s}$ . The  $^1\text{H}$ – $^{13}\text{C}$  CP contact time was 4 ms. High power TPPM  $^1\text{H}$  decoupling was applied with a field strength of 100 kHz. The number of rotor cycles of the REDOR sequence was varied to give the

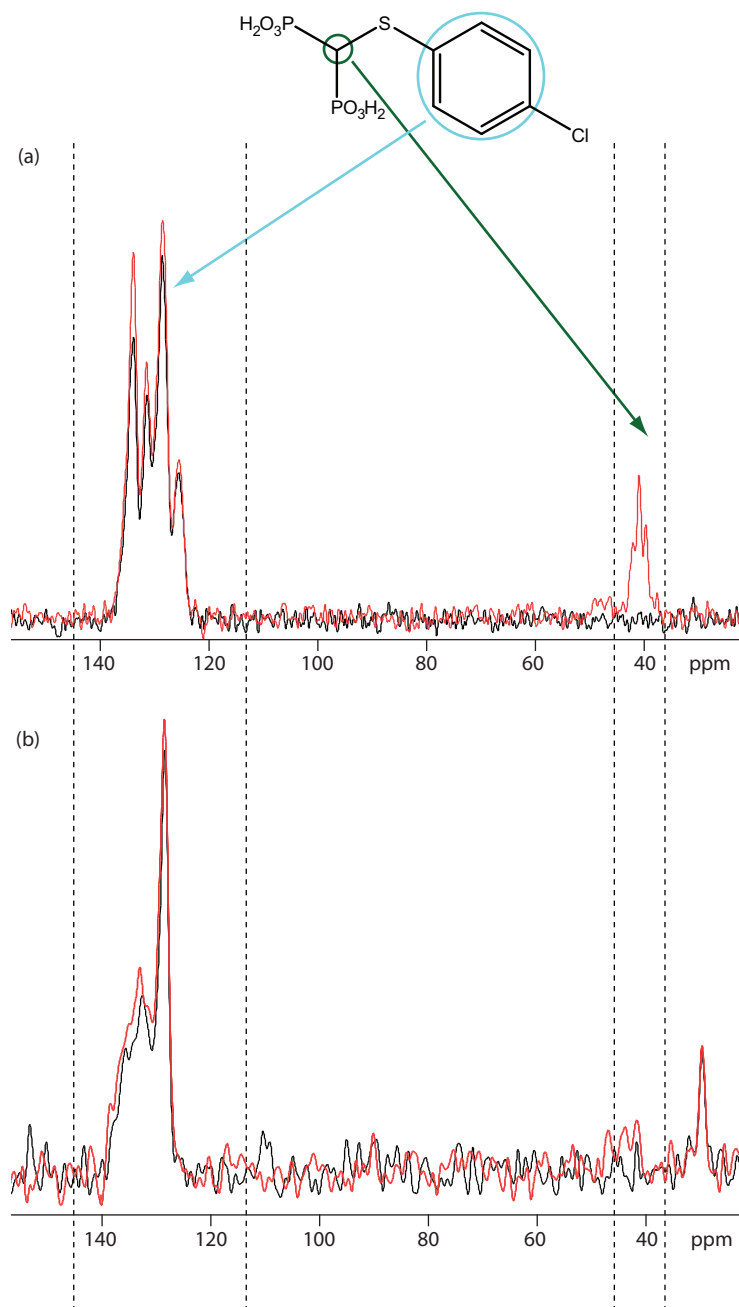


**Figure 7.18**  $^{13}\text{C}$ - $\{{}^{31}\text{P}\}$  REDOR spectra of (a) crystalline and (b) mineral-bound tiludronate, acquired with (black lines - dephased spectra) and without (red lines - reference spectra)  $^{13}\text{C}$ - ${}^{31}\text{P}$  dipolar coupling, for a dephasing time of 2.0 ms. Dashed lines mark the divisions between different  $^{13}\text{C}$  signals, if they are resolvable.

dephasing times shown in the figures. The number of scans was also varied between experiments, the effect of which is seen in the error bars. The recycle delay was 2 s for mineral-bound bis-phosphonates and 6 s for crystalline bis-phosphonates, with the exception of pamidronate for which it was 10 s for the pure crystalline material.

To construct the dephasing curves, the intensity was integrated over the peak widths shown in the figures, and the ratio of the dephased intensity to the reference intensity was calculated. The errors were calculated from the standard deviation in the noise.

### 7.5.3 CSA measurements

The  $^{31}\text{P}$  CST measurements were made on one-dimensional CP-MAS spectra of the bis-phosphonates, at MAS rates between 4 and 6 kHz. The exception is pamidronate, for which the powder–sideband correlation pattern approach was used, the details of which are given in Chapter 5.

The  $^{13}\text{C}$  CST measurements were made on CSA-amplified PASS [86] spectra of zoledronate and tiludronate. The actual spinning rate was 8 kHz, and the anisotropic scaling factor was  $\chi_a = 3.4$ , giving a reduced spinning rate of 2350 Hz. The  $^{13}\text{C}$   $\pi$ -pulse length was  $7.3\ \mu\text{s}$ . There were 16  $t_1$  data points recorded with 140 scans per point for crystalline and 560 scans per point for mineral-bound. High power TPPM  $^1\text{H}$  decoupling was applied with a field strength of 83 kHz.

## 7.6 Conclusions

The  $^{31}\text{P}$  CST have been measured very accurately for a range of bis-phosphonates, using a combination of CSA techniques including those discussed in the earlier chapters. The CSA and asymmetry show an interesting variation between the different bis-phosphonates, which has been attributed to the different protonation states phosphonate groups, although conformation may also have an effect. The isotropic shift shows a much less remarkable differentiation.

When bound to mineral, however, there is a remarkable similarity between the CSTs for the different bis-phosphonates, even for tiludronate which lacks the –OH group as  $R_1$ . The range of CST principal values does not quite fit those for any protonation state, so it is likely that some other factor is affecting the CSA, such as the replacement of  $\text{H}^+$  or  $\text{Na}^+$  with divalent  $\text{Ca}^{2+}$ . Further investigations should be made

by quantum chemical computation as to the effects of the positions of calcium ions, or the bond angles in the phosphonate group, on the  $^{31}\text{P}$  CST.

The  $^{31}\text{P}$  CST measurements have shown that the binding to digested bone is similar (at least in terms of bis-phosphonate head group conformation) to natural bone, as the CST is very similar for bis-phosphonates bound to natural bone mineral and digested bone mineral. The phosphonate head group is bound tightly to the surface, as shown by the low temperature  $^{31}\text{P}$  CST measurements.

Initial  $^{13}\text{C}-\{^{31}\text{P}\}$  REDOR results appear to support the conclusions of Mukherjee [186] with regards the conformation of pamidronate on the surface of bone mineral. The work here used digested bone mineral rather than natural bone, so this is evidence that digested bone mineral is a good model of bone mineral. If it is the case that digested bone is a good mimic of natural bone, then the conclusions drawn from the  $^{13}\text{C}-\{^{31}\text{P}\}$  REDOR experiments of other bis-phosphonates can be trusted, specifically that the alendronate carbon chain is largely static on the surface of bone, whilst neridronate is very floppy. It should be noted that the errors due to noise in the REDOR spectra are large, so the experiments should be repeated to give stronger support for these conclusions.

## **Chapter 8**

---

# **Application to crystalline neridronate**

---

The PXRD for our sample of one of the bis-phosphonates, neridronate, was found not to be in accordance with the published crystal structure [194]. It is possible that our sample of neridronate is a different polymorph to the published structure. There have been no other reported crystal structures for neridronate, so to the best of our knowledge, the structure of the polymorph that comprises our neridronate sample is currently undetermined.

The PXRD was not of high enough quality to be able to determine the crystal structure of this polymorph of neridronate on its own. Attempts were made, therefore, to find solid-state NMR data that could support the PXRD data to enable determination of the crystal structure of this polymorph, as has been done previously, for example, with the hydrates of risedronate [195].

The  $^{13}\text{C}$  and  $^{31}\text{P}$  CP-MAS spectra of neridronate also supported the view that the structure of our sample is different to the published one: some of the  $^{13}\text{C}$  and  $^{31}\text{P}$  signals are split in two, suggesting that there are two molecules per asymmetric unit, whereas the literature crystal structure only has one. A selection of other well-known solid-state NMR experiments were performed to gain further insight into the structure of the neridronate polymorph; the discussion of the results of these experiments forms

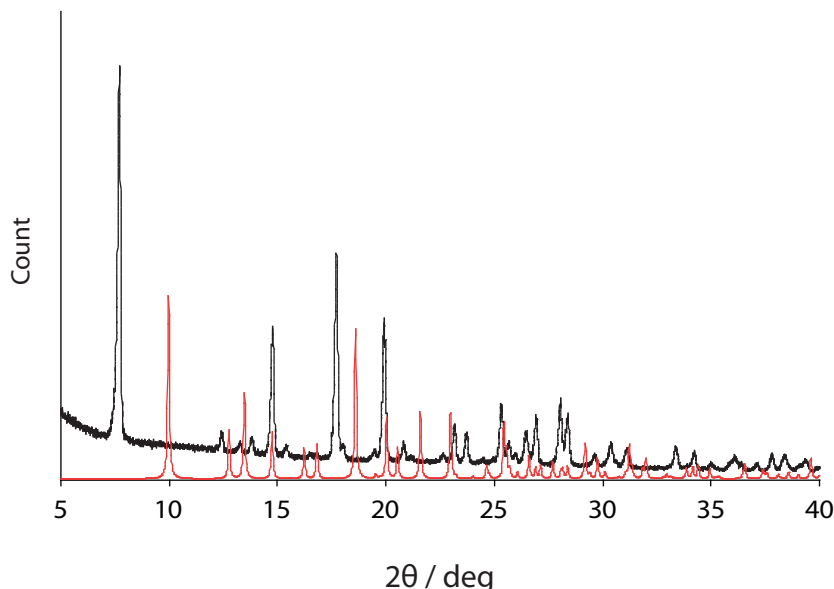


**Figure 8.1** Experimental PXRD pattern for neridronate (black), recorded on a Philips X’Pert diffractometer, sweeping  $2\theta$  angles between  $5^\circ$  and  $40^\circ$  in 6 minutes. The X-ray wavelength was  $1.5406\text{\AA}$ . Overlaid is the simulated powder pattern (red), calculated for the reported neridronate crystal structure [194].

this final chapter of this thesis. The  $^{31}\text{P}$  CST measurements (Table 7.3) and  $^{13}\text{C}-\{^{31}\text{P}\}$  REDOR dephasing curves (Figure 7.15) from the previous chapter should also be considered as part of this discussion.

## 8.1 PXRD

One possibility is that the neridronate sample is a mixture of the known polymorph with another. A very easy way of checking this is with PXRD. Figure 8.1 shows the experimental PXRD pattern with the expected pattern for the known polymorph. The two patterns show very few common lines; for instance the expected intense line at  $2\theta \approx 10^\circ$  is missing from the experimental pattern. This dispels any ideas that there may be some of the known polymorph in the sample.

The PXRD data can be used to get an estimate of the unit cell parameters, using the indexing programs, ITO [7], DICVOL [8] and TREOR [9]. The best fitting unit cell found by DICVOL and TREOR (but not ITO), based upon the goodness of fit parameter,  $M_{20}$ , was a monoclinic system with unit cell parameters of  $a = 7.039\text{\AA}$ ,  $b = 7.518\text{\AA}$  and  $c = 23.079\text{\AA}$ , with  $\beta = 90.3^\circ$ . The volume of this unit cell is  $1220\text{\AA}^3$ ,

and the goodness of fit parameter,  $M_{20} = 15.0$ , is reasonably high but short of absolute confidence [5]. An orthorhombic system ( $\beta = 90^\circ$ ) with very similar parameters also ranks highly ( $M_{20} = 13.4$ ). The ITO algorithm did not find any solutions with a high goodness of fit parameter. Note that the algorithms did not search for triclinic solutions to the PXRD pattern, since there were too many unknown unit cell parameters for triclinic crystal systems.

The density of the known polymorph is  $1.7 \text{ g cm}^{-3}$ . It has been suggested that polymorphs with more than one molecule per asymmetric unit have such an arrangement to maximise bonding interactions, at the expense of efficient crystal packing [196]. Therefore, the new polymorph might be expected to have slightly lower density; this would be consistent with there being four molecules per unit cell (two asymmetric units per unit cell), which gives a density of  $1.5 \text{ g cm}^{-3}$ .

The possible space groups that fit with this conclusion are P2, P2<sub>1</sub>, Pm and Pc. The more likely of these, based on frequency in known crystal structures in the Cambridge Crystallographic Database, are P2<sub>1</sub> (5% of all known structures) and Pc (0.5%). Neither of these cause systematic exclusions in the PXRD that could rule them out of contention.

## 8.2 Bond angle measurements by REDOR correlation with J-coupling

The P–C–P bond angle in a bis-phosphonate can be measured using the  $^{13}\text{C}-\{^{31}\text{P}\}$  REDOR dephasing curve for the bis-phosphonate (C1) carbon. The signal for this carbon is split into a triplet by *J*-coupling to the two  $^{31}\text{P}$ . The relative dephasing rate of the central component of the triplet to the outer components is related to the bond angle, due to the different dipolar coupling behaviour when the two phosphorus spins are aligned (outer components of triplet) or opposed (central component of triplet).

The dynamics of a three-spin system under REDOR recoupling has been described previously [197]. Under the assumption that the dipolar coupling between the two  $^{31}\text{P}$  atoms can be neglected, the dipolar coupling Hamiltonian can be expressed as a sum of pair-wise interactions (i.e. the coupling of the  $^{13}\text{C}$  spin to each  $^{31}\text{P}$  can be considered independently)\*.

---

\*How good this assumption is depends upon the bond angles, since this affects the P–P distance. It

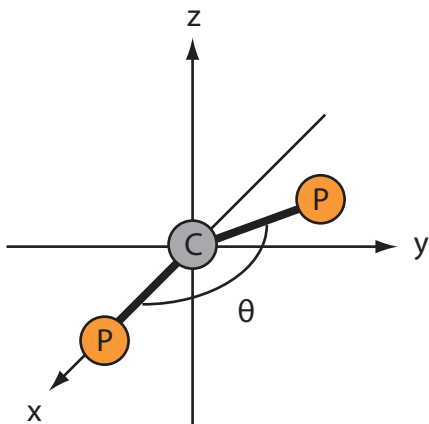


**Figure 8.2** The orientation of a molecular frame for a bis-phosphonate, showing the two phosphorus atoms in the  $xy$ -plane, separated by bond angle,  $\theta$ . For the purposes of the discussion in the text, the phosphorus atom on the  $x$ -axis is given the label, 'A', and the other phosphorus is given the label, 'B'.

Consider two phosphorus atoms (or equivalently dipolar coupling vectors) separated by an angle,  $\theta$ , the bond angle. The molecular reference frame can be chosen so that the  $x$ -axis of the frame co-incides with one of the C–P bonds, and the second C–P bond lies in the  $xy$ -plane, at an angle,  $\theta$ , from the first bond, as shown in Figure 8.2. A crystallite orientation,  $\Omega_{\text{MR}}$ , relates the molecular reference frame described above to the rotor frame.

The average  $^{13}\text{C}$  dipolar precession frequency for the REDOR experiment (that is, the mean precession frequency caused by dipolar coupling to a  $^{31}\text{P}$  nucleus in the absence of chemical shift over one rotor cycle of the REDOR sequence with dephasing pulses) for such a crystallite has been shown to be [198]:

$$\begin{aligned}\overline{\omega_A} &= \pm 2D_A [\cos^2 \alpha \sin 2\beta \sin \gamma + \sin 2\alpha \sin \beta \cos \gamma] \\ \overline{\omega_B} &= \pm 2D_B [\cos^2(\alpha - \theta) \sin 2\beta \sin \gamma + \sin 2(\alpha - \theta) \sin \beta \cos \gamma],\end{aligned}\quad (8.1)$$

where  $\overline{\omega_A}$  and  $\overline{\omega_B}$  are the values for the average dipolar precession frequency to each of the two  $^{31}\text{P}$  nuclei, and  $D_A$  and  $D_B$  are the corresponding dipolar coupling constants. Each of the  $^{31}\text{P}$  spins have two spin states, leading to four possible dipolar precession

---

also only holds at short dephasing times. However, in the final analysis of the experimental REDOR dephasing curves, it is recommended that the curves are simulated for a three-spin system using SPIN-EVOLUTION [55], which includes the  $^{31}\text{P}$ – $^{31}\text{P}$  dipolar coupling anyway.

frequencies for the  $^{13}\text{C}$  spin, which are:

$$\overline{\omega_i} = \pm\overline{\omega_A} \pm \overline{\omega_B}, \quad (8.2)$$

with  $i = 1 \dots 4$ , denoting the four dipolar frequencies, which are  $\Omega_{\text{MR}}$ -dependent.

Now, if the  $J$ -coupling is not strong enough to resolve the triplet, the observed signal for a molecule with molecular frame orientation,  $\Omega_{\text{MR}}$ , is the sum of the contributions from all four dipolar frequencies, which is found to be [197]:

$$S(\alpha, \beta, \gamma) \propto \sum_i \cos(\overline{\omega_i} n\tau_R). \quad (8.3)$$

The REDOR dephasing curve for the  $^{13}\text{C}$  spin,  $S(n\tau_R)$ , can then be found by integrating Equation (8.3) over all molecular frame orientation angles:

$$S(n\tau_R) = \frac{1}{8\pi^2} \sum_{i=1}^4 \int_{\alpha=0}^{2\pi} \int_{\beta=0}^{\pi} \int_{\gamma=0}^{2\pi} \cos(\overline{\omega_i} n\tau_R) \sin\beta d\alpha d\beta d\gamma. \quad (8.4)$$

If this is done, it is found that the initial REDOR behaviour for the observed spin (when  $\overline{\omega_i} n\tau_R \ll 1$ ) is independent of the bond geometry [197].

However, if the triplet is resolved, this is not the case. If the  $^{31}\text{P}$  spins are parallel (i.e. the outer components of the triplet), the possible average dipolar precession frequencies are:

$$\overline{\omega_{\uparrow\uparrow}} = \pm(\overline{\omega_A} + \overline{\omega_B}), \quad (8.5)$$

whereas if they are opposed (i.e. the central component of the triplet), the average dipolar precession frequencies are:

$$\overline{\omega_{\uparrow\downarrow}} = \pm(\overline{\omega_A} - \overline{\omega_B}). \quad (8.6)$$

The negative average dipolar precession frequencies in Equations 8.5 and 8.6 can be ignored, as the sign of the dipolar precession frequency has no effect on the cosine term in Equation 8.4. The integration in Equation 8.4 to calculate the dephasing curves can now be performed separately for the parallel  $^{31}\text{P}$  spins and opposed  $^{31}\text{P}$  spins, since these two cases are resolved by the  $J$ -coupling.

At short dephasing times, the cosine term in Equation (8.4) can be approximated to:

$$\cos(\overline{\omega_i} n\tau_R) = 1 - \frac{(\overline{\omega_i} n\tau_R)^2}{2}. \quad (8.7)$$

Also, assume that the C–P bond lengths are the same, so the coupling constants  $D_A$  and  $D_B$  are identical, with some value,  $D$ . With these approximations, performing the integration over crystallite orientations in Equation (8.4) using the dipolar transition frequency for parallel spins (Equation (8.5)), the initial section of the dephasing curve of the outer components of the triplet is described by:

$$S_{\uparrow\uparrow}(n\tau_R) = 1 - \frac{8}{15}(n\tau_R D)^2(5 + 3 \cos 2\theta). \quad (8.8)$$

The initial section of the dephasing curve for the central component of the triplet is found using Equation (8.6) to be:

$$S_{\uparrow\downarrow}(n\tau_R) = 1 - \frac{16}{5}(n\tau_R D)^2 \sin^2 \theta. \quad (8.9)$$

By comparison of these results with those of Pan *et al.* for a spin-pair [198]:

$$S(n\tau_R) = 1 - \frac{16}{15}(n\tau_R D)^2, \quad (8.10)$$

the initial part of the dephasing curve has been shown to be equivalent to an isolated two-spin dipolar coupling with apparent dipolar coupling constants of:

$$D_{\uparrow\uparrow} = D \sqrt{\frac{5 + 3 \cos 2\theta}{2}}, \quad (8.11)$$

for the outer components of the triplet and:

$$D_{\uparrow\downarrow} = D \sqrt{3} \sin \theta, \quad (8.12)$$

for the central component. The ratio of the two is thus:

$$\frac{D_{\uparrow\downarrow}}{D_{\uparrow\uparrow}} = \sqrt{\frac{6 \sin^2 \theta}{5 + 3 \cos 2\theta}}. \quad (8.13)$$

The forms of Equations (8.11)–(8.13) are plotted in Figure 8.3. From the ratio of the measured effective dipolar coupling constant at short dephasing time for the inner and outer peaks of the triplet, the P–C–P bond angle,  $\theta$ , can be determined. Note that Equation (8.13) is symmetrical about  $\theta = 90^\circ$ , so angles greater than  $90^\circ$  can not be told apart from angles less than  $90^\circ$ , although it can be presumed that bond angles in bis-phosphonates are approximately tetrahedral.

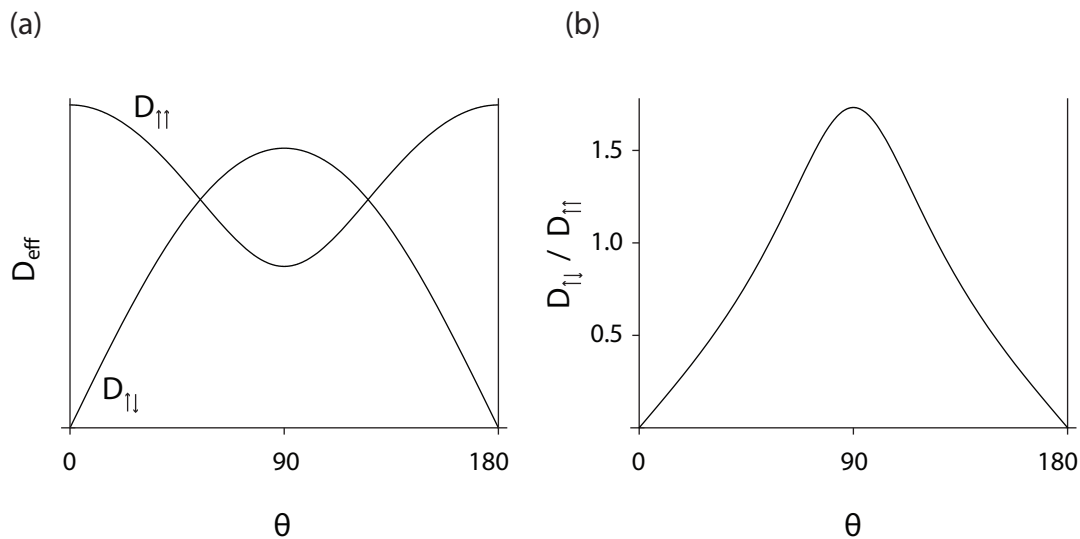


**Figure 8.3** (a) Plot of variation in apparent spin-pair coupling strength,  $D_{\text{eff}}$  at short dephasing time for the three spin system, where the coupling spins are parallel ( $D_{111}$ ) and opposed ( $D_{11}$ ), with the P–C–P bond angle,  $\theta$ . (b) Plot of the ratio  $D_{11} / D_{111}$  against bond angle.

With crystalline alendronate, for example, the dephasing curves (at short dephasing times) for the bis-phosphonate headgroup carbon triplet components can be fitted (using a least squares fitting routine) to values of  $D_{11} = -2510 \text{ Hz}$  and  $D_{111} = -1790 \text{ Hz}$ . Figure 8.4 shows the clear difference between the dephasing of the central and outer components of the triplet. The ratio of  $D_{11} : D_{111}$  of 1.40 equates to a bond angle of  $110^\circ$ , which is very close to the tetrahedral angle, and compares well with the known bond angle from XRD studies of  $109.9^\circ$  [193]. The error in the bond angle measurement from this REDOR approach is about  $\pm 5^\circ$  (calculated from the maximum errors in  $D_{11}$  and  $D_{111}$  caused by random noise in the  $^{13}\text{C}-\{{}^{31}\text{P}\}$  REDOR spectrum), which is admittedly much less accurate than the measurement from XRD.

For neridronate, also shown in Figure 8.4, the measured bond angle is  $119^\circ \pm 3^\circ$ . This is considerably away from the tetrahedral angle. However, a larger bond angle for neridronate is not unprecedented; the crystal structure for the known polymorph shows a bond angle of  $114^\circ$  [194]. So, it seems that the new polymorph of neridronate may also have a large P–C–P angle. If this bond angle is very different in neridronate to the other bis-phosphonates, this may go some way to explaining why the neridronate CST measurements in Table 7.3 were very different from other bis-phosphonates, even when the protonation state was the same. It must be added, however, that in the

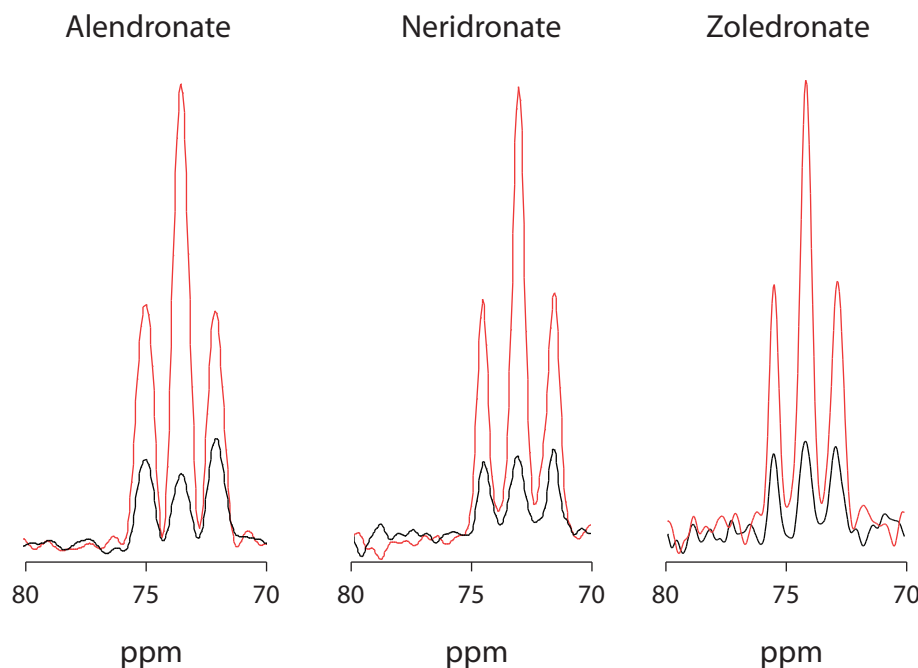


**Figure 8.4**  $^{13}\text{C}$ - $\{{}^{31}\text{P}\}$  REDOR spectra of the triplet in crystalline alendronate, neridronate and zoledronate, acquired with (black lines - dephased spectra) and without (red lines - reference spectra)  ${}^{31}\text{P}$  dipolar coupling, for a dephasing time of 0.5 ms. Spectra show that the central peak of the triplet dephases more rapidly than the outer peaks, though by slightly different amounts in each case. Note though that this particular dephasing time does not count as  $\overline{\omega_i}n\tau_R \ll 1$ . Shorter dephasing times are required to perform the bond angle analysis described in the text.

new neridronate polymorph there are two molecules per unit cell, but their triplet signals are overlapping and there is no way to resolve them. This may mean that the effective dipolar coupling constants (and the corresponding bond angles) measured are an average of the values for each of the two molecules in the asymmetric unit.

Unfortunately these measurements can not be repeated on the mineral-bound forms as there is no resolution of the triplet. For tiludronate and pamidronate the triplet is not well resolved even in the crystalline form. For zoledronate, the triplet dephasing, shown in Figure 8.4, appears qualitatively similar to that of neridronate, although an insufficient number of short dephasing times were recorded due to high demand for spectrometer time limiting the experiments available, so accurate quantitative analysis could not be performed. The measured bond angle from XRD is  $115^\circ$  [199].

Rather than measuring only the very shortest dephasing times, it would be better to simulate the full dephasing curve using SPIN-EVOLUTION [55], assuming a three-

spin system and using a least squares fitting procedure for the bond angle. This has not been implemented yet, as it requires significantly more computation and lacks the convenient simplicity of Equation 8.13.

### 8.3 $^{31}\text{P}$ - $^{31}\text{P}$ DQ-SQ correlation

Figure 8.5 shows neridronate  $^{31}\text{P}$  DQ-SQ correlation spectra for two different double quantum excitation times, using POST-C7 to excite the DQ coherence [106]. Cross peaks are expected to be intense if the two  $^{31}\text{P}$  spins that give rise to it are close in space. Immediately these spectra identify the signals labelled A and D as being from the same molecule, whilst B and C are from the other molecule in the asymmetric unit. The spins in each pair are separated by approximately 3 Å, given standard P-C bond lengths and tetrahedral geometry at the carbon atom.

The other signals in Figure 8.5 are considerably weaker and correspond to double quantum build-up between spins in different molecules. The presence of these confirms the fact that there are two molecules per asymmetric unit, as opposed to the possibility of being a mixture of two polymorphs, as in zoledronate. Amongst the stronger of these cross peaks are  $^{31}\text{P}_\text{A}-^{31}\text{P}_\text{A}$ ,  $^{31}\text{P}_\text{B}-^{31}\text{P}_\text{B}$  and  $^{31}\text{P}_\text{C}-^{31}\text{P}_\text{D}$ , whilst completely absent are signals corresponding to contacts between  $^{31}\text{P}_\text{A}-^{31}\text{P}_\text{B}$  and  $^{31}\text{P}_\text{D}-^{31}\text{P}_\text{D}$ . The last of these is interesting; the furthest apart a spin can be from its nearest equivalent spin in a neighbouring asymmetric unit is the shortest lattice parameter, which is a little over 7 Å. This means that all other observed contacts must be closer than 7 Å (but considerably more distant than the 3 Å between the phosphorus atoms in the same molecule).

Simulations were set-up to see if this criterion could be met for any of the four possible space groups, determined previously in Section 8.1. The asymmetric unit was randomly generated, given presumed  $^{31}\text{P}_\text{A}-^{31}\text{P}_\text{D}$  and  $^{31}\text{P}_\text{B}-^{31}\text{P}_\text{C}$  distances of 3.1 Å, and the positions of the rest of the phosphorus atoms in the unit cell was built-up from the crystal symmetry. The closest contacts for all pairs of  $^{31}\text{P}$  spins was measured and ranked. This rank order was then compared with the experimental cross peak intensities in Figure 8.5. For none of the four monoclinic space groups were solutions found, even after 24 hours of searching. However, with the unique lattice angle,  $\beta$ , being close to 90°, it is conceivable that the crystallographic axes are labelled wrongly. By switching the  $a$ ,  $b$  and  $c$  labels for the crystallographic axes, solutions

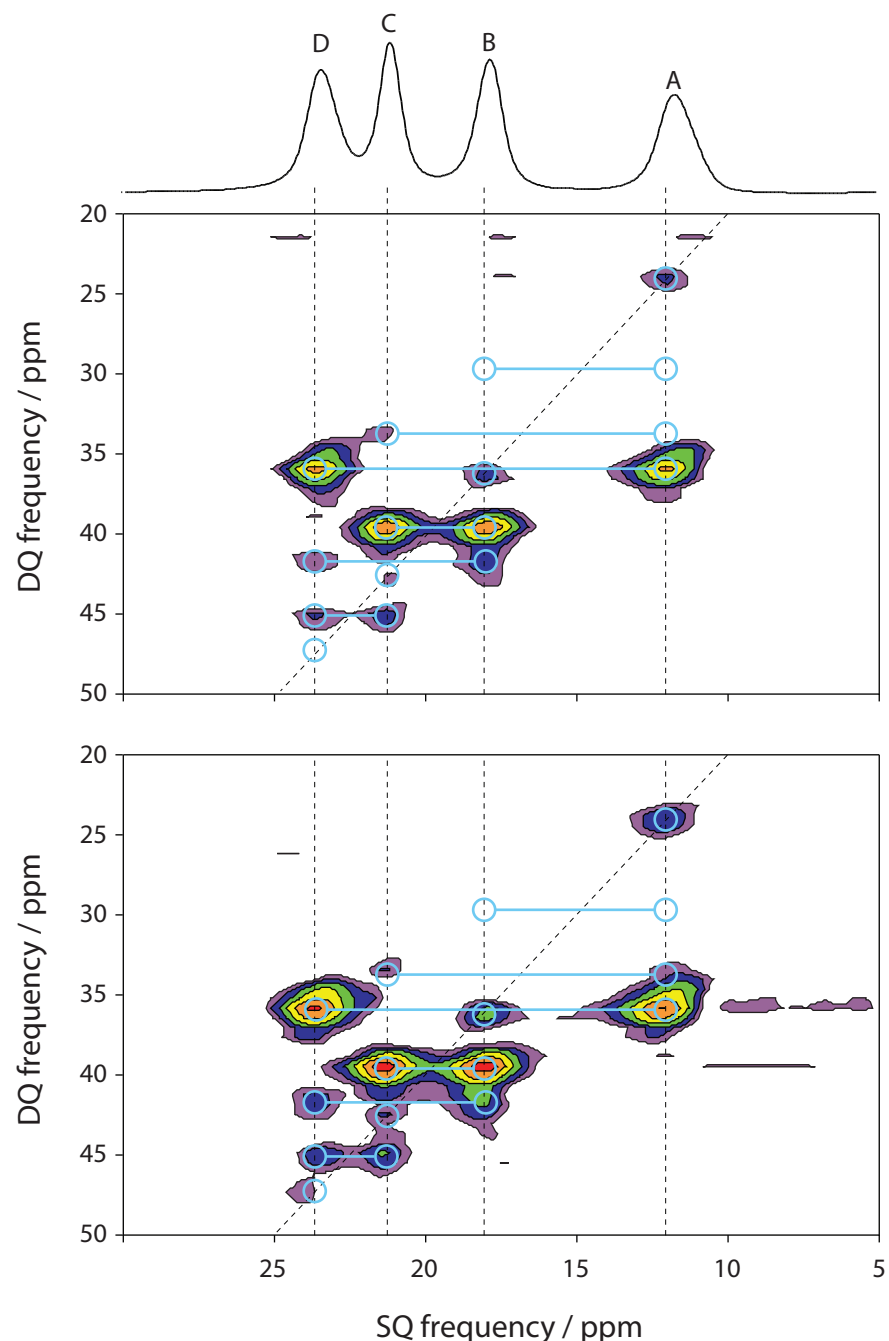


**Figure 8.5** Neridronate  $^{31}\text{P}$  SQ-DQ spectra using POST-C7 double quantum excitation, for two build-up times of 0.56 ms (top) and 1.12 ms (bottom). The light blue linked circles show the expected positions of peaks if two signals are correlated by being close in space. Red contours show the highest intensity peaks. Also marked is the diagonal on which self-correlation peaks may be expected.

could be found where the rank order of  $^{31}\text{P}$ - $^{31}\text{P}$  distances approximately matched the experimental rank order of cross peak intensities, for P2 and P2<sub>1</sub> when  $b = 7.04 \text{ \AA}$ , and for P<sub>c</sub> and P<sub>m</sub> when  $b = 23.08 \text{ \AA}$ .

The data from this experiment alone is, therefore, insufficient to determine the space group. It does, however, cast doubt onto the solutions of the PXRD patterns. Ideally, the  $^{31}\text{P}$ - $^{31}\text{P}$  double quantum build-up curve could give quantitative measurements of the  $^{31}\text{P}$ - $^{31}\text{P}$  distances. However, in this case, analysis is complicated by the fact that an isolated spin-pair approximation is inappropriate.

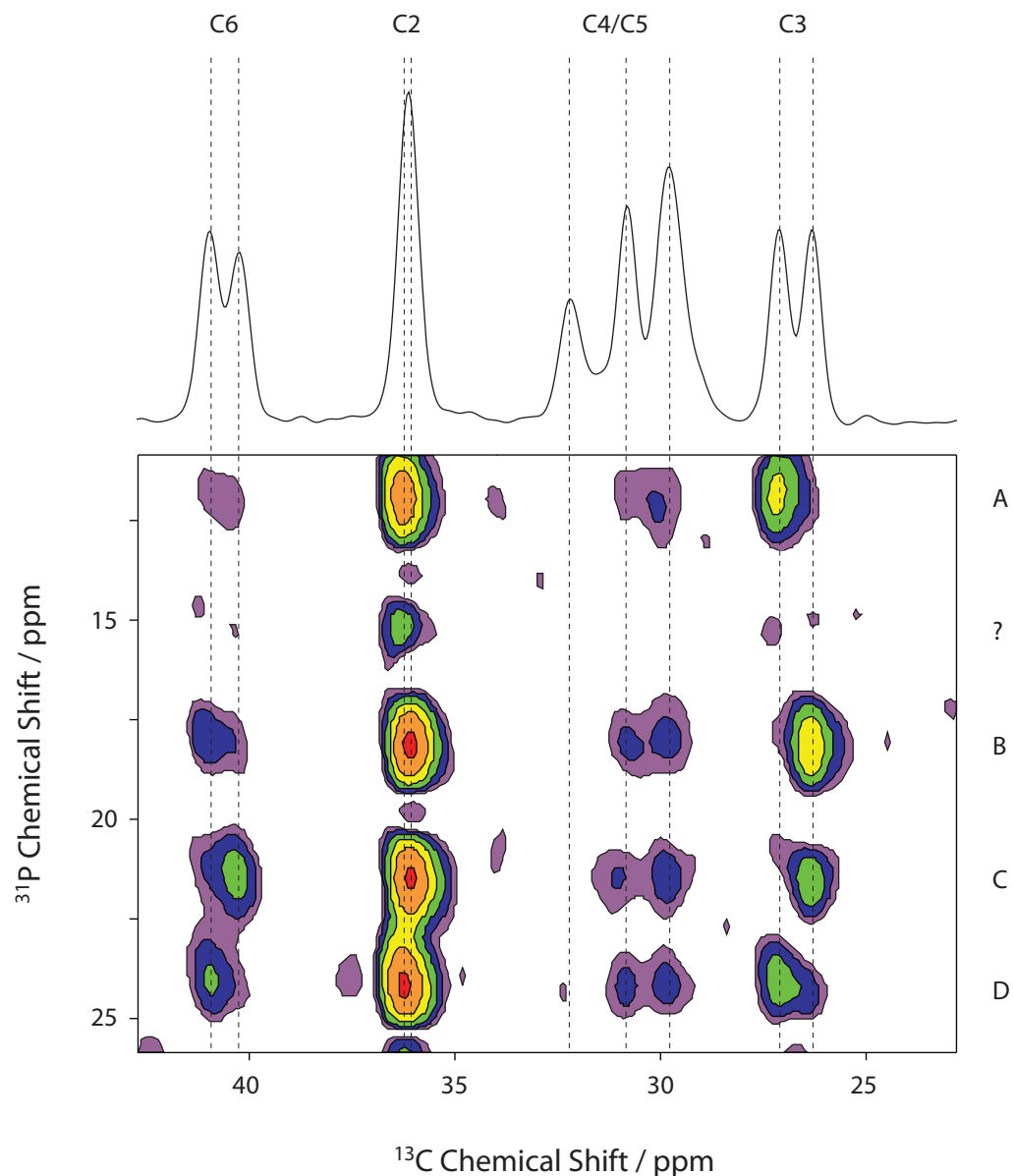
#### 8.4 $^{31}\text{P}$ - $^{13}\text{C}$ DCP

Figure 8.6 shows the  $^{31}\text{P}$ - $^{13}\text{C}$  correlations in neridronate determined by a DCP experiment [189]. Figure 7.14 shows the assignment of the  $^{13}\text{C}$  signals. Each  $^{13}\text{C}$  signal is split in two components, as there are two molecules per asymmetric unit, although in some cases these signals are not resolved. The three resolved peaks that correspond to C4 and C5 have not been assigned.

First, notice that the  $^{13}\text{C}$  peak for C2 is split (by 0.2 ppm), which was not seen in the CP-MAS spectrum. For C2 and C3, one of the two  $^{13}\text{C}$  signals of each form cross peaks with both  $^{31}\text{P}_A$  and  $^{31}\text{P}_D$ , whilst the other  $^{13}\text{C}$  signals form a cross peaks with  $^{31}\text{P}_B$  and  $^{31}\text{P}_C$ . This confirms the findings from the  $^{31}\text{P}$  SQ-DQ correlation experiment in the previous section, that  $^{31}\text{P}_A$  and  $^{31}\text{P}_D$  are in the same molecule, and  $^{31}\text{P}_B$  and  $^{31}\text{P}_C$  are in the other. Notice also that for the  $^{13}\text{C}$  signals for C3, the more intense cross peaks are with  $^{31}\text{P}_A$  or  $^{31}\text{P}_B$  (which were found to be mono-protonated, see Section 7.3), rather than  $^{31}\text{P}_C$  or  $^{31}\text{P}_D$  (which were found to be bis-protonated). This indicates that the carbon chains in both molecules in the asymmetric unit are *gauche* to the mono-protonated phosphonate, and *trans* to the bis-protonated phosphonate.

For C3, there appear to be weak cross peaks corresponding to intermolecular  $^{31}\text{P}$ - $^{13}\text{C}$  cross polarisation. Interestingly though, there are no cross peaks at all for at least one of the  $^{13}\text{C}$  signals in the C4/C5 region, indicating that the corresponding carbon is somehow more remote from both intramolecular and intermolecular phosphorus contacts than C3.

The cross peaks with the C6 signals presumably arise from solely intermolecular phosphorus contacts, since the distances to the phosphorus atoms in the same molecule is likely to be large. It appears that the C6 with the higher  $^{13}\text{C}$  chemical shift is



**Figure 8.6** Neridronate  $^{13}\text{C}$ - $^{31}\text{P}$  DCP spectrum, showing the sidechain region of the  $^{13}\text{C}$  spectrum only. This is the sum of several spectra with different  $^{13}\text{C}$ - $^{31}\text{P}$  CP contact times. The  $^{13}\text{C}$  CP-MAS spectrum is shown at the top.

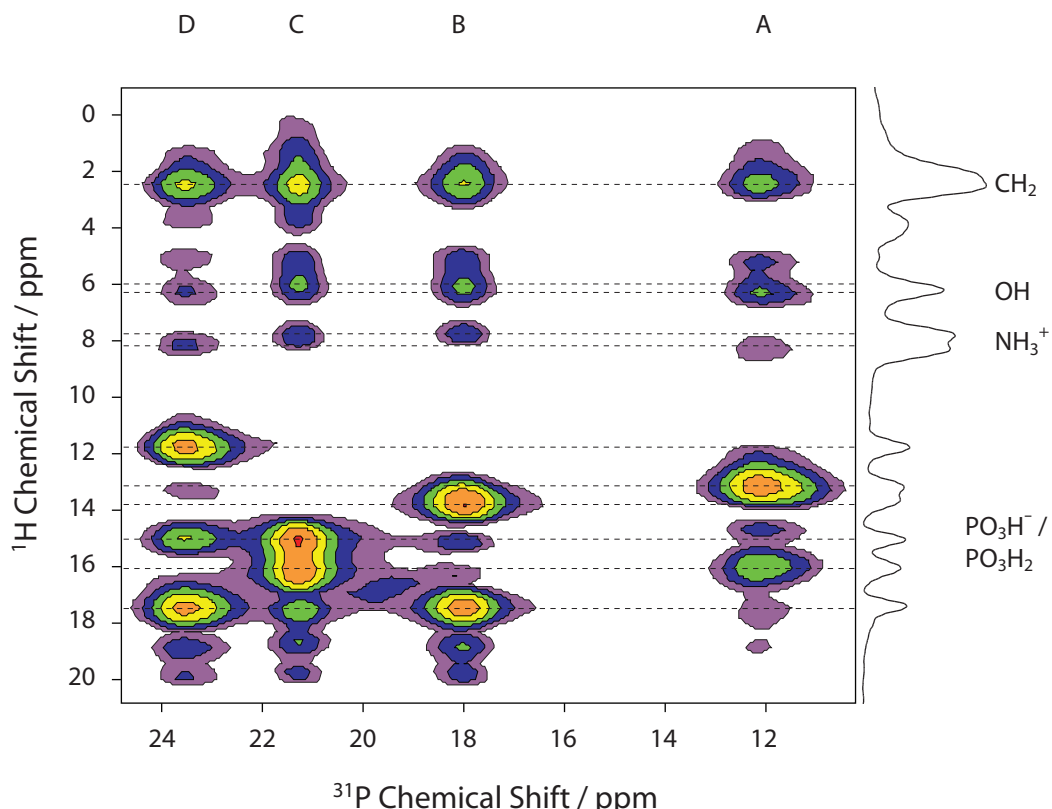


**Figure 8.7** Neridronate  $^1\text{H}$ - $^{31}\text{P}$  HETCOR spectrum, using FSLG homonuclear proton decoupling to obtain the high resolution proton dimension. This scales the proton chemical shift, so the scale has been adjusted by eye for best fit to the 30 kHz MAS one-dimensional proton spectrum. The  $^1\text{H}$ - $^{31}\text{P}$  contact time was 0.1 ms. Also shown on the right is the one-dimensional high resolution  $^1\text{H}$  spectrum using FSLG homonuclear decoupling, with assignments of the  $^1\text{H}$  signals.

closer in space to  $^{31}\text{P}_B$  and  $^{31}\text{P}_D$ , whilst the other C6 is closer to  $^{31}\text{P}_A$  and  $^{31}\text{P}_C$ . The more intense cross peaks are those with  $^{31}\text{P}_C$  and  $^{31}\text{P}_D$ , the bis-protonated phosphonate groups. This is slightly unexpected, as it is the other phosphonates,  $^{31}\text{P}_A$  and  $^{31}\text{P}_B$ , that are the charged phosphonate groups, which presumably have a stronger attraction to the  $-\text{NH}_3^+$  group, which is directly adjoining these C6 atoms.

## 8.5 $^1\text{H}$ - $^{31}\text{P}$ HETCOR

Figure 8.7 shows a  $^1\text{H}$ - $^{31}\text{P}$  HETCOR spectrum of neridronate with homonuclear proton decoupling by FSLG [200]. The proton signals were assigned using a combination of this spectrum, a  $^1\text{H}$ - $^{13}\text{C}$  HETCOR spectrum and chemical intuition.

The phosphonate proton region of the HETCOR spectrum in Figure 8.7 ( $^1\text{H}$  chemical shift greater than 10 ppm) can be used to assign the  $^1\text{H}$  signals to particular phosphonate groups. With the exception of the signal with the highest  $^1\text{H}$  chemical shift (17.4 ppm), the  $^1\text{H}$  signals can be assigned to the phosphonate group with which the  $^1\text{H}$ - $^{31}\text{P}$  cross peak is most intense. From lowest  $^1\text{H}$  chemical shift to highest, they are assigned to  $^{31}\text{P}_D$ ,  $^{31}\text{P}_A$ ,  $^{31}\text{P}_B$ ,  $^{31}\text{P}_C$  and  $^{31}\text{P}_C$ . Recalling that  $^{31}\text{P}_A$  and  $^{31}\text{P}_B$  have one proton and  $^{31}\text{P}_C$  and  $^{31}\text{P}_D$  have two, this places the final proton, that with the chemical shift of 17.4 ppm, with  $^{31}\text{P}_D$ . Since the cross peak of this proton with  $^{31}\text{P}_B$  is also intense, this indicates a close intermolecular contact. The protons with chemical shifts of 15.0 ppm and 16.1 ppm, which are both assigned to be part of the  $^{31}\text{P}_C$  phosphonate group, also show strong intermolecular phosphorus contacts, with  $^{31}\text{P}_D$  and  $^{31}\text{P}_A$  respectively.<sup>†</sup>

The spectrum also shows resolution of the  $^1\text{H}$  signals of the  $-\text{NH}_3^+$  groups of the two molecules in the asymmetric unit. The  $-\text{NH}_3^+$  group with the higher  $^1\text{H}$  chemical shift has cross peaks with  $^{31}\text{P}_A$  and  $^{31}\text{P}_D$ , and the other  $-\text{NH}_3^+$  group  $^1\text{H}$  signals have cross peaks with  $^{31}\text{P}_B$  and  $^{31}\text{P}_C$ . This is in contrast to the  $^{13}\text{C}$ - $^{31}\text{P}$  DCP spectrum (Figure 8.6), where it was found that  $^{31}\text{P}_B$  and  $^{31}\text{P}_D$  had stronger cross peaks with the same  $^{13}\text{C}$  signal from C6 (which is only two bonds away from the  $-\text{NH}_3^+$  group protons), and  $^{31}\text{P}_A$  and  $^{31}\text{P}_C$  with the other  $^{13}\text{C}$  signal from C6. There are also moderately strong cross peaks of the  $^1\text{H}$  signal of the C6 protons (these have a chemical shift of 3.8 ppm due to the nearby  $-\text{NH}_3^+$  group) with  $^{31}\text{P}_C$  and  $^{31}\text{P}_D$ . This perhaps indicates a conformation where  $^{31}\text{P}_C$  is close to C6 in one molecule, but closer to  $-\text{NH}_3^+$  in the other molecule (and similarly for  $^{31}\text{P}_D$ ). Whether there is a realistic crystal structure where this is the case remains to be seen. The sources of the cross peaks with  $^1\text{H}$  chemical shifts of 5 ppm, 19 ppm and 20 ppm are unknown; these do not appear in the one-dimensional  $^1\text{H}$  spectrum.

## 8.6 $^1\text{H}$ - $^{13}\text{C}$ HETCOR

Figure 8.8 shows the  $^1\text{H}$ - $^{13}\text{C}$  HETCOR spectrum for neridronate. One of the key features to observe here is again the splitting of the signals for the  $-\text{NH}_3^+$  protons, and

<sup>†</sup>The latter of these could also be a close contact between a phosphonate proton and the  $^{31}\text{P}$  of the other phosphonate group in the same molecule, but the known crystal structures of similar compounds show this distance is often larger than the distance to phosphonate groups in other molecules.

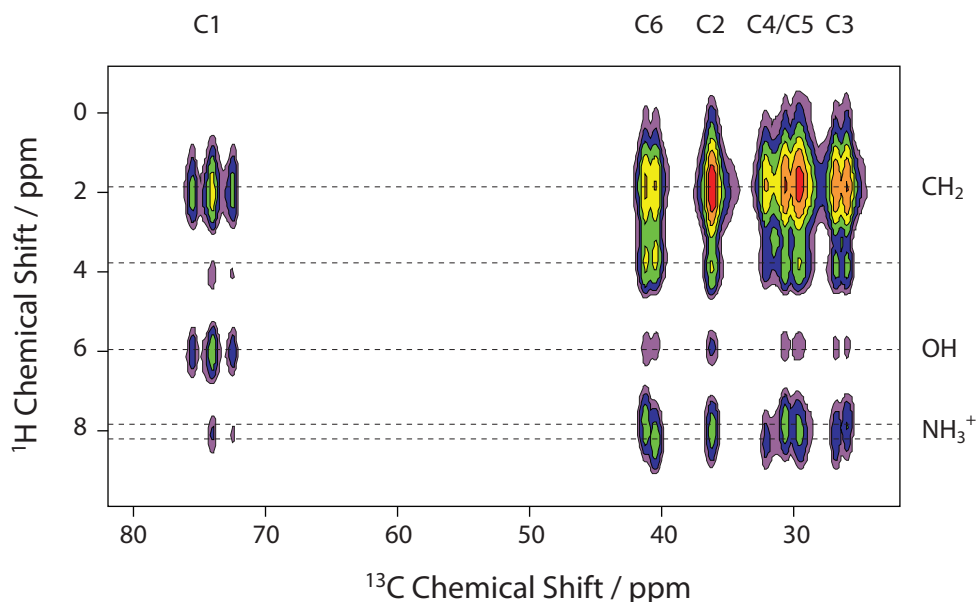


**Figure 8.8** Neridronate  $^1\text{H}$ - $^{13}\text{C}$  HETCOR spectrum, using FSLG homonuclear proton decoupling to obtain the high resolution proton dimension. The  $^1\text{H}$ - $^{13}\text{C}$  contact time was 1.2 ms, with ramped CP [161].

the correlations of these signals with the  $^{13}\text{C}$  signals for C3 and C6.

The  $-\text{NH}_3^+$  group signal with the higher  $^1\text{H}$  chemical shift (8.2 ppm) has a cross peaks with the  $^{13}\text{C}$  signals at 40.4 ppm (C6) and 27.1 ppm (C3), whilst the  $-\text{NH}_3^+$  group signal with the lower  $^1\text{H}$  chemical shift (7.6 ppm) has a cross peaks with the  $^{13}\text{C}$  signals at 41.1 ppm (C6) and 26.2 ppm (C3). Recall that, from the  $^{31}\text{P}$ - $^{13}\text{C}$  DCP experiment (Figure 8.6), the 27.1 ppm C3  $^{13}\text{C}$  signal was assigned to the same molecule as  $^{31}\text{P}_A$  and  $^{31}\text{P}_D$  and the 26.2 ppm C3  $^{13}\text{C}$  signal to the same molecule as  $^{31}\text{P}_B$  and  $^{31}\text{P}_C$ .

Now, in Figure 8.8, it appears that the cross peaks with  $^1\text{H}$  signals for the  $-\text{NH}_3^+$ ,  $-\text{OH}$  and  $-\text{CH}_2-$  groups with  $^{13}\text{C}$  signals from C2–C6 have very uniform intensity, even though the distances involved are greatly different. This is because, during the ramped CP contact time, the  $^1\text{H}$  magnetisation can diffuse freely along the protons attached to the carbon backbone, giving a uniform CP efficiency to  $^{13}\text{C}$  spins from C2–C6, but not to C1, which is separated from the extended proton network. This also explains why no cross peaks are seen for phosphonate  $^1\text{H}$  signals, since these protons are relatively isolated from the others. Transfer of magnetisation between different molecules in the unit cell is also weak.

Therefore it is postulated that the  $^{13}\text{C}$  spins with signals at 40.4 ppm (C6) and

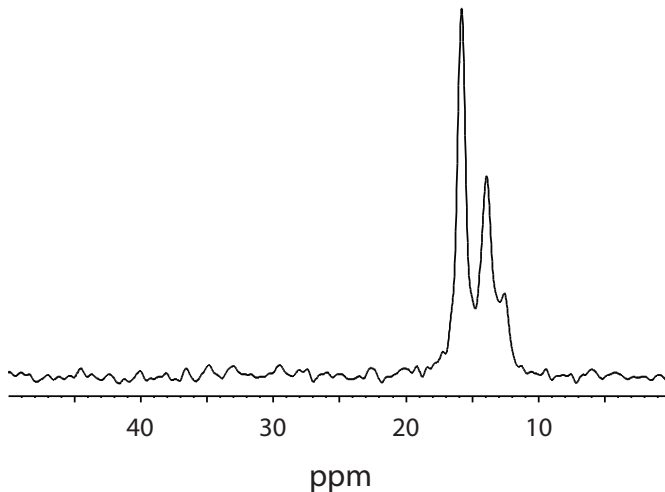


**Figure 8.9** Neridronate  $^{15}\text{N}$  CP-MAS spectrum.

27.1 ppm (C3) are in the same molecule, as are the  $^{13}\text{C}$  spins with signals at 41.1 ppm (C6) and 26.2 ppm (C3). Recall that, from the  $^{31}\text{P}$ - $^{13}\text{C}$  DCP experiment (Figure 8.6), the  $^{13}\text{C}$  signal at 27.1 ppm (C3) was assigned to the same molecule as  $^{31}\text{P}_\text{A}$  and  $^{31}\text{P}_\text{D}$  and the  $^{13}\text{C}$  signal at 26.2 ppm (C3) to the same molecule as  $^{31}\text{P}_\text{B}$  and  $^{31}\text{P}_\text{C}$ . Thus now, with the exception of the  $^{13}\text{C}$  signals of C4 and C5, all the resolved  $^{31}\text{P}$ ,  $^{13}\text{C}$  and  $^1\text{H}$  peaks have been assigned to one of the two molecules in the asymmetric unit.

## 8.7 $^{15}\text{N}$ CP-MAS and $^1\text{H}$ - $^{15}\text{N}$ HETCOR

Figure 8.9 shows the neridronate  $^{15}\text{N}$  CP-MAS spectrum. This shows three incompletely resolved signals, whereas only two are expected (one from each molecule in the asymmetric unit). The two more intense signals are highly asymmetric too; one is significantly broader than the other, although the total intensity is similar. There was no change in the appearance of the spectrum observed with different CP contact times and MAS rates.

The  $^1\text{H}$ - $^{15}\text{N}$  HETCOR spectrum is shown in Figure 8.10. This can be used to assign the  $^{15}\text{N}$  isotropic chemical shifts: the  $^{15}\text{N}$  signal at 13.9 ppm is assigned to the same molecule as  $^{31}\text{P}_\text{A}$  and  $^{31}\text{P}_\text{D}$ , and the  $^{15}\text{N}$  signal at 15.8 ppm is assigned to the same molecule as  $^{31}\text{P}_\text{B}$  and  $^{31}\text{P}_\text{C}$ . A cross peak is seen for the unidentified  $^{15}\text{N}$  signal at 27.1 ppm with the  $^1\text{H}$  signal at 8.2 ppm ( $-\text{NH}_3^+$ ), but not with the  $^1\text{H}$  signal at 2 ppm

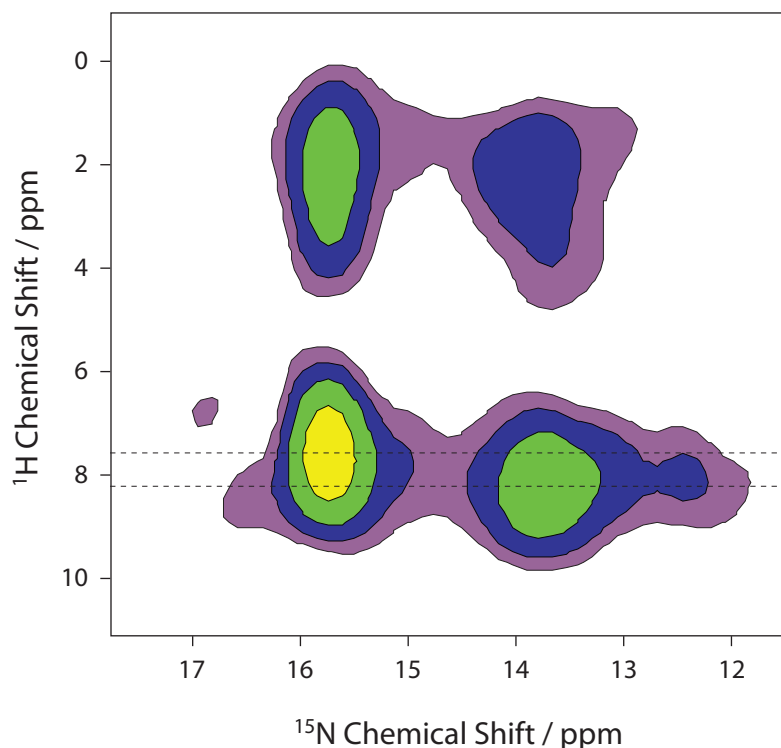


**Figure 8.10** Neridronate  $^1\text{H}$ - $^{15}\text{N}$  HETCOR spectrum, using FSLG homonuclear proton decoupling to obtain the high resolution proton dimension. The  $^1\text{H}$ - $^{15}\text{N}$  contact time was 1.5 ms.

( $-\text{CH}_2$ ).

The curious form of the  $^{15}\text{N}$  CP-MAS spectrum could indicate an impurity, but this has been ruled out using liquid-state NMR. It may instead indicate a degree of localised disorder.

## 8.8 Experimental procedure

Neridronic acid was purchased from Sigma, and used without further purification.

The  $^{31}\text{P}$  DQ/SQ correlation experiment used POST-C7 pulse sequence units [106] to excite and de-excite double quantum coherence. The MAS rate was 12.5 kHz. There were 128  $t_1$  data points recorded using a States-TPPI acquisition scheme, with 32 scans per point, with a  $t_1$  increment of  $80\ \mu\text{s}$ . During the POST-C7, FSLG decoupling [200] was applied with a field strength of 90 kHz, and during acquisition TPPM decoupling was applied with a field strength of 78 kHz. The DQ excitation

times were 0.56 ms and 1.12 ms.

The  $^{31}\text{P}$ - $^{13}\text{C}$  double cross polarisation (DCP) [189] experiment acquired 64  $t_1$  data points with a TPPI acquisition scheme, with 4160 scans per point and a  $t_1$  increment of 200  $\mu\text{s}$ . The CP contact times were 4 ms for  $^1\text{H}$ - $^{31}\text{P}$  and 9 ms for  $^{31}\text{P}$ - $^{13}\text{C}$ , both using a ramped CP profile [161]. The total experiment time was 18 days.

The  $^1\text{H}$ - $^{31}\text{P}$ ,  $^1\text{H}$ - $^{13}\text{C}$  and  $^1\text{H}$ - $^{15}\text{N}$  HETCOR experiments were performed at a MAS rate of 12.5 kHz. The 64  $t_1$  data points were acquired with a States-TPPI scheme with 128 scans per point for  $^{31}\text{P}$ , 256 scans per point for  $^{13}\text{C}$  and 2048 scans per point for  $^{15}\text{N}$ . The  $t_1$  increment was 54  $\mu\text{s}$ . The ramped CP [161] contact times were in the range 0.05 ms to 1.5 ms. The  $^1\text{H}$  high resolution spectrum was recorded using FSLG homonuclear decoupling [200] with a field strength of 104 kHz.

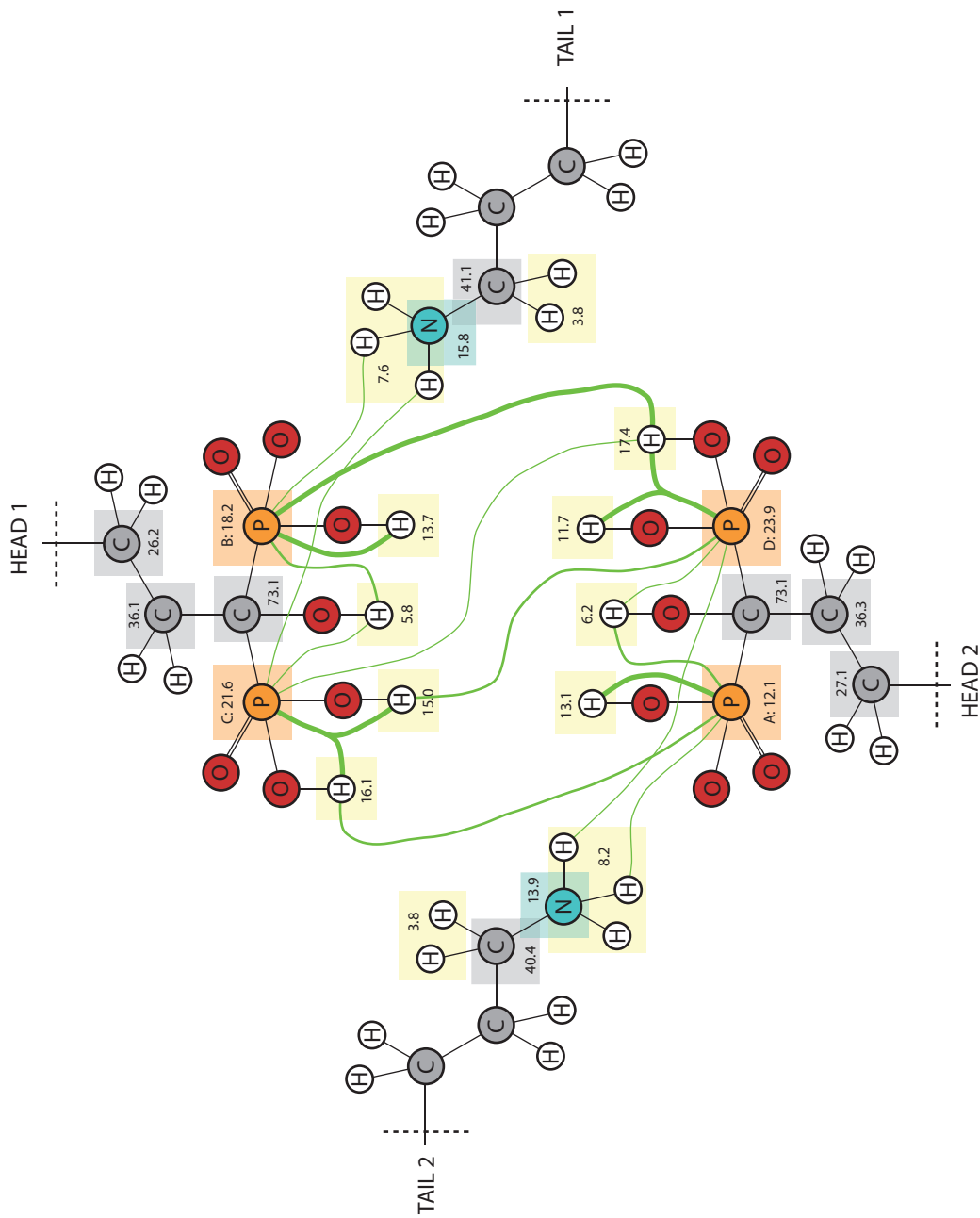
## 8.9 Conclusions

Figure 8.11 shows the current assignments of chemical shifts to the two molecules in the asymmetric unit of the neridronate polymorph. It also links atoms between which a cross peak has been seen in the  $^1\text{H}$ - $^{31}\text{P}$  correlation spectrum.

Some further questions need to be answered:

- Why are there three signals in the  $^{15}\text{N}$  CP-MAS spectrum?
- Why are some signals much broader than others (i.e. the  $^{15}\text{N}$  peak at 14 ppm, the  $^{13}\text{C}$  peak at 33 ppm and the  $^{31}\text{P}$  peak at 12 ppm)?
- How can the  $^{13}\text{C}$  signals for C4 and C5 be assigned?
- What structural interpretation can be made from the phosphorus CST measurements in Table 7.3?
- What confidence can be placed in the PXRD unit cell parameters? Can the space group be determined?

A lot of qualitative data has been recorded that could assist with crystal structure determination. However, this data alone has proven insufficient to determine the crystal structure. The constraints that they place are too vague to narrow the search space down. For instance, the PXRD data does not have a unique strong solution for



**Figure 8.11** Diagrammatic representation of structural conclusions drawn from experiments on crystalline neridronate. The diagram is not intended to represent genuine conformation of neridronate. For design purposes, the two molecules in the asymmetric unit have been split between C3 and C4, which are labelled 'Head 1' and 'Tail 1' from one molecule and 'Head 2' and 'Tail 2' from the other. Coloured lines denote close contacts uncovered by  $^1\text{H}$ - $^{31}\text{P}$  HETCOR. Thicker lines indicate a more intense cross peak, and possibly a shorter interatomic distance.

the unit cell dimensions, but several which are similar in standard but don't seem to quite fit all the data.

The next step in this study should be to get some trial crystal structures from a simulation program using classical interatomic forces. Such an approach tends to give a vast number of structures with similar energy to the global energy minimum. These trial structures could be compared with the PXRD, and the known close contacts from the  $^{31}\text{P}$  DQ/SQ correlation,  $^{31}\text{P}$ - $^{13}\text{C}$  DCP and  $^1\text{H}$ - $^{31}\text{P}$  HETCOR, to eliminate those trial structures that do not agree with the qualitative description from the solid-state NMR experiments.

Additionally, using CASTEP or otherwise, the  $^{31}\text{P}$  CSTs for the phosphonate groups in the surviving trial structures could be calculated and compared to the values in Table 7.3. A systematic approach of calculating the variation in CST with conformation, as in the study of Harper and Grant [130], is unlikely to be successful for neridronate because the molecule has too much flexibility (and so too many possible conformations to test).

So currently, interesting  $^{31}\text{P}$  CST data has been recorded for the neridronate. However, the process of converting CST data into useful structural data is decidedly non-trivial, and further work is required in this direction if progress is to be made on this project. The other NMR data also requires considerable interpretation to draw structural conclusions, as does the PXRD data. In all, a combination of these approaches, including CST measurement with other NMR data, PXRD and computation is likely to be the most productive approach.

## 8.10 Closing remarks

Initially we set out to investigate and improve the methods for measuring the CSA parameter of nuclear environments using solid-state NMR spectroscopy, particularly in the instances where multiple signals share the same isotropic chemical shift. First of all it was found, contrary to what is reported in the literature, that there are circumstances where it is possible to measure the CSA from overlapping signals by fitting one-dimensional sideband patterns with very slow MAS rate. However, the very slow spinning rate required to do this is not always practically obtainable, so attention was turned to two-dimensional isotropic–anisotropic shift correlation experiments. With these types of experiment, it has been demonstrated in this thesis that analysis of

a two-dimensional correlation pattern is superior to analysis of the one-dimensional projection pattern (due mostly to signal-to-noise ratio considerations), and it was again found that the CSA of overlapping signals could be determined, as was demonstrated experimentally on  $^{31}\text{P}$  signals from pamidronate. Even so, it was found that determination of CSA from these correlation experiments was not universally possible, and the limitations of these approaches are summarised in Chapter 4 (sideband–sideband correlation) and Chapter 5 (sideband–powder correlation).

Many of the problems with these methods stem from their model-fitting aspects, particularly determining the number of components that comprise an overlapping signal. The de Swiet experiment, which genuinely resolves signals by an anisotropic parameter, avoids model fitting, but has largely been forgotten about due to experimental difficulties. In Chapter 6, using a combination of modern approaches, the experimental procedure for the de Swiet experiment is improved, giving the experiment greater sensitivity, sharper signals and fewer artefacts. It is hoped that these improvements, which are demonstrated on pamidronate and FAME, will lead to a greater utilisation of the de Swiet experiment.

In Chapter 7, the CSA measurements of  $^{31}\text{P}$  signals in bis-phosphonates, made using the techniques developed in the preceding chapters, are used as part of a study into the structure of the bis-phosphonates when bound to bone mineral. Although no firm conclusions are reached regarding these structures, the CSA values determined do give an insight into the protonation states of the various phosphonate groups in the bone mineral complexes. Further work is required, probably involving computational methods, to determine the conformation of the carbon sidechains, which do not lend themselves to study by CSA measurements, because the CSA is typically very small.

In conclusion, the CSA is a useful parameter in structural investigation, and can often be more informative than the chemical shift alone, as demonstrated by numerous previous studies (see Chapter 3). It is important, therefore, to be able to measure it experimentally as accurately as possible and in as many circumstances as possible; the work in this thesis has made many steps towards this goal. However, it would be foolish to rely on this one parameter alone, and work towards solving the crystal structure of neridronate (Chapter 8) shows the importance of using a combination of solid-state NMR techniques and techniques from other fields of chemistry.

## Appendix A

---

# Euler angles

---

Euler angles are a handy, succinct way of describing a rotation between two reference frames, A and B. If the rotation is described by the Euler angles,  $\Omega_{AB} = (\alpha_{AB}, \beta_{AB}, \gamma_{AB})$ , then the rotation is defined as:

1. Rotate the frame co-incident with the A system by  $\alpha_{AB}$  about the  $z_A$ -axis.
2. Rotate by  $\beta_{AB}$  about the new  $y$ -axis.
3. Rotate by  $\gamma_{AB}$  about the new  $z$ -axis.

The axis frame is now coincident with B.

Euler angles are particularly useful when used with irreducible spherical tensors. This is because the tensor components evaluated in the new frame, B, are simply related to their values in the old frame A, by:

$$A_{mn}^B = \sum_k A_{mk}^A D_{kn}^{(2)}(\Omega_{AB}), \quad (A.1)$$

where  $D_{kn}^{(2)}(\Omega_{AB})$  is the Wigner rotation matrix, given by:

$$D_{kn}^{(2)}(\Omega_{AB}) = \exp(-im\alpha_{AB}) d_{kn}^{(2)}(\beta_{AB}) \exp(im\gamma_{AB}). \quad (A.2)$$

The reduced Wigner matrix elements,  $d_{kn}^{(2)}(\beta)$ , are given by:

$$\begin{aligned}
 d_{00}^{(2)}(\beta) &= \frac{1}{2}(3\cos^2\beta - 1) \\
 d_{0\pm 1}^{(2)}(\beta) = -d_{\pm 10}^{(2)}(\beta) &= \pm \sqrt{\frac{3}{8}} \sin 2\beta \\
 d_{0\pm 2}^{(2)}(\beta) = d_{\pm 20}^{(2)}(\beta) &= \pm \sqrt{\frac{3}{8}} \sin^2\beta \\
 d_{11}^{(2)}(\beta) = d_{-1-1}^{(2)}(\beta) &= \cos^2\beta - \frac{1}{2}(1 - \cos\beta) \\
 d_{1-1}^{(2)}(\beta) = d_{-11}^{(2)}(\beta) &= -\cos^2\beta + \frac{1}{2}(1 + \cos\beta) \\
 d_{12}^{(2)}(\beta) = d_{-2-1}^{(2)}(\beta) &= \frac{1}{2}(1 + \cos\beta) \sin\beta \\
 d_{21}^{(2)}(\beta) = d_{-1-2}^{(2)}(\beta) &= -\frac{1}{2}(1 + \cos\beta) \sin\beta \\
 d_{1-2}^{(2)}(\beta) = d_{2-1}^{(2)}(\beta) &= -\frac{1}{2}(1 - \cos\beta) \sin\beta \\
 d_{-21}^{(2)}(\beta) = d_{-12}^{(2)}(\beta) &= \frac{1}{2}(1 - \cos\beta) \sin\beta \\
 d_{22}^{(2)}(\beta) = d_{-2-2}^{(2)}(\beta) &= \frac{1}{4}(1 + \cos\beta)^2 \\
 d_{2-2}^{(2)}(\beta) = d_{-22}^{(2)}(\beta) &= \frac{1}{4}(1 - \cos\beta)^2.
 \end{aligned} \tag{A.3}$$

---

# Bibliography

---

- [1] J. Bernstein. *Polymorphism in molecular crystals* (Clarendon Press, Oxford, UK, 2002).
- [2] R. K. Harris. *Analyst*, **131**:351–373 (2006).
- [3] R. K. Harris. *J. Pharm. Pharmacol.*, **59**:225–239 (2007).
- [4] A. L. Arsenault & M. D. Grynpas. *Calcif. Tissue Int.*, **43**:219–225 (1988).
- [5] W. I. F. David. *Structure determination from powder diffraction data* (Oxford University Press, Oxford, UK, 2002).
- [6] K. D. M. Harris, M. Tremayne & B. M. Kariuki. *Angew. Chem. Int. Ed.*, **40**:1621–1651 (2001).
- [7] J. W. Wisser. *J. Appl. Cryst.*, **2**:89–95 (1969).
- [8] P. D. Louer & L. R. Vargas. *J. Appl. Cryst.*, **15**:542–545 (1982).
- [9] P. E. Werner, L. Eriksson & M. Westdahl. *J. Appl. Cryst.*, **18**:367–370 (1985).
- [10] H. M. Rietveld. *J. Appl. Cryst.*, **2**:65–71 (1969).
- [11] D. E. Bugay. *Adv. Drug Deliv. Rev.*, **48**:43–65 (2001).
- [12] G. M. Day, W. D. S. Motherwell, H. Ammon *et al.* *Acta Cryst. B*, **61**:511–527 (2005).
- [13] D. A. Case, T. E. Cheatham, T. Darden *et al.* *J. Computat. Chem.*, **26**:1668–1688 (2005).
- [14] A. T. Brunger & P. D. Adams. *Acc. Chem. Res.*, **35**:404–412 (2002).
- [15] D. R. Hartree. *Math. Proc. Camb. Philo. Soc.*, **24**:89–132 (1928).
- [16] V. Fock. *Z. Phys.*, **61**:126–148 (1930).

- [17] C. Møller & M. S. Plesset. *Phys. Rev.*, **46**:618–622 (1934).
- [18] M. J. Frisch, G. W. Trucks, H. B. Schlegel *et al.* Gaussian 03, Revision C.02 (2003). Gaussian, Inc., Wallingford, CT, 2004.
- [19] M. F. Guest, I. J. Bush, H. I. J. van Dam *et al.* *Mol. Phys.*, **46**:719–747 (2006).
- [20] P. Hohenburg & W. Kohn. *Phys. Rev.*, **136**:B864–B871 (1964).
- [21] W. Kohn & L. J. Sham. *Phys. Rev.*, **140**:A1133–A1138 (1965).
- [22] M. D. Segall, P. J. D. Lindan, M. J. Probert *et al.* *J. Phys. Cond. Matt.*, **14**:2717–2744 (2002).
- [23] C. J. Pickard & F. Mauri. *Phys. Rev. B*, **63**:245101 (2001).
- [24] R. K. Harris, P. Hodgkinson, C. J. Pickard, J. R. Yates & V. Zorin. *Magn. Reson. Chem.*, **45**:S174–S186 (2007).
- [25] M. H. Levitt. *Spin Dynamics: Basics of Nuclear Magnetic Resonance* (Wiley, Chichester, UK, 2001).
- [26] M. J. Duer (editor). *Solid-state NMR Spectroscopy: Principles and Applications* (Blackwell Science, Oxford, UK, 2002).
- [27] J. Keeler. *Understanding NMR Spectroscopy* (Wiley, Chichester, UK, 2005).
- [28] M. E. Rose. *Elementary Theory of Angular Momentum* (Wiley, New York, US, 1967).
- [29] O. N. Antzutkin. *Prog. Nucl. Magn. Reson. Spectrosc.*, **35**:203–266 (1999).
- [30] N. Bloembergen & T. J. Rowland. *Acta Metall.*, **1**:731–746 (1953).
- [31] S. K. Zaremba. *Ann. Mat. Pura. Appl.*, **73**:293–317 (1966).
- [32] H. Conroy. *J. Chem. Phys.*, **47**:5307–5318 (1967).
- [33] V. B. Cheng, H. H. Suzukawa & M. Wolfsberg. *J. Chem. Phys.*, **59**:3992–3999 (1973).
- [34] M. Bak & N. C. Nielsen. *J. Magn. Reson.*, **125**:132–139 (1997).
- [35] T. G. Oas, G. P. Drobny & F. W. Dahlquist. *J. Magn. Reson.*, **78**:408–424 (1988).

- [36] E. R. Andrew, A. Bradbury & R. G. Eades. *Nature*, **183**:1802 (1959).
- [37] I. J. Lowe. *Phys. Rev. Lett.*, **2**:285 (1959).
- [38] M. H. Levitt. *J. Magn. Reson.*, **82**:427–433 (1989).
- [39] P. Hodgkinson & L. Emsley. *J. Chem. Phys.*, **107**:4808–4816 (1997).
- [40] J. R. Sachleben. *J. Magn. Reson.*, **183**:123–133 (2006).
- [41] E. L. Hahn. *Phys. Rev.*, **80**:580–594 (1950).
- [42] P. Bachmann, W. P. Aue, L. Müller & R. R. Ernst. *J. Magn. Reson.*, **28**:29–39 (1977).
- [43] D. J. States, R. A. Haberkorn & D. J. Ruben. *J. Magn. Reson.*, **48**:286–292 (1982).
- [44] D. Marion & K. Wuthrich. *Biochem. Biophys. Res. Comm.*, **113**:967–974 (1983).
- [45] G. Bodenhausen, H. Kogler & R. R. Ernst. *J. Magn. Reson.*, **58**:370–388 (1984).
- [46] M. H. Levitt, P. K. Madhu & C. E. Hughes. *J. Magn. Reson.*, **155**:300–306 (2002).
- [47] A. Jerschow & R. Kumar. *J. Magn. Reson.*, **160**:59–64 (2003).
- [48] A. Pines, M. G. Gibby & J. S. Waugh. *J. Chem. Phys.*, **56**:1776–1777 (1972).
- [49] A. Pines, M. G. Gibby & J. S. Waugh. *J. Chem. Phys.*, **59**:569–590 (1973).
- [50] S. R. Hartmann & E. L. Hahn. *Phys. Rev.*, **128**:2042–2053 (1962).
- [51] L. R. Sarles & R. M. Cotts. *Phys. Rev.*, **111**:853–859 (1958).
- [52] A. E. Bennet, C. M. Rienstra, M. Auger & K. V. Lakshmi. *J. Chem. Phys.*, **103**:6951–6958 (1995).
- [53] B. M. Fung, A. K. Khitrin & K. Ermolaev. *J. Magn. Reson.*, **142**:97–101 (2000).
- [54] M. Bak, J. T. Rasmussen & N. C. Nielsen. *J. Magn. Reson.*, **147**:296–330 (2000).
- [55] M. Veshtort & R. G. Griffin. *J. Magn. Reson.*, **178**:248–282 (2006).

- [56] M. M. Maricq & J. S. Waugh. *J. Chem. Phys.*, **70**:3300–3316 (1979).
- [57] J. Herzfeld & A. E. Berger. *J. Chem. Phys.*, **73**:6021–6030 (1980).
- [58] D. Fenzke, B. Maess & H. Pfeifer. *J. Magn. Reson.*, **88**:172–176 (1990).
- [59] A. C. Kolbert, D. P. Raleigh, M. H. Levitt & R. G. Griffin. *J. Chem. Phys.*, **90**:679–689 (1989).
- [60] R. C. Zeigler, R. A. Wind & G. E. Maciel. *J. Magn. Reson.*, **79**:299–306 (1988).
- [61] A. Bax, N. M. Szeverenyi & G. E. Maciel. *J. Magn. Reson.*, **55**:494–497 (1983).
- [62] A. Bax, N. M. Szeverenyi & G. E. Maciel. *J. Magn. Reson.*, **52**:147–152 (1983).
- [63] Z. H. Gan. *J. Am. Chem. Soc.*, **114**:8307–8310 (1992).
- [64] J. Z. Hu, A. M. Orendt, D. W. Alderman *et al.* *Solid State Nucl. Magn. Reson.*, **3**:181–197 (1994).
- [65] J. Z. Hu, W. Wang, F. Liu *et al.* *J. Magn. Reson. A*, **113**:210–222 (1995).
- [66] D. W. Alderman, G. McGeorge, J. Z. Hu, R. J. Pugmire & D. M. Grant. *Mol. Phys.*, **95**:1113–1126 (1998).
- [67] M. A. Alla, E. I. Kundla & E. T. Lippmaa. *J. Exp. Theor. Phys. Lett.*, **27**:194–197 (1978).
- [68] Y. Yarim-Agaev, P. N. Tutunjian & J. S. Waugh. *J. Magn. Reson.*, **47**:51–60 (1982).
- [69] R. Tycko, G. Dabbagh & P. A. Mirau. *J. Magn. Reson.*, **85**:265–274 (1989).
- [70] S. F. Liu, J. D. Mao & K. Schmidt-Rohr. *J. Magn. Reson.*, **155**:15–28 (2002).
- [71] R. Witter, S. Hesse & U. Sternberg. *J. Magn. Reson.*, **161**:35–42 (2003).
- [72] R. M. Orr & M. J. Duer. *J. Magn. Reson.*, **181**:1–8 (2006).
- [73] A. Bax, N. M. Szeverenyi & G. E. Maciel. *J. Magn. Reson.*, **51**:400–408 (1983).
- [74] Y. Ishii & T. Terao. *J. Chem. Phys.*, **109**:1366–1374 (1998).
- [75] J. C. C. Chan & R. Tycko. *J. Chem. Phys.*, **118**:8378–8389 (2003).
- [76] Y. K. Lee, N. D. Kurur, M. Helmle *et al.* *Solid State Nucl. Magn. Reson.*, **242**:304–309 (1995).

- [77] W. T. Dixon. *J. Magn. Reson.*, **44**:220–223 (1981).
- [78] W. T. Dixon. *J. Chem. Phys.*, **77**:1800–1809 (1982).
- [79] S. F. de Lacroix, J. J. Titman, A. Hagemeyer & H. W. Spiess. *J. Magn. Reson.*, **97**:435–443 (1992).
- [80] O. N. Antzutkin, S. C. Shekar & M. H. Levitt. *J. Magn. Reson. A.*, **115**:7–19 (1995).
- [81] L. Shao & J. J. Titman. *Prog. Nucl. Magn. Reson. Spectrosc.*, **51**:103–137 (2007).
- [82] T. Gullion. *J. Magn. Reson.*, **85**:614–619 (1989).
- [83] M. Strohmeier & D. M. Grant. *J. Magn. Reson.*, **168**:296–307 (2004).
- [84] C. Crockford, H. Geen & J. J. Titman. *Chem. Phys. Lett.*, **344**:367–373 (2001).
- [85] L. Shao, C. Crockford, H. Geen, G. Grasso & J. J. Titman. *J. Magn. Reson.*, **167**:75–86 (2004).
- [86] R. M. Orr, M. J. Duer & S. E. Ashbrook. *J. Magn. Reson.*, **174**:301–309 (2005).
- [87] L. Shao, C. Crockford & J. J. Titman. *J. Magn. Reson.*, **178**:155–161 (2006).
- [88] R. M. Orr & M. J. Duer. *Solid State Nucl. Magn. Reson.*, **30**:1–8 (2006).
- [89] B. Eléna, S. Hediger & L. Emsley. *J. Magn. Reson.*, **160**:40–46 (2003).
- [90] Y. Mou, P. H. Chen, H. W. Lee & J. C. C. Chan. *J. Magn. Reson.*, **187**:352–356 (2007).
- [91] B. J. Wylie, W. T. Franks & C. M. Rienstra. *J. Phys. Chem.*, **110**:10926–10936 (2006).
- [92] M. Hong. *J. Am. Chem. Soc.*, **122**:3762–3770 (2000).
- [93] Y. Nishiyama, T. Yamazaki & T. Terao. *J. Chem. Phys.*, **124**:064304 (2006).
- [94] T. M. de Swiet. *J. Chem. Phys.*, **110**:5231–5237 (1999).
- [95] T. M. de Swiet. *J. Chem. Phys.*, **112**:8567–8572 (2000).
- [96] T. M. de Swiet, M. Tomaselli & A. Pines. *Chem. Phys. Lett.*, **285**:59–63 (1998).
- [97] Z. Gan, D. M. Grant & R. R. Ernst. *Chem. Phys. Lett.*, **254**:349–357 (1996).

- [98] M. S. Ironside. *Separation of overlapping solid-state NMR peaks by chemical shift anisotropy*. Master's thesis, University of Cambridge (2005).
- [99] D. H. Barich, J. C. Facelli, J. Z. Hu *et al.* *Magn. Reson. Chem.*, **39**:115–121 (2001).
- [100] S. Dusold & A. Sebald. *Prog. Nucl. Magn. Reson. Spectrosc.*, **41**:185–264 (2000).
- [101] T. Karlsson, J. M. Popham, J. R. Long, N. Oyler & G. P. Drobny. *J. Am. Chem. Soc.*, **125**:7394–7407 (2003).
- [102] T. Gullion & J. Schaefer. *J. Magn. Reson.*, **81**:196–200 (1989).
- [103] K. T. Mueller, T. P. Jarvie, D. J. Aurentz & B. W. Roberts. *Chem. Phys. Lett.*, **242**:535–542 (1995).
- [104] A. W. Hing, S. Vega & J. Schaefer. *J. Magn. Reson.*, **96**:205–209 (1992).
- [105] A. W. Hing, S. Vega & J. Schaefer. *J. Magn. Reson. A*, **103**:151–162 (1993).
- [106] M. Hohwy, H. J. Jakobsen, M. Eden, M. H. Levitt & N. C. Nielsen. *J. Chem. Phys.*, **108**:2686–2694 (1998).
- [107] D. P. Raleigh, M. H. Levitt & R. G. Griffin. *Chem. Phys. Lett.*, **146**:71–76 (1988).
- [108] B. C. Gerstein, R. G. Pembleton, R. C. Wilson & L. M. Ryan. *J. Chem. Phys.*, **66**:361–362 (1977).
- [109] D. A. Middleton, X. Peng, D. Saunders *et al.* *Chem. Commun.*, **17**:1976–1977 (2002).
- [110] S. Macholl, F. Börner & G. Buntkowsky. *Chem. Eur. J.*, **10**:4808–4816 (2004).
- [111] J. Dutour, N. Guillou, C. Huguenard *et al.* *Solid State Sci.*, **6**:1059–1067 (2004).
- [112] D. J. Hirsh, J. Hammer, W. L. Maloy, J. Blazyk & J. Schaefer. *Biochem.*, **35**:12733–12741 (1996).
- [113] E. R. Wise, S. Maltsev, M. E. Davies *et al.* *Chem. Mat.*, **19**:5055–5057 (2007).
- [114] D. A. Middleton, Z. Ahmed, C. Glaubitz & A. Watts. *J. Magn. Reson.*, **147**:366–370 (2000).

- [115] B. Eléna, G. Pintacuda, N. Mifsud & L. Emsley. *J. Am. Chem. Soc.*, **128**:9555–9560 (2006).
- [116] C. J. Pickard, E. Salager, G. Pintacuda, B. Elena & L. Emsley. *J. Am. Chem. Soc.*, **129**:8932–8933 (2007).
- [117] K. Nomura, K. Takegoshi, T. Terao, K. Uchida & M. Kainoshio. *J. Am. Chem. Soc.*, **121**:4064–4065 (1999).
- [118] L. Szilágyi. *Prog. Nucl. Magn. Reson. Spectrosc.*, **27**:325–443 (1995).
- [119] D. S. Wishart, B. D. Sykes & F. M. Richards. *J. Mol. Bio.*, **222**:311–333 (1991).
- [120] D. S. Wishart, B. D. Sykes & F. M. Richards. *Biochem.*, **31**:1647–1651 (1992).
- [121] S. Spera & A. Bax. *J. Am. Chem. Soc.*, **113**:5490–5492 (1991).
- [122] H. B. Le & E. Oldfield. *J. Biomol. NMR*, **4**:341–348 (1993).
- [123] M. Iwadate, T. Asakura & M. P. Williamson. *J. Biomol. NMR*, **13**:199–211 (1999).
- [124] A. C. de Dios, J. G. Pearson & E. Oldfield. *J. Am. Chem. Soc.*, **115**:9768–9773 (1993).
- [125] R. K. Harris, P. Y. Ghi, R. B. Hammond *et al.* *Magn. Reson. Chem.*, **44**:325–333 (2006).
- [126] E. D. L. Smith, R. B. Hammond, M. J. Jones *et al.* *J. Phys. Chem. B*, **105**:5818–5826 (2001).
- [127] J. C. Facelli & D. M. Grant. *Top. Stereo.*, **19**:1–61 (1989).
- [128] E. A. Christopher, R. K. Harris & R. A. Fletton. *Solid-state Nucl. Magn. Reson.*, **1**:93–101 (1992).
- [129] L. Shao, J. R. Yates & J. J. Titman. *J. Phys. Chem. A*, **111**:13126–13132 (2007).
- [130] J. K. Harper & D. M. Grant. *Cryst. Grow. Des.*, **6**:2315–2321 (2006).
- [131] J. Smith, E. MacNamara, D. Raftery, T. Borchardt & S. Bryn. *J. Am. Chem. Soc.*, **120**:11710–11713 (1998).
- [132] J. R. Smith, W. Z. Xu & D. Raftery. *J. Phys. Chem. B*, **110**:7766–7776 (2006).

- [133] M. Strohmeier, A. M. Orendt, D. W. Alderman & D. M. Grant. *J. Am. Chem. Soc.*, **123**:1713–1722 (2001).
- [134] Z. Ma, M. D. Halling, M. S. Solum *et al.* *J. Phys. Chem. A*, **111**:2020–2027 (2007).
- [135] J. K. Harper, J. C. Facelli, D. H. Barich *et al.* *J. Am. Chem. Soc.*, **124**:10589–10595 (2002).
- [136] D. Brouwer. *J. Magn. Reson.*, **194**:136–146 (2008).
- [137] N. Tjandra & A. Bax. *J. Am. Chem. Soc.*, **119**:9576–9577 (1997).
- [138] R. H. Havlin, H. B. Le, D. D. Laws, A. C. de Dios & E. Oldfield. *J. Am. Chem. Soc.*, **119**:11951–11958 (1997).
- [139] H. H. Sun, L. K. Sanders & E. Oldfield. *J. Am. Chem. Soc.*, **124**:5486–5495 (2002).
- [140] E. Czink, A. G. Csaszar, G. Magyarfalvi, P. R. Schreiner & W. D. Allen. *J. Am. Chem. Soc.*, **129**:1568–1577 (2007).
- [141] M. Strohmeier & D. M. Grant. *J. Am. Chem. Soc.*, **126**:966–977 (2004).
- [142] M. J. Potrzebowski, C. Schneider & P. Tekely. *Chem. Phys. Lett.*, **313**:569–574 (1999).
- [143] G. McGeorge, R. K. Harris, A. S. Batsanov *et al.* *J. Phys. Chem. A*, **102**:3505–3513 (1998).
- [144] T. G. Oas, C. J. Hartzell, F. W. Dahlquist & G. P. Drobny. *J. Am. Chem. Soc.*, **109**:5962–5966 (1987).
- [145] J. Precechtelova, M. L. Munzarova, P. Novak & V. Sklenar. *J. Phys. Chem. B*, **111**:2658–2667 (2007).
- [146] T. J. T. Pinheiro & A. Watts. *Biochem.*, **33**:2451–2458 (1994).
- [147] J. Jiao, M. Y. Lee, C. E. Barnes & E. W. Hagaman. *Magn. Reson. Chem.*, **46**:690–692 (2008).
- [148] S. S. Kidambi, D. K. Lee & A. Ramamoorthy. *Inorg. Chem.*, **42**:3142–3151 (2003).
- [149] X. L. Yao & M. Hong. *J. Am. Chem. Soc.*, **124**:2730–2738 (2002).

- [150] S. Wi, H. H. Sun, E. Oldfield & M. Hong. *J. Am. Chem. Soc.*, **127**:6451–6458 (2005).
- [151] A. C. Olivieri. *J. Magn. Reson. A*, **123**:207–210 (1996).
- [152] M. H. Levitt, G. Bodenhausen & R. R. Ernst. *J. Magn. Reson.*, **58**:462–472 (1984).
- [153] O. N. Antzutkin, Y. K. Lee & M. H. Levitt. *J. Magn. Reson.*, **135**:144–155 (1998).
- [154] J. E. Rich, M. N. Manalo & A. C. de Dios. *J. Phys. Chem. A.*, **104**:5837–5842 (2000).
- [155] M. S. Ironside, R. S. Stein & M. J. Duer. *J. Magn. Reson.*, **188**:49–55 (2007).
- [156] N. J. Clayden, C. M. Dobson, L. Y. Lian & D. J. Smith. *J. Magn. Reson.*, **69**:476–487 (1986).
- [157] Visual Numerics. PV-Wave Advantage (1993). Computer program.
- [158] P. Bevington. *Data Reduction and Error Analysis for the Physical Sciences* (McGraw-Hill, New York, 1967).
- [159] R. M. Orr. *Measuring anisotropic interactions using solid-state NMR spectroscopy*. Ph.D. thesis, University of Cambridge (2006).
- [160] D. Vega, D. Fernández & J. A. Ellena. *Acta Cryst.*, **C58**:m77–m80 (2002).
- [161] G. Metz, X. L. Wu & S. O. Smith. *J. Magn. Reson. A.*, **110**:219–227 (1994).
- [162] R. Freeman & E. Kupce. *J. Biomol. NMR*, **27**:101–113 (2003).
- [163] S. R. Deans. *The Radon transform and some of its applications* (Wiley, Chichester, UK, 1983).
- [164] S. Zhang, G. Gangal & H. Uludağ. *Chem. Soc. Rev.*, **36**:507–531 (2007).
- [165] M. D. Francis, R. G. G. Russell & H. Fleisch. *Science*, **165**:1264–1266 (1969).
- [166] R. G. G. Russell, H. Fleisch & M. D. Francis. *Science*, **165**:1262–1264 (1969).
- [167] F. H. Ebetino, M. D. Francis, M. J. Rogers & R. G. G. Russell. *Rev. Contemp. Pharmacother.*, **9**:233–243 (1998).

- [168] E. van Beek, M. Hoekstra, M. van de Ruit, C. Lowik & S. Papapoulos. *J. Bone Miner. Res.*, **9**:1875–1882 (1994).
- [169] G. H. Nancollas, R. Tang, R. J. Phipps *et al.* *Bone*, **38**:617–627 (2006).
- [170] A. Ebrahimpour & M. D. Francis. In O. L. M. Bijvoet, H. A. Fleisch, R. E. Canfield & R. G. G. Russell (editors), *Bis-phosphonate on bones*, pages 125–136 (Elsevier, Amsterdam, 1995).
- [171] P. Masarachia, M. Weinreb, R. Balena & G. A. Rodan. *Bone*, **19**:281–290 (1996).
- [172] E. van Beek, E. Pieterman, L. Cohen, C. Löwik & S. Papapoulos. *Biochem. Biophys. Res. Comm.*, **264**:108–111 (1999).
- [173] H. Monkkonen, S. Auriola, P. Lehenkari *et al.* *Brit. J. Pharm.*, **147**:437–445 (2006).
- [174] L. Widler, K. A. Jaeggi, M. Glatt *et al.* *J. Med. Chem.*, **45**:3721–3738 (2002).
- [175] E. van Beek, C. Lowik, I. Que & S. Papapoulos. *J. Bone Miner. Res.*, **11**:1492–1497 (1996).
- [176] J. C. Frith, J. Monkkonen, S. Auriola, H. Monkkonen & M. J. Rogers. *Arthritis Rheum.*, **44**:2201–2210 (2001).
- [177] L. I. Plotkin, R. S. Weinstein, A. M. Parfitt *et al.* *J. Clin. Invest.*, **104**:1363–1374 (1999).
- [178] L. I. Plotkin, S. C. Manolagas & T. Bellido. *Bone*, **39**:443–452 (2006).
- [179] J. E. Dunford, K. Thompson, F. P. Coxon *et al.* *J. Pharmacol. Exp. Ther.*, **296**:235–242 (2001).
- [180] E. R. van Beek, C. W. G. M. Löwik, F. H. Ebetino & S. E. Papapoulos. *Bone*, **23**:437–442 (1998).
- [181] R. G. G. Russell, Z. Xia, J. E. Dunford *et al.* *Ann. N.Y. Acad. Sci.*, **1117**:209–257 (2007).
- [182] R. G. G. Russell, N. B. Watts, F. H. Ebetino & M. J. Rogers. *Osteoporos. Int.*, **19**:733–759 (2008).
- [183] G. Grossmann, A. Grossmann, G. Ohms *et al.* *Magn. Reson. Chem.*, **38**:11–16 (2000).

- [184] Y. Zhang & E. Oldfield. *J. Phys. Chem. B*, **108**:19533–19540 (2004).
- [185] J. Robinson, I. Cukrowski & H. M. Marques. *J. Mol. Struc.*, **825**:134–142 (2006).
- [186] S. Mukherjee, Y. Song & E. Oldfield. *J. Am. Chem. Soc.*, **130**:1264–1273 (2008).
- [187] F. H. Ebetino, C. N. Roze, C. E. McKenna *et al.* *J. Organomet. Chem.*, **690**:2679–2687 (2005).
- [188] J. Mao, S. Mukherjee, Y. Zhang *et al.* *J. Am. Chem. Soc.*, **128**:14485–14497 (2006).
- [189] J. Schaefer, R. A. McKay & E. O. Stejskal. *J. Magn. Reson.*, **34**:443–447 (1979).
- [190] J. H. Davies, K. R. Jeffrey, M. Bloom, M. I. Valic & T. P. Higgs. *Chem. Phys. Lett.*, **42**:390–394 (1976).
- [191] J. T. Timonen, E. Pohjala, H. Nikander & T. T. Pakkanen. *Pharm. Res.*, **15**:110–115 (1998).
- [192] G. Cho, Y. Wu & J. L. Ackerman. *Science*, **300**:1123–1127 (2003).
- [193] D. Vega, R. Baggio & M. T. Garland. *Acta Cryst.*, **C52**:2198–2201 (1996).
- [194] V. M. Coiro & D. Lamba. *Acta Cryst.*, **C45**:446–448 (1989).
- [195] N. Redman-Furey, M. Dicks, A. Bigelow-Kern *et al.* *J. Pharm. Sci.*, **94**:893–911 (2005).
- [196] G. R. Desiraju. *Cryst. Eng. Comm.*, **9**:91–92 (2007).
- [197] M. Bertmer & H. Eckert. *Solid-state Nucl. Magn. Reson.*, **15**:139–152 (1999).
- [198] Y. Pan, T. Gullion & J. Schaefer. *J. Magn. Reson.*, **90**:330–340 (1990).
- [199] W. L. Gossman, S. R. Wilson & E. Oldfield. *Acta Cryst.*, **C58**:m599–m600 (2002).
- [200] A. Bielecki, A. C. Kolbert & M. H. Levitt. *Chem. Phys. Lett.*, **155**:341–346 (1989).